MULTI-SCALE STUDIES OF PARTICULATE-CONTINUUM INTERFACE SYSTEMS UNDER AXIAL AND TORSIONAL LOADING CONDITIONS

A Dissertation
Presented to
The Academic Faculty

by

Alejandro Martinez

In Partial Fulfillment
of the Requirements for the Degree
of Doctor of Philosophy in the
School of Civil and Environmental Engineering

Georgia Institute of Technology
December 2015

MULTI-SCALE STUDIES OF PARTICULATE-CONTINUUM INTERFACE SYSTEMS UNDER AXIAL AND TORSIONAL LOADING CONDITIONS

Approved by:

Dr. J. David Frost, Advisor
School of Civil and Environmental Eng.
Georgia Institute of Technology

Dr. Gregory L. Hebeler
Geotechnical Group
Golder Associates Inc.

Dr. Susan E. Burns
School of Civil and Environmental Eng.
Georgia Institute of Technology

Dr. Arun M. Gokhale
School of Material Science and Eng.
Georgia Institute of Technology

Dr. Paul W. Mayne
School of Civil and Environmental Eng.
Georgia Institute of Technology

Date Approved: 11/09/15

Dedicated to my past, current and future teachers

ACKNOWLEDGEMENTS

It is of great importance for me to acknowledge the support that several individuals have provided to me during my graduate studies. Foremost, I want to express my appreciation for the guidance and advice provided by my advisor, Dr. J. David Frost. His unique insights on engineering and science have taught me to look at solutions from different angles. During the last five years he has shared very important lessons on research, academia, education, career, collaborations and life in general. His unselfish support in many areas related to my career and personal development are evidence of his kind and generous personality.

I also want to thank my thesis committee for their guidance throughout my Ph.D. studies. The interactions I had with each one of them have provided me with invaluable academic lessons. Dr. Burns served as a role model for me and helped me understand the mechanics of granular media, the classes and discussions with Dr. Mayne helped me discern "what really matters" in the engineering profession, discussions with Dr. Hebeler provided me with expert's advice on my research topic and on the working of geotechnical engineering industry, and the classes I took with Dr. Gokhale allowed me to reach outside my field in order to bring important aspects of material science and engineering into my research. I should also acknowledge the geotechnical faculty that did not serve on my thesis committee but with whom I also interacted and had the opportunity to learn from them, including Dr. Santamarina, Dr. Arson, Dr. Huang, Dr. Assimaki and Dr. Rix. Finally, I want to thank Dr. Kurtis for nominating me for the International Student Leadership award and for providing me with career advice.

My family has provided me with unconditional support throughout my entire life. I want to express my highest appreciation for the support provided by my parents, Arturo Martínez and Hilda Vela de Martínez, sister, Liliana Martínez, grandmothers, Romelia

Barrera de Martínez and Berthila Díaz de Vela, and the rest of my family as well. Chelsea Hopkins has been a pillar for my life in the US, so I would like to thank her as well.

The friendship and interactions with the members of Dr. Frost's research lab have also been an important part of my graduate studies. In particular, I want to acknowledge Albert Liu, Jackson Su, Mahdi Roozbahani, Fikret Atalay, Jie Cao, Tianlong Xu, Andres Peralta, Mengmeng Liu, Andrew Fuggle, Mesut Turel and Topraj Gurung. I thoroughly enjoyed the conversations during lunch, group meetings and RMP gatherings. Furthermore, I want to acknowledge the friends that I have made in the US, which include Josh Smith, Marco Terzariol, Matthieu Leibovici, Chloe Fabien, Spyros Pavlidis, Longde Jin, Gaby Cortez, Andrea Ortiz, Eduardo Rivera, Sebastian Lopez, Sergio Salinas, Valentina Prado, Paulina Vargas, Andres Santamaria, Adrian Frias and Hugo Oliva. My friends from back home and all the members of the GT Geosociety should also be acknowledged.

I want to thank Dorsa Elmi for assisting with the performance of part of the tests presented in Chapter 8 of this thesis and Longde Jin for teaching me how to use the direct shear apparatus. I want to acknowledge the help of the CEE machine shop team, consisting of Andy Udell, Billy Plum and Blake Baklini, who provided me with significant help during the machining of my experimental setups. The powdered phenolic resin provided by PLENCO allowed for the performance of part of the tests presented in Chapters 4 and 8. Finally, the financial support provided by the Goizueta Foundation and the Golder Foundation are greatly acknowledged.

TABLE OF CONTENTS

LIST OF TABLES

LIST OF FIGURES

Page

SUMMARY

The study of the shear behavior of particulate (soil) – continuum (man-made material) interfaces has received significant attention during the last three decades. The historical belief that the particulate – continuum interface represents the weak link in most geotechnical systems has been shown to be incorrect for many situations. Namely, prescribing properties of the continuum material, such as its surface roughness and hardness, can result in interface strengths that are equal to the contacting soil mass internal shear strength. This research expands the engineering implications of these findings by studying the response of interface systems in different loading conditions. Specifically, the axial and torsional shear modes are studied in detail. Throughout this thesis it is shown that taking an engineering approach to design the loading conditions induced to the interface system can result in interface strengths that exceed the previously considered limiting shear strength of the contacting soil.

Fundamental experimental and numerical studies on specimens of different types of sand subjected to torsional and axial interface shear highlighted the inherent differences of these processes. Specifically, micro-scale soil deformation measurements showed that torsional shear induces larger soil deformations as compared to axial shear, as well as complex volume-change tendencies consisting of dilation and contraction in the primary and secondary shear zones. Studies on the global response of torsional and axial shear tests showed that they are affected differently by soil properties such as particle angularity and roughness. This difference in global behavior highlights the benefits of making systems that transfer load to the contacting soil in different manners available for use in geotechnical engineering. Discrete Element Modeling (DEM) simulations allowed for internal information of the specimens to be studied, such as their fabric and shear-induced loading conditions. These findings allowed for the development

of links between the measured micro-scale behavior and the observed global-scale response.

The understanding of the behavior of torsional and axial interfaces has allowed provides a framework for the development of enhanced geotechnical systems and applications. The global response of torsional shear found to induce larger cyclic contractive tendencies within the contacting soil mass. Therefore, this shear mode is more desirable than the conventional axial shear for the study of phenomena that depend on soil contractive behavior, such as liquefaction. A study on the influence of surface roughness form revealed that surfaces with periodic profiles of protruding elements that prevent clogging are capable of mobilizing interface friction angles that are 20 to 60% larger than the soil friction angle. These findings have direct implications in engineering design since their implementation can result in more resilient and sustainable geotechnical systems.

CHAPTER 1

INTRODUCTION

The studies presented in this thesis have the goal of setting the framework for new and/or enhanced geotechnical systems to be developed. Engineering the manner in which geotechnical systems that rely on interface friction transfer load to the soil can result in more efficient systems that in turn contribute to the evolution towards more economical, sustainable and resilient structures. Examples of these systems include driven piles and drilled shafts and the development of new site characterization tools. In general, Chapters 1, 2 and 3 provide introductory information for the research presented in this thesis, Chapters 4, 5 and 6 focus on the development of an understanding of the fundamental processes involved in axial and torsional shear, and Chapters 7 and 8 provide investigations of direct applications of enhanced interface behavior for geotechnical systems. The following section of this introductory chapter presents the motivation for this study, followed by brief descriptions of the following eight chapters.

1.1 Motivation for this Study

1.1.1 Characterization of Torsional Interface Shear-Induced Soil Deformations and Loading Conditions

During the last three decades, significant research has been performed on the behavior of particulate (soil) – continuum (man-made material) interfaces. These findings have resulted in important advances in the understanding of the behavior of these interfaces, as well as in improvements in the capacity of interface systems. However, all of these studies have focused on axially loaded interfaces, such as those present in the skin friction transfer occurring at the interface of a deep foundation. On the other hand, torsional interfaces (e.g. skin friction transfer when a cylindrical pile is rotated) have not

yet received direct attention. While there is a growing literature on the behavior of piles subjected to torsional loading, these studies focus on analytical solutions based on continuum mechanics and the theory of elasticity (see Chapter 2), thus not including an explicit account for the interactions between the soil and the structure.

In this context, part of the research presented in this thesis focuses on the characterization of the shear-induced soil deformations and loading conditions caused by torsional interface shear. The results indicate an inherently different behavior than that observed during axial shear. These findings can be used to develop applications where torsional interfaces can improve the performance of specific systems, as well as be used to study the soil behavior under different loading conditions.

1.1.2 Comparison of Torsional Interface Behavior with Axial Interface Behavior

A significant portion of this thesis has the objective of understanding the differences between the behavior of interfaces loaded torsionally and axially. As most geotechnical systems are loaded axially, identifying applications where torsional interfaces provide increased capacity is highly beneficial. Furthermore, this research shows that torsional and axial interface shear are affected differently by certain soil properties (e.g. particle angularity and roughness) and states (e.g. stress anisotropy), thus showing that studying the soil behavior under both conditions is desirable for geotechnical investigations. Future research work is identified including developing a site characterization probe that has the ability to measure soil response under axial and torsional interface shear loading.

1.1.3 Assessment of Torsional Shear as Means to Study Soil Strength Degradation and Excess Pore Pressure Generation

Recent natural disasters, such as the 2011 earthquakes in New Zealand, have drawn attention to the prediction of post-liquefaction soil properties. Considering the

well-known difficulties of obtaining undisturbed samples of sandy and silty liquefiable soils, in-situ tests have become the principal tools for the study of the behavior of these soils. As such, a study on the undrained cyclic behavior of torsional interface shear tests allows for the investigation of the potential benefits for developing an in-situ testing device that measures the soil response under torsional shear as part of the study of liquefiable soils.

1.1.4 Analysis of Axial Interface Behavior for Optimized System Performance

Uesugi and Kishida (1986) showed that the interface friction angle increases as the surface roughness of the continuum material increases up to a value called the critical roughness. At this point, $\delta = \varphi$ conditions have been reached and further increases in roughness result in no change in interface strength. This finding implies that the capacity of interface systems is limited by the strength of the contacting soil mass. Recent studies have shown that this relationship is true for interface systems with clogging surfaces and thus result in failure planes that effectively behave as soil-soil interfaces. Part of the research presented in this thesis studies the behavior of interfaces consisting of non-clogging surfaces that result in combined loading conditions of shear and passive resistances. Recent studies have shown that these surfaces can mobilize interface friction angles larger than the contacting soil's friction angle (i.e. $\delta > \varphi$ conditions). Therefore, the objective of this study is to understand the behavior of these non-clogging interfaces and to investigate their potential as interface systems of improved capacity.

1.2 Scope of Thesis

This thesis presents experimental and numerical studies on the behavior of interfaces in axial and torsional shear. Experimental devices and DEM models were built during these studies, and results from micro- and global-scales measurements are

presented. The following paragraphs provide a summary of each of the chapters of this thesis:

- Chapter 2 presents a literature review on the current understanding of interface behavior. The effects of soil and man-made material properties as well as testing configuration on interface shear behavior are reviewed. A summary on the state of the literature on torsional interface behavior is also presented. This chapter is concluded with a description of the multi-sleeve in-situ testing devices developed at the Georgia Institute of Technology which have the capability of investigating the surface roughness – interface strength relationship and in turn the potential to aid in the selection of interface parameters for geotechnical design.
- Chapter 3 presents a summary of the general experimental and numerical methods followed through the studies presented in this thesis. Details of the configuration and development of the laboratory devices complemented with an assessment of the results' repeatability are provided. A thorough description of the DEM models is provided, and is complemented with results of the parametric calibration study performed to determine modeling parameters.
- Chapter 4 presents an experimental study of the soil deformations induced by torsional and axial interface shear on rounded and angular sands against non-clogging surfaces of varying roughness magnitude. The results include shear zone deformation characteristics as a function of shear displacement and surface roughness, as well as local void ratio measurements which clearly show the differences in soil-structure interactions between torsional and axial shear. This chapter is concluded with postulated micromechanical processes involved in both shearing modes.
- Chapter 5 presents experimental and numerical results of the global response of axial and torsional interface shear tests. Mobilized loads and volumetric strain measurements on specimens composed of real and simulated sands of different

angularity and surface roughness sheared against surfaces of varying roughness highlight the differences in global response. Furthermore, the effect of varying confining stress is studied, and load transfer mechanisms are presented and quantified for both axial and torsional interface shear.

- Chapter 6 presents a numerical study that identifies links between the observed micro-scale behavior and the measured global response of torsional and axial interface shear tests. The numerical results are shown to agree with the experimental results and to provide quantitative information regarding the fundamental differences in soil deformation (fabric, particle trajectories, displacements and rotations, local void ratios) and loading conditions (stress paths, major principal stresses orientations) induced by torsional and axial shear.
- Chapter 7 presents a study on the undrained behavior of cyclic torsional interface shear tests. The effects of confining pressure, soil relative density, sand type, surface roughness and shearing direction are studied in terms of the state parameter, and processes for excess pore water pressure generation are proposed. The usefulness of an in-situ test for the evaluation of liquefaction potential based on torsional interface shear is assessed.
- Chapter 8 presents a combined experimental and numerical study on the effect of surface roughness form on the shear behavior of axial interfaces. This study considers surfaces of clogging-prone roughnesses (random and ribbed) as well as surfaces of non-clogging roughness (structured) of varying roughness magnitudes sheared against three sand types. The results, in the form of global behavior, soil deformation and loading condition measurements, show that the capacity of clogging interfaces is limited by the $\delta = \varphi$ condition while non-clogging interfaces can mobilize larger interface friction angles resulting in $\delta > \varphi$ conditions.
- Chapter 9 presents general conclusions of this thesis as well as recommendations for future work.

CHAPTER 2

LITERATURE REVIEW ON INTERFACE SHEAR BEHAVIOR

2.1 Interface Behavior

2.1.1 Importance of Interfaces in Geotechnical Engineering

During the last three decades, researchers have made important advances in the understanding of soil-structure interactions and interface behavior. In particular, it has been understood that significant potential for enhanced structure design and efficient use of resources can be achieved by prescribing the structure's surface characteristics, such as its roughness and hardness. However, a key component to this approach is the characterization of the soil's shear and interface behavior in an accurate and effective manner. Table 2.1a, from DeJong, et al. (2000), presents the significance of interface systems in different geotechnical applications and tests. Canal liners, deep foundations, landfills, leach ponds, micro-tunneling, retaining structures and slope stability are among the geotechnical applications that significantly rely on the performance of interfaces, and tests such as the CPT friction sleeve reading, SPT, interface shear, resonant column and torsional shear are also heavily influenced by interface behavior. With this in mind, research towards obtaining a thorough understanding of interface behavior is of particular interest. This chapter presents a summary of the current understanding of particulate (soil) - continuum (man-made material) interface behavior, along with a summary of the current in-situ testing devices that assess the behavior of these interfaces.

2.1.2 Particulate (Soil) – Continuum (Man-Made Material) Interface Systems

The Coulumb friction model states that the shear force required to make an object slide relative to another object is directly proportional to the normal force applied to the

system multiplied by a constant called the coefficient of friction (Williams, 1994). This is the classical approach applied to the analysis of sliding solid objects. In a mathematical form, the Coulumb friction model is as follows:

$$F = \mu N$$

where F is the friction force opposing the movement in the sliding condition, μ is the coefficient of friction and N is the normal force applied to the interface.

The normal and friction forces can usually be controlled and/or measured; therefore, determining the coefficient of friction between two surfaces is typically the focus in interface analyses and tests. This problem is more complex in soil-continuum interfaces due to the particulate nature of soils, which introduces many variables associated with the shear behavior of soils and its dependency on confinement and loading conditions. Several factors that significantly affect the behavior of interfaces include the surface roughness and hardness of the continuum material, the normal confining stress, soil density and the angularity of the particles, as shown in Table 2.1b.

Table 2.1: (a) Significance of interface behavior in geotechnical systems (after DeJong et al. 2000). (b) Significance of interface characteristics on its behavior (after Lee, 1998).

(a)

Applications / Tests	Significance
Applications	
Canal Liners	High
Foundations	
Deep	High
Shallow	Low
Landfills	High
Leach Ponds	High
Micro-Tunneling	High
Pavements	Low
Retaining Structures	High
Slope Stability	High
In-Situ Tests	
CPT, f_s	High
CPT, q_c	Low
DMT	Low
PMT	Low
SPT	High
Laboratory Tests	
Casagrande Dish	Medium
Consolidometer	Medium
Fall-Cone	Medium
Interface Shear	High
Resonant Column	High
Torsional Shear	High
Triaxial	Medium

(b)

Type	Factor	Significance
Soil	Angularity / Shape	High
	Cementation	Med
	Density	High
	Initial soil structure	Low
	Mean grain size (D_{50})	Medium
	Surface roughness	Low
	Uniformity coefficient (C_u)	Low
Geomaterial	Surface hardness	High
	Surface roughness	High
Testing	Normal stress	High
	Strain rate / Drainage	Low
	Test method	Low

2.1.3 Effect of Surface Roughness

The historical belief that granular material–construction material interfaces representing the weak link in geotechnical systems has been proven to be inaccurate for many situations encountered in geotechnical engineering. Namely, the quantitative bi-linear relationship between interface strength and continuum surface roughness presented by Uesugi and Kishida in 1986 for sand-steel interfaces was an important milestone for the understanding of interface shear behavior (Figure 2.1). The authors showed that at low levels of surface roughness, the interface strength increases linearly with increasing roughness up to a "critical" roughness value. At this value, shearing is transferred from the interface into the soil mass and further increases in surface roughness result in no change in the interface strength, which at this point has reached the internal friction of the contacting soil (i.e. $\delta = \varphi$ conditions).

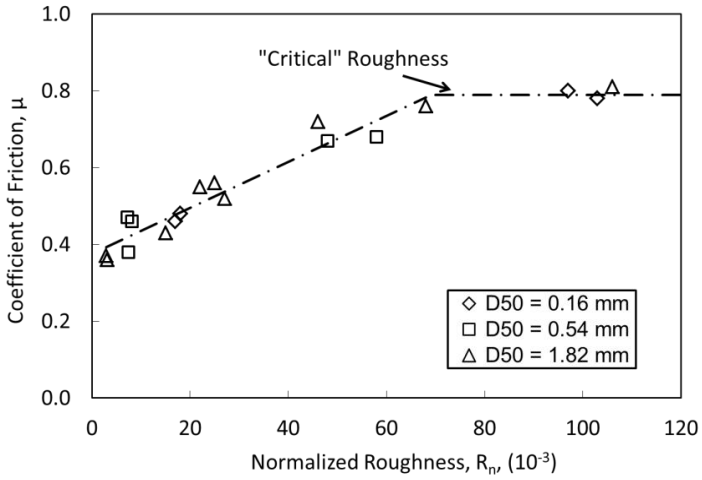

Figure 2.1: Relationship between interface friction and surface roughness (after Uesugi and Kishida, 1986).

Other researchers, such as Rao, et al. (1998) and Dietz and Lings (2006), have shown that the bi-linear relationship for interface behavior exists for both peak and critical state strengths. Furthermore, this relationship has been also observed by other researchers for interfaces composed of sand-geomembrane (Dove, et al. 1997), sand-FRP

(Frost and Han, 1999) and sand-construction materials (Frost, et al. 2002). This relationship is of paramount importance for geotechnical design because it suggests that soil-continuum interfaces can be designed to have a capacity equal to that of the contacting soil.

The magnitude of the continuum's surface roughness has also been shown to affect the characteristics of the stress-displacement and volume change-displacement responses measured during interface shear testing. Typically, stress-displacement curves obtained from tests against smooth surfaces reach their peak at very low shear displacements, with shapes that resembles those for perfectly plastic materials, and show no to modest shear-induced volume change behavior, as shown on Figure 2.2a from Lee (1998). On the other hand, interface shear stress-displacement curves from tests with rough surfaces reach their peak at larger displacements, mobilize larger shear stresses and have a more pronounced dilative strain-softening behavior, as presented in Figure 2.2b (note the different scales).

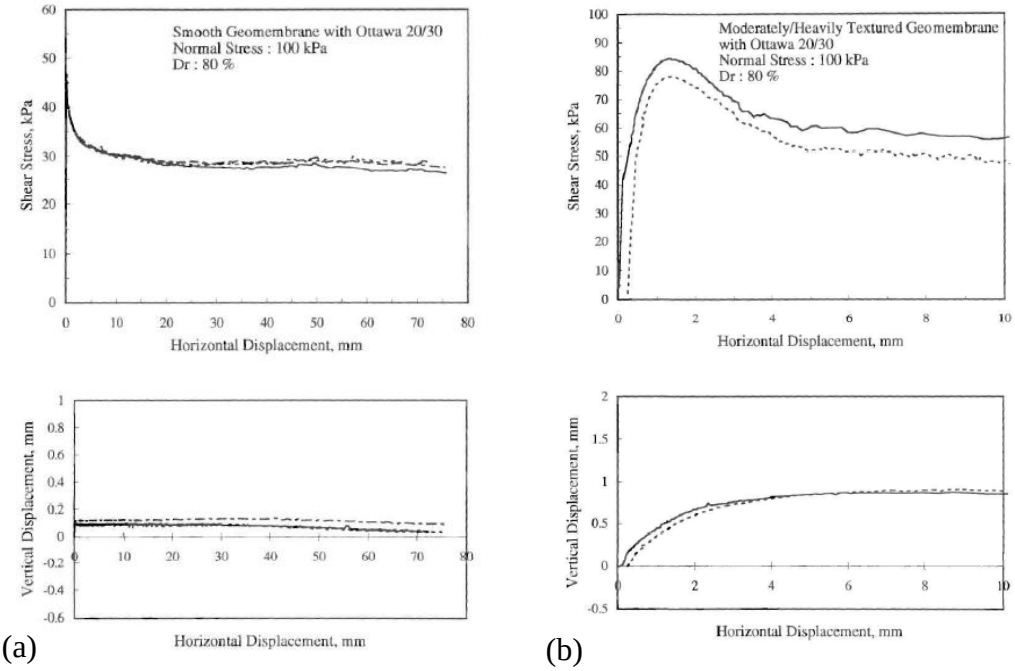

Figure 2.2: Typical shear interface tests of medium-sized sub-rounded sand against (a) smooth geomembrane and (b) textured geomembrane (after Lee, 1998).

2.1.4 Effect of Normal Confining Stress

The effect of normal confining stress on the shear behavior of interface systems is similar to its effect on the shear behavior of granular materials. Increasing normal stress influences the interface behavior by increasing the total shear stress needed to be mobilized for shear displacement to occur. Increasing the confining stress also decreases the measured shear to normal stress ratio because the dilative shear-induced volume change tendencies are suppressed, as shown by Been and Jefferies (1985) and Bolton (1986). Figures 2.3a and 2.3b, from Frost, et al. (2012), show the effect of confining normal force on the measured loads in interface tests performed with medium-sized sub-rounded sand against a smooth geomembrane. It can be seen that the measured loads of the tests performed under a confining stress of 300 kPa are considerably larger than those recorded during the test at 100 kPa (note the different scales). Figure 2.4a, from DeJong and Westgate (2009), shows the measured loads during an interface shear tests between medium-sized sub-rounded sand against rough steel surfaces for specimens of low and high initial relative density. In a similar manner as Figure 2.3, the measured loads increase dramatically for tests performed under increasing confining stress.

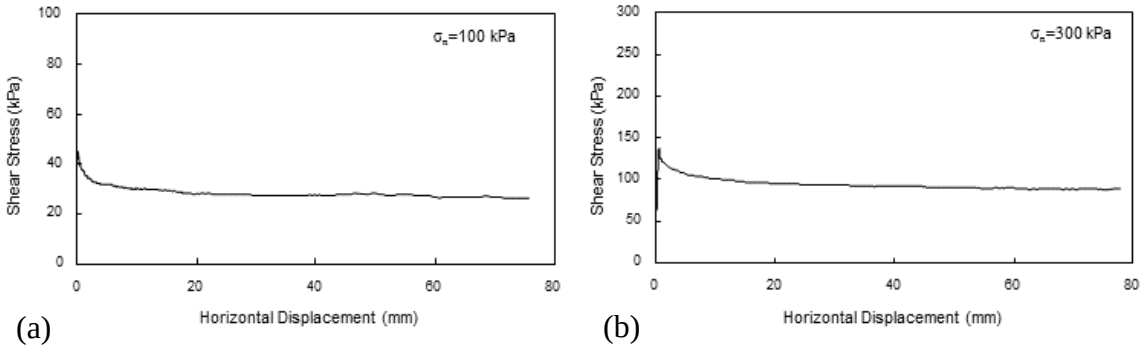

(a) (b)

Figure 2.3: Effect of normal confining stress on interface tests between medium-sized sub-rounded sand against a smooth geomembrane (after Frost, et al. 2012).

Figures 2.4b and 2.4c show results for interface shear tests between sand and rough surfaces. The data shows that both the mobilized stress ratio and the vertical

displacement of the specimens during shear, which indicates dilation, significantly decrease with increasing confining stress. It should be noted that the effect of normal confining stress on interface system dilation is more significant for interface systems with rough surfaces, because interfaces with smooth surfaces are not likely to undergo volume changes during shear.

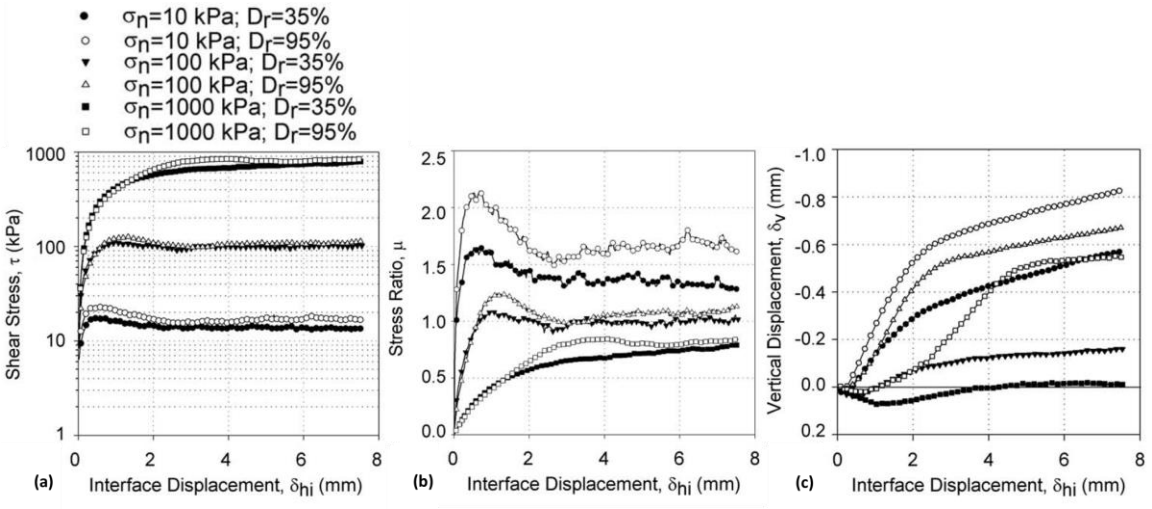

Figure 2.4: Interface tests between sub-rounded sand against a rough steel surface. a) Shear stress b) stress ratio and c) vertical displacement (adapted from DeJong and Westgate, 2009).

Another important effect of confining stress on the interface strength is its influence on the coefficient of friction for smooth interfaces. Dove and Frost (1999) showed that the interface coefficient of friction decreases with increasing normal stress. The reason is that under increasing normal stress, the number and area of particles in contact with the surface increase, resulting in the contact stresses per particle to decrease and therefore decreasing the interface friction generated during shear. At a "critical stress" value, the number and size of particle contacts reach a saturation point, causing any further increases in normal stress to be directly transmitted to the particle-surface contact and result into no further change of the coefficient of friction as long as the surface does not suffer any wear, as shown in the solid line in Figure 2.5.

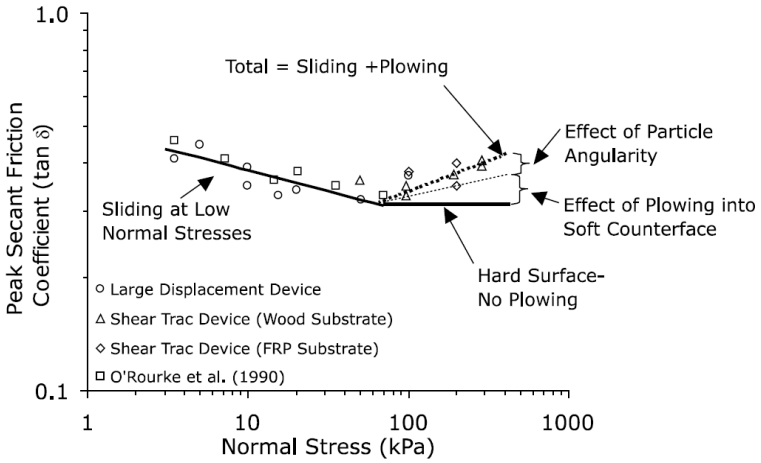

Figure 2.5: Effect of normal stress on the peak friction coefficient of granular soil-continuum interfaces (after Dove and Frost, 1999).

2.1.5 Effect of Surface Hardness on Interface Behavior of Smooth Surfaces

The effect of surface hardness in interface behavior was quantified by Dove and Frost (1999) and is presented in Figure 2.5. The solid line represents a material with a high hardness, which does not undergo any damage under increasing normal stress. The dashed lines represent softer materials, which undergo damage and wear in the form of plowing and indentation of soil particles into its surface during shearing at stress levels larger than the "critical stress". The additional energy required to wear and plastically deform the surface provides an increased shearing resistance, which results into a larger coefficient of friction. This effect is more pronounced for more angular soils. The interface shearing mechanism at stress magnitudes lower than the "critical stress" consists of particle sliding against the smooth surfaces. On the other hand, when the stress level is larger than the critical value, the shearing mechanism evolves into a combination of relative sliding and plowing of soil grains into the surface.

2.1.6 Coupled Effect of Surface Roughness and Hardness

Frost, et al. (2002) presented a series of interface shear laboratory experiments and Discrete Element Modeling (DEM) simulations where they parametrically varied the

surface roughness and hardness of the continuum material. They observed the same trends as previously described on the coupled effect of surface roughness and hardness on laboratory and numerical tests. The interface friction angles were shown to be more sensitive to initial increases in surface roughness and hardness, while changes in the surface properties at high values resulted in minimal to now change. Figure 2.6a and 2.6b show their DEM results for peak and residual interface friction angles, respectively.

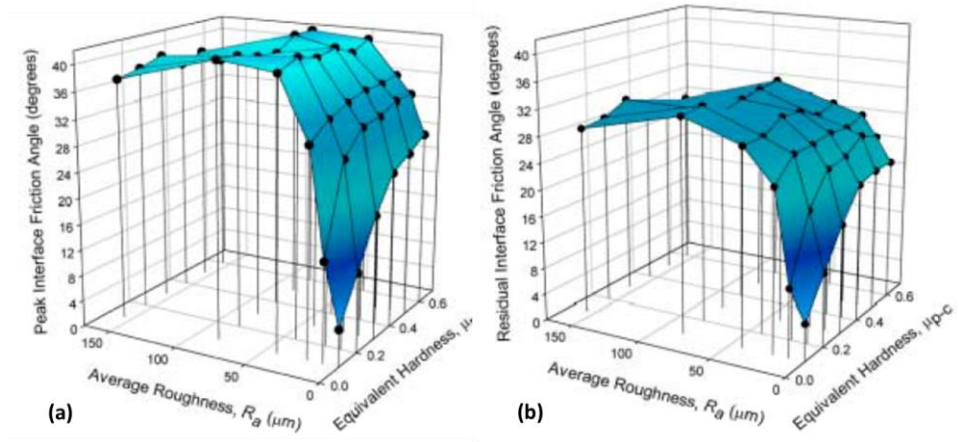

Figure 2.6: Coupled effect of surface roughness and hardness on mobilized (a) peak and (b) residual interface friction angles (after Frost, et al. 2002).

2.1.7 Effect of Initial Density and Particle Angularity

The effect of soil initial density on interface behavior is similar to its effect in soil behavior, described in critical state soil mechanics. Loose soil assemblies show a more contractive shear behavior while dense soil assemblies show a dilative behavior. The effect of initial density on interface behavior can be observed in Figure 2.7a (Dietz and Lings, 2006). As the density decreases the mobilized peak stress ratios decrease, but the residual stress ratios converge to a similar value. In a similar manner, the dilative shear-induced volume changes decrease as the soil density decreases (Figure 2.7b).

The grain angularity also has the same effect in interfaces with rough surfaces as in soil masses. This effect consists of increasing soil angularity resulting in larger

interface strength (Iscimen, 2004; Edil, et al. 2006). Figure 2.8 presents the results of interface shear tests with sands of different angularity against rough and smooth surfaces.

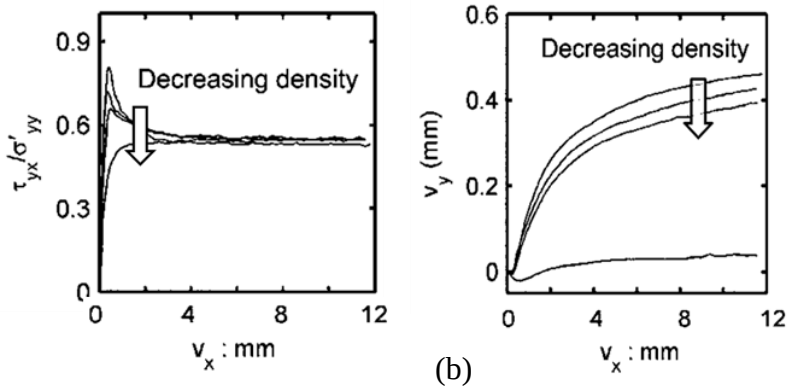

(a) (b)

Figure 2.7: Effect of initial density on (a) mobilized stress ratio and (b) shear-induced specimen volume changes (adapted from Dietz and Lings, 2006).

The effect of particle angularity on the mobilized stress ratio is clear for tests against rough surfaces, with larger stress ratios mobilized during the test with sub-angular sands. However, particle angularity showed to have a negligible effect on the mobilized stress ratios for tests against smooth surfaces. These results are in agreement with studies by DeJong (2001) and Hebeler, et al. (2015) who showed that particle sliding against the surface is the governing mechanism of soil shearing for systems composed of smooth surfaces.

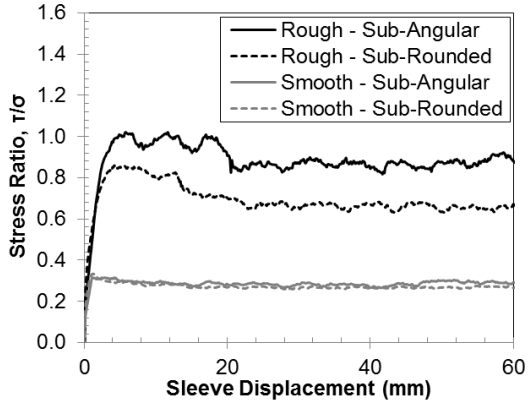

Figure 2.8: Effect of particle angularity on mobilized stress ratios for interface shear tests against rough and smooth surfaces.

2.1.8 Effect of Mean Particle Size

Identifying the effect of particle size on the shear behavior of interfaces is a difficult task because other factors such as particle angularity and surface roughness of the continuum material have a more significant effect, as shown in Table 2.1a. Authors such as Barmpopoulos, et al. (2010), Ho, et al. (2011) and Dove and Jarrett (2002) have presented the effect of mean particle size on the interface friction angle. For instance, Ho, et al. (2011) presented results that suggest that the interface friction angle decreases with increasing mean particle size (Figure 2.9). These tests were performed against surfaces of small roughness values (average roughness, R_a, between 4 and 15 μm); thus the results were less likely to be affected by differences in particle angularity between the different soils tested (seethe curves for smooth interfaces in Figure 2.8). It should be noted that the authors did not address the relative aspect of surface roughness in particulate-continuum interfaces. Namely, a small particle in contact with a surface will "experience" a larger relative roughness than a larger particle against the same surface, as shown in Figure 2.10. Other authors such as Uesugi and Kishida (1986) and Uesugi, et al. (1989) have considered a relative roughness parameter, R_n, in order to account for this effect. This relative roughness parameter is defined as the ratio between maximum roughness value (R_{max}) and the soil mean particle size, D_{50}. Therefore, a system composed of a surface of a specified roughness and fine particles will have a larger value of the R_n parameter than a system composed of the same surface and coarse particles. The authors showed that the R_n roughness parameter successfully accounted for the relative aspect of surface roughness for tests between different sands against steel surfaces.

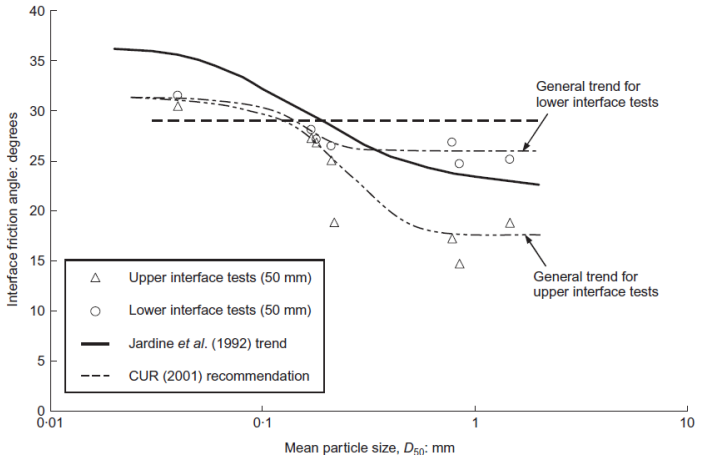

Figure 2.9: Effect of mean particle size on mobilized interface friction angle from interface shear tests against smooth surfaces (adapted from Ho, et al. (2011).

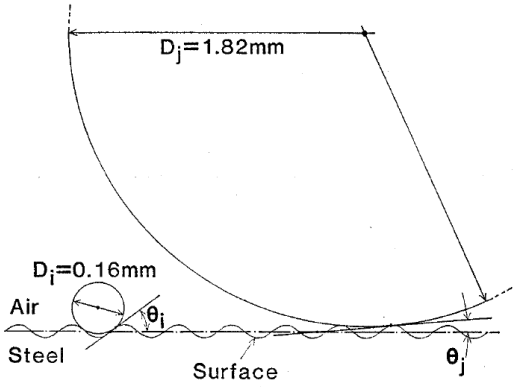

Figure 2.10: Profiles of fine and coarse particles against a steel surface (after Uesugi and Kishida, 1986).

2.1.9 Load Transfer Mechanisms and Interface Clogging

It has been shown by several researchers that the load transfer between soils and solid surfaces can take place by two distinct mechanisms: either from friction between the soil particles and the surface material or from passive resistances generated as the surface's topography forces particles to displace during shearing (Mitchell and Villet, 1987; Irsyam and Hyrciw, 1991). For smooth surfaces, most of the load is transferred by friction since the surface has no significant asperities that can induce soil deformations. On the other hand, surfaces with larger values of surface roughness to particle diameter

ratio (R_{max}/D_{50} or R_a/D_{50}) effectively mobilize a passive resistance component during shear. As such, it has been shown by DeJong (2001), Frost and DeJong (2005) and Hebeler, et al. (2004) that the mobilized loads during laboratory and field axial tests between sands and surfaces composed of friction sleeves textured with a diamond pattern (shown in Chapter 3) consist of friction resistance between the sleeve surface and the soil particles and passive resistance caused by the difference in diameters between the base of the sleeve and the protruding diamond texturing elements, termed the Annular Penetration force (AP). The authors provided the following expression that quantifies the relative contribution of the interface friction and passive resistance (i.e. AP force) to the total force measured:

$$f_a = f_r * N_r + AP$$

where f_a = average measured force, f_r = average force per ring of texture, N_r = number of rings of texture and AP = Annular Penetration force

Figure 2.11a shows a methodology proposed by Frost and DeJong (2005) for isolating the AP force from the interface friction force. This methodology involves performing a series of tests with friction sleeves with the same maximum surface roughness but different textured lengths. In this manner, the magnitude of the AP force can be determined by plotting the number of diamond rings (proportional to the textured length) versus the measured load on the diamond texture elements. The results show a linear trend based on the linear relationship between stress and contact area. Therefore, the magnitude of the AP force is equal to the intercept of the trend line with the y-axis that corresponds to a friction sleeve with a length of zero. Consequently, if no AP force is present, as for shearing against a smooth sleeve, the value of the intercept should be zero. Figure 2.11b shows this methodology applied to results from field tests performed with friction sleeves of varying surface roughness. Hebeler, et al. 2004 showed during field tests with the multi-sleeve devices that the magnitude of the AP force is directly proportional to the tip resistance reading, q_t, of conventional CPT probes, as follows:

$$q_c(kPa) = \frac{AP(kPa)}{A_{Diamonds}(m^2)}$$

q_c = measured tip stress, $A_{diamonds}$ = area of diamond texture.

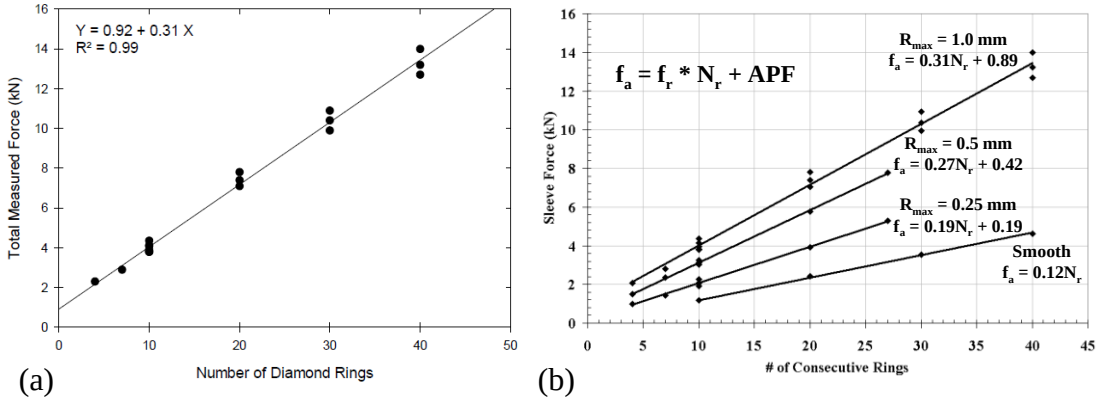

Figure 2.11: (a) Methodology for the determination of the passive resistance force magnitude (i.e. AP) from field tests with multi-sleeve CPT attachments (after Frost and DeJong, 2005). (b) Determination of passive resistance force from tests against friction sleeves of varying roughness (after Hebeler, et al. 2004).

Previous studies on surfaces with "structured" roughness consisting of rectangular steel ribs also found an additional shear resistance contribution other than interface friction (Irsyam and Hryciw, 1991; Hryciw and Irsyam, 1993). The findings of these studies showed that well-spaced ribs formed a passive wedge that mobilized an additional shear resistance component, which is analogous to the AP force in textured friction sleeve shearing (Figure 2.12a). On the other hand, closely placed rib surfaces showed to trap particles in the intra-rib region, thus clogging the interface and developing a shear band or zone above the ribs (Figures 2.12b and 2.12c). Consequently, the latter geometry mobilizes the internal shear strength of the sand because it effectively results into a sand-sand interface. In further testing, the authors used closely-spaced trapezoidal ribs and reported no passive resistance development; however, shear data or quantification of the relative contributions of interface friction and passive resistances were not reported.

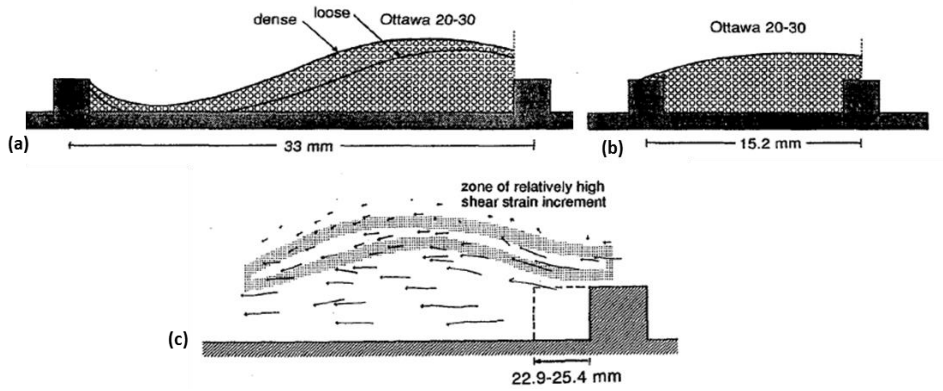

Figure 2.12: Rib-sand interactions for surfaces of (a) well-spaced and (b) closely-spaced ribs. (c) Schematic of shear zone developed above closely-spaced ribs (adapted from Hryciw and Irsyam, 1993).

2.1.10 Strain Localization and Micro-Scale Interface Shear Behavior

The study of soil deformations and particle-particle interactions at the micro-scale has been recognized to be paramount for the understanding of the behavior of soil masses. Pertaining to the study presented herein, studies of this kind have allowed understanding the phenomenon of strain-localization and its implications in the shear strength and dilation behavior of soils. Many researchers have studied shear localization in soil masses (i.e. shear bands) and in soil-continuum interfaces (i.e. shear zones) using a variety of different laboratory tests, such as biaxial, triaxial and direct shear tests (e.g. Vardoulakis, 1980; Finno, et al. 1996; Santamarina and Cho, 2003; Scarpelli and Wood, 1982), and Frost, et al (2004) presented results that indicate that half of an internal soil shear band is equivalent to a shear zone formed at a virtual soil-soil interface. The shear localization phenomenon can be described as follows: as the granular assembly is initially sheared, the load is mostly carried by force chains that develop throughout the soil specimen. These force chains are column-like arrangements of particles which are evenly and densely distributed throughout the soil mass by which compressive loads are transferred and provide shearing resistance (Oda, et al. 1982; Iwashita and Oda 2000). Once the peak state is reached, the force chain columns start to localize and orient in line

with the prominent shear band or shear zone formation. During failure, the force chains repeatedly buckle and rearrange as a result of a loss of lateral bracing and result in fewer particle contacts that provide a reduced shearing resistance. The global effect of this process is observed as strain-softening in the stress-strain curve. As the force chains collapse, the particles push neighboring particles away, and dilation of the soil-mass is likely to occur (Oda, et al. 1982; Oda and Iwashita 2000). This process is also developed during interface shear, with the difference that the shear zone is forced to develop adjacent to the soil-continuum interface. Researchers have also shown that particle rotations are much larger inside the shear zones and shear bands as opposed to the surrounding areas, as shown in Figure 2.13 (Bardet 1994; Iwashita and Oda 1998; Alshibli and Alramahi 2006). More recent DEM studies by Oda and Iwashita (2000), Wang, et al. (2007a) and Mohamed and Gutierrez (2010) have shown the importance of particle rotation resistance mechanisms, such as particle angularity, that when increased, result in assemblies of larger shear strength that show a more dilative behavior, as shown in Figure 2.14. In the figure, the "α" coefficient controls the magnitude of the particle rotation resistances.

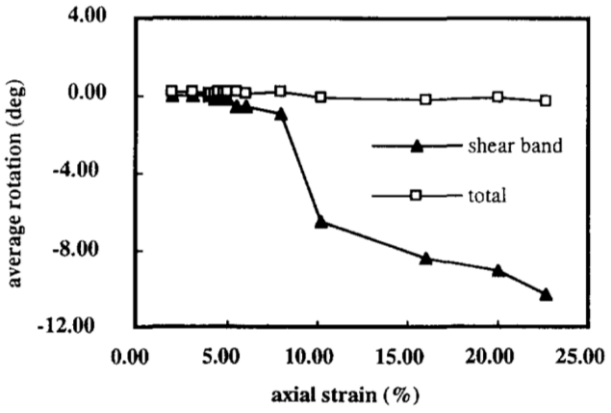

Figure 2.13: Average particle rotations as a function axial strain for complete specimen and shear band (after Bardet, 1994).

The extent of the shear zones formed during interface shear or shear bands during soil shear has received significant attention during the last three decades. A linear

relationship of increasing shear band thickness with increasing mean particle size, D_{50}, has been reported by Mühlhaus and Vardoulakis (1987) (based on bifurcation analysis coupled with micropolar theory) by Oda and Kazama (1998) (based on biaxial compression tests) and by Frost, et al. (2004) (based on direct interface shear tests). In contrast, Ho, et al. (2011) presented results that showed that the shear zone thickness increases with increasing D_{50} but reached a constant value at larger mean particle sizes. It should be noted that the authors only presented shear zone thickness measurements for sands with D_{50} smaller than 1.5 mm but reported a trend for sands of D_{50} of up to 2.0 mm; thus, their reported trend might be affected by the extrapolation procedure. A study by Hebeler, et al. (2015) showed that grain shape is an important factor for shear zone formation and evolution where more rounded sands showed shear zones with smaller particle displacements, which are a result of larger particle rotations as opposed to larger particle displacements observed with angular sands.

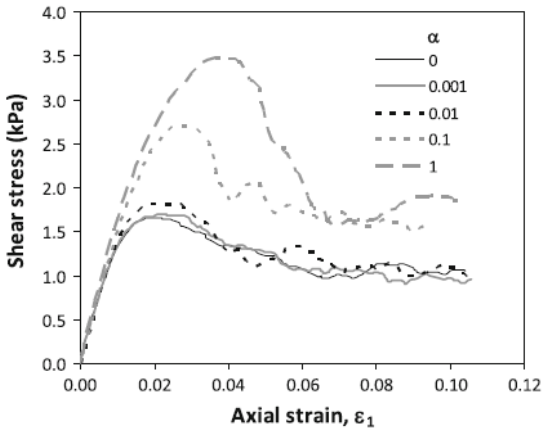

Figure 2.14: Effect of particle rotation resistance in stress ratio for biaxial tests (after Mohamed and Gutierrez, 2010).

The surface roughness has been identified as a factor of major influence on the shear-induced evolution of the soil structure in the vicinity of the interface by Lee (1998), Hebeler (2005), Frost, et al (2012) and Hebeler, et al (2015). Figure 2.15a (from Hebeler, 2005) shows the shear zones formed between medium-sized sub-rounded sands and

rough steel surfaces. During this study, colored sand layers were included in these tests to facilitate the identification of shear zones. The shear zone created when the sand was sheared against a rough surface had a thickness in the order of 6 times the D_{50} of the tested sand. On the other hand, the shear zone thickness of the interface with a smooth sleeve (Figure 2.15b) was in the order of 0 to 1 D_{50} of the sand.

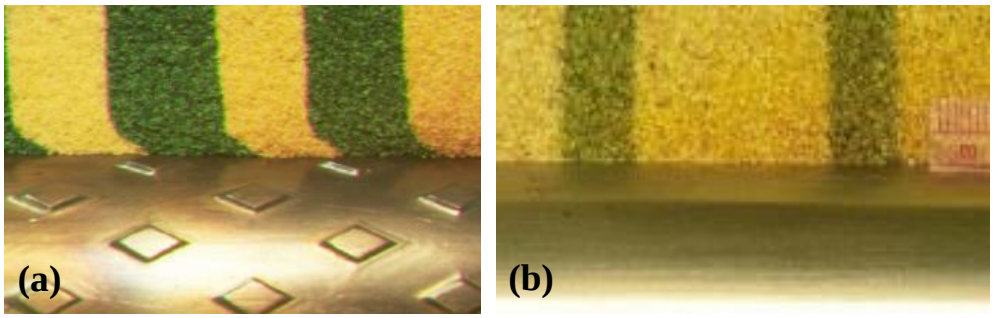

Figure 2.15: Shear zones created between medium-sized sub-rounded sand and (a) rough surface and (b) smooth surface (after Hebeler, 2005).

Frost, et al. (2012) performed a similar study with the addition of local void ratio measurements as a function of distance away from the surface. Their results concluded that shearing against smooth surfaces did not induce significant changes in void ratio, while shearing against rough surfaces induced large increases in void ratio within the shear zone in the form of dilation, as illustrated in Figure 2.16a through Figure 2.16d.

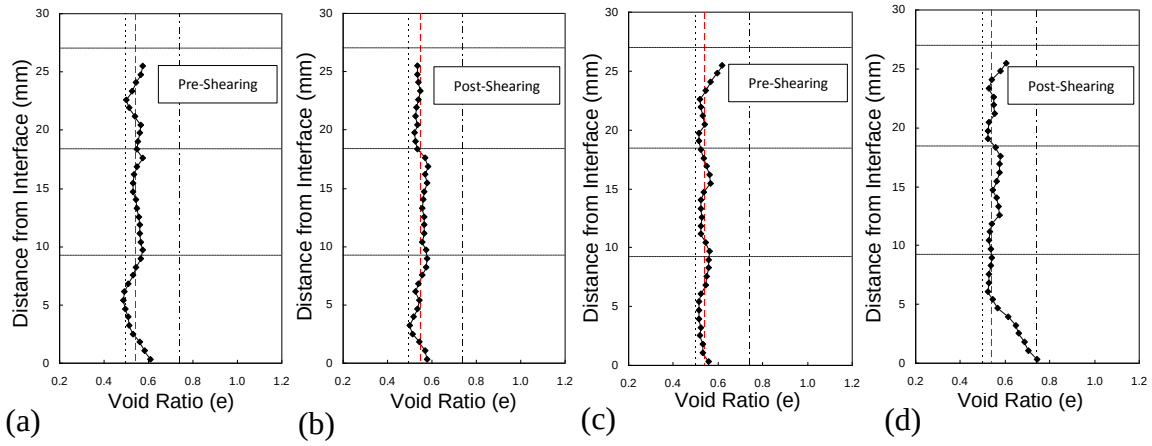

Figure 2.16: Shear induced changes in void ratio in interface tests against a (a) and (b) smooth surface and (c) and (d) rough surface (adapted from Frost, et al. 2012).

2.1.11 Torsional Interface Shear

The only three lines of research that have focused on the study of interface systems in torsional shear loading conditions are those of piles under torsion loading, the Standard Penetration Test supplemented with torsion measurements (SPT-T) and rotary jacking of piles. It should be noted that the vane shear test (VST) is not included in this discussion because it is utilized to study the undrained shear strength of clays, while the present study focuses on the drained response of soils. However, a numerical study of the VST is included in chapter 6. The following sections present a brief summary of the literature related to piles under torsion, SPT-T and rotary jacking of piles,

2.1.11.1 Piles under Torsional Loading

Several numerical, analytical and experimental studies of pile torsion have been performed since the 1970's. This topic is of interest because it has been recognized that eccentric horizontal forces on structures can result in torsional forces being transferred to the pile foundations of tall buildings and offshore structures (Azadi, et al. 2008).

Numerical studies on piles subjected to torsional loadings include solutions with continuum-based boundary elements (e.g. Poulos, 1975), analytical solutions (e.g. Randolph, 1981; Misra, et al. 2014), discrete element approaches (e.g. Chow, 1985), models for piles in non-homogenous or layered profiles (e.g. Guo and Randolph, 1996; Zhang, 2010) and boundary-element solutions for simultaneous axial and torsional loadings (e.g. Basack and Sen, 2014). Experimental studies include field load tests (e.g. Stoll, 1972), model-scale pile load tests (e.g. Poulos, 1975; Dutt and O'Neil, 1983) and centrifuge tests on single piles and pile groups (e.g. Zhang and Kong, 2006; Kong and Zhang, 2008). It should be noted that all these studies were performed on piles installed axially.

The main findings from the studies outlined above can be summarized as follows: (1) torsional forces applied to a pile will result in angular displacement deformation that in turn can act simultaneously with the already existing axial compression forces and reduce the pile capacity and increase the expected settlements (Georgiadis and Saflekou, 1990; Basack and Sen, 2014); (2) interface friction (termed as soil-pile adhesion in earlier papers) from axial and torsional model-pile load tests will be similar in magnitude when testing piles of low surface roughnesses under isotropic stress conditions (Figure 2.17a, from Poulos, 1975) ; (3) under anisotropic stress conditions the response from axial and torsional interface shear will differ (Figure 2.17b, from Zhang and Kong, 2006). It should be noted that none of these studies presented a systematic investigation on the effect of surface roughness magnitude and stress conditions on the interface friction response, or a study on the loading conditions induced on the surrounding soil at a particle scale.

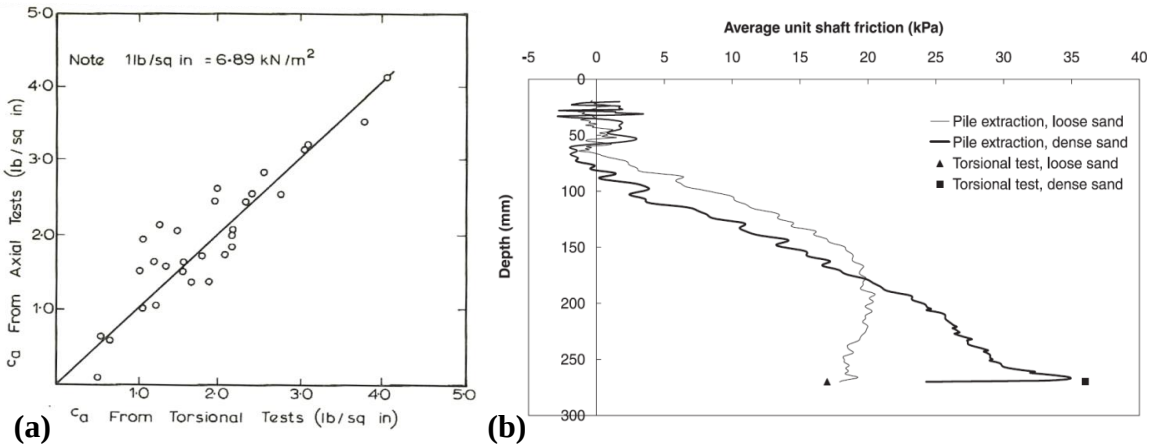

Figure 2.17: (a) Comparison soil-pile adhesion from axial and torsional load tests on a smooth model pile (after Poulos, 1975), (b) comparison of unit shaft friction from axial and torsional pile centrifuge load tests (after Zhang and Kong, 2006).

2.1.11.2 Standard Penetration Test Supplemented with Torsion Measurements (SPT-T)

The Standard Penetration Test supplemented with torsional measurements (SPT-T) consists of rotating the rod string with a torque-wrench and recording the maximum torque mobilized at the soil-sampler interface after the split spoon has been driven for 18

inches. Several authors have pointed out the potential for the torque measurement to have a better resolution than the blow number, and for it to be less dependent on sources of error such as hammer type, as shown in Figures 2.18a and 2.18b. Furthermore, authors have also described the advantages of obtaining a more isolated measurement of the sampler-soil friction interactions which has a better potential of correlating with certain soil properties, as opposed to the combined friction and bearing capacity measurement captured by the blow number. Researchers such as DéCourt and Filho (1994) and Piexoto and Carvalho (1999) have used the ratio of measured torque to blow number (called T/N ratio) to classify soil type, while other researchers such as Kelley and Lutenegger (2004) and Lutenegger and Kelley (1998) have used the torque measurements to estimate the unit skin friction between the sampler and the soil. Numerous investigations have been performed, mainly in Brazil and in the US, which have shown correlations between the blow count with the skin friction obtained from torque measurements.

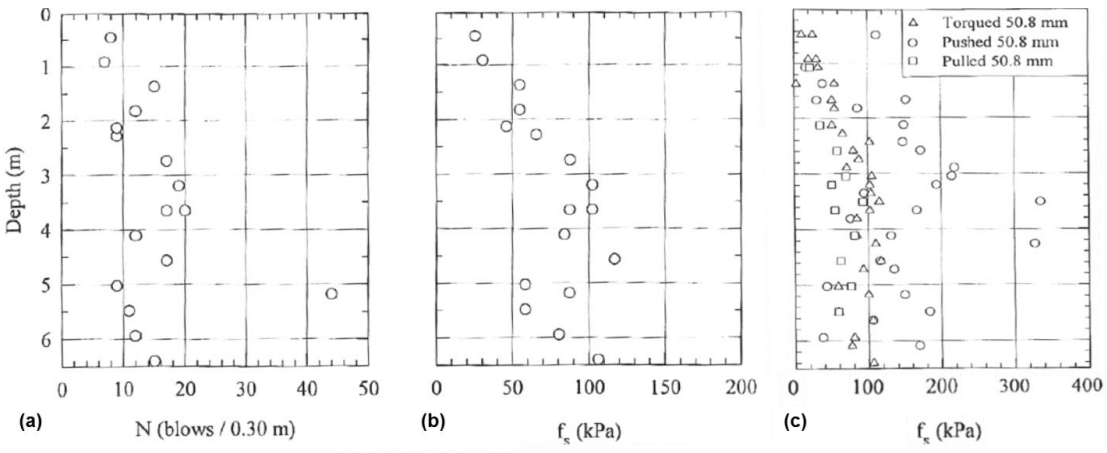

Figure 2.18: SPT results of (a) blow count, (b) skin friction estimated from torque measurements, and (c) comparison from skin friction estimated from torque measurements, pull-out and jacking tests (adapted from Lutenegger and Kelley, 1998).

The SPT-T measurement relies on several simplifications that can compromise the usefulness of this test for general design purposes. For instance, the measurement does not consider the effects of variations on sampler surface roughness that can result

from sampler rusting or wearing, which can have a significant effect on the magnitude of the interface friction. Furthermore, the change in state of stresses caused both by increasing depth and its increase caused by driving the sampler, as well as the torque generated by the friction between the drill rods and the soil, are not taken into account for the estimation of sampler-soil skin friction.

A study presented by Lutenegger and Kelley (1998) included a comparison of the skin friction obtained from SPT torque measurements (i.e. torsional shear) and that from SPT pull-out and jacking measurements (i.e. axial shear). The authors concluded that the estimated skin friction from torque and pull-out measurements was fairly similar, while the skin friction estimated from jacking measurements was larger (Figure 2.18c). The larger skin friction values estimated from the jacking tests might be a result of the stress increases induced by driving the sampler.

2.1.11.3 Rotary Jacking of Piles

Jacked piles, or press-in piles, have shown to mobilize superior stiffness and capacity as compared to equivalent sized non-displacement piles. Furthermore, they minimize the noise, vibration and dust pollution associated with the conventional pile driving process. However, one main drawback of this methodology is the limited capacity of the piling equipment, which can result in the inability to drive the piles to the desired depth. As described below, several studies on pile jacking have focused on the beneficial effects of rotary press-in jacking (i.e. simultaneous torsion-axial jacking).

The results of these studies have shown that the rotation of the axially jacked piles allows for the mobilization of the shaft friction at an angle, which reduces the required axial jacking force and allows for installation in harder ground (Deeks and White, 2008; Bond, 2011). Ultimately, the reduction in load cycles required to jack the piles can result into a smaller magnitude of friction fatigue, which in turn can result in larger pile capacity. Increasing pile surface roughness was shown to result in increasing driving skin

friction by a separate study by E. Hazla in conjunction with Giken Seisakusho Ltd., (Hazla, 2012). It should be noted that the simultaneous axial-torsional loading applied to the piles analyzed in these studies results in increased driving work as compared to the axial driving case; thus, a direct comparison of these two cases cannot be undertaken.

2.1.12 Cyclic Interface Shear Behavior

The majority of the research on the cyclic shear behavior of interfaces has been focused on expanding the understanding of the cyclic behavior of piles, which is especially important for offshore piles or those supporting machinery such as wind turbines. As such, there is a rich literature on studies of full-sized and model piles in the field, as well as studies on model piles and on shear box laboratory experiments. The following sections provide a brief synopsis of this research.

2.1.12.1 Friction Fatigue and Strength Degradation

The loss of shear strength observed in full-scale piles is commonly referred to as friction fatigue (e.g. Lehane, 1992; Chow, 1997; Gavin and O'Kelly, 2007). This effect is attributed to the contraction of a narrow shear zone immediately adjacent to the shaft-soil interface. The contraction results into a decrease of the effective horizontal stress acting at the interface because the shear zone is surrounded by soil with a relatively high lateral stiffness. Design methods proposed by authors such as Randolph, et al. (1994) and Jardine and Chow (1996) account for friction fatigue and identify its leading cause as the degradation of the available skin friction as the pile penetrates further into the ground (thus being a function of the distance behind the pile tip, h, typically normalized by the pile diameter, D or B). Other authors, such as White and Lehane (2004), propose that the primary mechanism controlling the friction fatigue is the cyclic history imposed to the pile during installation and loading. Figure 2.19a through 2.19c present results from White and Lehane (2004) that show the degradation of stationary horizontal stress as a function of installation method as well as distance from the pile tip (h/B ratio). The

authors showed that installation methods that impose cyclic loading on the pile shaft, such as "pseudo-dynamic" driving, result in larger degradation in the stationary horizontal stress acting on the pile shaft (note the different axis scales in the figures).

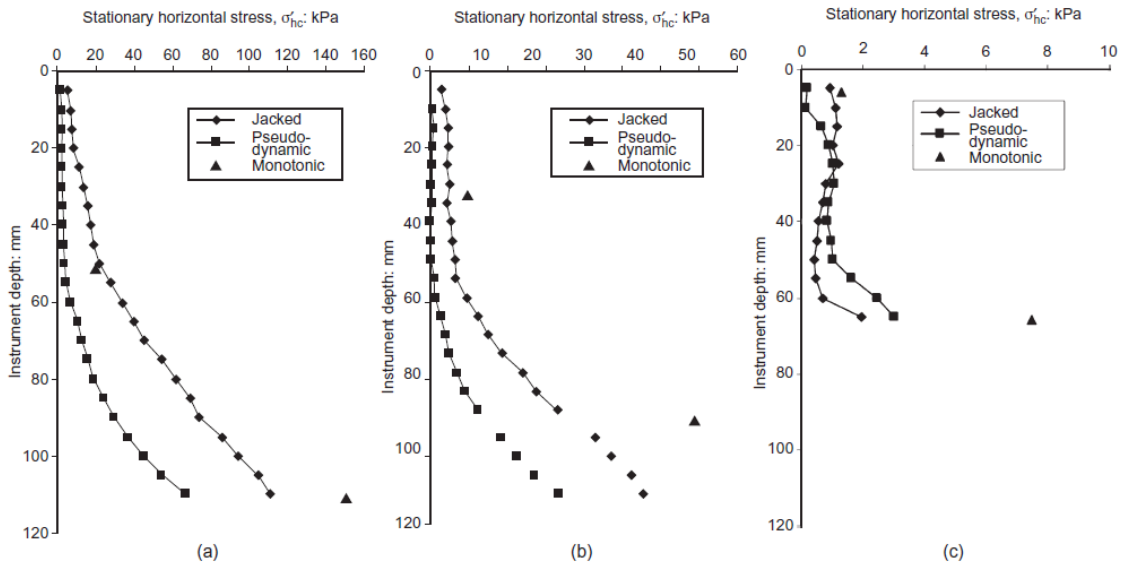

Figure 2.19: Variation in stationary horizontal stress with installation method: (a) h/B = 1, (b) h/B = 3, (c) h/B = 6 (after White and Lehane, 2004).

The phenomenon of friction fatigue, or cyclic degradation, has been studied by many researchers using cyclic interface direct shear tests with a constant normal stiffness confinement condition (CNS) (e.g. Boulon and Foray, 1986; Tabucanon, 1997; DeJong, et al. 2003; Mortara, et al. 2007). Figures 2.20a and 2.20b present stress paths from tests performed by Mortara, et al. (2007) that show the effect of surface roughness on the friction fatigue process. The authors used the relative surface roughness parameter, R_n, proposed by Uesugi and Kishida (1986). This way, the two interface systems studied by the authors had different R_n roughness by using surfaces of identical roughness against fine and coarse sands, resulting in "rough" and "smooth" interfaces, respectively. The authors showed that rough interfaces result in volume change tendencies that combine contraction with dilation, which result in a net contraction, while smooth interfaces only

underwent contraction. Furthermore, the rough interface showed to undergo cyclic degradation at a faster rate as a result of the more intense shearing induced.

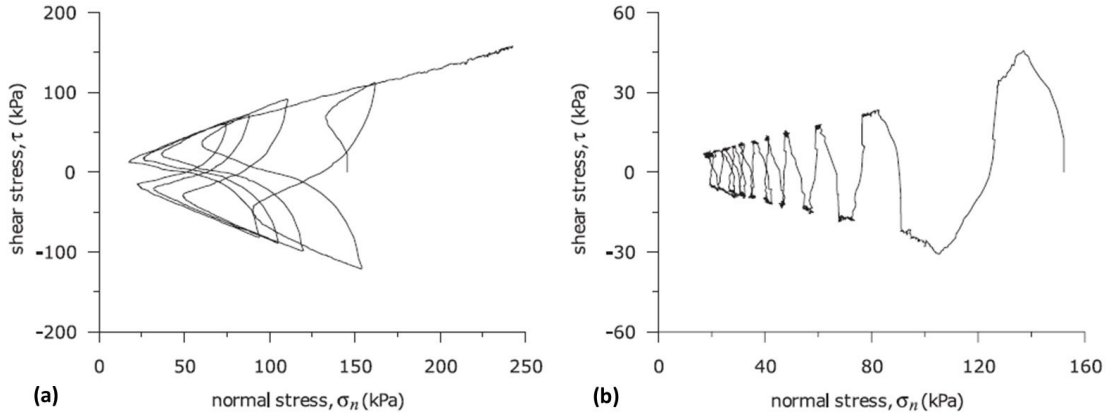

Figure 2.20: Stress path for cyclic direct shear interface tests: (a) rough interface and (b) smooth interface (after Mortara, et al. 2007).

2.1.12.2 Cyclic Shear-Induced Volume Changes

Cumulative contractive volume change tendencies are typically observed during cyclic loading of interface systems, irrespective of the confining loading conditions (i.e. constant load, constant stiffness or constant volume). A stress reversal results in significant rotation of the principal stress components, which causes particles to rearrange into different fabric configurations and ultimately causes contraction of the soil undergoing large shear strains (Alarcon-Guzman, et al. 1988). While several authors who performed studies based on global measurements point out that these contractive volumetric strains take place at the soil directly contacting the surface (e.g. White and Lehane, 2004; Airey and Kelly, 2010), researchers that performed tests incorporating local volume change measurements have concluded that the soil immediately adjacent to the surface undergoes dilation while a secondary zone further away undergoes significant contraction. This effects result in a net contraction of the specimen, especially for loose soil assemblies or for tests against rough surfaces, as shown on Figures 2.21a and 2.21b (DeJong, et al. 2006; DeJong and Westgate, 2009; DeJong and Westgate, 2010).

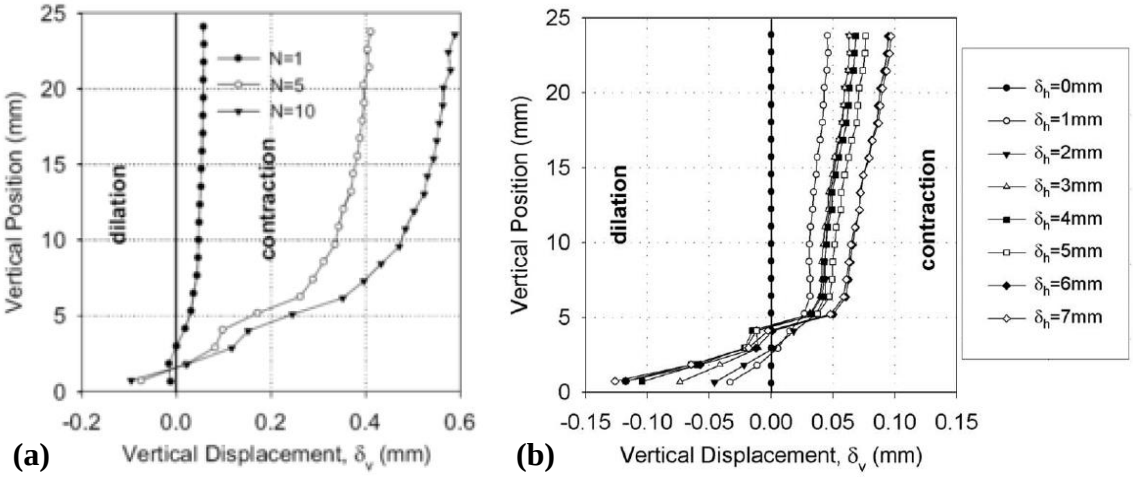

Figure 2.21: Local Particle Image Velocimetry (PIV) volume changes as a function of vertical distance away from the interface for (a) cyclic test at different number of cycles (after DeJong and Westgate, 2010) and (b) monotonic test at different shear displacements (after DeJong and Westgate, 2009).

2.1.12.3 Particle Breakage and Surface Wear

Another effect that has received significant attention is that of particle breakage and surface wear. Researchers such Uesugi, et al. (1989), Airey and Kelly (2010) and Dietz and Lings (2010) performed cyclic tests, while others such as Barmpopoulos, et al. (2010) and Ho, et al. (2011) have performed large displacement monotonic ring-shear tests. The authors studying both shear mechanisms have reported significant particle breakage occurring at the interface as the shear displacements increase. They note that particle breakage results in a change of the shear-displacement behavior caused by the modified particle properties, such as their sizes and shapes. Uesugi, et al. (1989) presented stress ratio results as a function of cycle number for interface systems of different normalized surface roughness, R_n. The authors concluded that after about 10 cycles, the mobilized stress ratio of all the interface systems converged to a similar value despite the initial surface roughness values (Figure 2.22a). They attribute this effect to the

progressive crushing of the larger particles that results in an increasing R_n value as the particles in the shear zone break into smaller particles.

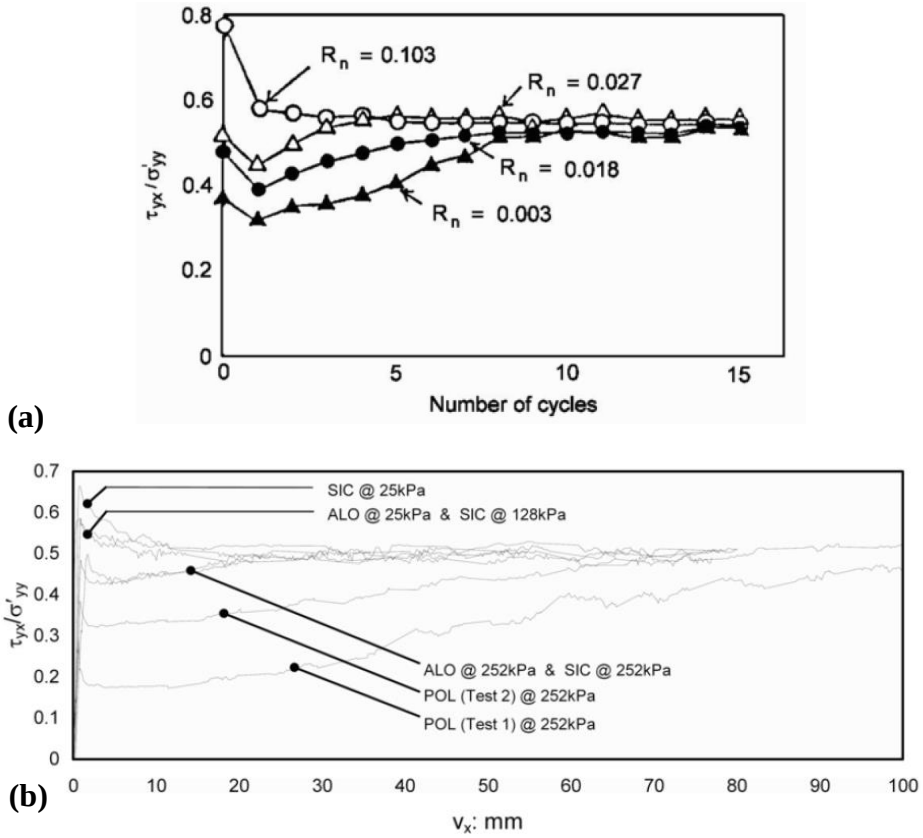

Figure 2.22: (a) Stress ratio as a function of cycle number for interface shear tests performed against surfaces of different roughnesses (after Uesugi, et al. 1989). (b) Stress ratio-displacement curves for cyclic interface shear tests performed against surfaces of different roughnesses under different confining stresses (after Dietz and Lings, 2010).

Dietz and Lings (2010) attribute the previously described effect to particle breakage combined with surface wear. In a smooth interface system composed of steel and sand, especially if subjected to large magnitudes of confining stress, increasing shear displacement results in particle sliding and rolling against the steel surface which causes abrasion. The surface wear, combined with the progressive breakage of particles, result in an increase of the R_n value for the interface system. The results presented in Figure 2.22b show stress ratio-displacement curves for cyclic tests performed under different confining

stresses against surfaces of different roughness (note: the steep-sided valleys making changes in direction of shearing have been removed to aid the viewer, and the subscripts POL, ALO and SIC denote surfaces of increasing roughness magnitude, respectively). The mobilized stress ratios tend to converge to similar values and show the following characteristics: (1) tests under small confining stresses against rough surfaces show high peaks caused by large dilation rates at small shear displacements, (2) tests under large confining stresses against smooth surfaces show an increasing stress ratio caused by surface abrasion and particle breakage. The results presented in this section highlight the importance of taking into consideration the change in soil and surface characteristics with increasing shear displacement for the accurate prediction of interface strength and shear behavior.

2.2 In-Situ Measurement of Interface Behavior: Multi-Sensor Technologies

The only widespread interface shear in-situ test conducted in current geotechnical practice is the friction sleeve measurement (f_s) as part of the cone penetration test (CPT). However, large variability in measured values and associated poor correlation performance has limited usage of CPT f_s values in engineering practice (Lunne, et al. 1997). Some of the shortcomings of the f_s measurement are caused by the design of the conventional CPT device including: the sleeve location within the highly stressed zone directly behind the CPT tip, the sleeve roughness (or lack thereof) and the unmonitored changes in friction sleeve surface roughness due to sleeve wear. A detailed assessment of the limitations of the CPT f_s measurement can be found in DeJong (2001) and in Hebeler (2005).

In response to the shortcomings of the CPT friction sleeve measurement, a series of multi-sleeve friction penetrometer attachments has been developed by researchers at the Georgia Institute of Technology (DeJong, 2001; DeJong and Frost, 2002; Frost and DeJong, 2005; Hebeler, 2005; Hebeler and Frost, 2006; Frost and Martinez, 2013; Frost

and Martinez, 2014). The following sections present a brief descriptions of these multi-sensor technologies.

2.2.1 First Generation: Multi-Friction Attachment (MFA)

All of the developed multi-sleeve attachments are designed to be placed behind a standard 15cm^2 CPT probe. The first generation attachment, the MFA shown in Figure 2.23, has the ability to be equipped with four additional friction sleeves, each with an individual load cell, along the body of the attachment, located farther behind the CPT tip and outside the highly stressed zone created during probe penetration (DeJong, 2001; DeJong and Frost, 2002; Frost and DeJong, 2005).

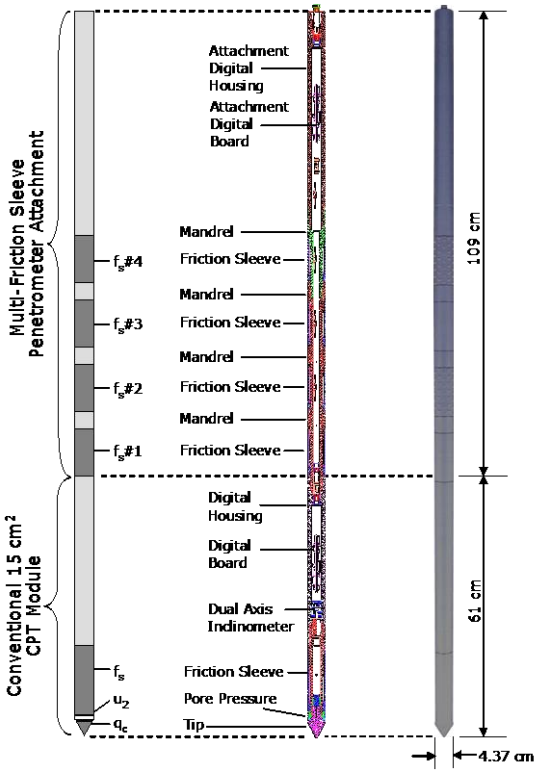

Figure 2.23: Schematic of the Multi-Friction Attachment (MFA) (after DeJong, 2001).

Custom-fabricated friction sleeves with varying roughnesses (shown in Figure 3.3) can be readily exchanged between the different positions of the attachment. These friction sleeves are intended to induce different degrees of shearing while the CPT probe is being pushed into the ground, as shown in Figure 2.24a. The differences in measured

loads provide enhanced capabilities for stratigraphy identification and soil classification (DeJong and Frost, 2002). The friction measurements obtained with friction sleeves of varying surface roughness can be readily used to reproduce the bilinear relationship between interface strength and surface roughness, as shown in Figure 2.24b. These soundings have the added benefit of eliminating spatial and temporal variability effects because all of the friction sleeve measurements are being obtained in the same sounding.

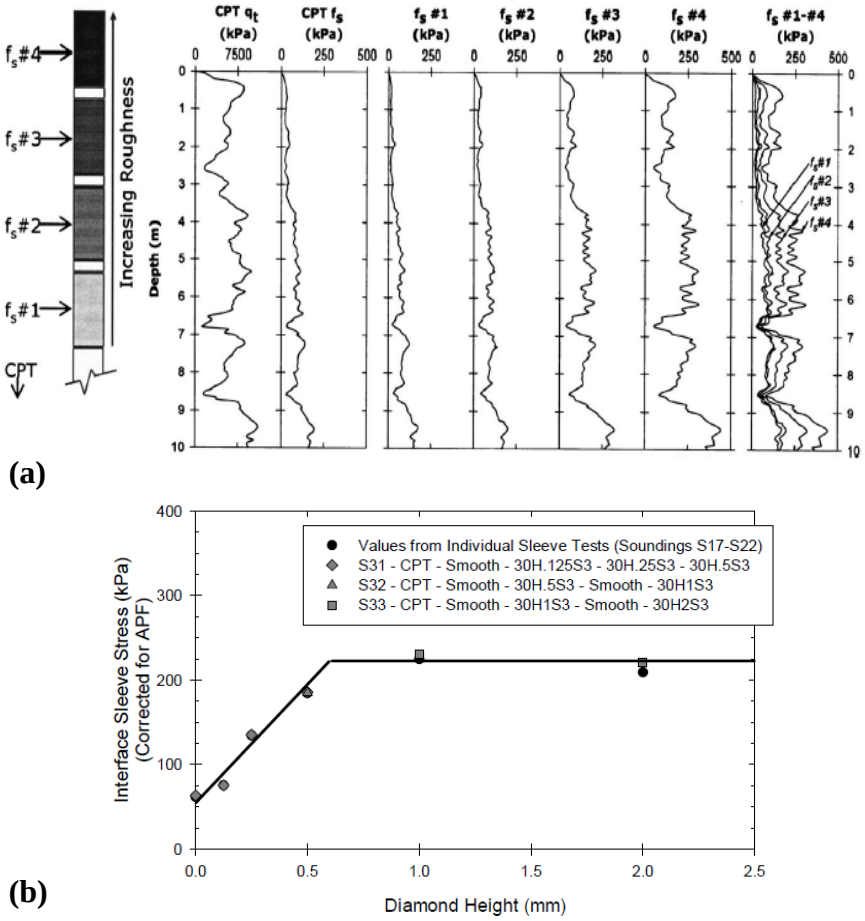

Figure 2.24: Typical results from MFA sounding equipped with friction sleeves of increasing texture (adapted from Frost and DeJong, 2005).

2.2.2 Second Generation: Multi-Piezo-Friction Attachment (MPFA)

The second generation of multi-sensor devices offers the ability to directly measure the interface response over a range of counterface profiles while simultaneously

measuring the excess pore water pressure ahead of and after each friction sleeve as the device is advanced into the subsurface (Hebeler and Frost, 2006). This is achieved by means of its four independent load cells attached to the textured sleeves and five independent dynamic pore pressure sensors. A schematic of the MPFA is presented in Figure 2.25 where the numbers on the left side of the figure represent distances behind the CPT tip in meters.

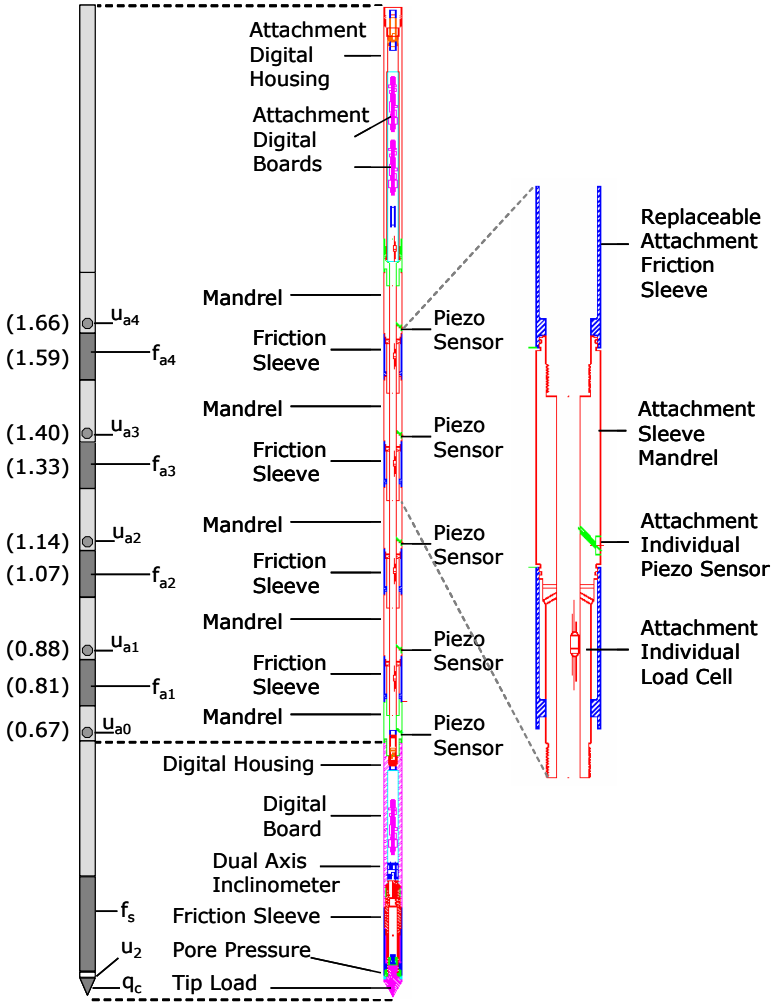

Figure 2.25: Schematic of the Multi-Piezo-Friction Attachment (MPFA) (after Hebeler, 2005).

The coupling of axial load and pore pressure sensors gives the MPFA the ability to provide a direct measure of pore water pressure generation due to shearing against surfaces of different roughnesses allowing for consideration of the measured interface

response within an effective stress framework, estimating flow and consolidation characteristics along the penetrometer's shaft, attaining more detailed data for improved stratigraphy profiling, and distinguishing between drained, undrained and partially drained conditions (Hebeler, 2005; Frost, et al. 2012). Results from the MPFA have shown reduction in penetration pore pressures from the shoulder of the cone (u_2 reading) to positions at larger offsets from the tip.

Examples of the unique and/or new insights resulting from the MPFA multi-sleeve sensor technology include soil classification charts that use interface behavior, tip stress (q_t), and pore pressure measurements (u_2), as shown in Figure 2.26. In contrast to existing classification charts (Robertson, 1990) the proposed approach uses an independent friction parameter based on the interface friction-sleeve roughness relationship obtained from MPFA results (x-axis in Figure 2.26) as opposed to friction ratio, F_R, which is dependent on the magnitude of the tip stress as well.

Another new insight resulting from the MPFA comes from monotonic and cyclic soundings with pore pressure dissipation measurements. Soundings with the MPFA were performed in two different sites in Western Australia: a site with predominantly sand geology and a site with clay geology. In sands, the monotonic pore pressure response generally followed the hydrostatic pore pressure conditions (Hebeler, 2005). In clays, the different degrees of sleeve roughness resulted into different pore pressure responses. These soundings showed the ability of the textured sleeves to induce different degrees of excess pore pressures during shearing.

Excess pore pressure generation was also investigated by performing a series of large and small cyclic displacement tests. The large amplitude tests consisted of ten 2-way full length cycles of 1 m, and the small amplitude tests consisted of 200 full length 2-way cycles of 5 mm displacement. These tests were designed to simulate different levels of cyclic loading that are typically applied to foundation elements by phenomena such as earthquakes, wind gusts, industrial equipment and construction activities and to

assess issues in soils such as sensitivity, stress degradation, excess pore pressure generation and post installation pile shaft friction.

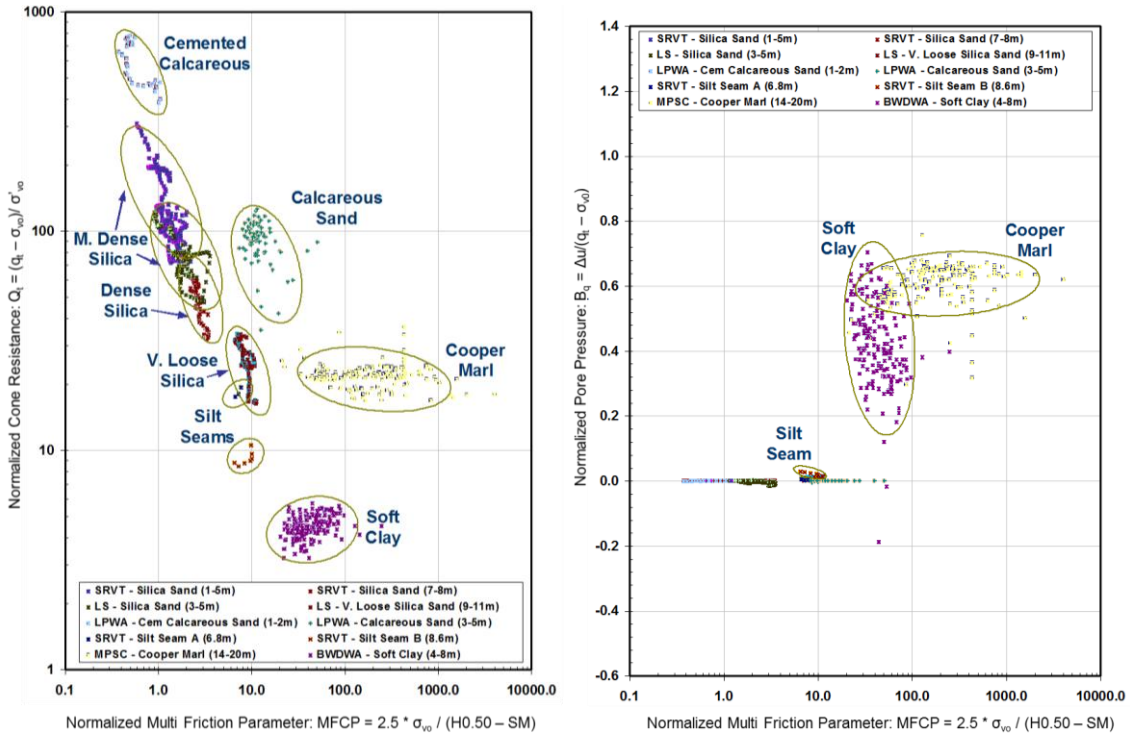

Figure 2.26: Soil Classification Chart based on MPFA data (after Hebeler, 2005).

Figure 2.27a shows the large amplitude cyclic behavior of the tip stress (q_t), pore pressure (u_2), sleeve stress measurements obtained with a textured sleeve (f_{s3}) and associated pore water pressure readings (u_{a3}). The q_t, u_2, f_{s3} and u_{a3} sensors all showed hysteresis loops with the degradation of the readings with increasing number of cycles. Figure 2.27b shows the normalized response from a small amplitude cyclic test. The u_2 readings exhibit a dilatory response before cycling, with cyclic variations on the order of 5% of the initial pore pressure. The u_{a0} sensor exhibited significant cyclic induced pore pressure over the first 5 to 15 cycles, indicating the ability of the small amplitude shear cycles to induce excess pore pressures. The u_{a1}, u_{a2}, u_{a3} and u_{a4} responses exhibited moderate cyclic induced excess pore pressure over the first 10 cycles; however, all pore

pressure responses indicated a delay of normal dissipation response, shown clearly in the change of dissipation rate after the end of the cycling process.

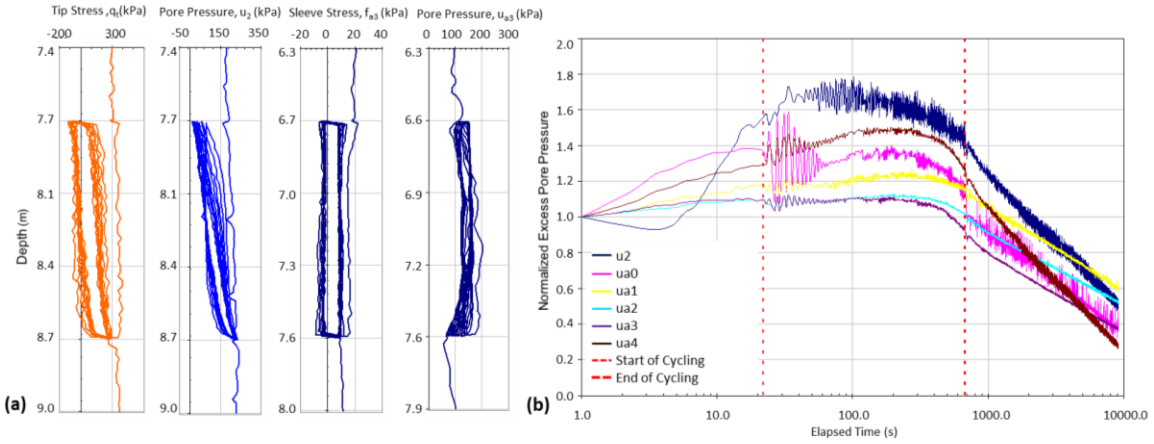

Figure 2.27: MPFA cyclic tests in clayey soils. (a) Large amplitude test showing tip resistance (q_t), pore pressure (u_2), sleeve stress with textured sleeve (f_{a3}) and associated pore pressures (u_{a3}) (b) small amplitude test showing u_2 and u_{a0}, u_{a1}, u_{a2}, u_{a3}, and u_{a4} sensors along MPFA shaft (after Hebeler, 2005).

2.2.3 Third Generation: Multi-Piezo-Friction-Torsion Attachment (MPFTA)

The next generation of multi-sensor devices builds on the insight gained with the previous versions but will represent several major enhancements over the current versions: (a) the ability to load the soil in torsional shear mode as well as the existing axial shear mode; (b) the development of a self-boring (SB) lead module so that the device can be deployed either behind the conventional CPT or an SB unit; and (c) the inclusion of a lateral stress module in the device. The new torsional functionality incorporated into the next generation devices will consist of a dual load-torsion cell being installed in each sleeve module, with the goal of measuring both axial and torsional shear responses of the soil throughout the same sounding. Furthermore, comparison of the results obtained from the device configured behind a CPT and behind an SB unit will provide the opportunity to understand the effects caused by the disturbance of the cone

tip insertion. Figure 2.28 shows schematics of the proposed CPT and SB led configurations.

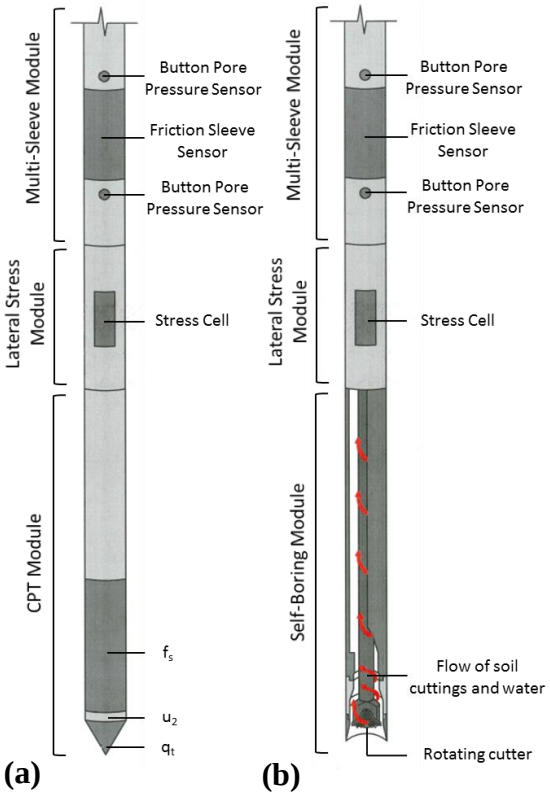

Figure 2.28: Schematic of (a) CPT and (b) self-boring (SB) unit led MPFTA devices.

A typical test sequence might consist of advancing the probe to the desired depth behind a CPT while recording axial loads on each sleeve location, followed by temporarily stopping the penetration process in order to rotate the device and measure torsional loads. In this manner, the effects of spatial variability (vertical and horizontal) will be eliminated and more detailed information about the soil's shear strength, anisotropy and state of stress can be provided. Adjacent soundings behind the CPT and self-boring units would record the axial and torsional loads on each sleeve. The primary difference would be the lack of insertion disturbance with the SB led sounding compared to the CPT led one.

CHAPTER 3

EXPERIMENTAL AND NUMERICAL METHODS

This chapter describes the general methodologies used to perform the experimental and numerical tests and to collect data from them. These include descriptions of the soils, surfaces, sensors, devices and numerical models utilized. The specific methodologies used for various phases of this research can be found in the corresponding chapters.

3.1 Experimental Procedures

3.1.1 Sands Used for Interface Shear Testing

The three soils used for this research consisted of Ottawa 20-30 sand (U.S. Silica), local Atlanta Blasting 20-30 sand (Atlanta Sand & Supply Co.) and Ottawa 50-70 sand (U.S. Silica). Ottawa 20-30 is a poorly-graded medium-sized rounded to sub-rounded sand, Blasting 20-30 sand is a poorly graded medium-sized sub-angular to angular sand, and Ottawa 50-70 sand is a poorly graded medium-fine sub-rounded to sub-angular sand. Figure 3.1a to 3.1c presents microscope photographs of the three sands, Figure 3.1d presents the grain size distributions and Table 3.1 presents other grain size, packing and particle properties. These sands were chosen in order to study the effect of particle shape, by comparing results from tests with Ottawa 20-30 to results from tests with Blasting 20-30 sands, and the effect of mean particle size by comparing either results from tests with Ottawa 20-30 to those with Ottawa 50-70, or by comparing results from tests with Blasting 20-30 to those with Ottawa 50-70.

The mechanical properties of the sands, namely their internal friction and dilation angles, were determined by performing a series of consolidated drained direct shear tests according to ASTM D 3080-11 standards. The direct shear machine (ShearTrac by Geocomp Corporation) was equipped with vertical and horizontal load cells and LVDTs

that allowed measuring the applied normal and mobilized shear loads and vertical and horizontal displacements. Using the specimen dimensions, the results were then analyzed in terms of stress and strain.

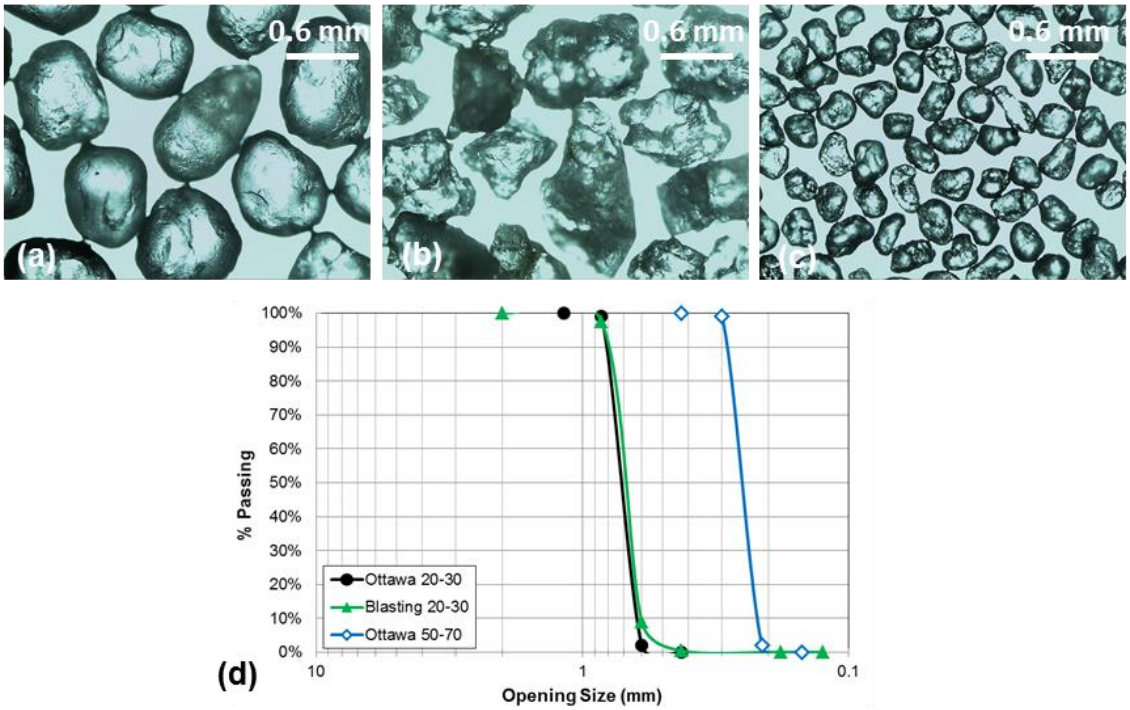

Figure 3.1: (a) Photograph of sub-rounded 20-30 (b) sub-angular 20-30 (c) sub-angular 50-70, and (d) grain size distribution curves for the three sands.

Table 3.1: Grain size, packing and particle properties of sands tested.

	Ottawa 20-30	Blasting 20-30	Ottawa 50-70
G_s[1]	2.65	2.65	2.65
D_{50} (mm)	0.72	0.72	0.26
C_u	1.17	1.22	1.24
C_c	0.96	0.96	0.97
e_{max}[2]	0.72	1.13	0.85
e_{min}[3]	0.54	0.70	0.58
Roundness[4]	0.73	0.32	0.50

[1]Reported by manufacturer, [2]ASTM D 4254, [3]ASTM D 4253, [4]Roundness = $(\Sigma r_i/N)/r_{max\text{-}in}$

The shear box had a diameter of 2.5 inches and the initial specimen height was prepared to 1 inch. A porous stone and a layer of filter paper were positioned at the top and bottom of the specimens. This configuration was such so that the split in the shear box was located at mid-height of the specimens. Figure 3.2a and 3.2b present the failure

envelopes for peak and residual shear conditions, respectively, and Table 3.2 presents the test results along with the calculated peak and residual friction and dilation angles. Appendix A presents the direct shear data used for the failure envelope calculations.

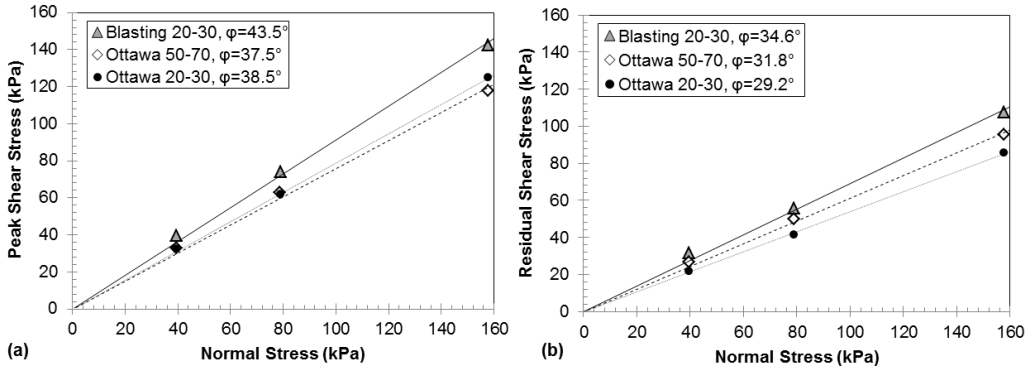

Figure 3.2: Direct shear failure envelopes for (a) peak and (b) residual shear conditions.

Table 3.2: Direct shear test and results data.

Sand Type	Relative Density (%)	Normal Stress (kPa)	Shear Stress (kPa)		Softening (kPa)	Friction Angle (°)		Measured Dilation Angle (°)
			Peak	Residua		Peak	Residual	
Ottawa 20-30	72.3	39.4	34.5	24.6	14.8			10.2
Ottawa 20-30	69.3	78.9	61.8	44.6	22.2	38.5	29.2	10.2
Ottawa 20-30	75.3	157.7	124.9	88.5	41.3			10.6
Ottawa 50-70	66.5	39.4	32.9	29.5	8.3			5.6
Ottawa 50-70	70.9	78.9	62.7	53.1	14.6	37.5	31.8	7.9
Ottawa 50-70	70.9	157.7	117.7	95.3	27.4			7.0
Blasting 20-30	65.2	39.5	42.5	35.4	12.1			12.1
Blasting 20-30	73.4	78.9	76.8	55.8	26.0	43.5	34.6	13.9
Blasting 20-30	69.9	157.8	147.4	106.5	40.9			12.2

The Blasting 20-30 sand showed the largest peak (43.8°) and residual (34.6°) friction and dilation (average 12.7°) angles, which reflect the larger angularity of its grains. The Ottawa 50-70 sand showed the next larger residual friction angle (31.8°), but the lowest peak friction (37.5°) and dilation (average 6.8°) angles. While this sand's angularity is larger than that for Ottawa 20-30 sand, which is reflected in its larger residual friction angle, its grain sizes are smaller giving it a smaller dilation which in turn results in the smaller peak friction angle. Finally, the Ottawa 20-30 sand showed the smallest residual friction angle (29.2°) but peak friction (38.5°) and dilation (average 10.3°) angles with magnitudes that fall in between the values for the other two tested sands. These results are in general agreement with results published in the literature. For

Ottawa 20-30 sand Iscimen (2004) reported direct shear peak and friction angles of 38.9° and 27.9°, respectively; for Ottawa 50-70 sand Zelasko, et al. (1975) reported a triaxial peak friction angle of 38.5° and Simpson (2014) reported a triaxial residual friction angle of 33.6°; and for local Atlanta Blasting 20-30 sand Iscimen (2004) reported direct shear peak and residual friction angles of 43.1° and 34.6°. The calculated values for peak and residual friction angles presented in this section are used for the analysis of results presented through this thesis. The "results repeatability assessment" section included later in this chapter further addresses the repeatability of the direct shear test results.

3.1.2 Steel Surfaces Used for Interface Shear Testing

Friction sleeves for 15 cm^2 CPT probes were used as the surfaces for most the axisymmetric interface shear tests presented in this thesis. Smooth sleeves that comply with the ASTM D 5778-07 standards (R_{max} = 0.01 mm) and textured sleeves of varying roughness were used. Different magnitudes of surface roughness in the friction sleeves was achieved by means of a staggered diamond pattern of varying diamond height, H, as shown in Figures 3.3a through 3.3d. It is important to note that the magnitude of H is equal to the maximum roughness of the sleeves, R_{max}, defined as the absolute maximum distance between the highest peak and the lowest valley of the surface roughness. The R_{max} values used for the current study were 0.01 (conventional CPT), 0.25, 0.50, 1.00 and 2.00 mm. The diamond width (5.3 mm), w, penetration angle (60°), β, diagonal spacing (6.3 mm), s, and texture angle (45°), α, of the diamond elements were kept constant. An untextured area between any two diamond elements (referred as "passthrough") results in flow paths around/between each of the diamond asperities and prevents soil particles from clogging the texture and thereby change its surface roughness throughout the performance of the tests (DeJong, et al. 2001). A study by Hebeler, et al. (2015) validated the ability of the textured friction sleeves to induce uniform shear zones in medium-sized sands and provided further details regarding the shear zone development process and its

implications on CPT friction sleeve measurements. For more information regarding the full progression of sleeve texture designs, including the use of different texturing elements such as ribs and diamonds of different widths, penetration angles and spacing configurations, the reader can refer to Cargill (1999), DeJong et al. (2000), DeJong et al. (2001), DeJong and Frost (2002), and Frost and DeJong (2005).

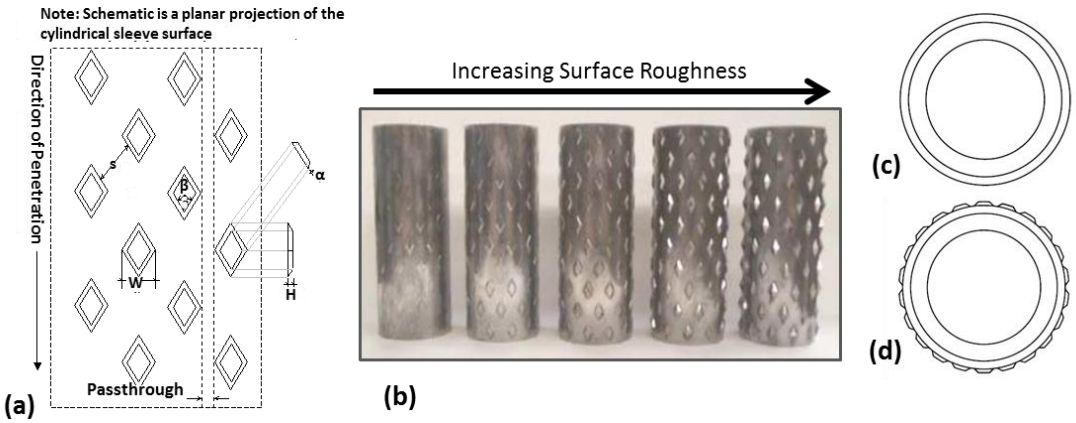

Figure 3.3: Friction sleeve texture. (a) schematic of texture, (b) photograph of friction sleeves, (c) cross-section of smooth and (d) textured CPT sleeves (adapted from DeJong, 2001 and Hebeler, 2005).

3.1.3 Sandpaper Surfaces Used for Interface Shear Testing and Roughness Form Study

The study presented in this thesis suggests that the surface roughness form can have a significant effect on the interface behavior. Namely, surfaces with identical roughness values, either average (R_a), maximum (R_{max}) or normalized (R_n), can mobilize different interface friction angles. Therefore, the study presented in Chapter 8 of this thesis addresses the effect of different roughness forms on the interface shear behavior. The surfaces of "structured" roughness consist of friction sleeves with a staggered diamond texturing pattern shown in Figures 3.3a through 3.3d. This pattern consists of texturing elements that protrude outside the base diameter of the sleeve which allow for the surface roughness to be controlled by varying their height while keeping the rest of

their dimensions fixed. An untextured space between any two diamond rows and columns (i.e. "passthrough") prevents particles from getting trapped on the leading edge of the diamonds during shearing and thus prevents interface clogging. The surfaces of "random" roughness consisted of smooth sleeves covered by one layer of sandpaper, which resulted in surfaces with profiles composed of non-periodic features that go above and below the surface's baseline. These non-periodic features cover the entire surface of these sleeves and promote roughness clogging. Figure 3.4a shows profiles of sandpaper sheets of different roughness, Figure 3.4b shows pictures of sandpaper sleeves of medium and high roughness (i.e. "random" roughness sleeve) mounted on the testing rod, and Figure 3.4c show a picture of a textured sleeve mounted on the testing rod (i.e. "structured" roughness sleeve).

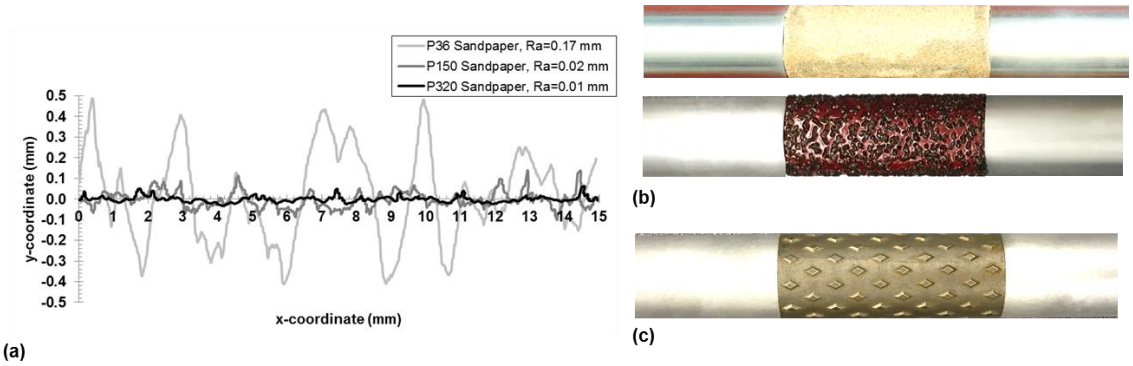

Figure 3.4: (a) Profile of various sandpaper sheets, (b) sandpaper and (c) textured sleeves mounted in between testing rods.

3.1.4 Axisymmetric Device for Drained Interface Shear Tests

The axisymmetric testing device for axial interface shear (Figure 3.5a) was originally developed by DeJong (2001), and was then modified as part of this research program to allow for torsional interface shear testing (Figure 3.5b). This device consisted of a cylindrical three-part steel chamber that allows for different magnitudes of uniform lateral confining stress to be applied via externally applied air pressure to a soil specimen inside a layer of needle-punched nonwoven geotextile and a latex membrane. The

constant confining stress was applied to all specimens through three external ports located at the center of each tri-mold section. The top and bottom plates of the chamber were made of aluminum and provided fixed boundaries, resulting in BC4 type calibration chamber boundary conditions (Ghionna and Jamiolkowski, 1991). These top and bottom plates have rubber seals at their centers through which the testing rod penetrated while avoiding loss of soil particles. The interface shear tests were performed by preparing the dry soil sample by a combined method of pouring and tamping around a 47.3 mm diameter cylindrical rod section consisting of a mounted friction sleeve between upper and lower smooth aluminum testing rods with a prescribed surface roughness equal to that of a conventional CPT friction sleeve. This preparation method modeled a "perfect insertion" scenario that eliminated the disturbance caused by the tip insertion and associated cavity expansion observed in field or calibration chamber penetration tests.

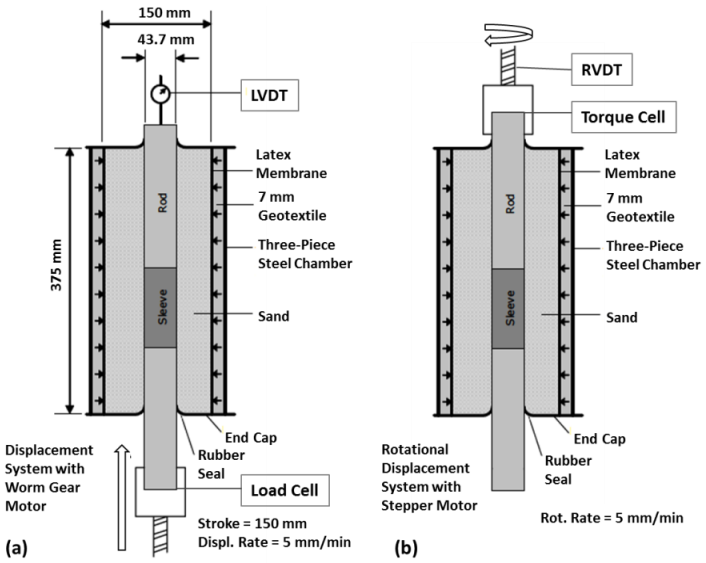

Figure 3.5: Axisymmetric device configuration for (a) axial and (b) torsional interface shear tests.

A displacement system controlled by a worm gear motor in the axial direction and by a stepper motor in the torsional direction were used at an average displacement rate of 5 mm/min (conforming to ASTM D 5321–14 standards for interface shear testing), and all samples were sheared for a total displacement of 63.5 mm, which is equivalent to a

rotation of 166.5°, or 0.46 revolutions, during torsional shear. Axial shear resistance loads were recorded by a load cell located between the bottom of the rod and the motor, while torsional shear loads are recorded by a torque cell located between the top of the rod and the motor. The vertical shear displacement was recorded by an LVDT located at the top end of the rod, and the angular shear displacement was recorded by an RVDT connected to the torsional motor shaft. It should be noted that this device was not enabled to measure specimen volume changes during consolidation or shear. The "results repeatability assessment" section included later in this chapter further addresses the repeatability of the drained axisymmetric test results.

3.1.5 Axisymmetric Device for Undrained Cyclic Interface Shear Tests

An axisymmetric device with the capability to perform interface shear tests in undrained axial and torsional conditions was developed as part of the research presented herein and is shown in Figures 3.6a and 3.6b. The testing chamber consisted of a plexiglass vessel (diameter = 8", height 18", 1" thickness) with three air pressure ports located at mid-height, 120° degrees apart from each other. The inside of the chamber was lined with a rubber membrane that transferred the confining stress to the specimen inside. Similarly to the axisymmetric device for drained interface shear tests, the top and bottom plates were equipped with seals through which the testing rod penetrated. These top and bottom plates provided rigid boundaries that along with the constant confining stress applied to the specimens result in BC4 type calibration chamber boundary conditions (Ghionna and Jamiolkowski, 1991). The testing rod configuration and geometry, specimen preparation method (i.e. perfect insertion) and sensor configuration were the same as described for the axisymmetric drained interface shear tests. During axial tests, a screw jack connected to a stepper motor displaced the testing rod axially, and during torsional tests a different stepper motor with a gearhead displaced the testing rod torsionally. Both stepper motors were programed to run a predetermined number of

cycles of specified displacement amplitude at a rate of 5 mm/min (conforming to ASTM D 5321–14 standards for interface shear testing). Unless specified otherwise, all tests were sheared for an initial one-way displacement cycle of 20 mm (52.5° in torsion) followed by 40 to 80 one-way cycles of amplitude of 15 mm (40.2° in torsion).

This device has the added complexity of requiring water-tight seals between the chamber and the top and bottom plates, as well as between the testing rod and the top and bottom rod seals. These seals were ensured by using a combination of o-rings and vacuum grease. Figure 3.6c shows a schematic of the plumbing configuration of the device. As shown in Figures 3.6a, 3.6b and 3.6c, the bottom plate has two inflow ports through which water is introduced during the specimen saturation process, and the top plate has two water outflow ports. A pressurized water reservoir was used to supply water during the specimen saturation process. This reservoir allowed for the volume of water flowing into the specimen to be measured. Similarly, the outflow water was collected and its volume was measured. Porous stones were placed between the specimen and the top and bottom plates, and a pressure sensor was connected in series with the lines going to the bottom plate. This sensor was used to measure the pore pressures during testing.

Specimen saturation was achieved by flowing water through the specimen under a pressure gradient of 1 psi while the specimen was under an effective confining stress of 3 psi. The amount of air removed from the voids was calculated by comparing the volume of the voids, estimated by multiplying the total specimen volume by the average specimen porosity, with the measured volume of water inside the specimen. The specimen was considered to be saturated when the ratio of water in the specimen to volume of the voids was equal or greater to 95%. Next, the specimen was consolidated under the test effective confining stress for 30 minutes and the water outflow was measured. After consolidation, the inflow and outflow valves were closed and the undrained cyclic shear stage began. This device has the capability of measuring sample volume changed during drained tests by measuring water inflow/outflow. However, all

the results presented as part of this study were performed in undrained (i.e. constant volume) conditions. The "results repeatability assessment" section included later in this chapter further addresses the repeatability of the undrained axisymmetric test results.

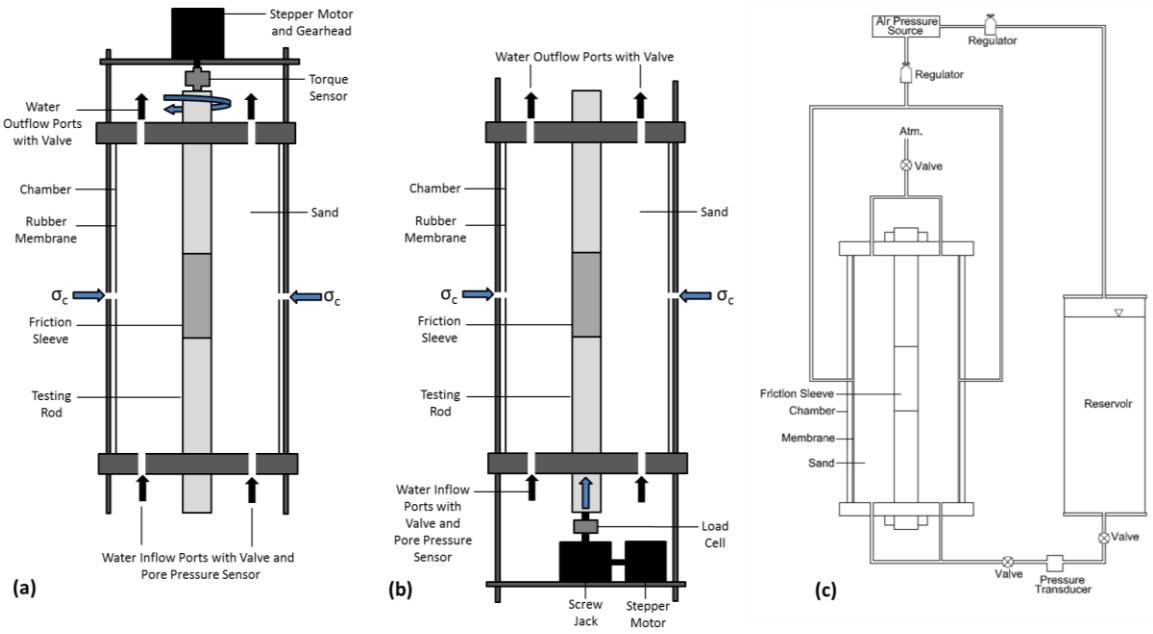

Figure 3.6: Configuration for (a) torsional and (b) axial undrained cyclic shear tests. (c) Schematic of plumbing system for undrained axisymmetric apparatus.

3.1.6 Global Stress Measurements

The apparatus configurations shown in Figures 3.5a, 3.5b, 3.6a and 3.6b enabled the measurement of the force required to displace a rod equipped with a friction sleeve axially or torsionally. As such, it is important to define the approaches used to estimate the interface shear stress, stress ratio (τ/σ) and interface friction angle (δ). A schematic detailing these is presented in Figures 3.7a and 3.7b for axial and torsional shear, respectively. For both axial and torsional shear, the measured force (T) is equal to the integral of the induced shear stress distribution (τ) (regardless of its shape) over the area at which it acts. This area is a ring with an inner diameter equal to the sleeve diameter (D_{sleeve}) and an outer diameter equal to the extent of the induced shear stress (t_I). The measured force T is divided by the sleeve surface area (π x D_{sleeve} x H_{sleeve}) in order to

obtain the shear stress on the sleeve surface (τ_{sleeve}), and the stress ratio is defined as the shear stress on the sleeve (τ_{sleeve}) divided by the confining pressure applied (σ_c). The following equations detail these calculations:

$$T = H_{sleeve} \int_{D_{sleeve}}^{t_I} \tau \quad dr$$

$$\tau_{sleeve} = \frac{T}{\pi \;\; x \;\; D_{sleeve} \;\; x \;\; H_{Sleeve}}$$

$$Stress \quad Ratio, \quad \frac{\tau}{\sigma} = \frac{T_{sleeve}}{\sigma_c}$$

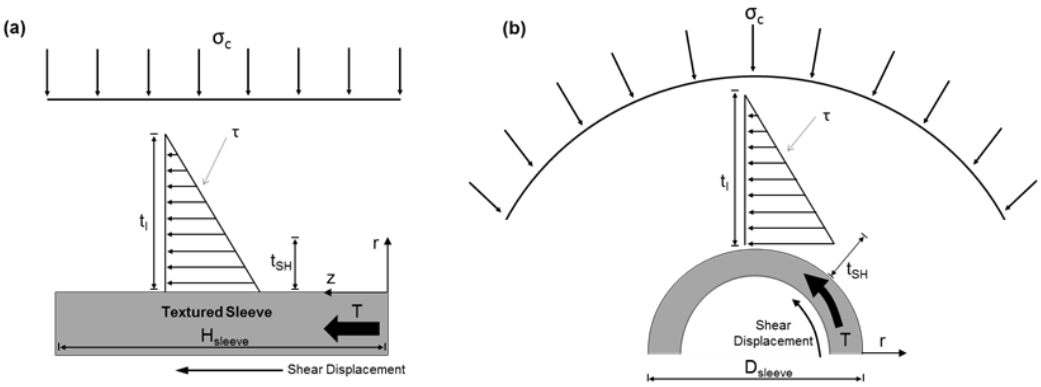

Figure 3.7: Induced and applied stresses during (a) axial and (b) torsional shear test, where: T = measured load, H_{sleeve} = sleeve height, D_{sleeve} = sleeve diameter, τ = induced shear stress, t_I = extent of induced shear stresses, t_{SH} = shear zone thickness, σ_c = confining stress.

3.1.7 Phenolic Resin Impregnation and Shear Zone Characteristics Measurements

A series of tests with the objective of quantifying the characteristics of the shear zones formed during drained axisymmetric axial and torsional tests were performed on Ottawa 20-30 and Blasting 20-30 sands and are presented in Chapter 4 of this thesis. In order to do this, the method proposed by Juang and Holtz (1986) for resin-cemented specimens was followed. In summary, the sands were mixed with PLENCO 10510 powder phenolic resin (1% by weight) before testing. Prior to activation, this powdered resin has no significant effect on the mechanical response of the sands as shown by three

control axisymmetric tests with and without phenolic resin that resulted in coefficients of variation (COV) lower than 5% for measured peak and residual loads. Further, direct shear tests on Ottawa 20-30 and Blasting 20-30 sands (specimen diameter = 2.5") with and without phenolic resin indicated peak and residual friction angle differences of less than one degree, as shown in Figures 3.8a and 3.8b for Ottawa and Blasting 20-30 sands.

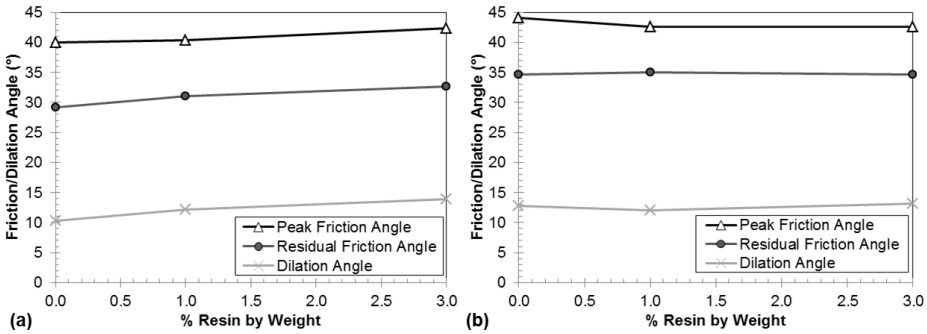

Figure 3.8: Effect of % resin by weight on the measured peak and residual friction and dilation angles of (a) Ottawa 20-30 and (b) Blasting 20-30 sands.

After the test was completed, the specimen was heated for six hours in order to activate the powder phenolic resin, which acted as a lightly cementing agent that held the sand matrix intact. This process resulted in weakly cemented and highly brittle specimens which underwent cementation breakage at the contacts if the particles were disturbed. Thus, when a vertical dissection was made, the particles that remained as part of the specimen were representative of the undisturbed sand structure. It is believed that heating the specimen did not affect the post-shear sand micro-structure given that the testing chamber restricted any temperature-related volume changes that might otherwise occur. These volume changes can be considered to be negligible for sands tested, as a quartz Ottawa 20-30 particle will increase in diameter by 0.005% (0.0004 mm) if increased in temperature by 50° C. After the phenolic resin hardened, the specimen was readily dissected and vertical and horizontal planes were exposed for detailed study by means of high resolution photographs that allowed for accurate measurement of shear zone thicknesses and lengths to be performed. Figures 3.9a through 3.9f show pictures of

cemented specimens retrieved from the chamber, dissected vertical and horizontal faces and close-ups of the shear zones formed during axial and torsional test.

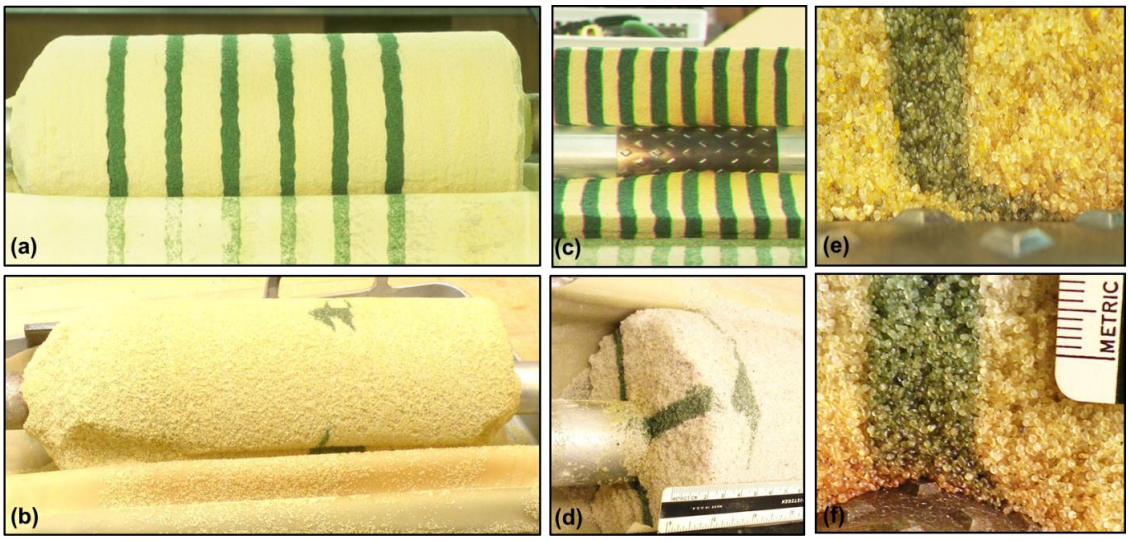

Figure 3.9: Extrusion and dissection process of shear zone characterization tests. Whole sample extruded from chamber after (a) axial and (b) torsional tests. Vertical face dissection after (c) axial and (d) torsional tests. Vertical face close-up from specimens subjected to (e) axial and (f) torsional shear.

Recognizing that the friction sleeves encounter "undisturbed" sand at the sleeve's leading edge at every displacement increment during axial shear, in contrast to the friction sleeves during torsional shear which largely remold the same sand throughout the entire test, it is important to account for this in the interpretation and comparison of the results. This was achieved by only comparing deformation of sand that was continuously sheared against the friction sleeve throughout the axial tests, as shown in Figure 3.10. As such, making measurements only on the sand layers that experienced 100% shearing against textured sleeves allowed for a direct comparison between the sand deformation measurements obtained from axial and torsional tests.

The shear zone characteristics were measured in terms of thickness and length. The shear zone thickness is defined as the distance perpendicular to the friction sleeve

where a high gradient of particle displacement takes place, and the shear zone length is defined as the maximum distance along the friction sleeve where particle displacements are detected. Figures 3.11a, through 3.11c show a schematic of the measurements taken, as well as photographs of shear zones formed during axial and torsional shear, respectively.

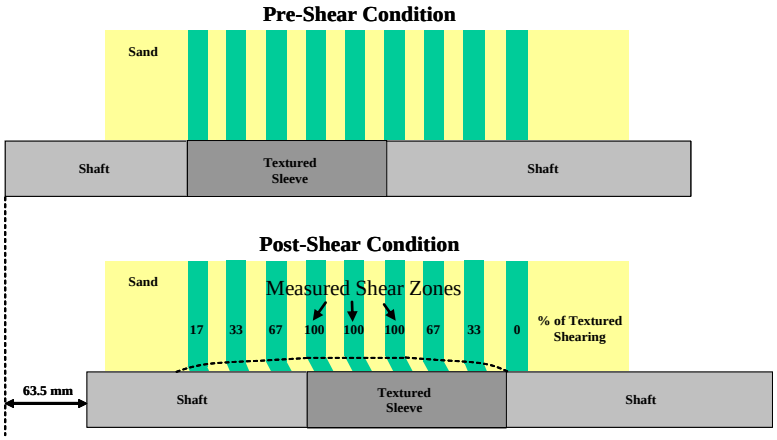

Figure 3.10: Schematic showing the configuration of colored sand layers within each axisymmetric test sample (adapted from Hebeler, 2005).

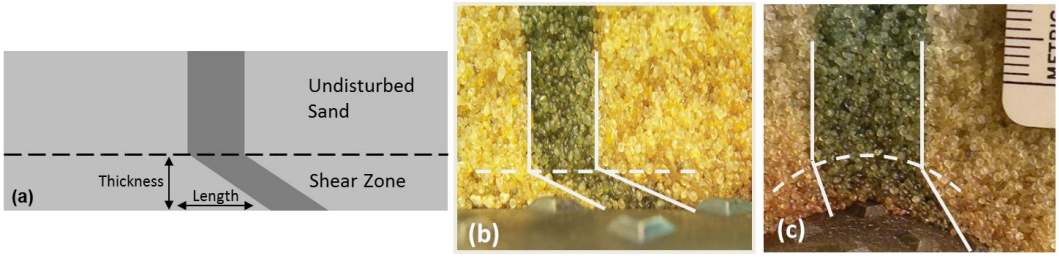

Figure 3.11: (a) Schematic of shear zone measurements. Shear zones formed during (a) axial and (b) torsional interface shear tests.

The shear zone characteristics results presented throughout this document represent an average of at least 32 measurements taken at different locations within the shear zone, including along the top of the diamond texture elements and along the passthrough zones. Quality control monitoring of four tests showed a small variation in the measurements taken at different locations within the shear zone, with COV values of

4.9% for thickness and of 6.4% for length. A detailed assessment of the variation in shear zone thickness and length measurements taken at the top of the diamond texture elements and along the passthrough zones for axial shear tests is included in Hebeler, et al. (2015), which showed a difference of less than one D_{50} for the same sands used in this study.

3.1.8 Epoxy Resin Impregnation and Shear-Induced Volume Change Measurements

Measurements on resin-impregnated Ottawa 20-30 and Blasting 20-30 sand specimens sheared against smooth and textured sleeves of R_{max} of 1.00 mm were taken in order to study the effect of shearing direction (i.e. axial vs. torsional shear), surface roughness and grain angularity on the evolution of the sand void ratio. These results are presented in Chapter 4. First, specimens were prepared in the same manner as described for the phenolic resin impregnation procedure. This allowed for undisturbed sand coupons to be taken at locations determined using a "systematic-random" criterion which is believed to yield an accurate representation of the entire shear zone. Afterwards, the specimens were fully impregnated with EPO-TEK 301, a two-part epoxy resin provided by Epoxy Technologies. This process was undertaken in order to create a rigid binding for the sand micro-structure which allowed for cross-sections perpendicular to the sleeve surface to be cut with a diamond wafering blade while eliminating the possibility of sample disturbance or grain plucking during the cutting, grinding and polishing processes. This epoxy resin was selected because of its low viscosity, which facilitated the impregnation process, its high strength which prevented grain plucking as well as its low volume change during curing (Jang, et al. 1999). Once the cross-sections were exposed, pore volume fraction values were calculated using the discrete point counting technique (Thomson, 1930) calculated as averages of more than one hundred points at each location, which were then used to estimate void ratio values. A "systematic random"

procedure was used to select the locations of the counted points. Figure 3.12 shows a picture of a cross-section used to determine pore volume fractions. The following equations show the expression used for determining pore volume fraction, which is geometrically general thus it does not consider any assumption with regards to image magnification or size or any geometrical features of the microstructure under study.

$$V_V = \langle P_v \rangle = n$$

where:

V_V = pore volume fraction,

$\langle P_V \rangle$ = population average of the fraction of points in the void phase,

n = porosity.

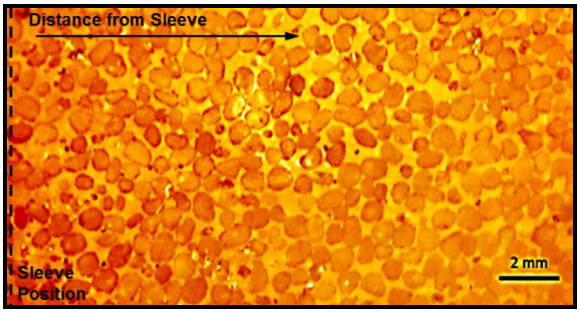

Figure 3.12: Cross-section used to calculate local void ratio as a function of distance from the sleeve.

3.1.9 Experimental Results Repeatability Assessment

As part of the experimental procedures and device performance assessment processes, replicate tests were performed under various conditions. The purpose of these tests is to evaluate the repeatability of the following device configurations:

- Direct shear
- Axial and torsional drained axisymmetric shear with smooth and textured sleeves
- Axial drained axisymmetric shear with sandpaper sleeves

- Torsional drained axisymmetric shear with powder phenolic resin
- Torsional undrained axisymmetric shear with textured sleeves

Table 3.3 shows a summary of the measured peak and residual loads during replicate tests, and the mean, standard deviation, COV and maximum differences of those values.

Table 3.3: Summary of Measured Loads during Replicate Tests.

			Test 1		Test 2		Test 3		Average (kPa)		Standard Deviation (kPa)		COV (%)		Maximum Difference (kPa)	
Test Type	Sand	Surface Roughness, R_{max} (mm)	Peak (kPa)	Residual (kPa)	Peak (kPa)	Residual (kPa)	Peak (kPa)	Residual (kPa)	Peak (kPa)	Residual (kPa)	Peak (kPa)	Residual (kPa)	Peak (kPa)	Residual (kPa)	Peak (kPa)	Residual (kPa)
DS*	OT-20-30††	N/A	36.0	27.9	37.4	28.8	37.4	29.0	36.9	28.6	0.8	0.6	2.2	2.1	1.4	1.1
	OT-50-70†††	N/A	67.4	44.1	66.0	43.8	N/A	N/A	66.7	44.0	1.0	0.2	1.5	0.5	1.4	0.3
	BL-20-30††††	N/A	148.2	105.3	147.9	105.5	N/A	N/A	148.1	105.4	0.2	0.1	0.1	0.1	0.3	0.2
DAA**	OT-20-30†	0.00	14.6	14.6	15.5	14.7	N/A	N/A	15.0	14.6	0.7	0.1	4.5	0.7	1.0	0.2
	OT-20-30†	0.25	31.0	25.0	30.8	25.2	N/A	N/A	30.9	25.1	0.2	0.1	0.6	0.4	0.3	0.1
	BL-20-30†††	2.00	64.1	62.5	65.8	62.3	N/A	N/A	64.9	62.4	1.2	0.2	1.9	0.3	1.7	0.2
DTA***	OT-20-30†	1.00	48.1	37.1	46.8	38.0	N/A	N/A	47.4	37.5	0.9	0.7	1.9	1.8	1.3	1.0
	BL-20-30†††	0.50	63.5	49.5	62.5	51.5	N/A	N/A	63.0	50.5	0.7	1.4	1.1	2.8	1.0	2.0
DAA-SP****	BL-20-30†††	60 Grit	51.6	41.0	51.9	42.0	N/A	N/A	51.8	41.5	0.2	0.7	0.4	1.7	0.3	1.0
DTA-R‡	OT-20-30†	1.00	48.0	40.0	48.5	41.0	N/A	N/A	48.3	40.5	0.4	0.7	0.7	1.7	0.5	1.0
UTA†	OT-20-30†	1.00	6.4††	N/A	6.1††	N/A	N/A	N/A	6.3	N/A	0.2	N/A	3.4	N/A	0.3	N/A

DS* = Direct Shear, DAA** = Drained Axial Axisymmetric, DTA*** = Drained Torsional Axisymmetric, DAA-SP**** = Drained Axial Axisymmetric with Sandpaper Sleeves

DTA-R‡ = Drained Torsional Axisymmetric with Resin, UTA† = Undrained Torsional Axisymmetric, OT-20-30†† = Ottawa 20-30

OT-50-70††† = Ottawa 50-70, BL-20-30††††= Blasting 20-30, †† reported as average across all cycles

3.1.9.1 Direct Shear Tests

Figures 3.13a through 3.13f show shear stress-displacement and volume change-displacement results for a series of replicate direct shear tests. Figure 3.13a and 3.13d correspond to tests on Ottawa 50-70 sand under a confining stress of 40 kPa, Figures 3.13b and 3.13e present results for tests on Ottawa 20-30 under a confining stress of 80 kPa, and lastly Figures 3.13c and 3.13f show results for tests on Blasting 20-30 under a confining stress of 160 kPa. The figures and Table 3.3 show that the results for mobilized shear stress, as well as the vertical displacement results, show a high degree of reproducibility irrespective of sand type or confining stress. The COV values for peak loads are slightly larger than for residual loads, possibly caused by small unintended differences in initial density as well as the homogenizing effect of shearing. However, all COV values are lower than 2.3%, showing the small variability in the results.

These small differences observed might have been caused by small uncontrolled differences in relative density, or in external friction mobilized between the two sides of

the shear box. The latter reason is believed to be unlikely because the shear boxes are covered in Teflon coating and they were thoroughly cleaned before every test in order to prevent particles from getting trapped and inducing extraneous frictional resistances.

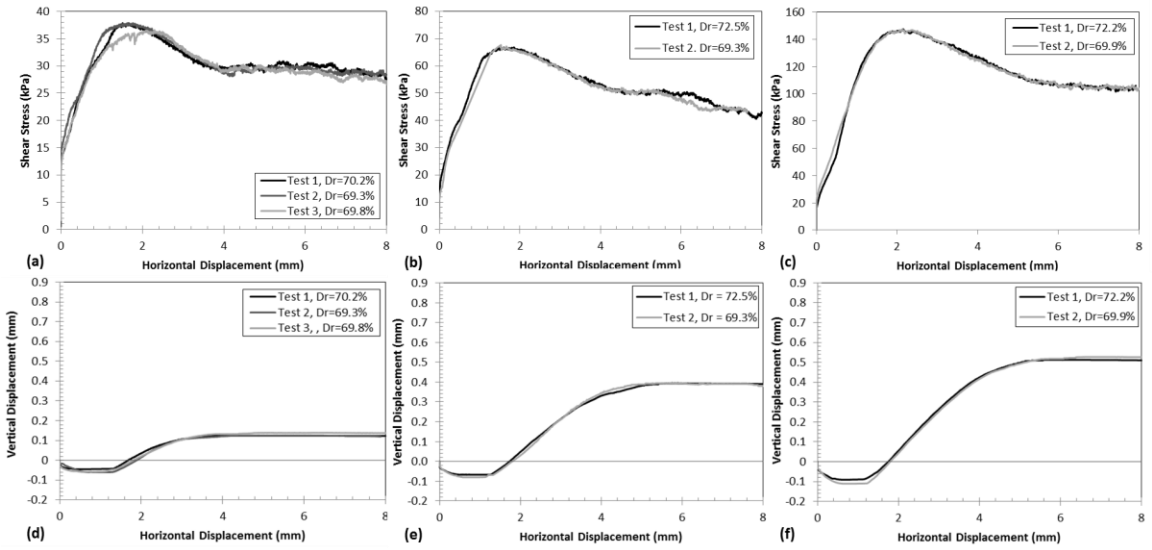

Figure 3.13: Replicate direct shear test results on (a) and (d) Ottawa 50-70 sand under 40 kPa, (b) and (e) Ottawa 20-30 sand under 80 kPa, and (c) and (f) Blasting 20-30 sand under 160 kPa.

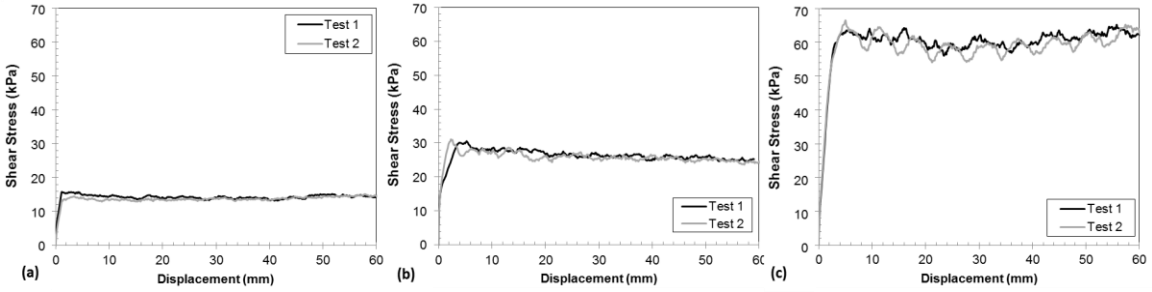

Figure 3.14: Replicate axial tests (a) on Ottawa 20-30 sand against smooth sleeves, (b) on Ottawa 20-30 sand against textured sleeves (R_{max} = 0.25 mm), and (c) on Blasting 20-30 sand against textured sleeves (R_{max} = 2.00 mm). All tests performed under σ_c = 50 kPa.

3.1.9.2 Axial Drained Axisymmetric Shear Tests

Figures 3.14a through 3.14c present results from axial drained axisymmetric shear tests. Figure 3.14a corresponds to tests on Ottawa 20-30 sand against smooth sleeves,

Figure 3.14b shows results from tests on Ottawa 20-30 sand against moderately textured sleeves (R_{max} = 0.25 mm) and Figure 3.14c presents results from tests on Blasting 20-30 sand against heavily textured sleeves (R_{max} = 2.00 mm). These results show small variations in shear stress mobilized during replicate tests and small COV values. The peak loads show larger variability, possibly caused by small differences in initial relative density. The results show low variability irrespective of sleeve surface roughness and sand type. The principal potential source of error for this experimental configuration is the possible presence of air leaks in the latex membrane that would result in unintended lower confining stresses applied to the specimens, resulting in smaller mobilized loads. However, continuous monitoring for leaks allowed fixing them before testing.

3.1.9.3 Torsional Drained Axisymmetric Shear Tests

Figures 3.15a and 3.15b show replicate torsional tests on Ottawa 20-30 sand against textured sleeves of R_{max} = 1.00 mm and on Blasting 20-30 sand against textured sleeves of R_{max} = 0.50 mm. The figures and Table 3.3 show that the torsional test results are highly reproducible for both sands tested, with the maximum COV value (2.8%) corresponding to the residual of the test on Blasting 20-30 sand. Similar to the axial configuration, air leaks in the latex membrane represent a potential source of error.

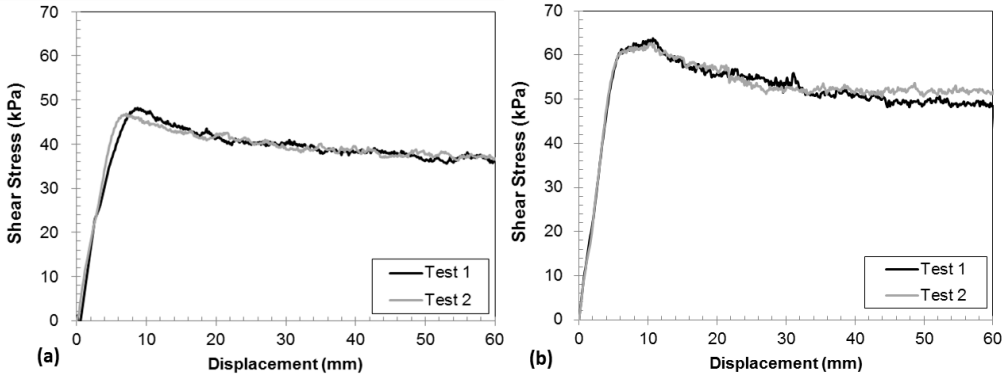

Figure 3.15: Replicate torsional tests (a) on Ottawa 20-30 sand against textured sleeves (R_{max}=1 mm) and (b) on Blasting 20-30 sand against textured sleeves (R_{max}=0.50 mm).

3.1.9.4 Axial Drained Axisymmetric Shear Tests with Sandpaper Sleeves

Figure 3.16 shows replicate tests for axial drained tests with sandpaper sleeves (60 grit). The results also show a large degree of reproducibility, as shown in the figure and in Table 3.3. The COV values for peak and residual loads were of 0.4 and 1.7%, respectively. It should be noted that a new sheet of sandpaper was used for every tests in order to avoid unintended changes in friction sleeve surface roughness.

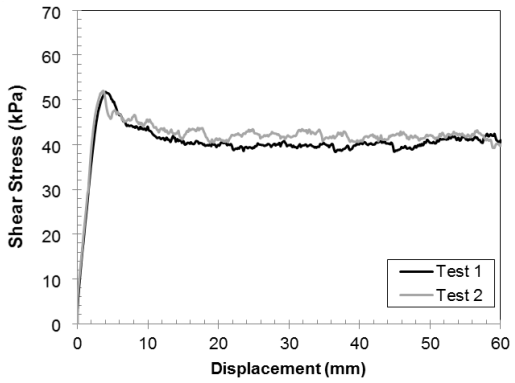

Figure 3.16: Replicate axial tests on Blasting 20-30 sand against 60 grit sandpaper sleeves.

3.1.9.5 Effect of Powder Phenolic Resin on Axisymmetric Shear Tests

This test series was performed to complement the studies on the effect of the powdered phenolic resin previously presented in Figures 3.2a and 3.2b and Table 3.2. As previously concluded, the results showed negligible differences in the stress-displacement response between tests without resin and tests with 1% resin by weight. Figure 3.17 presents the results for replicate torsional tests with and without powdered phenolic resin on Ottawa 20-30 sand against textured sleeves of R_{max} of 1.00 mm. The effect of the resin was only investigated during torsional tests because the heating system did not allow for the load cell to be placed under the testing rod during axial testing. Therefore, loads were only recorded during torsional tests. The maximum COV value was found to be 1.7%, which is comparable in magnitude to the values obtained from tests without resin, thus indicating the negligible effect of the resin on the test results.

3.1.9.6 Torsional Undrained Cyclic Axisymmetric Shear Tests

One replicate test was performed in order to evaluate the performance of the newly developed undrained axisymmetric shear tests. This was done in terms of torsional test results because this shear mode made up the majority of the undrained cyclic shear study. The results in Figures 3.18a and 3.18b show the stress paths followed by two replicate tests, with the only difference that the cycles in the test presented in Figure 3.18b followed an initial 60 mm cycle, as opposed to the test shown in Figure 3.18a that followed an initial 15 mm cycle. Nonetheless, the results presented in Figure 3.18c indicate the negligible effect of the longer initial cycle as well as the high reproducibility of results, as shown by the COV value of 3.4% in measured peak shear stresses, which corresponds to a difference in measured stress of 0.3 kPa.

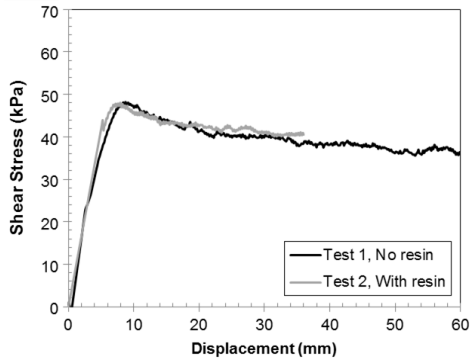

Figure 3.17: Replicate torsional test with and without powdered phenolic resin on Ottawa 20-30 sand against textured sleeves (R_{max}=1.00 mm).

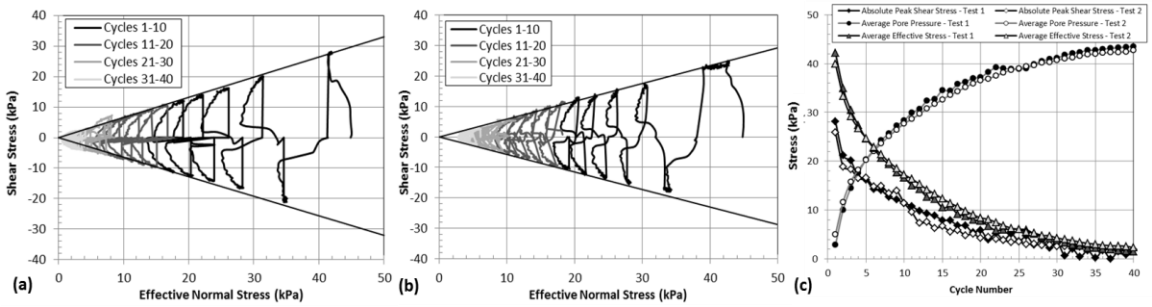

Figure 3.18: (a) and (b) Replicate torsional undrained tests on Ottawa 20-30 sand against textured sleeves (R_{max}=1.00 mm) and (c) measurement evolution with cycle number.

3.2 Numerical Procedures

3.2.1 Discrete Element Modeling (DEM)

The Particle Flow Code (PFC2D) from Itasca, Inc. was used to perform 2D DEM interface shear simulations. As presented by other authors, (e.g. Cundall and Strack, 1979; O'Sullivan, 2011) the DEM method is based upon the solution of Newton's motion equation for every particle in the assembly. While a detailed description of the mathematical formulation is out of the scope of this chapter, such information can be found in the references provided above. The DEM models used in this study were built to simulate as close as possible the axisymmetric device for drained interface shear tests previously described and shown in Figures 3.5a and 3.5b, resulting in almost identical geometries with the laboratory apparatus and friction sleeves as well as mean particle sizes (D_{50} = 0.90 mm for the numerical simulations and D_{50} = 0.72 mm for the experiments). Figure 3.19 presents a 3D rendering of the geometry of the friction sleeves used for the simulations.

Figure 3.19: 3D rendering of friction sleeve of increasing surface roughness.

The virtual chamber used for the axial interface simulations consisted of a two-sided shear box that is 350 mm high and 55 mm wide on each side, shown in Figure 3.20a. The outer walls applied constant stress boundary conditions by means of a servo-control algorithm. A 110 mm long wall surface located at the inner boundaries of the shear box represented a friction sleeve that was moved downwards during the shearing

simulation. These friction sleeves had a two-dimensional profile identical to the textured friction sleeves used for the previously described laboratory experiments. The remaining portions of the inner boundaries and the top and bottom walls were composed of rigid walls. The virtual chamber used for torsional interface shear tests consisted of a 140 mm diameter circular wall, which also closely resembled the experimental configuration and applied a constant stress boundary condition (Figure 3.20b). The friction sleeve was located at the center of the chamber and was rotated clockwise during shearing.

All simulations were performed with about 8500 two-particle clumps with an aspect ratio of 1.5. The linear elastic contact model was utilized for all simulation since it has been shown to be appropriate for the study of the large-strain behavior of granular materials in 2D (Latzel, et al. 2000).

All numerical specimens were prepared using the radius expansion method and then consolidated under constant stress in order to achieve the desired density. This method was considered to result in similar conditions to the perfect insertion preparation used in the laboratory tests. Unless otherwise noted, an interparticle friction coefficient of 0.00 was used during consolidation in order to prepare dense specimens.

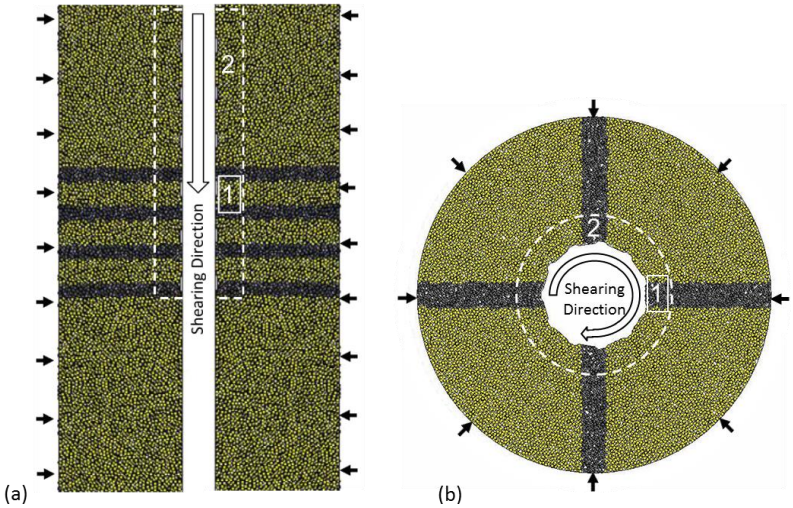

Figure 3.20: DEM simulation models for (a) axial and (b) torsional shear. Sampling windows labeled 1 and 2 are used for different particle-level observations.

3.2.2 Global Measurements Procedure

The global shear stress and volume change responses of the specimens were monitored and recorded during all simulations. The mobilized sleeve shear force was obtained by adding all the contact forces generated between the particles and the friction sleeve as a result of the sleeve displacement. Next, the total force on the sleeve was divided by the sleeve's length in order to obtain the shear stress on the sleeve surface in units of (Force / Area) x Length. This measurement methodology is equivalent to that described in Figures 3.7a and 3.7b for the laboratory experiments. The global specimen volume changes were determined by monitoring the displacement of the chamber walls responsible for maintaining the constant confining stress boundary conditions via the servo-control algorithm. These wall displacements were then used to compute specimen volume changes and volumetric strains. This procedure is equivalent to that used to monitor global specimen volume changes during conventional testing of soils.

3.2.3 Local Measurements Procedure

Local measurements of vertical and horizontal normal and shear stresses, porosity, coordination numbers and fractions of sliding contacts were calculated using measurement circles evenly distributed through the specimens. These measurement circles had a diameter of 3 mm, resulting in a particle to measurement circle diameter ratio of about 3.3. Figure 3.21a shows the measurement circle configuration used to monitor the previously mentioned quantities from specimens subjected to torsional shear (approximately 1000 circles). Similarly, Figure 3.21b shows the measurement circle pattern used to monitor quantities from specimens subjected to axial shear (approximately 1200 circles).

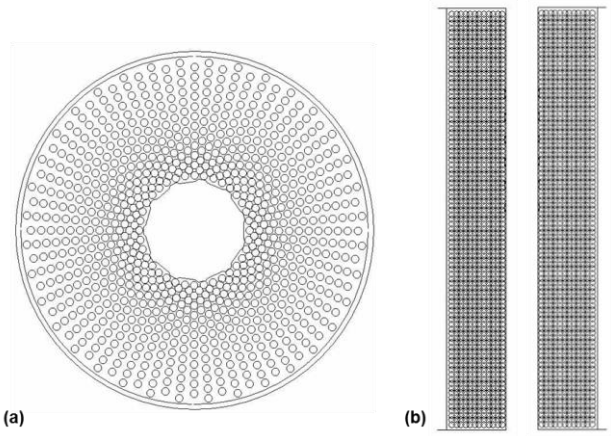

Figure 3.21: Measurement circles configuration for (a) torsional and (b) axial shear.

Measurements related to individual particles, such as particle displacements and rotations, normal and shear contact forces, contact normal orientations and particle trajectories were monitored by recording those quantities at pre-specified stages during the simulation. For instance, particle displacement and rotation fields were obtained by tracking the cumulative displacement and rotations of every particle in the specimen. Other quantities such as the state of stresses, average magnitudes of particle rotations and contact normal orientations and contact normal and shear force magnitudes were obtained from measurement circles and particles located inside sampling windows labeled 1 and 2 shown in Figures 3.20a and 3.20b.

3.2.4 Calibration Parametric Studies

The model calibration was achieved by iteratively changing the model parameters of torsional simulations until a satisfactory match was obtained with the experimental stress-displacement results. The results of a torsional axisymmetric drained test on Ottawa 20-30 sand sheared against a friction sleeve of R_{max} of 1.00 mm (σ_c = 50 kPa) were utilized for the model calibration. The same selected model parameters were used for all axial simulations. Figures 3.22a and 3.22b shows a comparison of the results from experimental and calibrated numerical tests for axial and torsional shear, respectively.

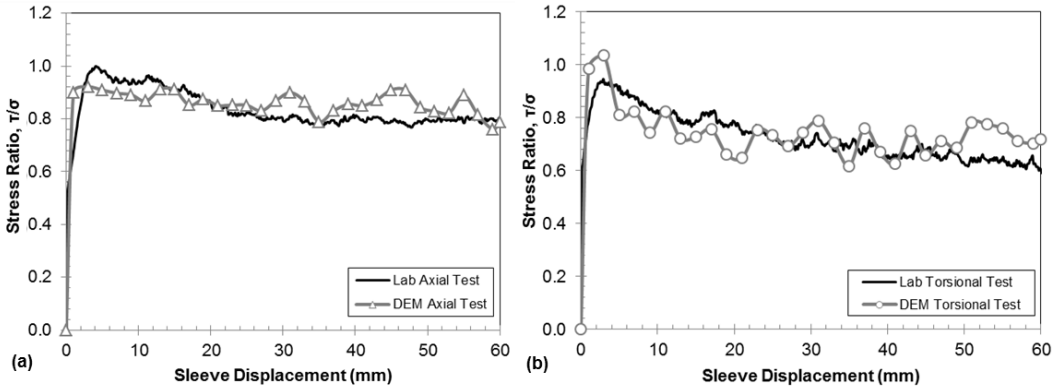

Figure 3.22: Calibration results for simulations against surfaces of R_{max} = 1.00 mm for (a) axial and (b) torsional shear (confining stress = 50 kPa).

Table 3.4 presents the parameters used for all the simulations, unless otherwise noted. The numerical stress-displacement curves showed larger fluctuations than the experimental ones, which are attributed to the different friction sleeve-particle interactions between 2D numerical and 3D experimental scenarios. The numerical results also show a stiffer response at low shear displacements, which has been reported to be characteristic of DEM simulations by other authors (e.g. Huang, et al. 2014). The following sections present a summary of the parametric studies performed to determine the model parameters used throughout this research. During the parametric studies, the model parameters were set equal to those shown in Table 3.4 while the specific parameter under study was varied.

Table 3.4: DEM simulation parameters.

Mean Particle-Clump Size, D_{50} (mm)	Particle Clump Aspect Ratio, AR	Particle Density (kg/m^3)	Interparticle Friction Coefficient, $\mu_{p\text{-}p}$	Particle Normal Stiffness, k_n (N/m)	Particle Shear Stiffness, k_s (N/m)	Sleeve Friction Coefficient, μ_s	Wall Friction Coefficient, μ_w	Wall Normal Stiffness, $k_{n\text{-}w}$ (N/m)	Wall Shear Stiffness, $k_{s\text{-}w}$ (N/m)
0.90	1.50	2650	0.45	$1x10^7$	$1x10^7$	0.25	0.20	$1x10^8$	$1x10^8$

3.2.4.1 Effect of Particle Clump Aspect Ratio

Particle clumps with an aspect ratio (AR) of 1.5 composed of two spherical particles have been shown to successfully model the behavior of Ottawa 20-30 sand by Lu, 2010. Nonetheless, a parametric study was performed where the global response of

assemblies composed of particles of three different particle shapes was monitored. The particle AR values considered are 1.00 (spheres), 1.50 and 1.75. Figure 3.23a shows the measured sleeve stress during torsional tests for assemblies composed of the three particle shapes, while Figure 3.23b shows the shear-induced volumetric strains. As expected, the assembly composed of particles of AR of 1.00 mobilized the smallest shear stress as well as the smallest dilative volumetric strains. A significant increase in both measured stress and dilative volumetric strains can be observed between the results of the assembly with particles of AR = 1.0 and that with AR = 1.50. Finally, the results of the simulation with particles of AR 1.75 showed only modest increases in shear stress and dilative volumetric strains. These results are in agreement with the principles of soil mechanics where particles with more angular shapes mobilize larger shear resistances due to an increased particle interlocking that in turn results in larger dilation.

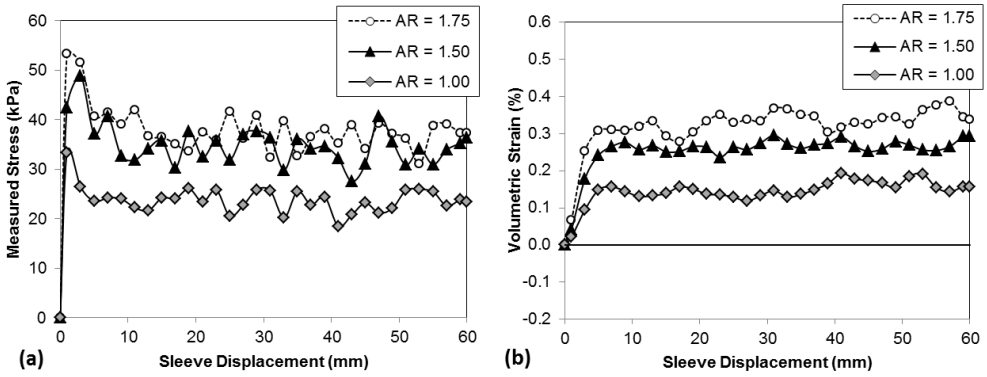

Figure 3.23: Parametric study on the effect of particle aspect ratio on the (a) stress-displacement and (b) volume change response of DEM torsional simulations.

Numerical simulations by Oda and Iwashita (2000), Mohamed and Gutierrez (2010) and Wang, et al. (2007a) have shown the importance of particle rotation resistance mechanisms during DEM simulations, such as particle angularity. Increasing angularity results in assemblies of larger shear strength that show a more dilative behavior. Therefore, in order to avoid artificially large estimations of particle rotations, simulations with particles of AR of 1.00 were not considered. Lee (1998) measured the aspect ratio of

Ottawa 20-30 sand particles from 2D microscope images and found a range of AR values between 1.0 and 1.9, with a mean value of 1.28. Based on these measurements, a slightly larger AR value of 1.5 was selected for the simulations presented in this study because a particle rotation resistance or hindering model was not employed.

3.2.4.2 Effect of Interparticle Friction Coefficient

Figures 3.24a and 3.24b show the stress-displacement and volumetric-displacement responses, respectively, for tests performed with interparticle friction coefficients, $\mu_{p\text{-}p}$, of 0.30, 0.45 and 0.60. It can be observed that the mobilized shear stresses (particularly the peak) as well as the dilative volume changes increase with increasing friction coefficient. These results are in general agreement with the trends reported by other authors (e.g. Yang, et al. 2012 and Huang, et al. 2014). Ultimately, a $\mu_{p\text{-}p}$ value of 0.45 was selected because it represents a mineral friction angle of 24.2°, which is in the range between 17.4° and 31° reported by Mitchell and Soga (2005) for quartz.

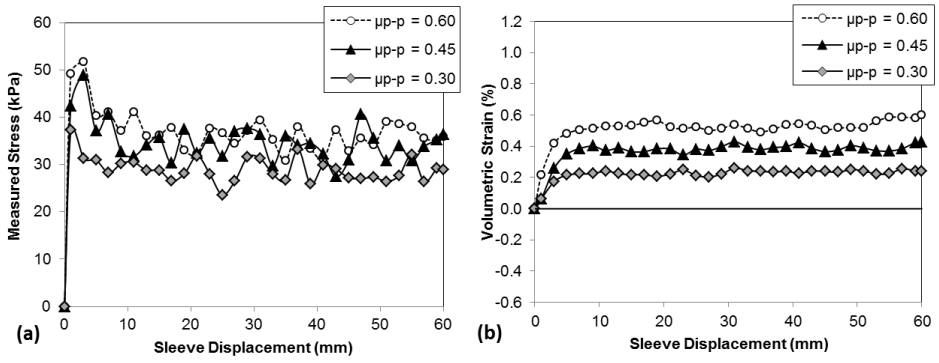

Figure 3.24: Parametric study on the effect of interparticle friction coefficient on the (a) stress-displacement and (b) volume change response of DEM torsional simulations.

3.2.4.3 Effect of Particle Normal Stiffness

Figures 3.25a and 3.25b present the results for simulations performed with varying particle normal stiffness, k_n. The values considered were $1x10^6$, $1x10^7$ and $1x10^8$ N/m. A k_n value of $1x10^6$ N/m resulted in very small shear stresses being mobilized, as

well as in contractive shear-induced volume changes. These results were considered unrealistic since they showed to significantly differ from the magnitude of measured stresses in laboratory tests, and because the experimental stress-displacement shear curves showed significant strain softening indicative of dilative behavior as opposed to the contractive trend showed by this simulation. The results obtained from the simulation with a k_n value of $1x10^8$ N/m showed very large fluctuations in the stress-displacement curve, as well as a very large strain-softening response and larger dilative volume changes. A k_n value of $1x10^7$ N/m was selected as appropriate because it resulted in a better match with stress-displacement results from laboratory tests.

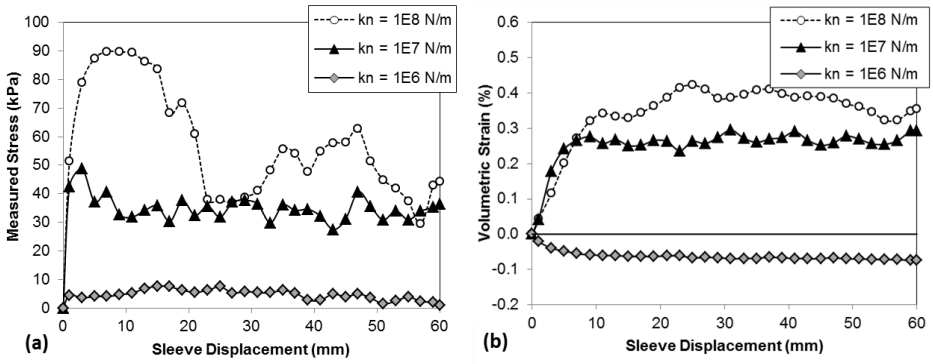

Figure 3.25: Parametric study on the effect of particle normal stiffness on the (a) stress-displacement and (b) volume change response of DEM torsional simulations.

3.2.4.4 Effect of Particle Shear Stiffness

There is no unanimous agreement on the most appropriate methodology for selecting a shear stiffness, k_s, value for DEM simulations. Typically, a value is selected such that the k_s/k_n ratio is between 1 and 1/100. The results presented in Figures 3.26a and 3.26b correspond to simulations with k_s values of $1x10^5$, $1x10^6$ and $1x10^7$ N/m, which correspond to k_s/k_n ratios of 1.0, 1/10 and 1/100, respectively. It can be observed that the simulation with a k_s value of $1x10^5$ N/m resulted in the smallest mobilized shear stresses as well as smaller dilative specimen volume changes. The results for the simulations with k_s values of $1x10^6$ and $1x10^7$ N/m were similar to one another thus not

showing a specific trend. These results follow the same trends as a parametric study presented by Lu (2010). According to Hu, et al. (2010), for simulations with smaller k_s/k_n ratios there is a tendency for the load to be attracted to the stiffer normal contacts, thus affecting the point at which sliding will initiate at the contacts. Therefore, a k_s value of $1x10^7$ N/m was chosen in order to keep a k_s/k_n ratio equal to 1.0.

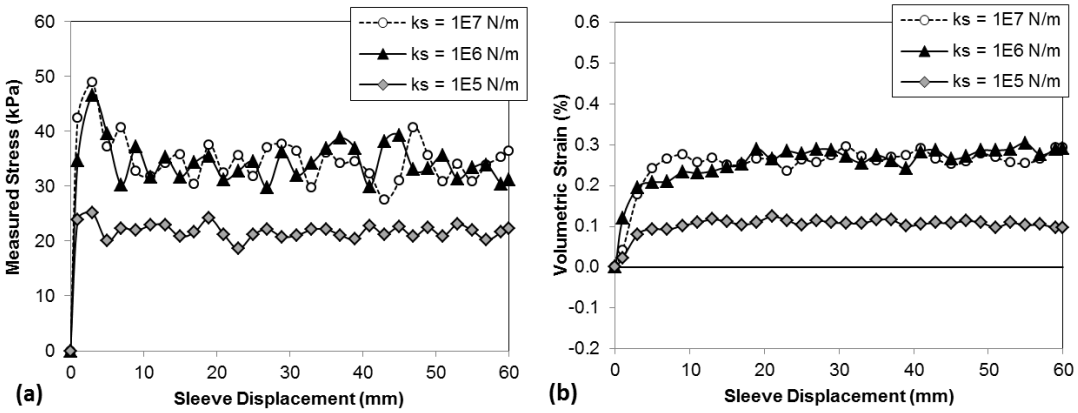

Figure 3.26: Parametric study on the effect of particle shear stiffness on the (a) stress-displacement and (b) volume change response of DEM torsional simulations.

3.2.4.5 Effect of Friction Sleeve Friction Coefficient

A set of three simulations were performed in order to study the effect of the friction sleeve friction coefficient, μ_s. The μ_s considered were 0.10, 0.25 and 0.40, and the stress-displacement and volumetric strain-displacement responses are presented in Figures 3.27a and 3.27b, respectively. Increasing μ_s resulted in significantly larger mobilized peak shear stresses, but in more modest increases in the residual shear stresses.

The larger peak shear stresses are related to the increasing magnitude of dilative specimen volume changes with increasing μ_s. As the sleeve displacement increases, the dilation rate reaches a value close to zero, causing the contribution from dilation to diminish, which is represented in the three stress-displacement curves converging to close values. The increased dilative behavior at the pre-peak and peak shear stages with increasing μ_s is possibly caused by the larger energy needed to cause slippage between

the friction sleeve and the particles, thus increasing the probability of particle rotations that in turn result in dilative volume changes. Considering that laboratory results indicated a friction sleeve μ_s value close to 0.25 combined with the fact that a value of 0.25 showed to produce a better match with the laboratory results, a value of 0.25 was selected for all the simulations.

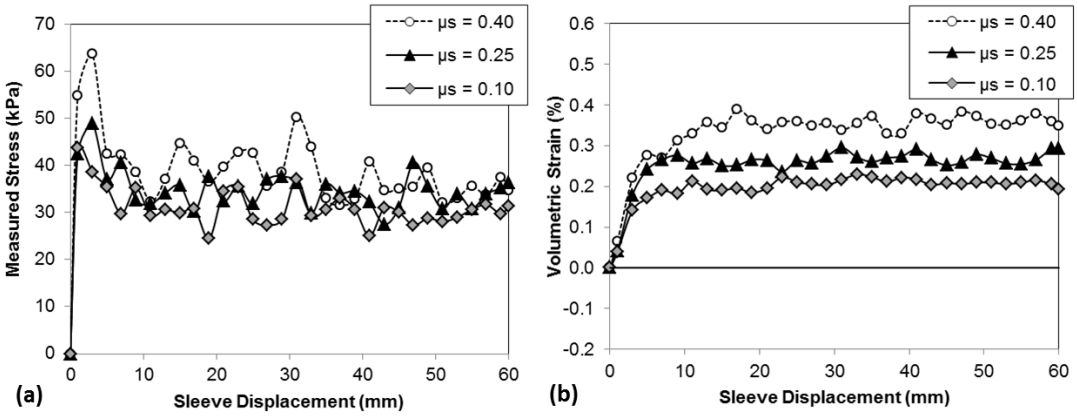

Figure 3.27: Parametric study on the effect of sleeve friction coefficient on the (a) stress-displacement and (b) volume change response of DEM torsional simulations.

3.2.4.6 Effect of Chamber Wall Friction Coefficient

The effect of the friction coefficient value of the chamber wall, μ_w, is not trivial. If not appropriately chosen, then the contacts between the chamber wall and the outer particles can represent the weakest link in the assembly and the specimen will rotate as a rigid block with most of the shearing happening at that interface. The results presented in Figures 3.28a and 3.28b show this effect. As the μ_w value was increased from 0.00 to 0.10, the friction mobilized at the chamber wall increased. Further increases in μ_w result in no change of mobilized shear stress.

Figure 3.28b makes a comparison between the particle displacements along the chamber wall with the shear stress mobilized at the wall. As the μ_w value increased, the particle displacement along the wall significantly decreased, reaching a constant value close to zero at friction coefficient values equal to or larger than 0.10. Similarly, the shear

stress mobilized along the wall reached an approximate constant value of 2.7 kPa at μ_w values equal to or larger than 0.10. The magnitudes of the measured shear stress on the friction sleeve and of the particle displacements inside the shear zone were not significantly affected by the value of μ_w. Therefore, a μ_w value of 0.20 was chosen in order to ensure no slippage between the chamber wall and the outer particles.

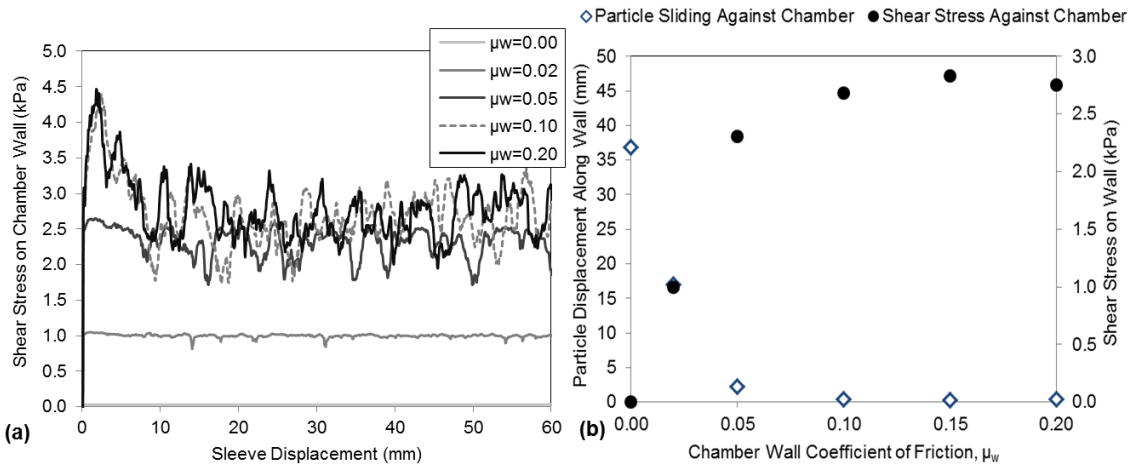

Figure 3.28: (a) Shear stress on chamber wall during torsional shear simulations and (b) effect of chamber wall friction coefficient on particle displacement along chamber wall and magnitude of shear stress on wall.

CHAPTER 4

EXPERIMENTAL STUDY OF SHEAR ZONES FORMED AT SAND-STEEL INTERFACES IN AXIAL AND TORSIONAL AXISYMMETRIC TESTS

4.1 Introduction

The interface shear behavior of granular materials is central to many engineering applications, including the performance of structures like deep foundations, landfills and retaining walls. Consequently, it is paramount to understand the construction material-soil interfaces involved in these applications. Furthermore, it has been shown that the study of interface behavior, in the laboratory and in-situ, can provide robust information about the soil's properties and engineering performance. This chapter presents laboratory evaluations of micro and meso-scale shear deformation of medium-sized sands aimed at developing an improved fundamental understanding of the stress-strain behavior of granular-continuum interfaces. Comparison of interface testing results from two different shear directions, axial and torsional, demonstrates that the evolution and progression of shear zone formation is affected differently by changes in the interface surface roughness and particle angularity. In particular, it was observed that torsional shear is a more dilative process that induces a larger degree of soil shearing and is more greatly affected by particle angularity. Studies of shear-induced volume changes also revealed that the volume of the influence zone for torsional shearing is larger than that for axial shearing, with soil dilation occurring inside the shear zone in contact with the material counterface and soil contraction in a surrounding outer zone. Fundamental micromechanical processes that aim to explain the differences between the behavior of axial and torsional tests are proposed.

This study is part of an effort to characterize the shear zone behavior and evolution formed between soil sheared against both conventional smooth and textured friction sleeves. These friction sleeves are used in a series of novel modules for CPT exploration that allow for use of multiple friction sleeves of different roughness (DeJong 2001; DeJong and Frost 2002; Hebeler 2005; Frost and DeJong 2005; Frost, et al. 2012) and shearing in different orientations (Frost and Martinez 2012; Frost and Martinez 2013; Frost and Martinez, 2014; Martinez and Frost 2014a; Martinez and Frost 2014b). The reader can refer to the literature review in this thesis (Chapter 2) for a more detailed description of these multi-sensor technologies. The ability to perform tests involving torsional loading is important both for understanding soil behavior in general, as well as the soil response under a range of natural and man induced loading conditions. Therefore, the principal goal of this study is to investigate the micro-scale processes involved in the axial and torsional shear tests in order to create a link between these and the observed shear behavior.

The results presented in this chapter correspond to tests with Ottawa 20-30 and Blasting 20-30 sands which allow for the study of the effect of particle angularity on the shear deformation characteristics in the shear zones created during axisymmetric drained tests (device shown in Figure 3.5) against smooth and textured sleeves (Figures 3.3a through 3.3d). All the results presented in this chapter pertain to tests on specimens at relative densities between 60 and 65% under a confining stress of 50 kPa. More detailed information on the devices, sands, methodologies and results repeatability were presented in Chapter 3 of this thesis.

4.2 Results

4.2.1 Typical Global Shear Stress-Displacement Results for Interface Shear Tests

Figure 4.1a shows typical stress ratio-displacement curves for axial and torsional tests performed with Blasting 20-30 sands against textured sleeves with maximum

surface roughness, R_{max}, of 1.00 mm. The torsional test curve has a higher peak, followed by a significant amount of strain-softening compared to the axial test. The higher torsional peak implies a more dilative behavior given the drained loading applied to the medium-dense sand assemblies. Both curves converge to a stress ratio of about 1.05. It is important to note that a larger degree of strain softening was observed in all the torsional tests for both sands tested and over the range of surface roughness values tested.

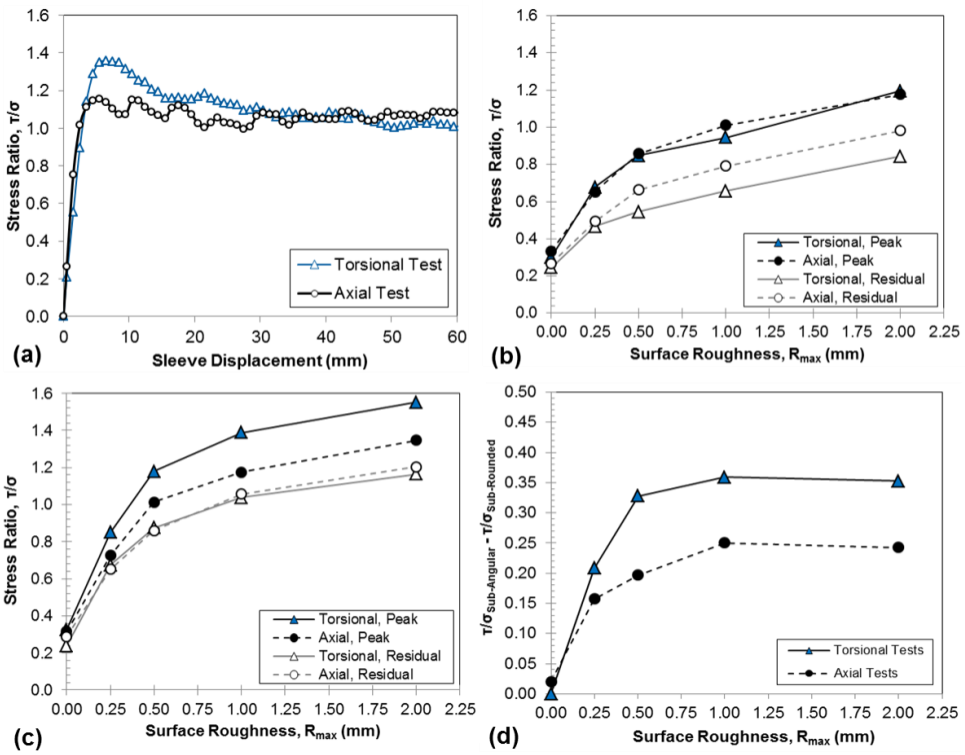

Figure 4.1: (a) Axial and torsional interface shear tests on Blasting 20-30 sand against a textured sleeve of R_{max} = 1.00 mm. Measured peak and residual stress ratios as a function of R_{max} for tests with (b) Ottawa 20-30 and (c) Blasting 20-30 sands. (d) Difference in stress ratios measured between tests on Blasting 20-30 and Ottawa 20-30 sands.

Figure 4.1b and 4.1c show measured peak and residual stress ratios for a series of axial and torsional tests on Ottawa 20-30 and Blasting 20-30 sands, respectively, as a function of R_{max}. Increases in surface roughness produced increases in measured stress in both axial and torsional tests. The rate of increase decreased with increasing surface

roughness, reaching more stable conditions at R_{max} values larger than 1.00 mm. Further, tests with Blasting 20-30 sands (angular) yielded larger stress ratios than tests with Ottawa 20-30 sands (rounded) for all the tests against textured friction sleeves, showing the influence of the soil internal friction angle. The tests performed with conventional smooth CPT sleeves did not show a significant effect of the soil internal friction or shearing mode. Figure 4.1d shows the difference in stress ratio from tests performed with Blasting 20-30 sands compared to tests performed with Ottawa 20-30 sands for any given surface roughness ($\tau/\sigma_{Blasting\ 20\text{-}30}$ - $\tau/\sigma_{Ottawa\ 20\text{-}30}$). The results reveal that the torsional tests exhibited a larger increase in measured stress ratio with increasing grain angularity for all the tests performed against textured sleeves, a fact that represents a key difference between the results of axial and torsional tests.

The measurements and evaluations presented in this chapter aim to determine the reasons for the observed differences in global behavior from an experimental micro-scale perspective. A more comprehensive set of shear stress-displacement results can be found in Chapter 5 of this thesis. Furthermore, Chapter 6 presents studies that link the micro- and global-scale behaviors by means of Discrete Element Modeling (DEM) simulations and further laboratory testing.

4.2.2 Shear Zone Characterization Tests

Figures 4.2a through 4.2d show pictures of exposed shear zones with colored sand layers to facilitate visualization from axial and torsional shear tests against smooth and textured friction sleeves. Shearing against smooth sleeves did not create any identifiable shear zone in the tested sands, a fact that agrees well with previous studies that concluded that sliding between the sand grains and the smooth sleeve surface is the main interface mechanism present in interface shear tests with smooth surfaces (Frost and DeJong 2005; Martinez and Frost 2014b). These results are also reflected in the stress ratio values presented in Figures 4.1b, 4.1c and 4.1d, which showed no effect of the soil internal

friction or shearing mode. On the other hand, the shear zones created during tests with textured sleeve are well defined, as further described below.

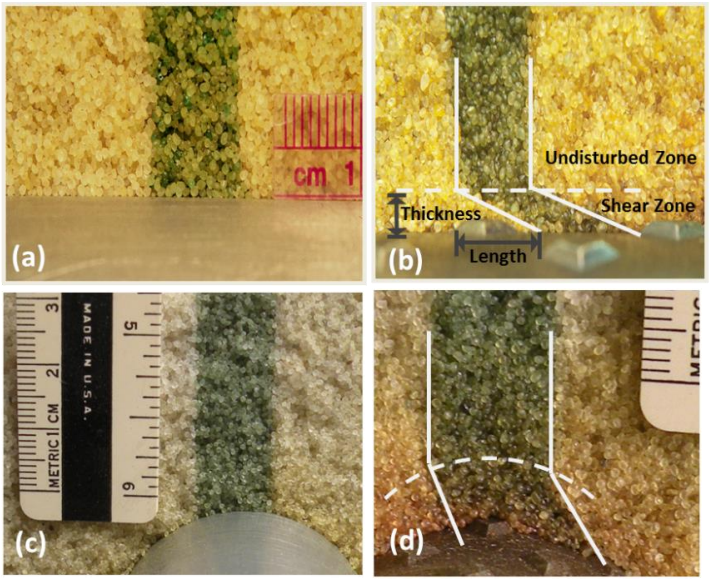

Figure 4.2: Shear zones developed during axial test with (a) conventional smooth CPT sleeve and textured sleeve (after Hebeler, et al. 2015). Torsional test with (c) conventional smooth CPT sleeve and (d) with textured sleeve.

4.2.3 Progression of Shear Zone Formation with Increasing Sleeve Displacement

Figures 4.3a shows a schematic of the definitions of shear zone thickness and length, while Figures 4.3b and 4.3c along with Table 4.1 show results as a function of sleeve displacement for torsional and axial tests on Ottawa 20-30 sands and friction sleeves of R_{max} = 1.00 mm continuously sheared against textured sleeves. The shear zone thickness increased rapidly at small shearing displacements as observed in both the axial and torsional tests results. At a displacement of about 10 mm the shear zone thickness increased to a value of approximately 5.1 mean particle diameters (D_{50}). Subsequent increases in displacement up to 35 mm resulted in modest increase up to a value of 6.0 times D_{50} for torsional shearing while displacement of up to 43 mm resulted in a modest increase up to values of about 6.4 times D_{50} for axial shearing. Considering the similar progression of shear zone thickness for both shearing modes, it is reasonable to conclude

that relatively small displacements are needed in order to fully develop shear zones in both axial and torsional shear.

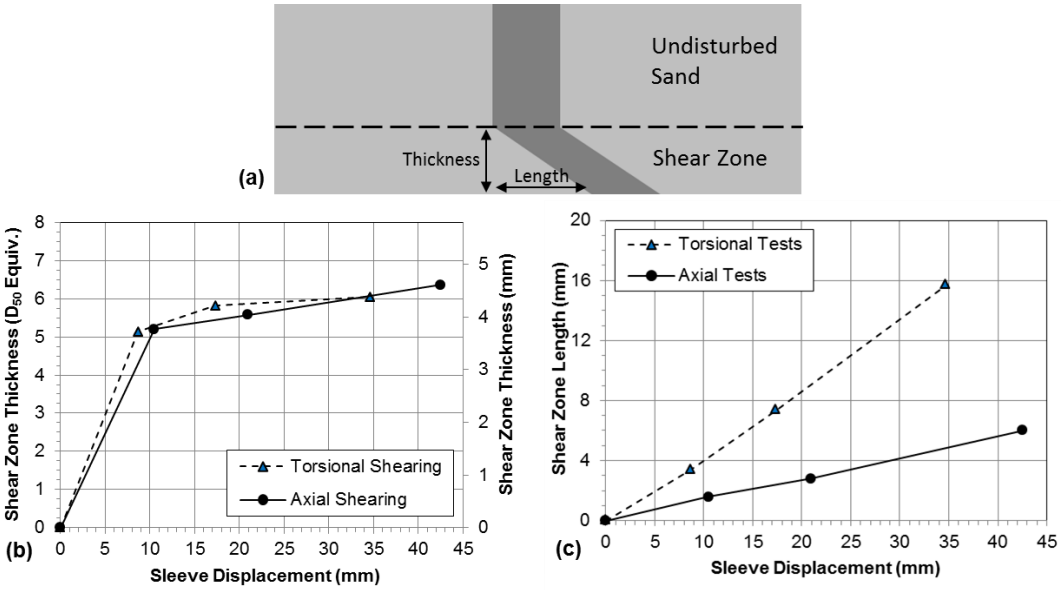

Figure 4.3: (a) Schematic of shear zone characteristics. (b) shear zone thickness and (c) shear zone length progression for torsional and axial.

Figure 4.3c shows that the shear zone length increased linearly with increasing sleeve displacements for both axial and torsional tests. Torsional shearing created much longer shear zones than those created in axial tests for any given sleeve displacement, a fact that suggests that the torsional shear process induced a larger degree of soil shearing than the axial shear process. This observation is further discussed later in this chapter. Normalizing the shear zone length results by the total sleeve displacement yields normalized shear zone lengths of about 14% for axial tests and 42% for torsional tests that are approximately constant with sleeve displacement.

4.2.4 Progression of Shear Zone Formation with Increasing Surface Roughness

A comparison of the shear zone characteristics between the shear zones developed during axial and torsional shear tests as a function of surface roughness, R_{max}, is presented in Figures 4.4a through 4.4d and Table 4.1 for Ottawa 20-30 and Blasting 20-30 sands. The results corresponding to torsional tests were performed as part of this study

while the results from axial tests were taken from Hebeler, (2005) and Hebeler, et al. (2015), who used the same experimental methods for their study. The shear zone thickness increased with increasing surface roughness for axial and torsional tests with both sands tested reaching stable values at R_{max} values between 0.50 and 1.00 mm. Axial tests resulted in slightly larger values of shear zone thickness across all tested surface roughnesses. In general, this increase was less than one particle diameter. The tests on Ottawa 20-30 sands yielded larger shear zone thicknesses compared to tests on Blasting 20-30 sands, also on the order of one particle diameter. These differences were consistently observed throughout the tests performed.

Table 4.1: Results of axial and torsional shear characterization tests with Ottawa 20-30 and Blasting 20-30 sands.

Test Type	Sand	Sleeve Roughness, R_{max} (mm)	Sleeve Displacement (mm)	Shear Zone Thickness (D_{50})	Shear Zone Thickness (mm)	Shear Zone Length (mm)	Shear Zone Length (%)
Axial	Ottawa 20-30	0.01	63.5	0.0	0.0	0.0	0.0
Axial	Ottawa 20-30	0.25	63.5	3.6	2.6	2.5	3.9
Axial	Ottawa 20-30	0.50	63.5	5.3	3.8	7.9	12.4
Axial	Ottawa 20-30	1.00	63.5	6.3	4.5	8.3	13.1
Axial	Ottawa 20-30	2.00	63.5	6.9	5.0	9.2	14.5
Axial	Blasting 20-30	0.01	63.5	0.0	0.0	0.0	0.0
Axial	Blasting 20-30	0.25	63.5	3.1	2.2	2.0	3.1
Axial	Blasting 20-30	0.50	63.5	5.1	3.7	4.6	7.2
Axial	Blasting 20-30	1.00	63.5	5.3	3.8	7.3	11.4
Axial	Blasting 20-30	2.00	63.5	6.3	4.5	14.6	23.0
Torsional	Ottawa 20-30	0.01	17.3	0.0	0.0	0.0	0.0
Torsional	Ottawa 20-30	0.50	17.3	5.1	3.7	4.7	27.3
Torsional	Ottawa 20-30	1.00	17.3	5.8	4.2	7.4	42.4
Torsional	Ottawa 20-30	2.00	17.3	5.8	4.2	7.5	43.1
Torsional	Blasting 20-30	0.01	17.3	0.0	0.0	0.0	0.0
Torsional	Blasting 20-30	0.50	17.3	4.7	3.4	4.3	25.0
Torsional	Blasting 20-30	1.00	17.3	5.2	3.8	7.0	40.7
Torsional	Blasting 20-30	2.00	17.3	5.6	4.0	9.1	52.6
Axial	Ottawa 20-30	1.00	0.0	0.0	0.0	0.0	0.0
Axial	Ottawa 20-30	1.00	10.5	5.2	3.7	1.6	15.3
Axial	Ottawa 20-30	1.00	21.0	5.6	4.0	2.8	13.4
Axial	Ottawa 20-30	1.00	42.5	6.4	4.6	6.0	14.1
Torsional	Ottawa 20-30	1.00	0.0	0.0	0.0	0.0	0.0
Torsional	Ottawa 20-30	1.00	8.7	5.1	3.7	3.4	38.9
Torsional	Ottawa 20-30	1.00	17.3	5.8	4.2	7.4	42.4
Torsional	Ottawa 20-30	1.00	34.7	6.0	4.4	15.7	45.2
Axial	Ottawa 20-30	1.00 (modified)	63.5	6.1	4.4	18.4	29.0
Torsional	Ottawa 20-30	1.00 (modified)	17.3	5.5	4.0	5.3	30.5

A clear difference in the axial and torsional results was observed in the shear zone length results presented in Figures 4.4c and 4.4d. While the shear zone length increased with increasing roughness for both axial and torsional tests on both Ottawa 20-30 and Blasting 20-30 sands, the shear zone length was consistently 2 to 4 times greater for torsional tests for all surface roughness values. It is hypothesized that this difference in

shear zone length reflects the different micro-mechanisms involved in the shearing of each test configuration, which are related to the induced particle shear displacements as addressed later in this chapter. For tests with Ottawa 20-30 sands, the shear zone length reached a stable value at an R_{max} of 1.00 mm for torsional tests and of 0.50 mm for axial tests (Figure 4.4c). On the other hand, the shear zone length for torsional and axial tests on Blasting 20-30 sands did not reach a stable value and kept increasing with roughness (Figure 4.4d). It is believed that particle rotation resistance plays a key role in this observed difference. For assemblies composed of Blasting 20-30 particles, the grain angularity acts as a rotational resistance mechanism and hence increases the potential of particle translation as translation becomes less energy demanding than particle rotation. In comparison, Ottawa 20-30 grains are less likely to resist particle rotation and their translation is smaller in magnitude.

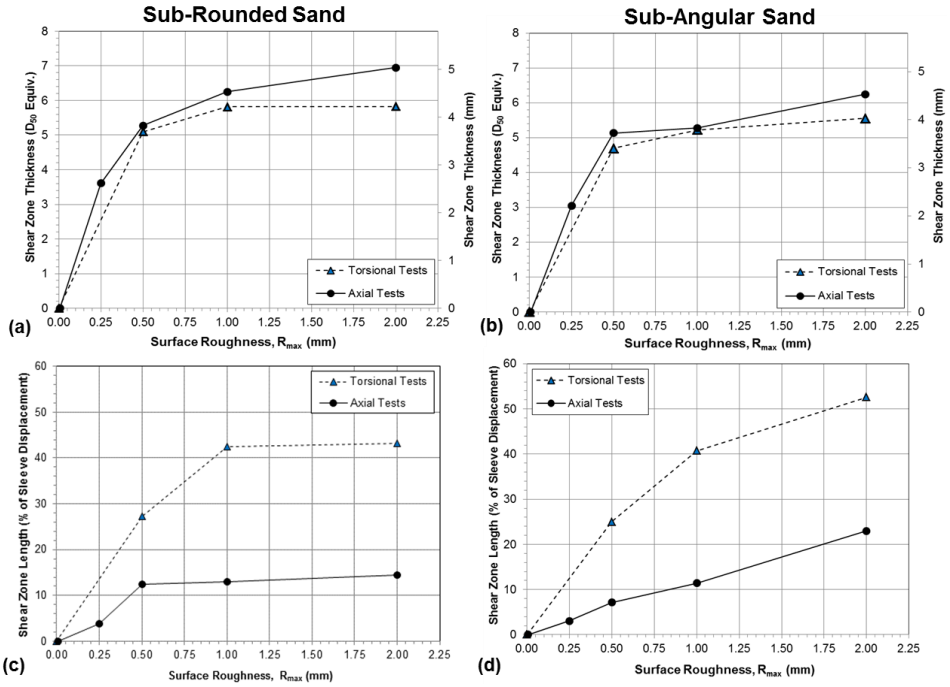

Figure 4.4: Shear zone characteristics as a function of sleeve surface roughness, R_{max}. (a) shear zone thickness for tests on Ottawa 20-30 sand, (b) shear zone thickness for tests on Blasting 20-30 sand, (c) shear zone length for tests on Ottawa 20-30 sand, and (d) shear zone length for tests on Blasting 20-30 sand.

4.2.5 Influence of Texture Element Configuration on Shear Zone Characteristics

In an effort to further study the difference in shear zone length between axial and torsional tests observed in Figures 4.3c, 4.4c and 4.4d, an additional series of tests was performed with friction sleeves textured with a modified configuration. It is important to note that the conventional texture consists of diamond elements with the longer axis parallel to the longitudinal axis of the sleeve, resulting into a larger area normal to the direction of torsional shearing, as shown in Figure 4.5a. The series of additional tests were performed on Ottawa 20-30 sands against friction sleeves of R_{max} = 1.00 mm with diamond elements rotated 90 degrees, thereby having their long axis normal to the direction of axial shearing, as shown in Figure 4.5b. The area normal to each texture element's long side is of 7.2 mm^2, and that of the short side is of 3.3 mm^2.

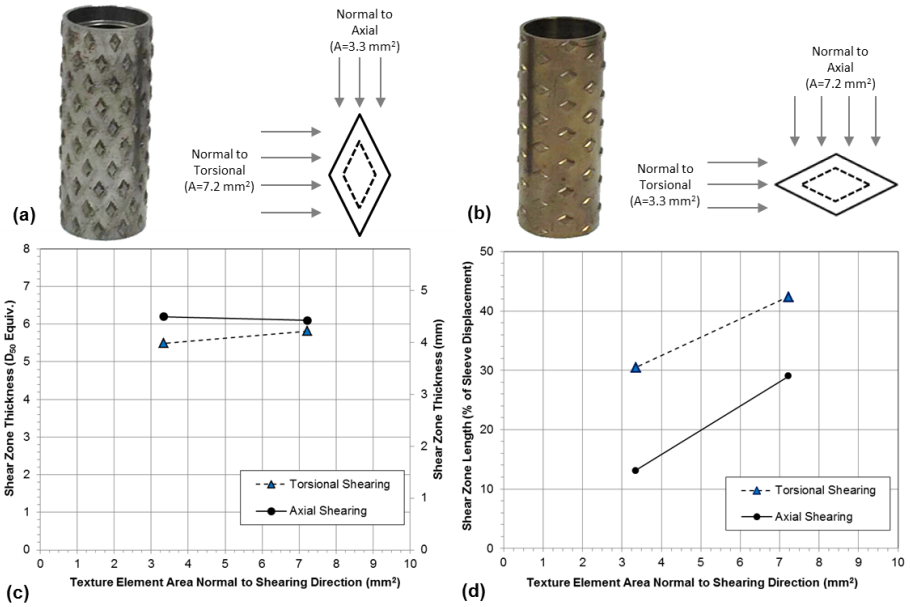

Figure 4.5: (a) Picture of standard sleeve and schematic of standard texture element. (b) Picture of modified sleeve and schematic of modified texture element. (c) Shear zone thickness and (d) shear zone length as a function of texture element area normal to shearing direction for tests on Ottawa 20-30 sands against sleeves of R_{max} = 1.00 mm.

Figures 4.5c and 4.5d and Table 4.1 show the results of the test series using the horizontally rotated diamond textures. The shear zone thicknesses were shown to be

fairly independent of the area normal to shearing with values between 5.5 and 6.3 mean particle diameters observed for both axial and torsional shearing tests. This result may parallel those observed in the shear zone thickness – surface roughness relationship in Figures 4.4a and 4.4b, as both values of normal area are within the stable plateau zone where the shear zone is fully developed. Figure 4.5d shows that shearing against the long side of the diamond elements results in a larger shear zone length for both shearing modes. However, the shear zone length created during torsional shear is shown to be consistently larger for any given normal area, leading to the conclusion that the longer shear zones observed in torsional tests are not due to the sleeve texturing orientation but correspond to fundamental differences in the micromechanical processes involved in axial and torsional shear, such as induced particle rotations and translation.

4.2.6 Void Ratio Evolution Tests

Shear-induced changes in void ratio as a function of distance from the sleeve were calculated for tests on Ottawa 20-30 and Blasting 20-30 sands in both axial and torsional tests. These tests allowed studying the effect of shear direction on the characteristics and extent of the influenced zones, and to shed light into the micro-mechanical processes.

The results of this test series can be found in Tables 4.2 and 4.3 and Figures 4.6a through 4.6d. Figures 4.6a, 4.6b and Table 4.2 present the void ratio results of a sample before shearing, along with void ratio values from axial and torsional tests performed on Ottawa 20-30 and Blasting 20-30 sands sheared against conventional smooth CPT sleeves. The horizontal lines on the figures represent the target sample preparation void ratio (solid lines) and maximum and minimum void ratios (upper and lower dashed lines). The pre-shear void ratio values are similar to the target void ratio, with some variation that is attributed to local variations in density. The results from axial and torsional tests against smooth sleeves also show small variations in void ratio at all distances away from the sleeve, which fall closely to the target void ratio. These results are fairly similar to the

pre-shear results and indicate that shearing against smooth sleeves does not induce detectable changes in void ratio in either axial or torsional shear for the sands tested. The coefficient of variation values calculated for these test results are all fairly low, with values lower than 2.8%. The mean, standard deviation and coefficient of variation values are presented in Table 4.2.

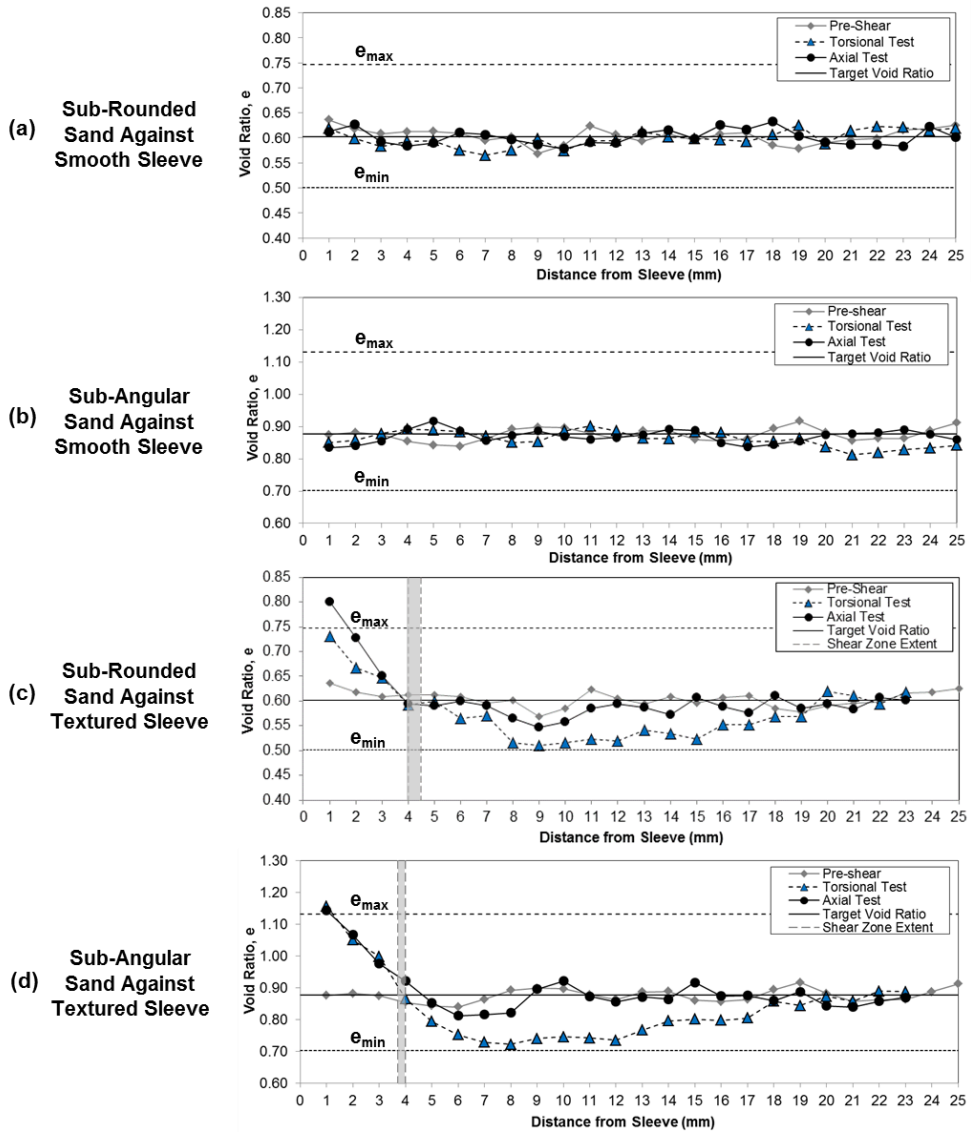

Figure 4.6: Shear-induced changes in void ratio for torsional and axial tests on (a) Ottawa 20-30 and (b) Blasting 20-30 sands against smooth sleeves and (c) Ottawa 20-30 and (d) Blasting 20-30 sands against textured sleeves (R_{max} = 1.00 mm) (shaded vertical area is range of observed shear zone thicknesses).

Table 4.2: Shear induced and pre-shear changes in void ratio for axial and torsional tests on Ottawa 20-30 and Blasting 20-30 sands sheared against smooth sleeves.

Distance from Sleeve (mm)	Void Ratio, e					
	Axial Tests on Sub-Rounded Sand	Axial Tests on Sub-Angular Sand	Torsional Tests on Sub-Rounded Sand	Torsional Tests on Sub-Angular Sand	Pre-Shear State, Sub-Rounded Sand	Pre-Shear State, Sub-Angular Sand
1	0.612	0.834	0.619	0.851	0.636	0.875
2	0.627	0.840	0.599	0.858	0.618	0.882
3	0.592	0.855	0.583	0.879	0.609	0.875
4	0.584	0.892	0.593	0.892	0.612	0.854
5	0.590	0.918	0.595	0.889	0.613	0.842
6	0.611	0.888	0.575	0.884	0.609	0.839
7	0.607	0.856	0.565	0.871	0.595	0.863
8	0.597	0.872	0.575	0.851	0.602	0.892
9	0.587	0.887	0.598	0.853	0.568	0.898
10	0.578	0.869	0.574	0.886	0.585	0.896
11	0.591	0.860	0.595	0.902	0.624	0.878
12	0.590	0.866	0.595	0.886	0.606	0.863
13	0.610	0.874	0.612	0.864	0.593	0.886
14	0.616	0.892	0.602	0.862	0.608	0.888
15	0.599	0.888	0.598	0.883	0.595	0.860
16	0.626	0.849	0.596	0.881	0.608	0.856
17	0.617	0.836	0.593	0.855	0.611	0.863
18	0.632	0.845	0.606	0.854	0.585	0.894
19	0.604	0.855	0.625	0.863	0.578	0.916
20	0.591	0.875	0.588	0.838	0.591	0.882
21	0.587	0.878	0.614	0.812	0.596	0.857
22	0.587	0.881	0.623	0.819	0.598	0.863
23	0.583	0.891	0.621	0.828	0.616	0.863
24	0.623	0.876	0.615	0.834	0.618	0.887
25	0.601	0.860	0.619	0.842	0.625	0.912
Mean	0.602	0.869	0.599	0.861	0.604	0.875
Std. Deviation	0.016	0.020	0.017	0.024	0.016	0.020
Coeff. Of Var (%)	2.6	2.4	2.8	2.8	2.6	2.3

Figure 4.5c presents the void ratio results of a sample before shearing along with void ratio values from axial and torsional tests performed on Ottawa 20-30 sands against friction sleeves of R_{max} = 1.00 mm, where the vertical shaded area represents the limit of the average shear zone thickness calculated from the shear zone characterization tests (5.8 to 6.2 D_{50}, translated as 4.0 to 4.5 mm, for Ottawa 20-30 sands and 5.2 to 5.4 D_{50}, translated as 3.7 to 3.9 mm, for Blasting 20-30 sands). The large void ratio values calculated for both axial and torsional tests inside the shear zone limit indicate dilation caused by the shearing process. The results from the torsional test show a significant decrease in void ratio at distances from 5 to about 19 mm away from the sleeve with void ratio values at distances of 8 to 12 mm that are close to the minimum void ratio. At a distance of about 20 mm (28 D_{50} equivalents) from the sleeve, the void ratio reverts to the target void ratio value, implying that this distance is the extent of the influenced or disturbed zone in the torsional shearing mode. The axial tests results show a similar effect but at a much lower intensity that affects a smaller zone, from 7 to 12 mm. At distances

of 12 mm (16 D_{50} equivalents) and greater, the sand reverts to the target sample preparation void ratio. Tests performed with Blasting 20-30 sands and friction sleeves of R_{max} = 1.00 mm followed a similar trend to the tests performed on Ottawa 20-30 sands (Figure 4.5d). Both shearing modes indicate dilation within the shear zone, and there is a decrease in the void ratio values at distances greater than the extent of the shear zone. For torsional tests, the sand at a distance of 7 to 12 mm away from the sleeve reaches void ratio values close to the minimum void ratio line, and reverts to the target sample preparation void ratio at a distance of about 20 mm. The axial test also shows a slight decrease in void ratio values from distances of 5 to 8 mm, followed by increased void ratios of 9 to 11 mm. These results are in agreement with similar findings by DeJong and Wastgate (2009) and DeJong and Westgate (2010) who performed axial cyclic interface direct shear tests under constant stiffness confining conditions (CNS) complemented by local soil deformations using Particle Image Velocimetry (PIV) and reported dilation within a small zone immediately adjacent to the continuum's surface and contraction at a secondary zone further away from the interface.

Table 4.3: Shear induced changes in void ratio for axial and torsional tests on Ottawa 20-30 and Blasting 20-30 sands sheared against textured sleeves of R_{max} = 1.00 mm.

Distance from Sleeve (mm)	Void Ratio, e			
	Axial Tests on Sub-Rounded Sand	Axial Tests on Sub-Angular Sand	Torsional Tests on Sub-Rounded Sand	Torsional Tests on Sub-Angular Sand
1	0.785	1.143	0.718	1.157
2	0.720	1.066	0.666	1.051
3	0.654	0.976	0.646	0.999
4	0.600	0.921	0.597	0.865
5	0.592	0.853	0.597	0.793
6	0.597	0.812	0.568	0.752
7	0.588	0.815	0.565	0.728
8	0.566	0.821	0.521	0.722
9	0.551	0.895	0.513	0.740
10	0.561	0.921	0.515	0.745
11	0.583	0.873	0.522	0.741
12	0.592	0.856	0.522	0.735
13	0.588	0.871	0.538	0.766
14	0.577	0.864	0.534	0.796
15	0.602	0.916	0.527	0.801
16	0.589	0.874	0.551	0.797
17	0.581	0.875	0.553	0.805
18	0.605	0.859	0.569	0.857
19	0.587	0.888	0.574	0.844
20	0.594	0.842	0.613	0.873
21	0.586	0.839	0.609	0.858
22	0.604	0.858	0.599	0.889
23	0.602	0.869	0.614	0.887

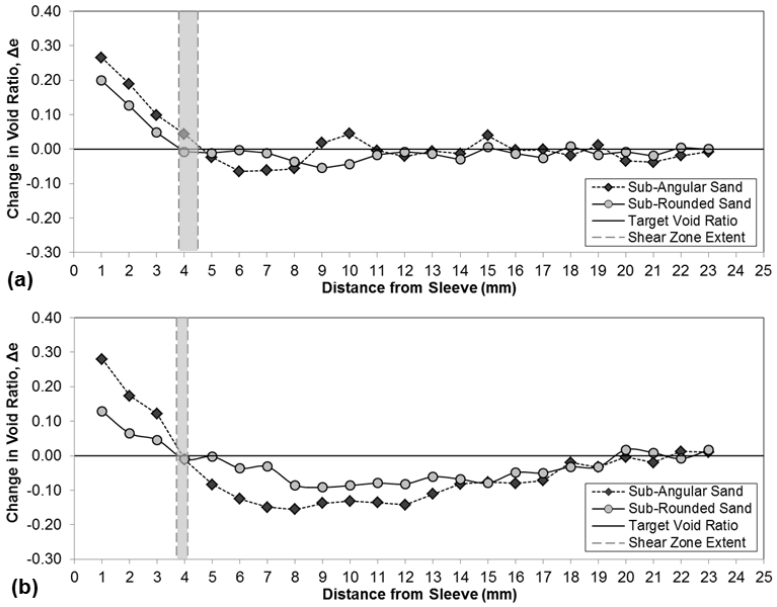

Figure 4.7: Shear-induced changes in void ratio for tests with Ottawa 20-30 and Blasting 20-30 sands sheared against a textured sleeves of R_{max} = 1.00: (a) axial and (b) torsional tests (shaded vertical area is range of observed shear zone thicknesses).

The effect of particle angularity on the shear-induced changes in void ratio is presented in Figures 4.7a and 4.7b for axial and torsional tests, respectively. These results are presented in terms of changes in void ratio with respect to the target sample preparation void ratio ($\Delta e = e_{measured} - e_{target}$) in order to allow for a direct comparison. Figure 4.7a presents a comparison of the axial tests, where both show soil dilation inside the shear zone. Outside the shear zone the results show a modest reduction in void ratio as compared to the target value, but no other clear trend can be identified and thus no definitive conclusion can be made in regards of the effect of angularity on axial tests. The results from torsional tests (Figure 4.7b) demonstrate that tests with Blasting 20-30 sands resulted in larger magnitudes of dilation inside the shear zone and larger decreases in void ratio at distances of 4.5 to 20 mm away from the sleeve. These results agree with the classical notion of soil mechanics that more angular assemblies undergo a larger degree of dilation when subjected to shearing. It is hypothesized that the clear effect that grain

angularity has in the shear-induced changes in void ratio of torsional tests plays an important role in the difference in global behavior observed in Figures 4.1a through 4.1d, which include a larger degree of strain-softening and a larger increase in measured stress ratio with increasing grain angularity.

4.2.7 Proposed Micro-Mechanisms

It is postulated that the forces transferred from the textured friction sleeves to the soil particles during shearing can be categorized in two main components, as described in Chapter 2 and presented by other authors such as Mitchell and Villet (1987) and Irsyam and Hryciw (1991). In axial tests, the force components consists of the Interface Friction (IF) force, originated by the friction between the sleeve texture and the soil particles, and the Annular Penetration (AP) force, a passive resistance caused by the difference in diameters between the steel rod and the protruding diamond texturing elements. The existence and influence of the AP force have been studied by other researchers in laboratory and field tests, and its magnitude was found to be directly proportional to the CPT tip resistance measured during field tests (DeJong 2001; Hebeler, et al. 2004). In a similar manner, the force components in torsional tests are the same IF force observed in the axial configuration and a Tangential Component (TC) force that is a passive resistance originated by the transfer of forces to the soil particles in a direction that is oriented tangentially away from any point in the friction sleeve surface during shearing. Shearing in the axial direction transfers forces (IF and AP components) that act, in average, parallel to the direction of shearing, causing particles in the vicinity of the sleeve to displace in this direction (Figure 4.8a) and results in only modest changes in void ratio outside the shear zone, as seen on Figures 4.6c, 4.6d and 4.7a. In contrast, torsional shearing transfers load in directions that tend to push particles away from the sleeve (Figure 4.8b). These mechanisms can be related to the results presented in Figures 4.6c, 4.6d and 4.7b, where torsional tests showed a sharp decrease in void ratio in the soil

outside of the shear zone, implying that the TC force causes a migration of sand grains from within the shear zone and/or a compaction of the sand outside the shear zone.

It is proposed that these processes are responsible for differences in the axial and torsional shear behavior, such as greater strain softening (Figure 4.1a), more significant influence of particle angularity (Figure 4.1d) and a larger shear zone length (Figures 4.3c, 4.4c and 4.4d) in torsional tests. Discrete Element Modeling simulations presented in Chapter 6 allowed for individual particle interactions to be tracked and thus for the micromechanical processes proposed herein to be further studied and validated.

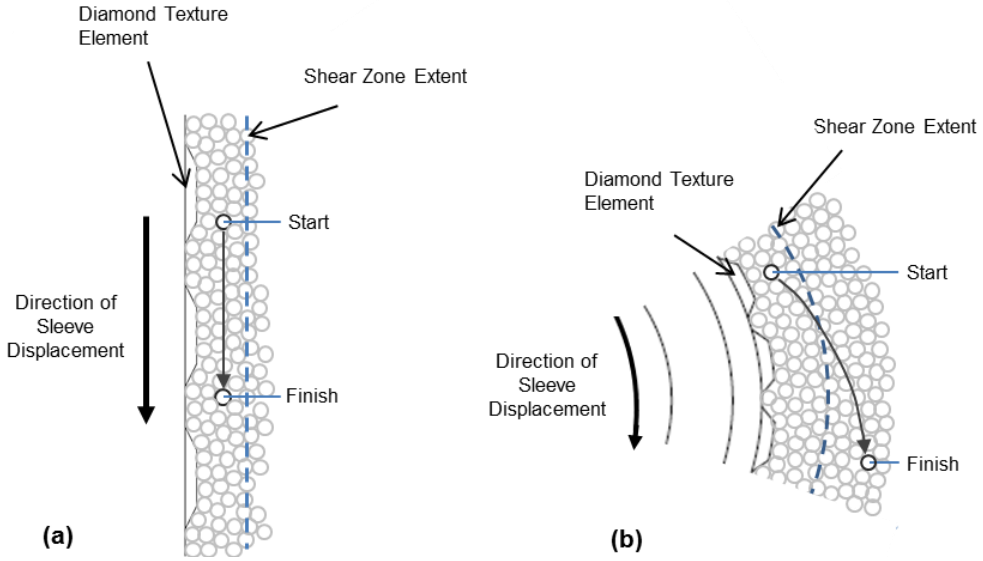

Figure 4.8: Mechanisms of induced particle displacement and shear zone formation during (a) axial and (b) torsional shear.

The classical understanding of soil dilation can be used to postulate a second mechanism taking place during torsional shear, as presented in Figures 4.9a and 4.9b. Inside the shear zone, at locations from 0 to 6 D_{50} away from the friction sleeve's surface, the induced displacements are sufficiently large and well within the dilative portion of the volume change-shear displacements relationship of dilative-drained granular soils. At distances outside the shear zone as large as 20 mm (from 6 to 30 D_{50}), the shear strains are relatively small and thus they remain in the contractive zone typically observed

before dilation occurs. At larger distances from the sleeve surface, no shear or volumetric strains are induced. On the other hand, during axial shear the sand outside the shear zone undergoes smaller shear strains that result in a smaller secondary zone of compressive shear-induced void ratio changes. As such, the results indicate that the extent of the influence area is smaller for axial shear as compared to torsional shear.

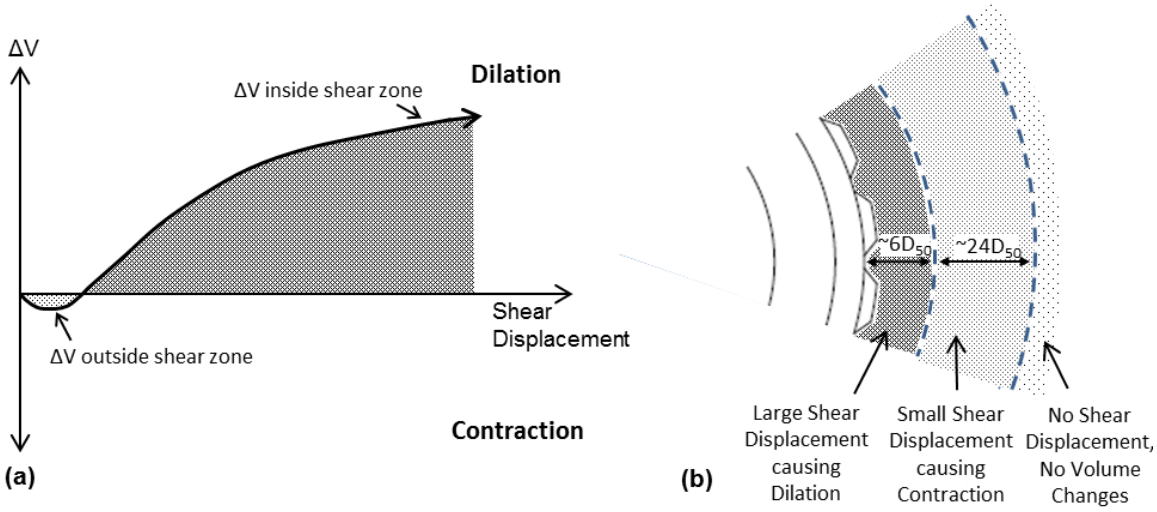

Figure 4.9: (a) Classical volume change-shear strain behavior of dilative-drained soils and (b) observed volume changes in torsional tests.

The experimental results presented herein indicate that axial and torsional shear induce inherently different soil deformations within the contacting soil. Typical influence zones for axial and torsional shear can be estimated from the results, as presented in Figure 4.10. Axial and torsional shear create shear zones that extend 5 to 6 D_{50} from the sleeve when highly rough sleeves are used, as observed in the shear zone characterization study. Void ratio evolution measurements showed that torsional shear induces a reduction in void ratio at locations outside the shear zone up to distances of about 20 mm, which correspond to a distance of about 30 D_{50}. On the other hand, axial shear influences or disturbs an volume outside the shear zone that only extends to distances of 8 to 11 mm, which correspond to distances of 10 to 15 D_{50}. Furthermore, the global behavior of torsional shear was shown to be more sensitive to particle angularity (Figures 4.1a

through 4.1d), which reflects the larger soil engagement shown as larger induced shear zones (Figures 4.3c, 4.4c and 4.4d) and a larger extent of influence zone (Figures 4.6c and 4.6d). These observations can be used to conclude that torsional shear induces soil shear deformations that results in greater particle rotations, which are restricted when shearing Blasting 20-30 sand that in turn results in larger soil engagement and higher loads being measured. Based on the different shear deformations and global shear behavior observed, the induced loading conditions are expected to be different for axial and torsional shear. Both of these observations are further addressed in the DEM simulations study presented in Chapters 5 and 6.

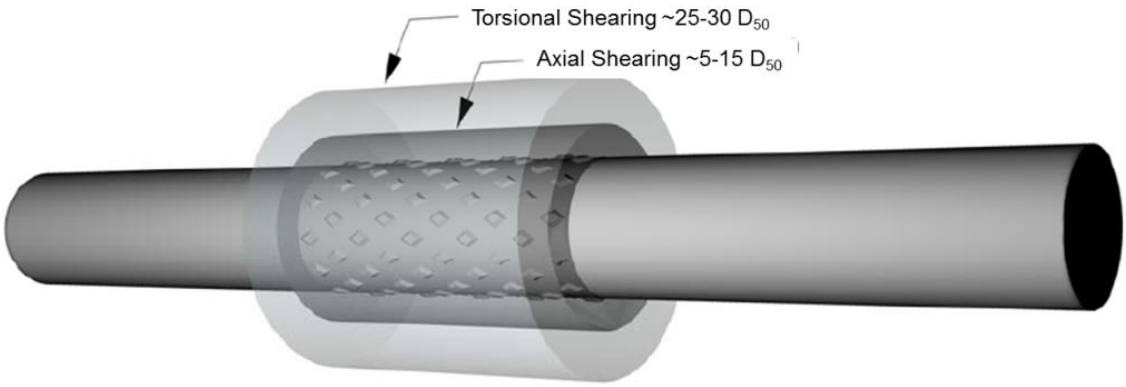

Figure 4.10: Volume of soil influenced/disturbed by axial and torsional shear.

4.2.8 Conclusions

The axisymmetric shearing device and the experimental methodology used in this study were shown to be effective tools to investigate the behavior of shear zones in sands in both axial and torsional shearing directions. The use of resins for specimen impregnation was also shown to provide useful results that expand the current understanding of the shearing and interface behavior of coarse-grained soils.

- The measured trends in global loads agreed well with the current understanding of interface shear behavior. It was observed that increases in continuum's surface roughness and particle angularity results in increased shear resistance. Furthermore,

prevalent differences between axial and torsional shearing modes were observed, such as the larger magnitude of strain softening and a larger effect of grain angularity on the measured loads in torsional shear. Shearing against conventional smooth CPT sleeves did not show an influence from sand angularity or shearing direction, supporting previous studies indicating that shearing against smooth surfaces results in only sliding at the soil-continuum interface and thus induces negligible soil shearing.

- The staggered diamond texture of the friction sleeves used in this study was shown to create uniform shear zones for the medium sized sands tested. The results showed that the shear zone thickness for torsional and axial tests is fully developed at small displacements and R_{max} surface roughness values as small as 0.5 mm. Furthermore, the shear zone thickness was found to be slightly larger for axial tests than for torsional tests, and also larger for tests with Ottawa 20-30 sands than for tests on Blasting 20-30 sands for both axial and torsional tests. These slight differences were within one mean particle diameter.
- The shear zone length was shown to have a linear relationship with shear displacement. The length of the shear zones created in torsional tests was significantly larger than for axial tests for all surface roughnesses and sleeve displacements, suggesting a greater ability of the torsional shear tests to induce soil shearing. Shear zone length measurements from tests with modified sleeve configurations (diamond elements rotated 90°) reveal that this difference in behavior is related to the different micro-mechanisms involved in each shearing mode and not to the particular sleeve texture configuration.
- Dilation in the shear zone was observed in all tests with textured sleeves. However, a sharp decrease in void ratio in torsional tests at distances outside the shear zone reinforces the idea of particle migration away from the sleeve. This effect was more pronounced for tests with Blasting 20-30 sands due to the larger dilative behavior

of these more angular assemblies. Axial tests also induced slight decreases in void ratio at locations outside the shear zone, but to a much smaller degree. A study on the effect of particle angularity showed that it has a larger effect on torsional shear, as compared to axial shear, and presents a plausible explanation for the differences observed in the global behavior between the two interface shear modes.

- The extent of the zone influenced by torsional shear was shown to be two to three times larger than that for axial shear for tests with textured sleeves. For torsional tests, the influenced zone extended to about 30 mean particle diameters from the friction sleeves, as opposed to a smaller zone affected by axial shear in the order of 10 to 15 mean particle diameters. These results have important implications in the volume of soil that is engaged during shearing and will ultimately affect the interpretation from laboratory and field interface shear tests.
- The proposed micro-mechanisms state that axial shearing results in particle displacements that are in average parallel to the sleeve displacement direction. On the other hand, torsional shearing results into displacement of particles in directions both parallel and tangent to the direction of shearing, potentially resulting in particle migration away from the shear zone. The results of the evolution of shear-induced changes in void ratio validated the hypothesis. A complementary explanation is derived from the relationship between soil volume change and shear displacement for dilative-drained assemblies where the large shear particle displacements inside the shear zone cause dilation while the smaller particle displacements outside the shear zone induce sand contraction during torsional shearing. DEM simulations presented in Chapter 6 provide a more detailed study of the micro-mechanical processes taking place during axial and torsional interface shear.

Torsional shear is shown in this study to be an effective shearing mode for use in experimental studies and testing, and reflects a number of common in-situ conditions

induced by earthquake ground motions and shearing induced by lateral loading of piles and foundation vibrations. Further, loading modes that can isolate the effect of horizontal and not just vertical stress conditions are of importance for an improved understanding of soil behavior. Torsional shear was shown to more quickly engage interface shear as compared to axial shear, and to provide significant insights into soil behavior.

CHAPTER 5

COMPARISONS OF THE GLOBAL BEHAVIOR OF AXIAL AND TORSIONAL INTERFACE SHEAR AXISYMMETRIC TESTS

5.1 Introduction

The study presented in this chapter evaluates the results of axial and torsional interface shear axisymmetric laboratory tests with sands and Discrete Element Modeling (DEM) simulations performed between sands and friction sleeves of varying surface roughness. The results, which include mobilized loads and sample volume changes during shear, quantify the effects of surface roughness, particle shape, particle roughness and confining pressure. The torsional shear tests showed larger sample dilation rates, more defined peaks and larger magnitudes of strain softening in stress ratio-displacement curves than axial shear tests. Torsional shear is shown to be more sensitive to particle angularity while axial shear is more sensitive to particle roughness, results that imply that different micromechanical processes are involved during shearing in both directions. The failure envelopes obtained for both shear directions reinforce the notion of the "non-uniqueness" of shear behavior in granular materials, which is influenced by the different loading conditions induced by axial and torsional shear. Interface friction and passive resistance load transfer mechanisms between the friction sleeves and the soil are quantified, and it is shown that the interface friction between the particles and the sleeve surface is independent on the shear direction but the passive resistances mobilized in axial and torsional shear reflects the differences observed in the global- and particle-scale shear behaviors. The ability to separate the friction and passive resistance components from the measured loads provides an interpretation framework with a fundamental basis that will aid in the direct measurement of soil properties from laboratory and field tests.

During the last decades researchers have made important advances in the understanding of soil-structure interaction and interface behavior. In particular, it has been understood that significant potential for enhanced structure design and efficient use of resources can be achieved by prescribing the structure's surface characteristics, such as its roughness and hardness. However, a key component to this approach is the characterization of the soil's shear and interface behavior in an accurate and effective manner. In an effort to create the link between soil properties and improved geotechnical systems, a series of multi-sleeve attachments for site characterization studies have been developed at the Georgia Institute of Technology. These devices are designed to be placed behind a 15 cm^2 CPT probe, hence providing additional capabilities to this widely used device. The specific objective of this study is to characterize the behavior of axial and torsional interface shear tests as part of the development of a new multi-sleeve attachment for site characterization called the Multi-Piezo-Friction-Torsion Attachment (MPFTA), shown in Figure 2.28. The effect of surface roughness and the different shearing directions (i.e. axial and torsional) are taken into consideration in order to characterize the interface behavior and shear strength of soil-inclusion interface systems.

The experimental results presented in this chapter correspond to tests with Ottawa 20-30, Blasting 20-30 and Ottawa 50-70 sands (with the exception of one test performed on monosized glass beads, as described later) which allowed studying the effect of particle angularity and particle size on the shear response of interface axisymmetric drained tests (device shown in Figures 3.5a and 3.5b) against smooth and textured sleeves. All the results presented in this section pertain to tests on specimens at relative densities between 60 and 65% under a confining stress of 50 kPa. The numerical results presented herein were performed with the DEM models (Figures 3.20a and 3.20b) and simulation parameters (Table 3.4) presented in Chapter 3 sheared against smooth and textured friction sleeves (Figure 3.19). More detailed information regarding the devices, methodologies and results repeatability can be found in Chapter 3 of this thesis.

5.2 Results

A series of drained interface shear tests were performed using the axisymmetric device on Ottawa 20-30 and Blasting 20-30 sands (medium-sized) and Ottawa 50-70 sand (small-sized) sheared against friction sleeves of varying roughness. This study was expanded with DEM simulations performed on two-particle clumps against friction sleeves of varying roughness.

5.2.1 Effect of Surface Roughness

The stress ratio-displacement curves for axial and torsional laboratory tests with the three sands tested against friction sleeves of maximum surface roughness, R_{max}, of 0.006 (i.e. conventional smooth CPT), 0.25, 0.50, 1.00 and 2.00 mm are presented in Figures 5.1a through 5.1f. These results agree well with the current understanding of interface shear behavior and show a clear trend of increasing mobilized loads with increasing sleeve surface roughness. The effect of grain angularity is also evident, with larger loads mobilized for tests performed with Blasting 20-30 sand (most angular) (Figures 5.1c and 5.1f), followed by tests on Ottawa 50-70 sand (medium angular) (Figures 5.1b and 5.1e), and then by tests with Ottawa 20-30 sand (least angular) (Figures 5.1a and 5.1d). The interface shear tests performed with conventional smooth CPT sleeves resulted in smaller measured loads that were not affected by sand properties or shearing direction. This was expected since the main failure mechanism between smooth surfaces and medium-sized sands is sliding between the sand grains and the surface, rather than soil shearing as observed in tests performed with rough surfaces such as the textured friction sleeves (Martinez and Frost, 2014a; Martinez and Frost, 2014b; Hebeler, et al. 2015).

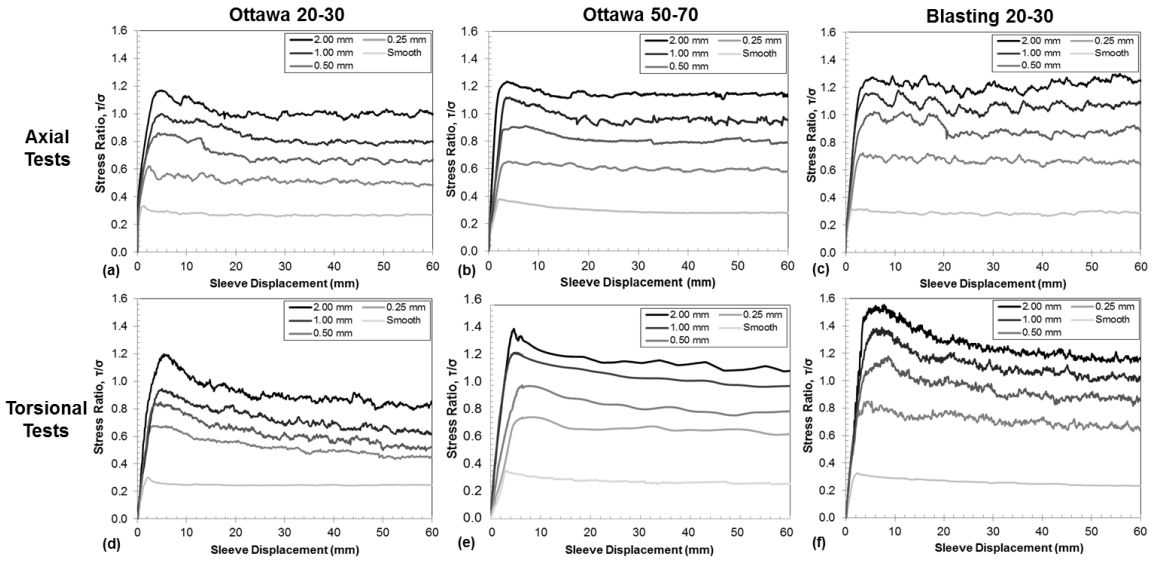

Figure 5.1: Stress ratio-displacement curves tests against friction sleeves of varying R_{max}. Axial test on (a) Ottawa 20-30, (b) Ottawa 50-70 and (c) Blasting 20-30. Torsional tests on (d) Ottawa 20-30, (e) Ottawa 50-70 and (f) Blasting 20-30.

The average residual and peak stress ratios as a function of surface roughness for the tests shown in Figures 5.1a through 5.1f are presented in Figures 5.2a through 5.2c and Table 5.1. The results show increasing mobilized loads with surface roughness; however, the rate of increase decreases with roughness. For the tests with Ottawa 20-30, the axial tests with textured sleeves resulted into larger residual stress ratios than those from torsional tests, and similar peak stress ratios (Figure 5.2a). On the other hand, the residual loads from axial tests with Blasting 20-30 sands and textured sleeves were similar in magnitude to those from torsional tests, and the peak loads were larger for torsional tests (Figure 5.2c). Similar trends were observed for the tests on Ottawa 50-70 sand (Figure 5.2b). Figure 5.2d present this difference in behavior in terms of the difference in measured stress ratio between tests with Blasting 20-30 and Ottawa 20-30 sands for any given surface roughness ($\tau/\sigma_{Blasting20\text{-}30} - \tau/\sigma_{Ottawa20\text{-}30}$). It can be observed that the difference in measured loads is consistently larger for torsional tests across all the

surface roughnesses tested, with increments as large as 0.35 and 0.40 for residual and peak values, respectively, as compared to increments of 0.24 and 0.15 for axial tests.

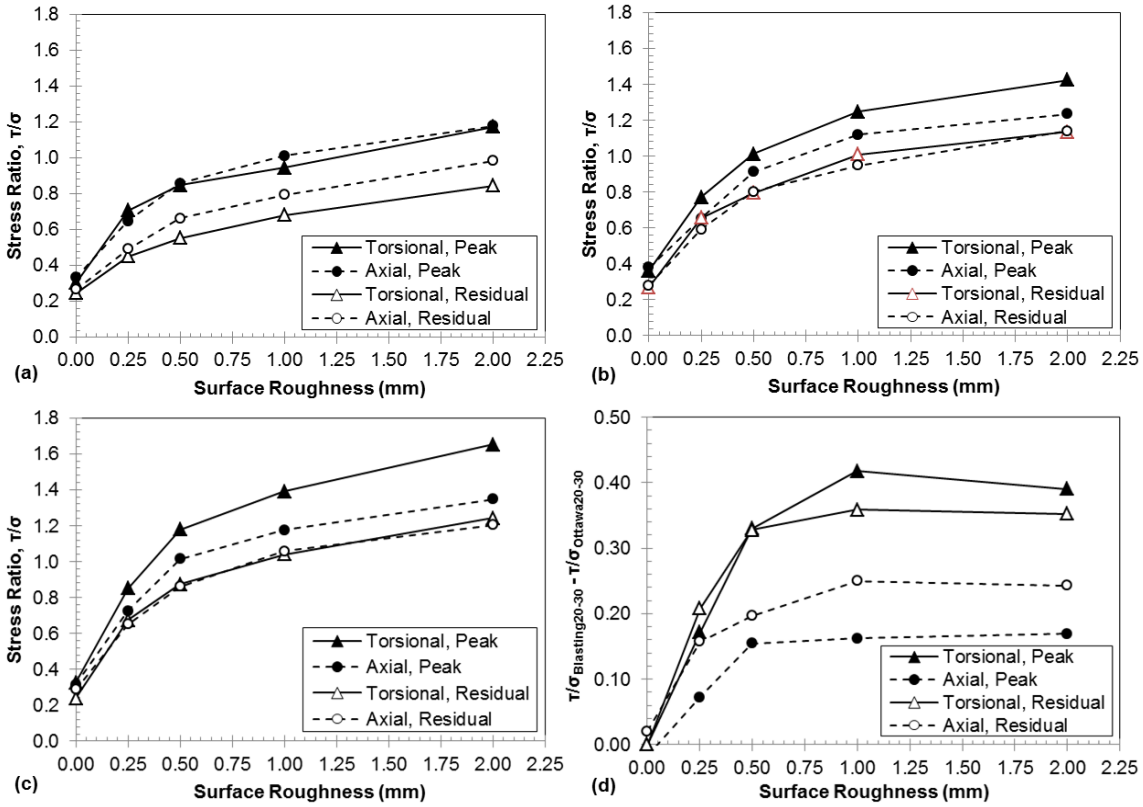

Figure 5.2: Peak and residual stress ratios as a function of surface roughness for axial and torsional tests on (a) Ottawa 20-30, (b) Ottawa 50-70 and (c) Blasting 20-30 sands. (d) Peak and residual difference between tests on Blasting 20-30 and Ottawa 20-30 sands.

The magnitudes of strain softening as well as the sleeve displacement needed to mobilize the peak loads also showed a unique relationship with surface roughness, as shown in Figures 5.3a and 5.3b and Table 5.1. The magnitudes of both quantities from axial and torsional tests increased with surface roughness up to an R_{max} value of about 0.50 mm, with subsequent increases in roughness resulting in no further change. These results imply similar behavior as that observed in the bi-linear relationship between surface roughness and interface strength shown in Figure 2.1, where the interface behavior at surface roughness values smaller than the "critical" roughness is controlled

by properties of both the surface material as well as the contacting granular material. However, at larger surface roughness values, the interface behavior is controlled solely by properties of the granular material. The magnitude of the strain softening and the sleeve displacement needed to mobilize the peak loads were both shown to be consistently larger for torsional tests. The former represents a key difference between axial and torsional results and indicates a larger dilation rate during torsional tests as shown in the following section by means of DEM simulations.

Table 5.1: Results of Axial and Torsional Interface Shear Laboratory Tests and DEM Simulations.

Shear Direction	Sand Type	R_{max} (mm)	$(\tau/\sigma)_{peak}$	$(\tau/\sigma)_{residual}$	Strain Softening (τ/σ)	Disp. to Peak Load (mm)	Max. Dilation Angle (°)	Annular Penetration Force, AP (τ/σ)	Tangential Component Force, TC (τ/σ)	δ_{peak} (°)	δ_{res} (°)
Axial	Ottawa 20-30	0.006	0.33	0.27	0.07	1.29	N/A	0.00	N/A	17.2	14.0
Axial	Ottawa 20-30	0.25	0.65	0.49	0.16	2.33	N/A	0.05	N/A	29.4	22.9
Axial	Ottawa 20-30	0.50	0.86	0.67	0.10	4.36	N/A	0.09	N/A	35.5	28.1
Axial	Ottawa 20-30	1.00	1.01	0.79	0.22	4.85	N/A	0.17	N/A	37.7	29.6
Axial	Ottawa 20-30	2.00	1.18	0.98	0.19	4.94	N/A	0.34	N/A	37.1	30.0
Torsional	Ottawa 20-30	0.006	0.30	0.25	0.06	2.10	N/A	N/A	0.00	15.6	13.4
Torsional	Ottawa 20-30	0.25	0.68	0.47	0.21	4.26	N/A	N/A	0.04	32.0	22.0
Torsional	Ottawa 20-30	0.50	0.85	0.55	0.30	4.77	N/A	N/A	0.07	35.6	25.2
Torsional	Ottawa 20-30	1.00	0.95	0.66	0.29	5.53	N/A	N/A	0.13	37.0	27.9
Torsional	Ottawa 20-30	2.00	1.20	0.84	0.35	5.65	N/A	N/A	0.26	40.0	29.2
Axial	Ottawa 50-70	0.006	0.38	0.28	0.10	2.10	N/A	0.00	N/A	19.3	14.5
Axial	Ottawa 50-70	0.25	0.65	0.59	0.06	3.60	N/A	0.05	N/A	29.1	26.6
Axial	Ottawa 50-70	0.50	0.91	0.80	0.11	4.00	N/A	0.09	N/A	36.7	32.9
Axial	Ottawa 50-70	1.00	1.12	0.95	0.17	4.10	N/A	0.18	N/A	40.4	33.7
Axial	Ottawa 50-70	2.00	1.23	1.14	0.09	3.90	N/A	0.36	N/A	38.8	34.2
Torsional	Ottawa 50-70	0.006	0.36	0.27	0.09	3.00	N/A	N/A	0.00	17.6	13.3
Torsional	Ottawa 50-70	0.25	0.77	0.66	0.11	6.00	N/A	N/A	0.05	31.8	27.8
Torsional	Ottawa 50-70	0.50	1.01	0.79	0.22	7.50	N/A	N/A	0.09	37.7	31.0
Torsional	Ottawa 50-70	1.00	1.25	1.01	0.24	6.00	N/A	N/A	0.19	41.3	34.9
Torsional	Ottawa 50-70	2.00	1.42	1.13	0.29	5.80	N/A	N/A	0.38	41.0	32.9
Axial	Blasting 20-30	0.006	0.32	0.29	0.03	1.17	N/A	0.00	N/A	16.4	15.0
Axial	Blasting 20-30	0.25	0.73	0.65	0.07	3.43	N/A	0.06	N/A	32.1	29.1
Axial	Blasting 20-30	0.50	1.01	0.86	0.15	4.92	N/A	0.11	N/A	40.3	35.3
Axial	Blasting 20-30	1.00	1.17	1.06	0.12	5.70	N/A	0.21	N/A	44.9	38.5
Axial	Blasting 20-30	2.00	1.35	1.20	0.14	5.87	N/A	0.41	N/A	46.8	36.7
Torsional	Blasting 20-30	0.006	0.33	0.24	0.09	2.44	N/A	N/A	0.00	16.8	12.5
Torsional	Blasting 20-30	0.25	0.85	0.67	0.18	4.37	N/A	N/A	0.06	26.2	31.0
Torsional	Blasting 20-30	0.50	1.18	0.87	0.31	6.56	N/A	N/A	0.12	41.0	35.0
Torsional	Blasting 20-30	1.00	1.39	1.04	0.35	7.10	N/A	N/A	0.24	46.8	36.6
Torsional	Blasting 20-30	2.00	1.55	1.16	0.39	6.90	N/A	N/A	0.48	47.3	35.2
Axial	DEM, AR=1.5	0.00	0.26	0.24	0.02	N/A	0.0	N/A	N/A	N/A	N/A
Axial	DEM, AR=1.5	0.25	0.55	0.51	0.04	N/A	1.1	N/A	N/A	N/A	N/A
Axial	DEM, AR=1.5	0.50	0.92	0.73	0.18	N/A	3.9	N/A	N/A	N/A	N/A
Axial	DEM, AR=1.5	1.00	1.04	0.87	0.17	N/A	7.0	N/A	N/A	N/A	N/A
Axial	DEM, AR=1.5	2.00	1.18	0.97	0.20	N/A	9.6	N/A	N/A	N/A	N/A
Torsional	DEM, AR=1.5	0.00	0.29	0.29	0.00	N/A	0.0	N/A	N/A	N/A	N/A
Torsional	DEM, AR=1.5	0.25	0.65	0.47	0.18	N/A	5.4	N/A	N/A	N/A	N/A
Torsional	DEM, AR=1.5	0.50	0.87	0.57	0.30	N/A	6.6	N/A	N/A	N/A	N/A
Torsional	DEM, AR=1.5	1.00	1.01	0.71	0.31	N/A	8.4	N/A	N/A	N/A	N/A
Torsional	DEM, AR=1.5	2.00	1.13	0.77	0.35	N/A	12.1	N/A	N/A	N/A	N/A

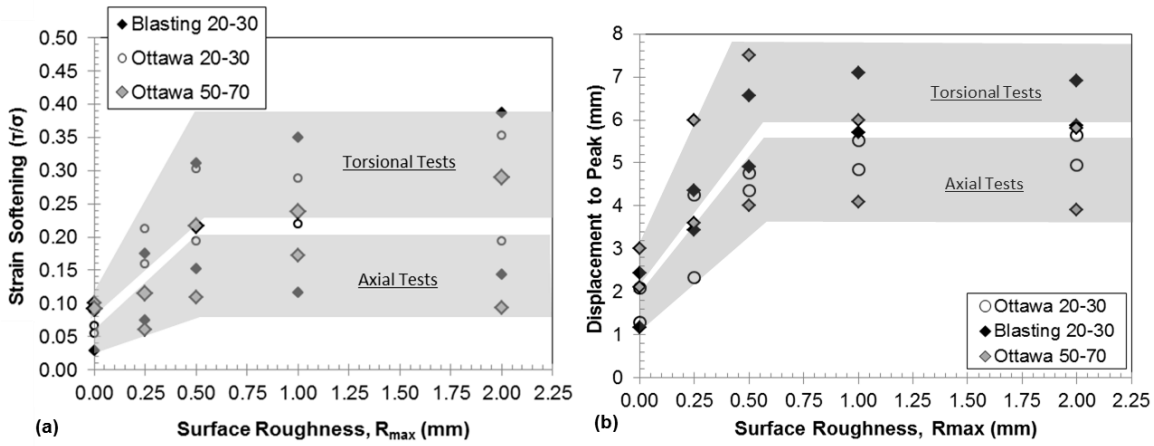

Figure 5.3: (a) Strain softening and (b) sleeve displacement to peak load as a function of surface roughness for axial and torsional tests on Ottawa 20-30, Ottawa 50-70 and Blasting 20-30 sands.

5.2.2 Specimen Volume Changes During Shear

Since the axisymmetric device used for the experimental studies was not able to measure specimen volume changes during shear, DEM simulations were used to investigate the global shear-induced volume changes of the specimens subjected to axial and torsional shear. The results of a set of simulations performed against friction sleeves of varying roughnesses are presented in Figures 5.4a through 5.4e. Figures 5.4a and 5.4b show the stress ratio-sleeve displacement curves for axial and torsional shear tests, respectively, while Figures 5.4c and 5.4d show the corresponding volume change-sleeve displacement curves for axial and torsional tests. The simulations with smooth friction sleeves resulted into negligible volume changes, while all the tests with textured sleeves induced dilation within the samples. The dilation rate during torsional tests decreased with increasing displacement, reaching a point of shearing under constant volume, or critical state, at shear displacements between 10 and 20 mm that continued throughout the rest of the tests. On the other hand, the axial specimens showed dilation continuing at all sleeve displacements thus not reaching a true critical state. The reason is that during axial shear the friction sleeve encounters "undisturbed" sand at the sleeve's leading edge at

every displacement increment, in contrast to the friction sleeves during torsional shear which largely remold the same sand during the entire test. For simulations against surfaces of R_{max} of 0.25, 0.50 and 1.00 mm, samples subjected to torsional shearing underwent a larger degree of total volume change. However, for the simulation against a surface of R_{max} = 2.00 mm axial shearing induced larger increases in volume at large sleeve displacements.

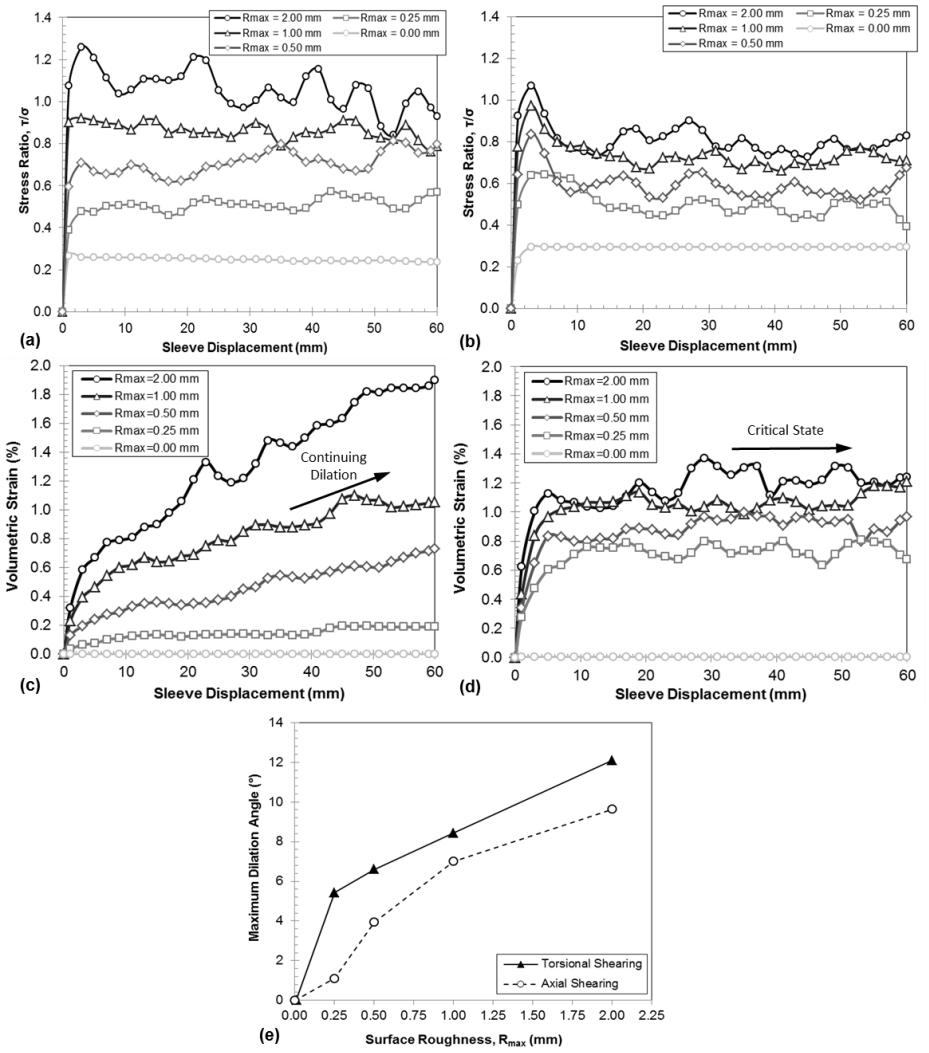

Figure 5.4: Stress ratio values mobilized during (a) axial and (b) torsional shear tests. (c) Volumetric strain during shear for axial and (d) torsional simulations. (e) Maximum dilation angle for axial and torsional simulations.

Maximum dilation angles, corresponding to dilation velocities at peak loads, were calculated for the axial and torsional results (Figures 5.4c and 5.4d) as follows:

$$\psi = -\tan^{-1}\left(\frac{\delta\varepsilon_{vol}}{\delta\varepsilon_{sh}}\right)$$

where $\delta\varepsilon_{vol}$ is the increment in volumetric strain and $\delta\varepsilon_{sh}$ is the increment in shear strain.

The results show that the maximum dilation angles are larger for torsional shearing for all tests performed against textured sleeves, as shown on Figure 5.4e and Table 5.1. These values increase linearly with R_{max} for torsional shearing against textured sleeve, but their rate of increase reduces for axial shearing. The maximum dilation angles at high roughnesses are believed to best represent the internal shear behavior of the granular assemblies, which are between 8° and 12° for torsional shearing and between 7° and 10° for axial shearing. Considering the limitations associated with DEM methods such as excessive particle rotations and hindered sample dilation predictions, these results agree reasonably with previously published maximum dilation angles for plane strain compression laboratory tests on sub-rounded quartz sands under low confining pressures, with a value of 14.7° (Bolton, 1986; Barden, et al. 1969). The larger sample dilation observed during torsional shear is considered to be in part responsible for the different behaviors observed; in particular, it is most likely related to the more defined peak stress ratio observed in torsional tests and the associated larger degree of strain softening.

5.2.3 Effect of Particle Shape and Particle Friction Coefficient

Two additional series of laboratory tests and numerical simulations were performed against friction sleeves with R_{max} = 1.00 mm in order to further study the effect of particle properties on the interface shear behavior of both shear orientations. Specifically, axial and torsional laboratory tests with glass beads (monosized, D_{50} = 0.5 mm) and GRC-3 lunar simulant (C_u = 10.0, C_c = 1.29, D_{50} = 0.17 mm, from He, et al, 2013) allowed to further study the relationship between mobilized loads and particle

roundness (Figures 5.5a and 5.5b and Table 5.2), and DEM simulations with varying particle coefficients of friction served as a proxy in order to study the effect of particle surface roughness (Figures 5.5c and 5.5d and Table 5.2). DEM simulations were shown to be a highly useful tool for these kinds of studies because they allowed changing the particle friction coefficient while keeping the same particle shape; however, this is highly challenging during laboratory tests. From visual examination, it was determined that the Blasting 20-30 sand and the GRC-3 lunar simulant have a "high" particle roughness, the Ottawa sands have a "medium" particle roughness and the glass beads have a "low" particle roughness. While these unintended differences in particle roughness most likely affected the laboratory test results, it was still possible to identify important differences in behavior between axial and torsional tests as a function of particle roundness. It should also be noted that while the particle friction coefficient in DEM does not account for the micro-roughness present in natural particles, it does emulate the effect of particle roughness on mobilized loads and volume change behavior of soils (Yang, et al. 2012).

The magnitude of the peak and residual stress ratios for torsional tests was shown to increase at a nearly constant rate with decreasing particle roundness (i.e. increasing particle angularity), while the rate of increase for axial tests decreased with decreasing particle roundness. This trend is more evident for the peak stress ratios (Figure 5.5a), which probably is an indication of the larger peak dilation induced by torsional shearing, especially evident when testing assemblies composed of more angular particles. Particle angularity is a particle rotation resistance mechanism that has been recognized to contribute to shearing resistance by mechanisms such as soil dilation (Cho, et al. 2006). Therefore, the fact that torsional shear is more sensitive to particle angularity suggests that this process tends to induce a larger degree of particle rotations within the contacting soil. This hypothesis makes logical sense if the friction sleeve and a soil particle are thought of as engaged gears. When there is complete engagement, the full rotational displacement of the friction sleeve gets transferred as particle rotation. While partial

engagement between the sleeve and the particle is a more realistic situation, where particle sliding and translation are also taking place, these results suggest that particle rotation is a dominant process taking place during torsional shearing. The study presented in Chapter 6 of this thesis addresses sleeve-particle interactions in greater detail.

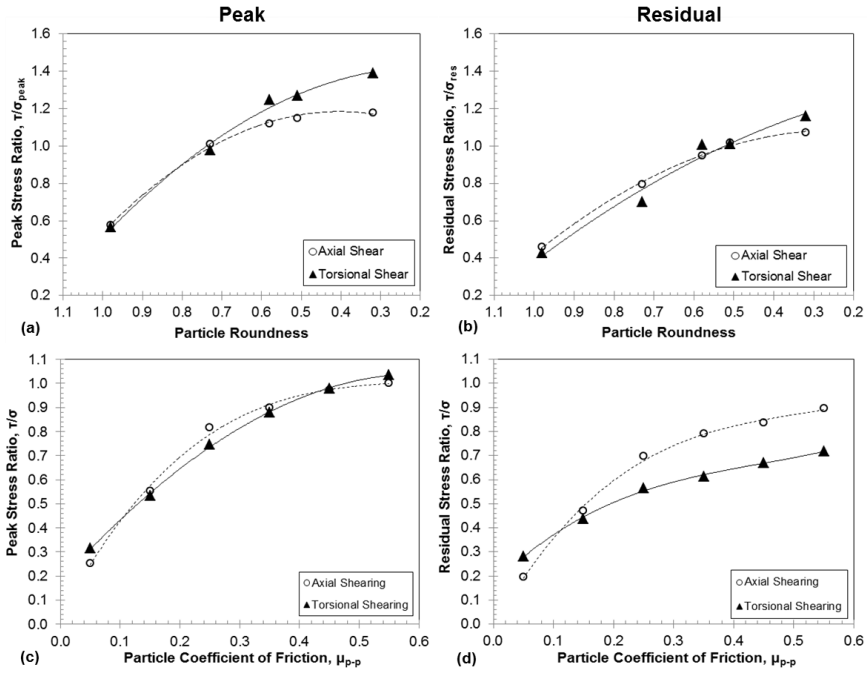

Figure 5.5: (a) Peak and (b) residual stress ratios as a function of particle roundness for axial and torsional laboratory tests against friction sleeves of R_{max} = 1.00 mm. (c) Peak and (d) residual stress ratios as a function of particle coefficient of friction for axial and torsional DEM simulations against friction sleeves with R_{max} = 1.00 mm.

The DEM simulations showed that the peak stress ratios have similar magnitudes for both axial and torsional shear tests across the range of friction coefficients studied (Figure 5.5c). However, the residual stress ratios from axial simulations are more sensitive to changes in particle coefficient of friction than those from torsional tests, as shown in Figure 5.5d. This is especially evident at low friction coefficients, between 0.05 and 0.25. In DEM simulations, the particle friction coefficient represents the particle roughness of the particles. Thus, increasing the particle friction coefficient contributes to shearing resistance by increasing the amount of energy required to induce particle-to-

particle contact slippage. Consequently, the fact that the residual loads during axial shear are more sensitive to particle friction coefficient suggests that contact slippage is a more dominant process involved in axial shearing. The similarity between the effects of the coefficient of friction on the axial and torsional peak loads might be caused by the high dilatancy taking place at this stage of the shearing process. In this case, it is likely that the stable force chains present throughout the soil mass have not yet started to undergo significant failure and buckling, hence yielding a lower probability of contact slippage as compared to that for the residual stage, which is closer to a critical state scenario.

Table 5.2: Results of axial and torsional laboratory tests and DEM simulations on textured sleeves of R_{max} = 1.00 mm.

Granular Material	Particle Shape	Particle Roughness	Axial $(\tau/\sigma)_{peak}$	Axial $(\tau/\sigma)_{residual}$	Torsional $(\tau/\sigma)_{peak}$	Torsional $(\tau/\sigma)_{residual}$
Glass Beads*	0.98**	Low***	0.61	0.49	0.56	0.43
Ottawa 20-30 Sand*	0.73**	Medium***	1.01	0.80	0.95	0.70
Ottawa 50-70 Sand*	0.58**	Medium***	1.12	0.95	1.25	1.01
Blasting 20-30 Sand*	0.32**	High***	1.18	1.07	1.39	1.16
Particle Clumps†	1.5††	0.05†††	0.25	0.20	0.31	0.28
Particle Clumps†	1.5††	0.15†††	0.55	0.47	0.53	0.44
Particle Clumps†	1.5††	0.25†††	0.82	0.70	0.75	0.56
Particle Clumps†	1.5††	0.35†††	0.90	0.79	0.88	0.61
Particle Clumps†	1.5††	0.45†††	0.97	0.84	0.98	0.67
Particle Clumps†	1.5††	0.55†††	1.00	0.90	1.03	0.72

*Laboratory Test; **Particle Roundness; ***Particle Roughness from Visual Inspection
†DEM Simulations; ††Aspect Ratio; †††Particle Coefficient of Friction

5.2.4 Effect of Confining Stress

In soil behavior, it has been shown that the failure envelope in dilative soils has a concave shape as a result of the decrease in dilation under increasing normal stress (e.g. Lambe and Whitman, 1969). When plotted in terms of stress ratio, the failure envelope shows a decrease in stress ratio with increasing normal stress. Furthermore, it has also been documented that the shear strength and behavior of granular materials is dependent on the boundary and loading conditions, which result in a "non-uniqueness" of soil strength based on the different shear strengths mobilized in different loading modes, such as triaxial compression compared to triaxial extension (e.g. Kulhawy and Mayne, 1990).

The simulation results presented in Figures 5.6a, 5.6b and Table 5.3, all performed against friction sleeves of R_{max} = 1.00 mm, agree with this understanding of

soil strength “non-uniqueness” since axial and torsional shear show different peak and residual failure envelopes. Both the peak and residual failure envelopes for axial and torsional shear show a decrease of mobilized stress ratio that follows a power law shown as a straight line in log-log space. The reader can refer to Figure 6.2 of Chapter 6 for failure envelopes and stress paths of axial and torsional tests. For the axial test results, the difference between peak and residual loads decreases as the confining pressure increases, indicating a decrease in dilation. However, this difference remains nearly constant for torsional tests. Figures 5.6c and 5.6d and Table 5.3 show a quantification of the contribution of dilation to the mobilized stress ratios presented in Figures 5.6a and 5.6b. These plots, in terms of tangent of the dilation angles for both peak and residual stages, show an expected decrease in the peak values with increasing normal stress. The peak dilation contributions are larger for torsional shear tests, a fact which is in accordance with the larger dilation observed in this shear mode (Figure 5.4e). For axial tests, the results from the residual stage also show a measurable contribution that decreases with confining pressure. However, for torsional tests the dilation results oscillate between fairly small positive and negative values indicating a negligible contribution from dilation (data points not shown for clarity) that is in agreement with critical state being reached at large shear displacements. The difference between the measured stress ratio values (Figures 5.6a and 5.6b) and the contribution from dilation (Figures 5.6c and 5.6d) for any given confining pressure gives a quantification of the contribution from shearing under a constant volume, which is analogous to the critical state coefficient of friction (i.e. tan (δ_{cs})). It is important to note that the critical state friction angle is often considered to be independent of normal stress in soil behavior, as presented by various authors such as Rowe (1962) and Bolton (1986). However, the results presented in Figures 5.6e and 5.6f show a decrease with increasing confining pressure. This kind of behavior has been observed by Dove and Frost (1999) for peak friction coefficient on interface systems consisting of sand and smooth (soft and hard) surface materials. The authors reported that

the reason for this behavior is an increase in the number of particles contacting the surface and an increase in contact area with increasing normal load. The increase in contact area follows a power law of the following form:

$$A_C = kW^n$$

where A_c is the contact area, k the friction factor constant of proportionality, W is the normal load and the exponent n is the load index, which varies between 2/3 and 1.0. Furthermore, Dove and Frost (1999) also provided the following power-law relationship between the boundary measured shear stress, the number of particle contacts and the boundary applied normal stress:

$$\tau = N^{1-n} k_3 \sigma^n A_g$$

where τ is the boundary measured shear stress, N is the number of particles contacting the surface, k_3 is a content of proportionality, σ is the boundary applied normal stress and A_g is the gross contact area between the surface and the soil particles.

The authors performed experiments that quantified the effect of normal load on the number and area of particle contacts against a solid surface and found that both increase with increasing load. Figures 5.6g and 5.6h show a quantification of the number of particle contacts and the average overlap between these and the friction sleeves at the peak and residual stages for axial and torsional DEM simulations. Conventional DEM codes do not simulate the increase in contact area between particles or particles and solid surfaces with increasing load; this is accounted for indirectly by calculating an interpenetration or overlap between the objects. Therefore, the average overlap values are used to calculate contact forces. Here, the average overlap between the particles and the friction sleeve is taken as an analog of the average contact area, and is computed as following, based on the linear-elastic contact model chosen for the simulations:

$$\delta = \frac{F_C / N}{k_n}$$

where F_c is the sum of the contact forces against the sleeve, N is the number of particles in contact, k_n is the normal stiffness of the particles and δ is the average overlap.

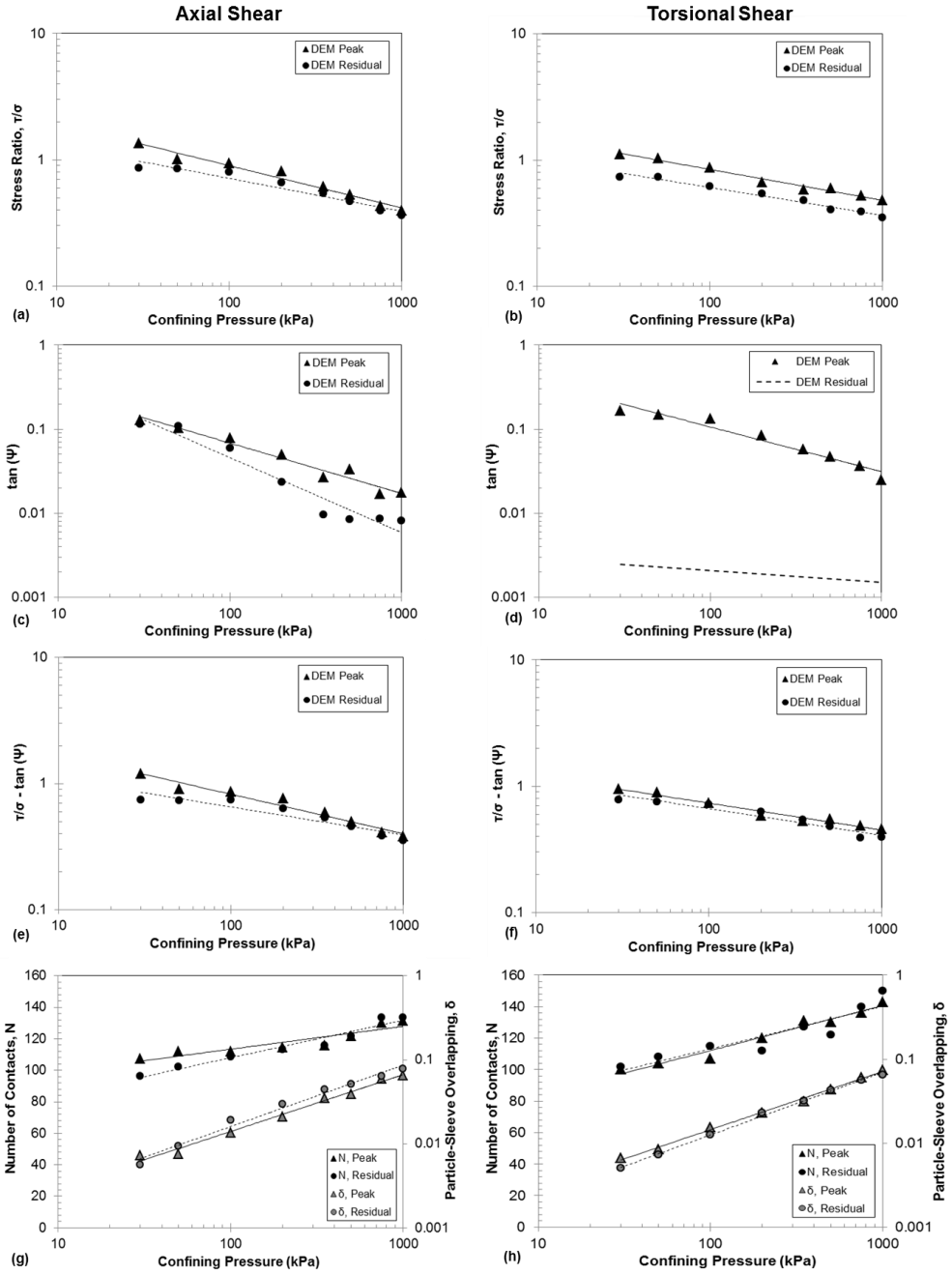

Figure 5.6: Failure envelopes for (a) axial and (b) torsional simulations. Tangent of dilation angle of (c) axial and (d) torsional simulations. Difference of stress ratio and tangent of dilation angle of (e) axial and (f) torsional simulations. Increase in contact number and particle-sleeve overlap for (g) axial and (h) torsional simulations.

For the range of confining pressures studied, the results show an increase in number of contacts and particle-sleeve overlap with increasing pressure, which follow power laws. Therefore, the results are considered to be in accordance with the results from Dove and Frost (1999), which suggests that the interface behavior described by them is also present in interfaces of periodic textured roughness, such as the textured friction sleeves, and provides a plausible explanation for the decrease in the "critical state" coefficient of friction with increasing confining pressure.

Table 5.3: Results of axial and torsional DEM simulations with R_{max} = 1.00 mm.

Confining Pressure, σ_c (kPa)	Shear Direction	τ/σ_{peak}	$\tau/\sigma_{residual}$	$\tan(\Psi)_{peak}$	$\tan(\Psi)_{res}$	$(\tau/\sigma - \tan(\Psi))_{peak}$	$(\tau/\sigma - \tan(\Psi))_{res}$	No. of Contacts at Peak, N_{peak}	No. of Contacts at Residual, N_{res}	Avg. Particle-Sleeve Overlap at Peak, δ_{peak} (mm)	Avg. Particle-Sleeve Overlap at Residual, δ_{res} (mm)
30	Axial	1.34	0.86	0.13	0.11	1.21	0.75	107	96	0.007	0.006
50	Axial	1.01	0.84	0.10	0.11	0.91	0.73	112	102	0.008	0.009
100	Axial	0.94	0.80	0.08	0.06	0.86	0.74	112	108	0.014	0.019
200	Axial	0.81	0.66	0.05	0.02	0.76	0.63	114	113	0.021	0.030
350	Axial	0.61	0.54	0.03	0.01	0.59	0.53	116	116	0.035	0.045
500	Axial	0.53	0.47	0.03	0.01	0.49	0.46	122	122	0.039	0.051
750	Axial	0.43	0.39	0.02	0.01	0.41	0.39	130	134	0.060	0.064
1000	Axial	0.40	0.36	0.02	0.01	0.38	0.35	131	134	0.065	0.078
30	Torsional	1.12	0.69	0.16	0.01	0.95	0.68	100	102	0.007	0.005
50	Torsional	1.03	0.71	0.15	-0.01	0.89	0.72	104	108	0.008	0.007
100	Torsional	0.87	0.62	0.13	0.02	0.74	0.61	107	115	0.015	0.013
200	Torsional	0.66	0.54	0.08	-0.01	0.58	0.55	120	112	0.023	0.023
350	Torsional	0.58	0.48	0.06	0.00	0.53	0.47	131	127	0.032	0.032
500	Torsional	0.60	0.41	0.05	0.00	0.55	0.41	130	122	0.043	0.043
750	Torsional	0.52	0.39	0.04	0.02	0.49	0.37	136	140	0.061	0.056
1000	Torsional	0.48	0.35	0.02	0.00	0.46	0.35	143	150	0.074	0.065

5.3 Discussion and Analysis

5.3.1 Interface Load Transfer Mechanisms

It has been shown by several researchers that the load transfer between soils and solid surfaces can take place in two manners: either from friction between the soil particles and the surface material or from passive resistances generated as the surface's topography forces particles to displace during shearing (Mitchell and Villet, 1987; Irsyam and Hyrciw, 1991). For smooth surfaces, such as conventional smooth CPT sleeves, most of the load is transferred by friction since the surface has no significant asperities that can induce soil deformations. On the other hand, the diamond elements in the textured sleeves represent asperities that range in height from 0.3 to about 3 D_{50} equivalents of

Ottawa 20-30 and Blasting 20-30 sands, and of 1 to about 8 D_{50} equivalents for Ottawa 50-70 sands, which can effectively mobilize passive resistances during shear. As such, it has been shown by DeJong (2001) and Frost and DeJong (2005) that the measured loads during laboratory and field axial testing with textured sleeves consist of friction between the sleeve surface and the soil particles, called the Interface Friction force (IF), and a passive resistance caused by the difference in diameters between the base of the sleeve and the protruding diamond texturing elements, termed the Annular Penetration force (AP). It has also been previously shown during field tests with the multi-sleeve devices that the magnitude of the AP force is directly proportional to the tip resistance reading, q_t, of conventional CPT probes (Hebeler, et al. 2004).

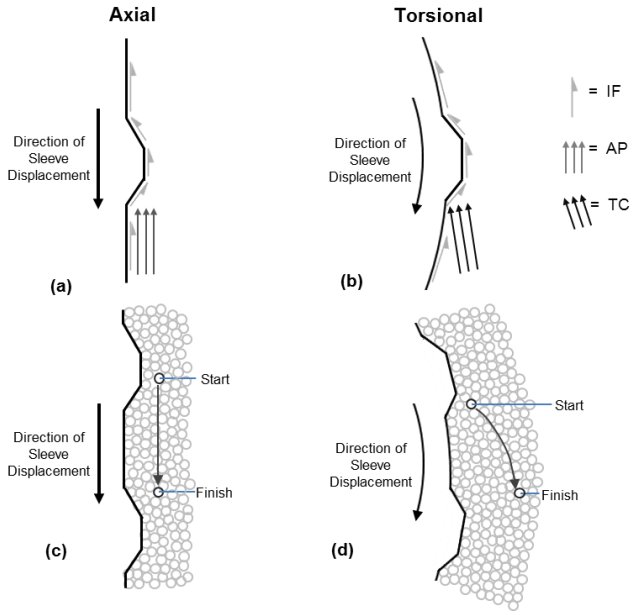

Figure 5.7: Schematic of load transfer mechanisms present in (a) axial and (b) torsional shear. IF = Interface Friction force, AP = Annular Penetration force and TC = Tangential Component force. Schematic of particle displacements induced during (c) axial and (d) torsional shear.

As described in Chapter 4 and in Martinez, et al. (2015), the AP force acts in a direction parallel to the direction of sleeve displacement during axial tests, causing

associated shear soil deformations in the same direction as shown in Figures 5.7a and 5.7c. In a similar manner, it is proposed that the force components in torsional shear are the same IF component observed in the axial configuration and the Tangential Component force (TC). The latter is a passive resistance originated from the transfer of load from the friction sleeve to the soil particles in a direction that is oriented tangentially away from any point in the sleeve surface (Figure 5.7b). The TC force causes particles to displace in this same direction, likely to locations farther away from the friction sleeve (Figure 5.7d). Chapter 4 of this thesis presented a detailed experimental study on the shear zone formation and evolution formed in axial and torsional shear tests that agrees with the shear transfer mechanisms described above.

5.3.2 Isolation of Interface Friction and Passive Resistance

A methodology for isolating the AP force from the IF force has been proposed by Frost and DeJong (2005). This methodology involves a series of tests with partially textured friction sleeves that have the same roughness texture pattern but different degrees of textured versus non-textured areas. For the current study, sleeves consisting of full textured (10 diamond rings), 40% textured (4 diamond rings) and 20% textured (2 diamond rings) were used, as shown in Figure 5.8a. In this manner, the magnitude of the AP force can be determined by plotting the measured load on the diamond texture elements versus the number of diamond rings (Figure 5.9c and Table 5.1). The load on the diamond elements is calculated as the difference between the measured sleeve stress and the contribution from the untextured area. The results show a linear trend with the number of diamond rings on the sleeves based on the linear relationship between stress and contact area. Therefore, the magnitude of the AP force is equal to the intersect of the trend line with the y-axis. Consequently, if no AP force is present then the value of the intersect should be zero (measured stress – smooth sleeve contribution = IF – IF = 0). An analogous approach is proposed in order to estimate the magnitude of the TC force from

torsional tests, which consists of a series of tests with partially textured sleeves consisting of textured diamond columns instead of diamond rows, as shown in Figure 5.8b. This study involved full textured (22 diamond columns), 55% textured (12 diamond columns) and 18% textured (4 diamond columns), and the results are presented in Figure 5.9d and Table 5.1.

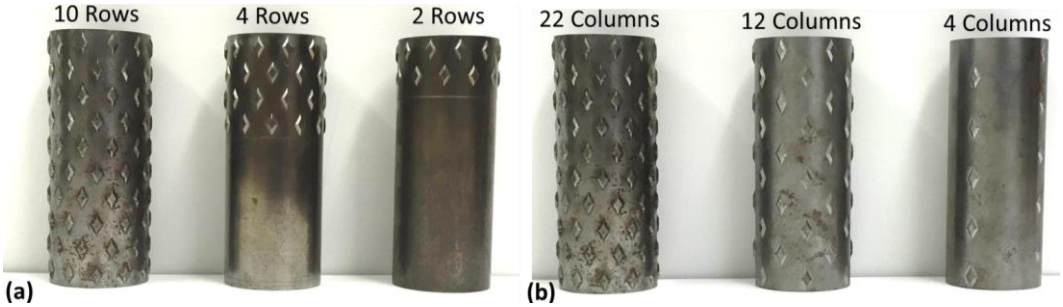

Figure 5.8: Partially textured sleeves (R_{max} = 1.00 mm) used for (a) axial and (b) torsional shear tests.

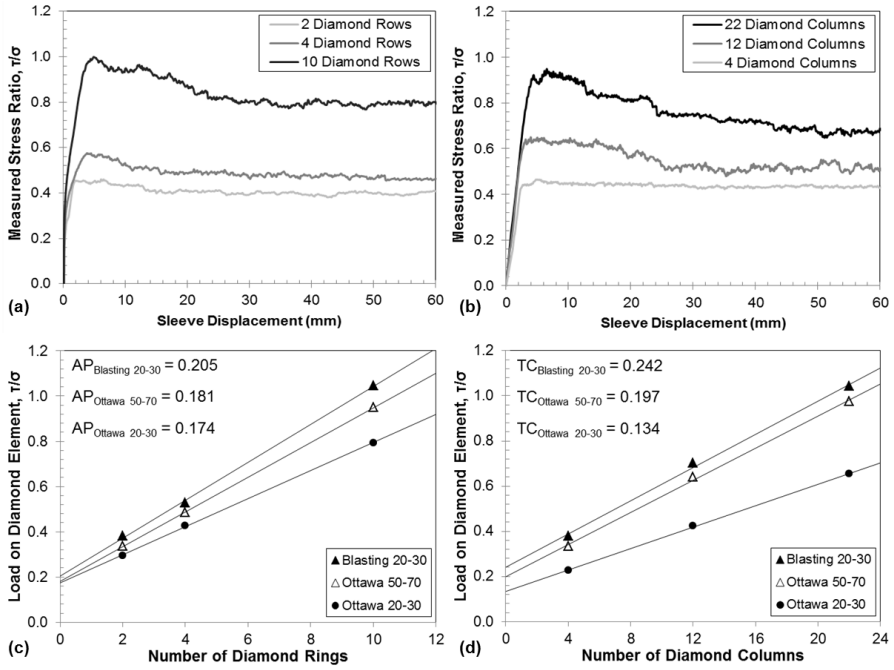

Figure 5.9: (a) Axial and (b) torsional tests on Ottawa 20-30 sand with partially textured sleeves. Residual stress ratios on diamond elements for (a) axial and (b) torsional tests with partially textured sleeves of R_{max} = 1.00 mm on Ottawa 20-30, Ottawa 50-70 and Blasting 20-30 sands.

The results of this test series performed with friction sleeves of R_{max} of 1.00 mm yielded AP stress ratios of 0.174 for tests on Ottawa 20-30 sand, of 0.181 for tests on Ottawa 50-70 sand of 0.205 for tests on Blasting 20-30 sand, showing an increase of 0.031 between tests on rounded (Ottawa 20-30) and angular (Blasting 20-30) sands. The corresponding stress ratios of the TC component were of 0.134 for tests on Ottawa 20-30 sand, of 0.197 for tests on Ottawa 50-70 sand and of 0.242 for tests on Blasting 20-30 sand, showing a much larger increase than axial tests, of 0.108. These results also agree with the fact that the shear behavior of torsional shear is more sensitive to particle angularity, as shown in Figures 5.2d, 5.5a and 5.5b.

Following this methodology to determine the magnitudes of the AP and TC forces acting on the sleeves of different roughnesses (R_{max} of 0.01, 0.25, 0.50 and 2.00 mm) and subtracting their contribution from the measured stress ratios presented in Figures 5.2a, 5.2b and 5.2c yielded "isolated" IF force values for axial and torsional tests. These IF force values are then used to compute interface friction angles, as shown in Figures 5.10a through 5.10d and Table 5.1. It can be observed that the isolated IF results follow a bi-linear relationship with surface roughness that is independent of the shearing direction. For comparison, soil friction angles from direct shear tests on these same sands are included in the figures (dashed lines). The results show that at high surface roughness values the interface friction angles, both residual and peak, are fairly similar to the soil friction angles. These results, which correspond only to the magnitude of the IF force, agree with the current understanding of interface shear behavior and show bi-linear relationships with surface roughness (e.g. Uesugi and Kishida, 1986).

This study has shown that shearing in the torsional direction results in larger soil engagement and dilation, which is manifested as the larger influence of particle shape on measured stress ratios, as well as previously shown by in Chapter 4 and in Martinez, et al. (2015) based on larger induced shear zones and influence zones. It can be further concluded that the differences observed in the global behavior of axial and torsional tests

are related to their corresponding passive resistance components, the AP and the TC, while the IF components are identical in magnitude and impact the shear behavior in the same manner in both tests, as shown in Figures 5.10a through 5.10f.

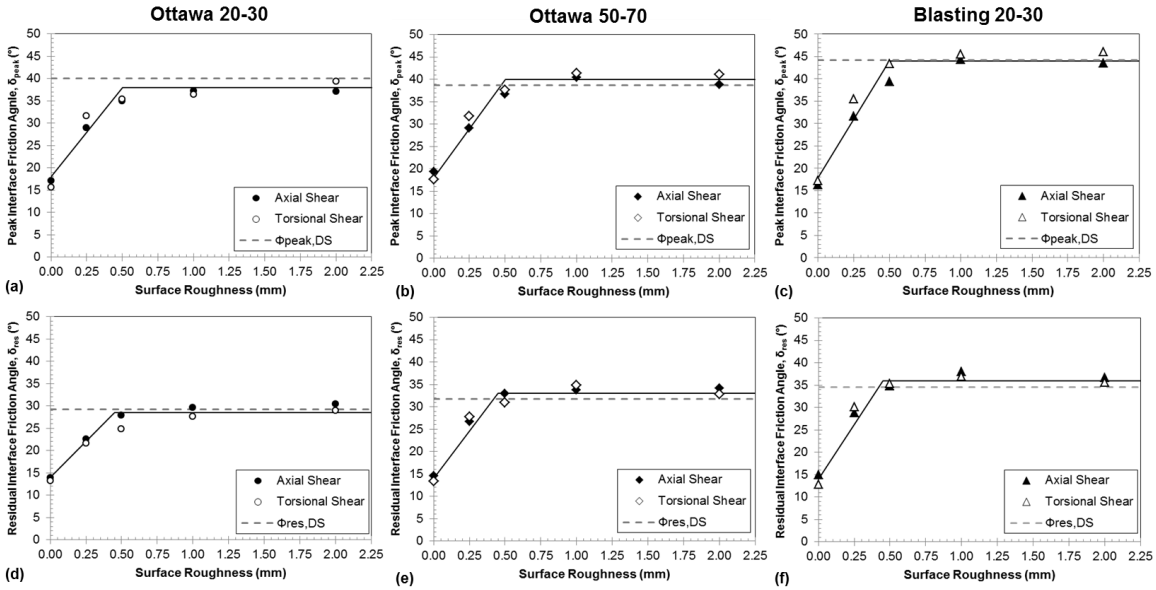

Figure 5.10: Isolated interface friction angle – surface roughness relationships for axial and torsional tests. Peak interface friction angles for (a) Ottawa 20-30, (b) Ottawa 50-70 and (c) Blasting 20-30 sands. Residual interface friction angles for (d) Ottawa 20-30, (e) Ottawa 50-70 and (f) Blasting 20-30 sands.

This observation was further tested by performing a series of axial and torsional shear laboratory tests against smooth surfaces covered by sandpaper (Figures 3.4a through 3.4c) with the purpose of testing surfaces prone to clogging that only mobilize IF resistances but no passive resistance components, as described in Chapter 2 and shown in Figures 2.12 a through 2.12c. During shear, particles get trapped in between the asperities of the sandpaper surfaces, resulting in clogged surfaces that effectively behave like sand-sand interfaces. Figure 5.11a shows a comparison of the stress ratios mobilized during axial and torsional tests with textured sleeves. The results show a wide range of variation that follows specific trends. For instance, the upper dashed line indicates the trendline for residual stress ratios from tests with Ottawa 20-30 sand, while the lower dashed line

represents the trend for the peak stress rations from tests with Blasting 20-30 sand. These different trends are defined by the relative difference in magnitudes of the passive resistance forces mobilized during axial and torsional tests. Figure 5.11b shows a similar plot for the tests performed with the clogging-prone sandpaper sleeves (refer to Chapter 7 for a study on the clogging behavior of sandpaper sleeves). The results show to follow the 1:1 line more closely. The specific trends for residual loads with Ottawa 20-30 and peak loads with Blasting 20-30 sands also follow the 1:1 line closely, showing that the stress ratios mobilized by these surfaces are controlled by the sand internal friction and roughness magnitude of the counterface, but they are independent on shear direction (i.e. axial versus torsional shear) because no passive resistances are mobilized.

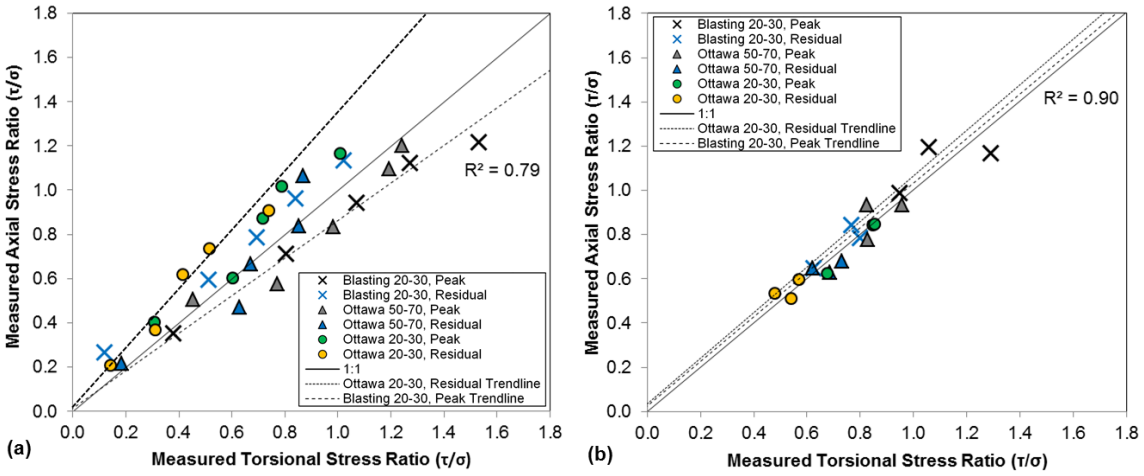

Figure 5.11: Measured axial versus torsional stress ratios for laboratory tests against (a) textured friction sleeves and (b) sandpaper sleeves.

5.3.3 Implications on Geotechnical Engineering Applications

These results presented in this chapter have important practical implications for geotechnical systems. For instance, systems that involve highly angular particles, such as pavement subgrades, structures in contact with highly angular soils such as aeolian sands or extraterrestrial soils, will be more efficient if they are designed to transfer loads to the soil torsionally, instead of axially. Additionally, a more robust site characterization can

be obtained if different controlled loading conditions are applied to the soil, such as axial and torsional shear in CPT soundings with the MPFTA attachment. The ability to induce shearing in vertical (i.e. axial) and horizontal (i.e. torsional) directions provides the ability to better reproduce natural and man-induced loading conditions. For instance, axial shear is analogous to the skin friction of deep foundations. However, torsional shear might better induce soil loading conditions that reproduce earthquake ground motions, laterally loaded piles or active or passive conditions present in earth retaining structures. Finally, it has been shown that torsional shear is more effective at inducing critical state conditions within the contacting soil. Thus, this shear mode shows advantages for characterizing interface shear behavior at large soil strains as compared to the axial shear induced by conventional tests such as the CPT friction sleeve measurement. Chapter 8 further investigates the interface strength capacity of surfaces with "structured roughness" (i.e. textured friction sleeves) as compared to clogging-prone surfaces with "random roughness" (i.e. sandpaper).

5.4 Conclusions

The results presented in this study allowed for quantifying the effects of surface roughness, confining pressure, particle shape and particle roughness on the shear behavior of axial and torsional shear tests. Also, this study showed that these tests impose loading conditions that result in different global shear behaviors. In particular, the following conclusions can be drawn from the results presented herein:

- The mobilized loads in laboratory tests and DEM simulations increased with increasing maximum surface roughness (R_{max}) and particle angularity. The magnitude of strain softening and shear displacement needed to mobilize peak loads increased as surface roughness increased up to a critical R_{max} value of about 0.50 mm, while further increases in surface roughness resulted in negligible changes to these quantities. These results suggest a similar bi-linear behavior as

the relationship between surface roughness and interface strength. Results from tests against smooth sleeves did not reflect the soil properties as they were unaffected by shearing direction and grain angularity. These results suggest that particle-sleeve sliding was the main failure mechanism.

- Specimen volume changes from DEM simulations revealed that torsional shear is a more dilative process that mobilizes larger maximum dilation angles across all surface roughnesses tested. These results agree with results from laboratory and DEM tests that showed larger strain softening during torsional shear. Furthermore, torsional shear tests were shown to effectively induce a critical state at sleeve displacements larger than about 10 mm because it continuously engages the same particles, while specimens subjected to axial shear kept dilating throughout the entire shear process.
- The magnitude of the peak and residual stress ratios from torsional laboratory tests was shown to be more sensitive to changes in particle angularity as compared to those from axial tests, with increases in loads that were 50% to 300% larger. Tests on glass beads complemented this study and allowed studying the relationship between measured stress ratio and particle shape. These results suggest that torsional shear induces a larger degree of particle rotations which are restricted when particle rotation resistance mechanisms are introduced (i.e. particle angularity), resulting in larger soil engagement and higher loads being mobilized. Chapter 6 further addresses this topic by means of particle-scale observations.
- Residual axial stress ratio values from DEM simulations were shown to be more sensitive to changes in particle coefficient of friction than those from torsional tests. Particle coefficient of friction, or particle roughness, determines the amount of energy required for contact slippage to take place. Therefore, these results suggest that a relatively larger amount of contact slippage takes place during axial

shearing at the residual stage than during torsional shear. This effect is further studied in Chapter 6.

- The different peak and residual failure envelopes for axial and torsional tests further validated the non-uniqueness of soil shear strength which is impacted by the different loading conditions applied to it. Increases in confining pressure resulted in decreases of measured stress ratio and dilation. The results show that the stress ratio contribution from shearing at a constant volume also decreases with increasing normal stress. Analysis from DEM simulations showed that the number and area of contacts between particles and the friction sleeves increases as global normal stress increases. The result is a boundary-measured shear stress that increases at a lower rate than the boundary-applied normal stress and yields decreasing friction coefficients with increasing normal stress.
- Interface friction and passive resistance components of the mobilized loads were quantified for both axial and torsional shear tests. Methods for isolating these resistance components were presented, and the magnitude of the Interface Friction force was shown to be independent of the shearing direction and to follow a bi-linear relationship with surface roughness. The passive resistance components, the Annular Penetration force for axial tests and the Tangential Component force in torsional tests, were shown to be responsible for the differences observed in the global shear behaviors and associated shear deformations.

The deployment of a site characterization device that measures the soil response to both axial and torsional shearing, such as the MPFTA, offers the benefit of studying the behavior of soils under different loading conditions. These studies provide more detailed information regarding soil properties, such as relative differences in particle angularity and roughness. Furthermore, the ability to separate friction and passive resistance components from measured loads provides a fundamentally-based framework interpretation for the direct in-situ measurement of soil properties.

CHAPTER 6

PARTICLE-SCALE EFFECTS ON GLOBAL AXIAL AND TORSIONAL INTERFACE SHEAR BEHAVIOR

6.1 Introduction

This chapter presents a Discrete Element Modeling (DEM) study, along with comparisons from experimental data, of interface behavior under axial and torsional drained loading conditions. Detailed studies allow for links between micro-scale particle behavior and observed global response, and for the latter to be evaluated in light of particle-particle and particle-surface interactions. Throughout this chapter it is shown that axial and torsional shear are inherently different processes, as shown by the different failure envelopes, stress paths, shear-induced volume changes and loading conditions. Furthermore, it is shown that different particle-level mechanisms, such as particle rotations and contact slippage, play different roles in axial and torsional shear. Coordination number, polar histograms, particle displacement fields, particle rotations fields and local void ratio fields provide further insights into the fabric evolution, loading conditions and failure modes present in these two shear modes. This study expands the current understanding of interface behavior and opens the door to consider potential improvements to geotechnical systems leveraging the characteristics of different imposed loading conditions.

In geotechnical engineering it is recognized that the shear behavior of interfaces is a key component of numerous geotechnical systems because they are present across a wide range of scales. Interfaces can be natural, such as within and between different stratigraphic layers, or can be man-made, such as the interface between soil and a driven pile or between the different layers that compose the liner of a landfill. While man-made

interfaces can be engineered to optimize their performance, little work has been done to investigate interface systems that function under different loading conditions. Investigations like these performed in soils have led to the understanding that the same soil mass can mobilize a different strength under different conditions (e.g. axial compression versus axial extension). The usefulness of investigating interface behavior under different loading conditions is not limited to improving the understanding of current geotechnical systems, but also develops a framework to develop improvements to systems that have undergone little change during the last half century.

The 2D DEM numerical simulations presented in this chapter were performed using the Particle Flow Code (PFC2D) from Itasca, Inc. As described in detail in Chapter 3, the DEM models were built to simulate as close as possible the axisymmetric device for drained axial and torsional interface shear tests previously described and shown in Figures 3.5a and 3.5b. All specimens were sheared against textured friction sleeves, such as those shown in Figure 3.19. The models are shown again in Figures 6.1a and 6.1b for axial and torsional shear, respectively. The sampling windows labeled 1 and 2 in the figures were used to take different particle-level measurements during the simulations.

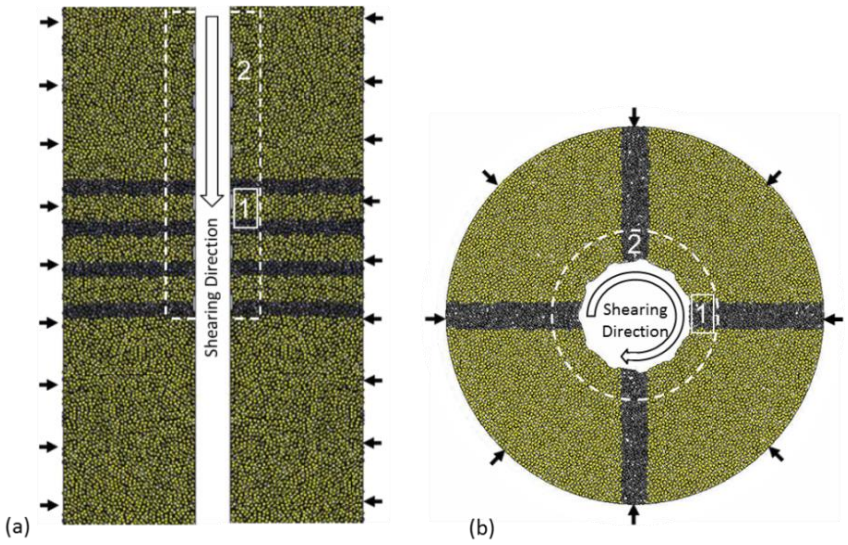

Figure 6.1: Configuration of DEM simulation models for (a) axial and (b) torsional shear. Sampling windows labeled 1 and 2 are used for different particle-level observations.

The virtual chambers used for the axial and torsional shear simulations applied constant stress boundary conditions on the specimens within them. The linear elastic contact model was utilized for all simulations since it has been shown to be appropriate for the study of the large-strain behavior of granular materials in 2D (Latzel, et al. 2000). All the specimens consisted of about 8500 two-particle clumps with an aspect ratio of 1.5 and a mean particle diameter of 0.9 mm A detailed description of the parametric calibration study performed in order to select the simulation parameters can be found in Chapter 3. A summary of the simulation parameters used for all the simulations, unless specified otherwise, can be found in Table 6.1.

Table 6.1: DEM simulation parameters.

Mean Particle-Clump Size, D_{50} (mm)	Particle Clump Aspect Ratio, AR	Particle Density (kg/m^3)	Interparticle Friction Coefficient, $\mu_{p\text{-}p}$	Particle Normal Stiffness, k_n (N/m)	Particle Shear Stiffness, k_s (N/m)	Sleeve Friction Coefficient, μ_s	Wall Friction Coefficient, μ_w	Wall Normal Stiffness, $k_{n\text{-}w}$ (N/m)	Wall Shear Stiffness, $k_{s\text{-}w}$ (N/m)
0.90	1.50	2650	0.45	$1x10^7$	$1x10^7$	0.25	0.20	$1x10^8$	$1x10^8$

6.2 Simulation Results

A series of axial and torsional interface shear simulations involving friction sleeves of varying roughness and particle assemblies of different initial density, interparticle friction coefficient, and different confining stresses were performed using DEM simulations, while tests with varying particle angularity were performed experimentally as part of this study. Different measurements were made at micro- and marco-scales, which allowed for the study of the shear behavior in great detail.

6.2.1 Shear Stress-Displacement Response

Stress-displacement curves in terms of stress ratio were generated for all simulations by measuring the force required to displace the friction sleeves axially or torsionally and normalizing it by the sleeve's length and the applied confining pressure. Additionally, the specimen volumetric strains were calculated from the measured

displacements of the walls that apply the constant stress boundary conditions. Further details on the global response measurement methodology can be found in Chapter 3.

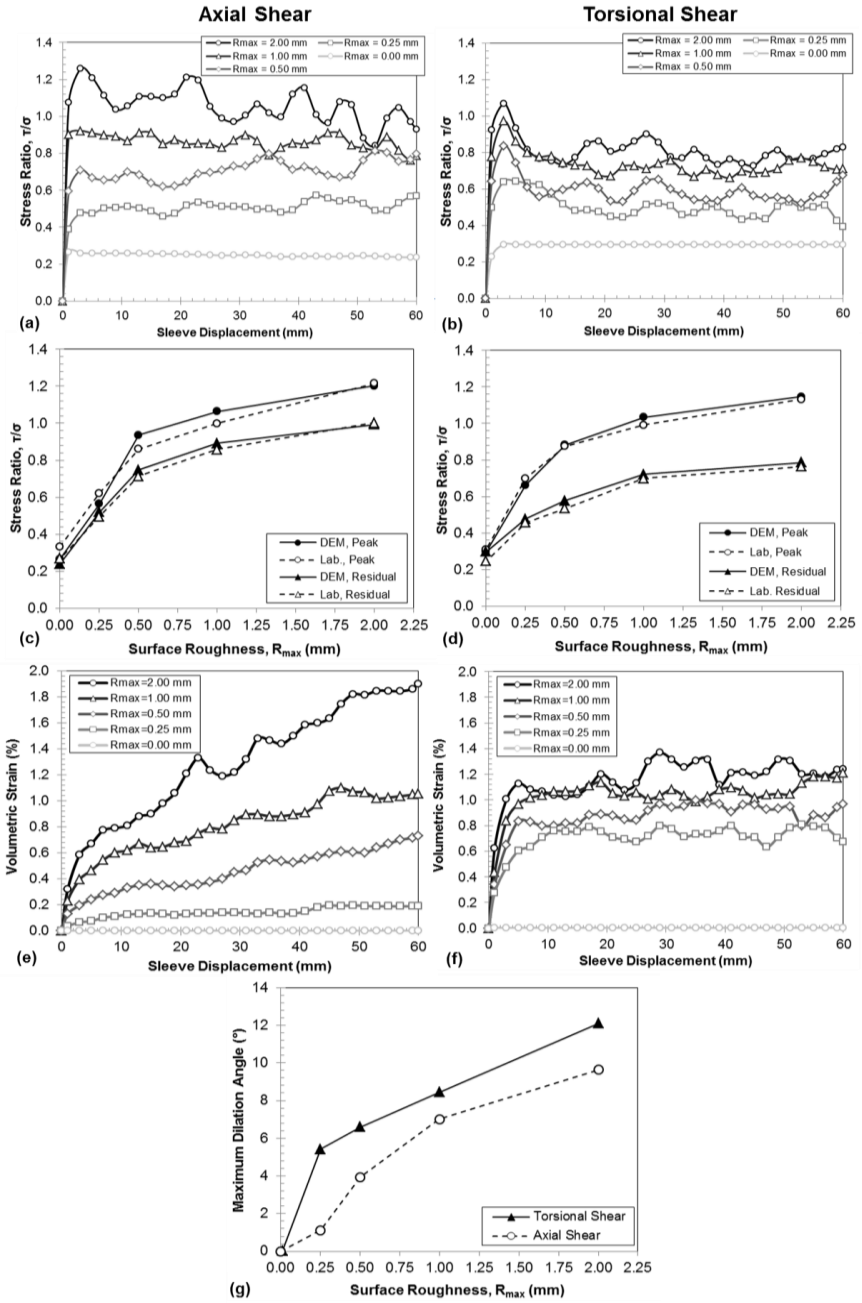

Figure 6.2: Stress ratio-displacement curves for (a) axial and (b) torsional simulations, peak and residual stress ratios for (c) axial and (d) torsional simulations and experiments, volumetric strain-displacement curves for (e) axial and (f) torsional simulations, and (g) maximum dilation angles (note: confining pressure = 50 kPa).

The effect of varying surface roughness of the friction sleeves on the mobilized loads during axial and torsional shear simulations agrees with the current understanding of interface behavior. As the sleeve surface roughness was increased, larger loads were mobilized as shown in Figures 6.2a and 6.2b for axial and torsional simulations, respectively, performed under a confining pressure of 50 kPa. In general terms, the axial simulations mobilized larger loads but showed smaller strain softening compared to the torsional simulations. Figures 6.2c and 6.2d show peak and residual stress ratios as a function of surface roughness for axial and torsional shear simulations, respectively, and indicate a close match between the numerical and experimental results.

The axial and torsional specimen volumetric strains during shear are shown in Figures 6.2e and 6.2f, respectively. All simulations showed a dilative behavior, with the exception of those performed against friction sleeves of R_{max} = 0.00 mm which did not undergo any measurable volume changes. This behavior was expected since the samples were prepared dense. Also, it has been previously shown that shearing against smooth surfaces induces minimal soil shearing and the principal failure mechanism is sliding between the surface and the particles in both shearing orientations (Martinez and Frost, 2014a). The specimen volumetric strains increased sharply at small sleeve displacements, reaching maximum dilation rates at displacements similar to those for peak mobilized stress ratios. The axial specimens continued dilating throughout the entire simulation, thus not reaching a state of shearing under constant volume, or critical state. On the other hand, the torsional curves reached a true "critical-state" at displacements larger than about 10 mm. The reason is that during axial shear "undisturbed" material is encountered at the leading edge of the friction sleeves at every displacement increment, in comparison to the soil in the sleeve's vicinity that is continuously sheared during torsional simulations. Maximum dilation angles show that samples subjected to torsional shear are more dilative, as shown in Figure 6.2g. These results are consistent with torsional simulations and experiments showing larger magnitudes of strain softening.

6.2.2 Stress Paths

The stress paths followed by axial and torsional shear simulations show important differences in loading conditions. The stress paths were obtained from measurement windows adjacent to the friction sleeves, covering the narrow zone of intense shear-induced particle displacements (indicated as window 2 in Figures 6.1a and 6.1b), while the void ratio values reported were obtained taking an average of the whole specimen. Figures 6.3a through 6.3d show the stress paths, in p-e (mean stress versus void ratio) and p-q (mean stress versus maximum shear stress) spaces, followed by axial and torsional specimens confined under different stresses. These results allow defining "pseudo-critical state" (for axial shear) and "critical state" (for torsional shear) lines, as well as the corresponding failure envelopes.

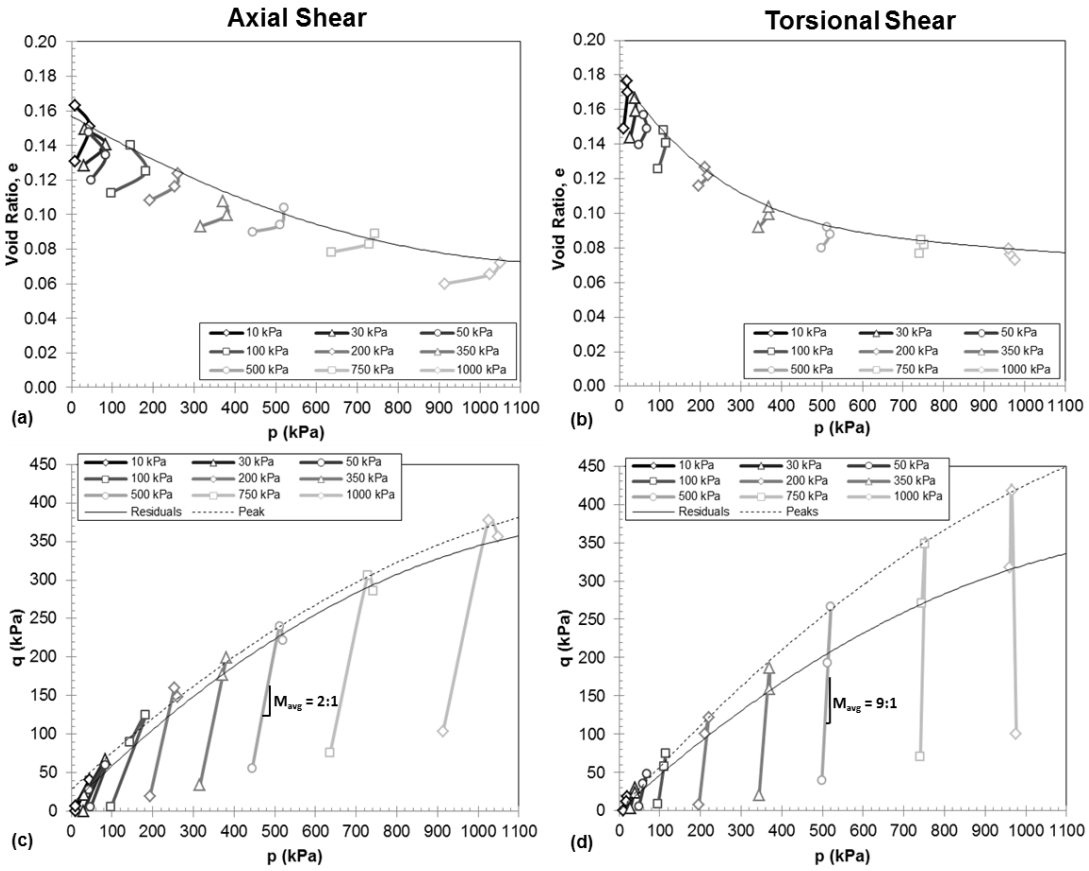

Figure 6.3: Void ratio evolution of (a) axial and (b) torsional shear tests. Stress paths for (c) axial and (d) torsional shear tests. (Note: R_{max} = 1.00 mm).

The stress paths in axial simulations followed an average slope of 2:1 (Figure 6.3c), while those for torsional simulations followed a slope of about 9:1 (Figure 6.3d). Additionally, the stress paths from torsional shear reached a higher peak shear stress, shown by the dashed line, and a lower residual value, shown by the solid line. This agrees with the earlier observations indicating larger strain softening magnitudes observed during torsional shear. The failure envelopes curve concavely because dilation decreases as the confining pressure increases. The differences in stress paths and failure envelopes verify that axial and torsional shear modes induce different loading condition on the contacting soil mass. However, it should be noted that the axial and torsional simulations were consolidated under different 2D conditions (lateral consolidation for axial shear vs. radial for torsional shear) and sheared in chambers of different geometry. It is considered that any possible effects of this would have little effect on the particle-level response.

6.3 Micromechanical Processes

6.3.1 Particle Trajectories

The processes taking place during axial and torsional shear previously proposed in Chapters 4 and 5 are presented again in Figures 6.4a and 6.4b. During axial shear, the loads transferred from the friction sleeve to the soil mass results in particles being displaced in a direction parallel, in average, to the direction of sleeve displacement. On the other hand, during torsional shear the particles displace along trajectories of larger radii than the sleeve's surface. This results in particles migrating to locations further away from the sleeve. These mechanisms were further investigated by monitoring particle centroid positions during DEM simulations. The results presented in Figures 6.4c and 6.4d (note: plots have different scales), where the gray lines represent individual particle trajectories obtained from sampling windows 1 (Figures 6.1a and 6.1b), verify the proposed micro-mechanisms (R_{max} = 1.00 mm, confining pressure = 50 kPa). The

particles show to displace mainly in a downward direction during axial shear. During torsional shear, the particles displace to positions that are farther away from the sleeve's surface. These results show different interface interactions and are considered to be the root mechanisms contributing to the different observed global behaviors, including the larger dilation during torsional shear, different failure envelopes and different stress paths (Figures 6.2g and , 6.3a through 6.3d).

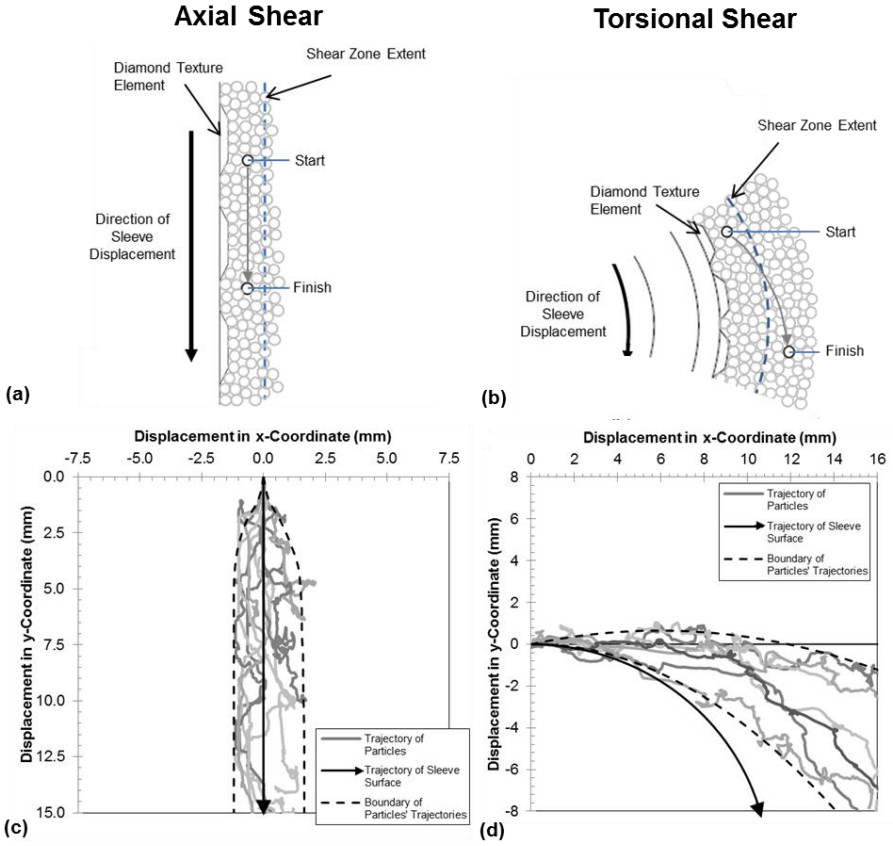

Figure 6.4: Proposed micro-mechanisms taking place during (a) axial and (b) torsional shear. Particle trajectories from DEM simulations during (c) axial and (d) torsional simulations against surfaces of R_{max} = 1.00 mm (Note that (c) and (d) are plotted using different scales).

6.3.2 Particle Displacement, Rotation and Void Ratio Fields

Figures 6.5a and 6.5b show contour maps of particle displacement and rotation fields for axial (right side of shear box only) and torsional simulations (R_{max} = 1.00 mm,

confining pressure = 50 kPa), respectively, at the peak, transition and residual stages. The magnitudes represented by colors are in a log-scale, as shown on the color bars in the left side of the figures. This was done in order to enhance the visual resolution of the maps. The rightmost images present the same results for the residual case in linear scale for reference only.

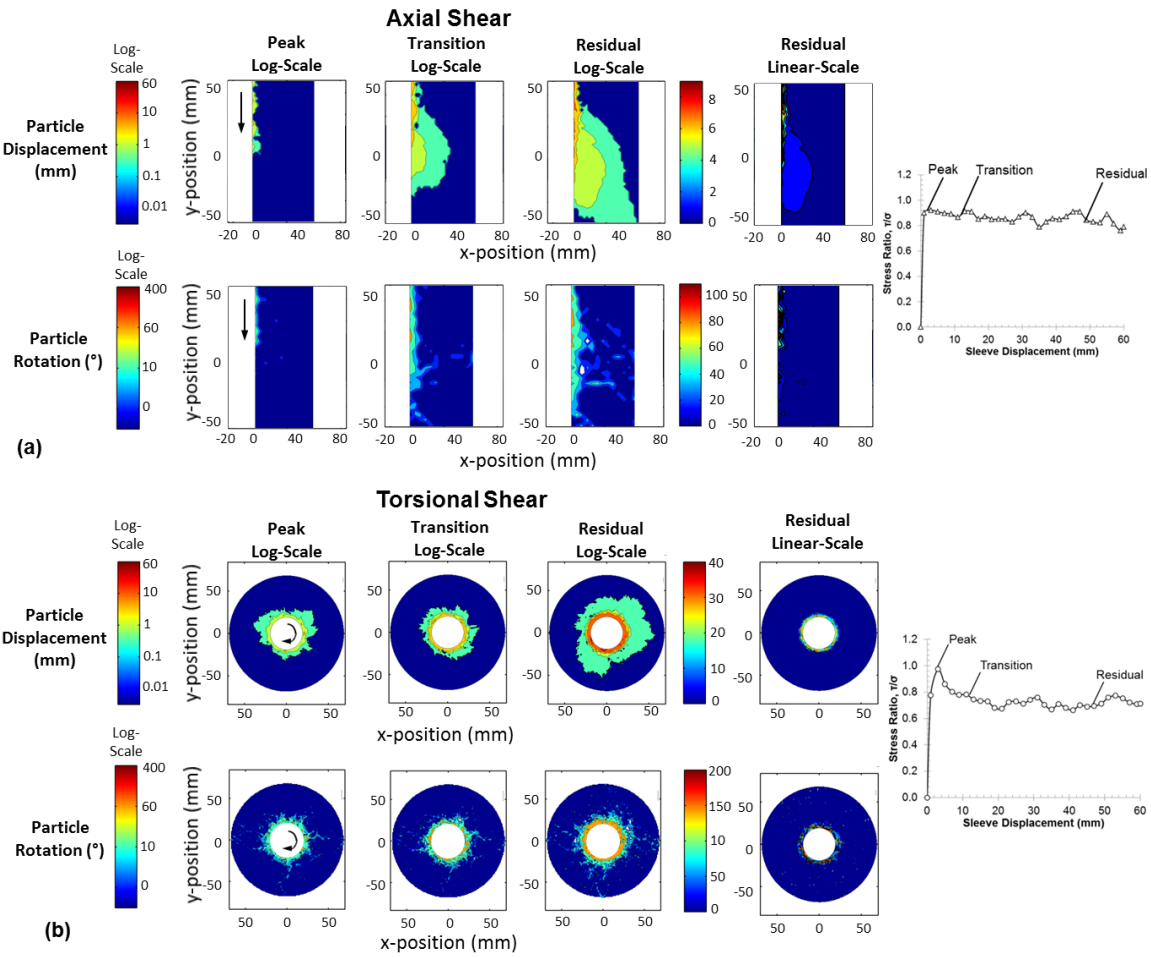

Figure 6.5: Particle displacement and particle rotation at different stages of (a) axial and (b) torsional simulations (R_{max} = 1.00 mm, confining pressure = 50 kPa).

The particle displacement fields for axial simulations show an increasing zone of influenced particles, which migrates down vertically as the sleeve is displaced. This vertical growth of the shear zone is related to axial shear not reaching critical state. The extent of the shear-induced displacement also extends laterally, showing particle

displacements in the order of 1 mm at distances up to 32 mm from the sleeve, and displacements of about 0.1 mm at distances up to 50 mm at the residual stage. The particle displacement field for torsional simulations is also shown to grow radially, but the displacements larger than 1 mm are contained in a narrow zone of about 5 – 8 mm, and displacements in the order of 0.1 mm extend to distances of only 35 mm from the friction sleeve. Torsional shear is shown to induce larger particle displacement at locations close to the friction sleeves than axial shear, a fact that agrees with results presented in the shear zone characteristics study in Chapter 4 (Figures 4.3c, 4.4c and 4.4d).

The particle rotation fields show similar trends, indicating a larger magnitude of particle influence during torsional shear and growing areas of influence as the shearing continues in both shear orientations albeit with more scatter observed in the torsional results. The extent of these areas is smaller than the extent of particle displacements. The size of the zones with large particle rotations correlates well with those with particle displacements larger than about 1.5 mm, while only a limited amount of particle rotations can be found in zones where the particle displacements are smaller than 1 mm. These results are in general agreement with 2D DEM simulations by (Masson and Martinez, 2001) that showed that zones of intense particle rotations in soils correlate well with zones of intense strain localizations.

The void ratio fields, presented in Figures 6.6a and 6.6b, illustrate the local shear-induced volume changes. These results are presented for the initial, peak and residual stages. The results show a large spatial variability in local void ratio values at all shear stages. The average initial void ratio for both specimens is 0.17. At the peak stage, axial shear has induced some void ratio increase, but the torsional results show a better-defined dilation zone adjacent to the friction sleeve. At the residual stage both axial and torsional modes show a significant amount of dilation, with increases of up to 0.20 yielding void ratio values of 0.37. These zones of dilation are smaller than the zones of particle

displacements. This is expected since small displacements might remain in the small strain regime and thus not induce dilation. The rightmost images in Figure 6.6 show magnified views of the void ratio fields at the residual stage. The upwards arrows in the figure for torsional shear indicate low void ratio zones. Comparing this contour map with the initial conditions confirms that these zones were not present initially, thus they are induced by the torsional shearing process. These zones are not evident in the corresponding axial shear simulation, further highlighting the differences between the soil deformations induced by the axial and torsional shear modes. These results agree with those presented in Chapter 4 and in Martinez, et al. (2015) for the secondary zones of compressive volume changes developed during torsional shear (Figures 4.6c, 4.6d and 4.7b). The following section further investigates the characteristics of these dilation and compression zones under different conditions.

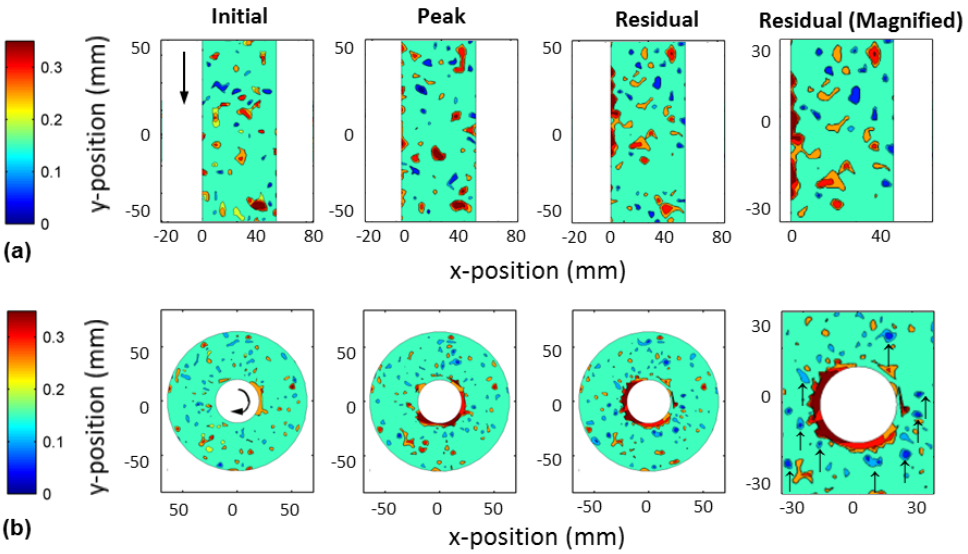

Figure 6.6: Void ratio evolution during (a) axial and (b) torsional simulations.

6.3.3 Shear-Induced Changes in Volume

The experimental studies presented in Chapter 4 showed important differences in the disturbed zones of axial and torsional interface shear tests. While dilation was observed within the shear zones for both shearing orientations, significant contraction

was observed in zones up to distances of 20 mm (about 30 D_{50} equivalents) away from the friction sleeve in torsional tests, which can be explained by the micro-mechanical processes presented in Figure 6.4. DEM simulations allowed for study of the effect of sleeve surface roughness, initial assembly density and confining pressure on the extent of these dilation and contraction zones. Figures 6.7a through 6.7f show the shear-induced changes in local void ratio ($\Delta e = e_{measured} - e_{initial}$) as a function of distance away from the sleeve obtained from measurement circles uniformly distributed throughout the specimens (Figure 3.14). The extent of the dilation, contraction and total zones of influence are presented on the right side of the corresponding figures. The dashed horizontal line represents the "as compacted" void ratio, indicating a Δe value of zero.

Figure 6.7a presents the results for axial simulations against friction sleeves of varying roughness. Both the magnitude and extent of the dilation zone increases with increasing surface roughness, and small compression zones develop in simulations against rougher friction sleeves. The torsional simulations (Figure 6.7b) also show increasing dilation magnitude and extent with increasing roughness. However, the contraction zones extend much farther, reaching a maximum distance of 20 mm, compared to a maximum of 7 mm for axial shear. These contractive zones developed during torsional shear were also observed in Figure 6.6b (and indicated using upwards arrows). The simulations against sleeves of R_{max} of 0.00 mm only show a very small void ratio increase of the order of 0.01. Figures 6.7c and 6.7d show that as the initial assembly void ratio increases, the size of the dilation zone decreases but the size of the contraction zone and total zones increases for both axial and torsional modes, respectively. This effect can be observed more explicitly with the torsional shear results. These results are conceptually robust since looser soil masses tend to have a more contractive behavior. Figures 6.7e and 6.7f show that as the confining pressure increases, the sizes of all zones decrease. It can be observed that for low confining pressures (i.e. 25 kPa) the contractive zone is not located immediately outside the dilation zone. It is located between 14 and 24

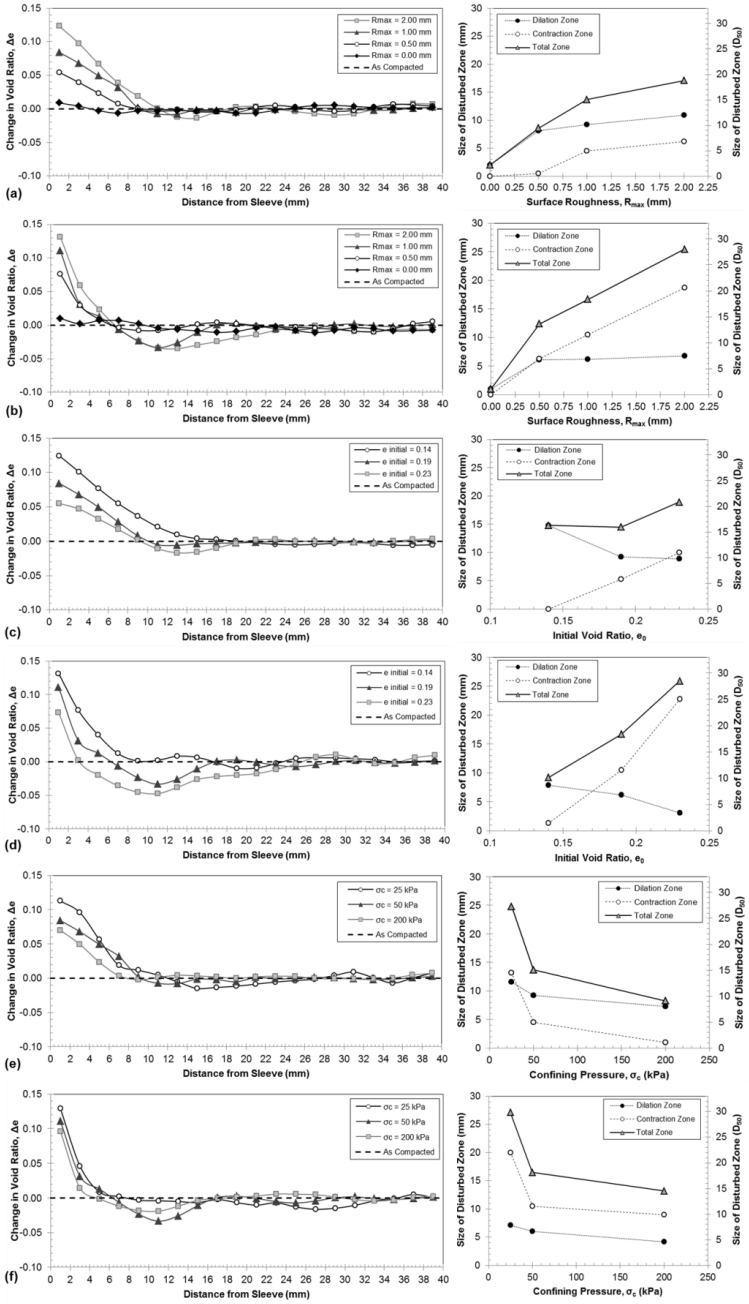

Figure 6.7: Effect of surface roughness on (a) axial and (b) torsional simulations ($e_{initial}$ = 0.19, σ_c = 50 kPa). Effect of initial void ratio on (c) axial and (d) torsional simulations (R_{max} = 1.00 mm, σ_c = 50 kPa). Effect of confining pressure on (a) axial and (b) torsional simulations (R_{max} = 1.00 mm, $e_{initial}$ = 0.19).

mm for axial and between 24 and 36 mm for torsional simulations. Throughout these simulations, the magnitude and extent of the compression volume changes were shown to

be significantly larger for torsional simulations, and the magnitude of dilation was also slightly larger. However, the size of the dilation zones was larger for axial simulations.

6.3.4 Shear Zone Characteristics

A study of the particle displacements induced by axial and torsional shear can facilitate a better understanding of the particle-scale interface interactions in both shearing modes. The positions of particle centroids (particles shown as columns of darker color in Figures 6.1a and 6.1b) were monitored during simulations. This allowed for identification of zones of intense particle displacement, referred as "shear zones". These results are considered as directly comparable to those presented in the shear zone characterization tests shown in Chapter 4 (Figures 4.3a, 4.3b and 4.4a through 4.4d). Figures 6.8a through 6.8h present comparisons of observed shear zones for numerical and experimental axial and torsional tests sheared against smooth and textured friction sleeves. The simulations in this study (confining pressure = 50 kPa) yielded results such as those presented in Figures 6.9a and 6.9b. The shear zone length is defined as the maximum magnitude of particle displacement within the shear zone, and the shear zone thickness is defined as the distance from the interface at which measurable particle displacements (> $0.5*D_{50}$) are located.

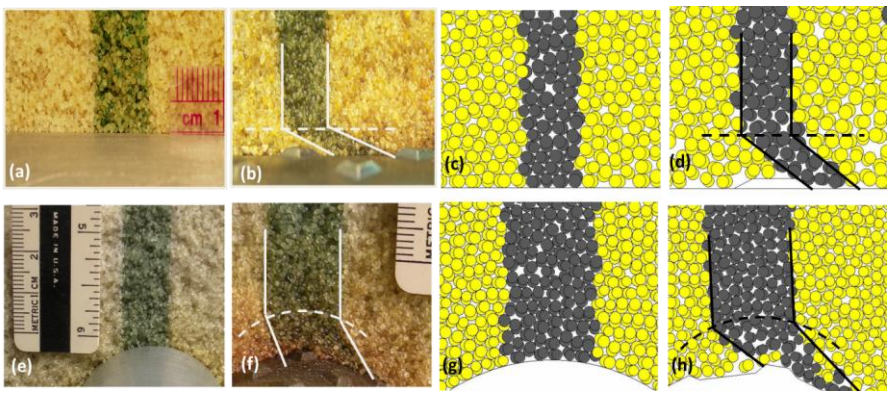

Figure 6.8: Shear zones from experimental and numerical studies formed during: axial shear against (a) and (c) smooth and (b) and (d) textured surfaces; torsional shear against (e) and (g) smooth and (f) and (h) textured surfaces.

The progressive growth of the shear zones was investigated by monitoring the particle centroid positions as a function of sleeve displacement. Figures 6.10a and 6.10b present the results for axial and torsional simulations and experimental results, all performed against friction sleeves of R_{max} = 1.00 mm. It is shown that the shear zone thickness progression in axial and torsional shear modes is similar, with sharp increases at small displacements and more stable values reached at large displacements. The shear zone length results are shown to have a linear relationship with sleeve displacement. The simulations yielded larger shear zone lengths than those from experimental tests. This difference is attributed to the 2D geometry in the simulations because particles are more likely to get trapped at the leading edge of a diamond, as opposed to the 3D scenario in the experimental data where the untextured zone between any two diamond elements prevents roughness clogging, as can be observed in Figure 3.3 and 3.19. Nonetheless, the numerical and experimental results predict a similar trend with larger shear zones developed during torsional shear.

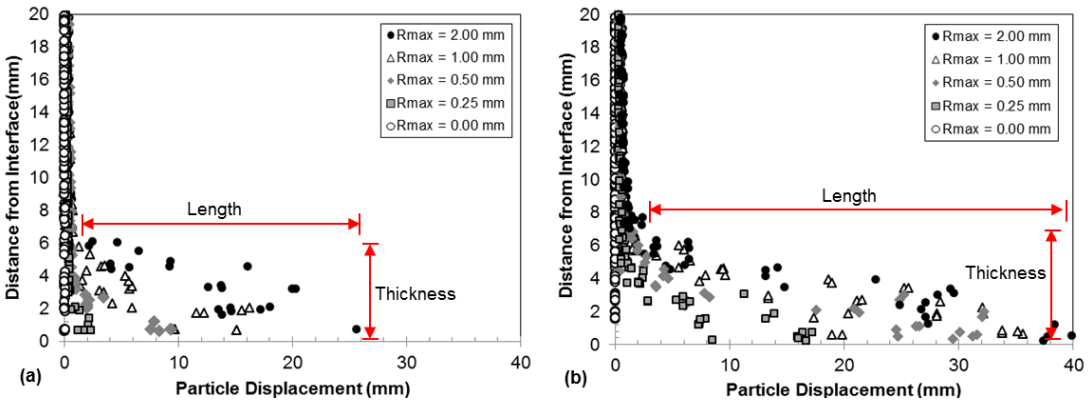

Figure 6.9: Shear zones formed during (a) axial and (b) torsional shear simulations against sleeves of varying surface roughness, R_{max} (confining pressure = 50 kPa).

The progressive growth of the shear zone with increasing friction sleeve surface roughness is presented in Figures 6.10c and 6.10d. The numerical and experimental results for shear zone thickness show that axial and torsional shear follow a similar trend, with sharp increases at low roughness values and more stable thicknesses developed at

larger roughnesses. A similar trend is followed by the shear zone lengths, with the important difference being that the shear zone lengths from torsional shear are much larger than those from axial shear, a behavior which was also observed in the experimental results. The difference between the numerical and experimental shear zone length results is also attributed to the 2D geometry in the DEM simulations.

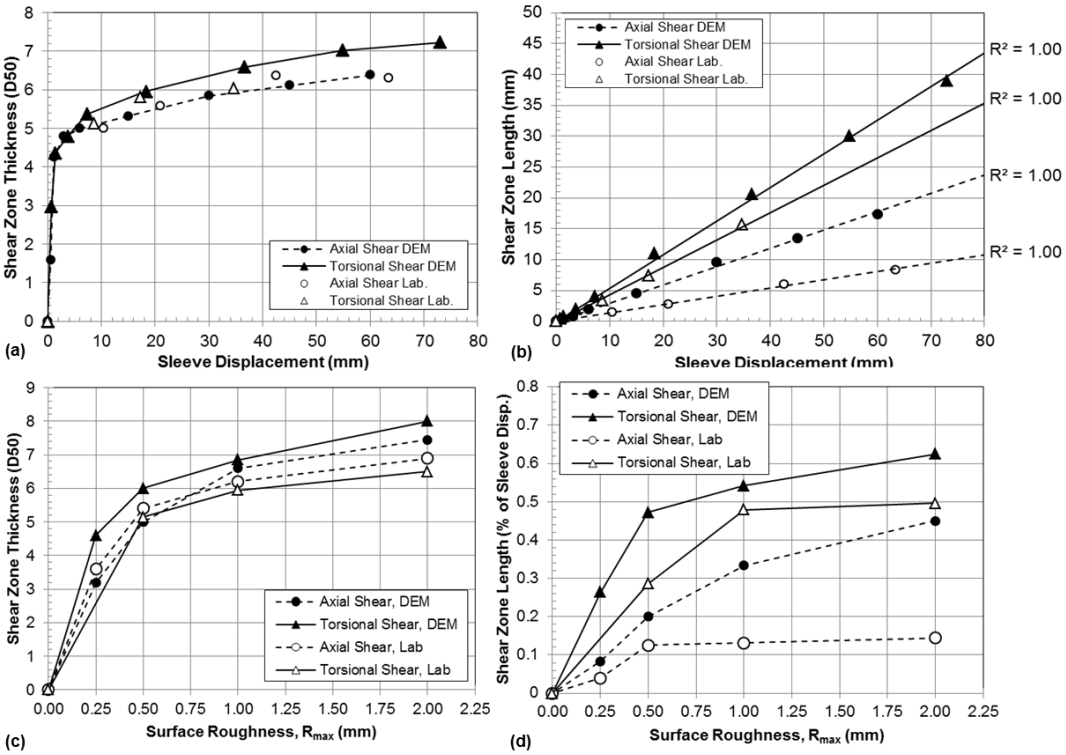

Figure 6.10: (a) Shear zone thickness and (b) length as a function of sleeve displacement for DEM simulations and laboratory tests against surfaces of R_{max} = 1.00 mm. (c) Shear zone thickness and (d) length as a function of surface roughness for DEM simulations and laboratory tests. (confining pressure = 50 kPa).

6.3.5 Zones of Influence and Shear Zones

The zones affected by the shear processes can be defined in terms of shear-induced particle displacements or volume changes. Zones of different size are obtained when using the two different definitions. The zones of intense particle displacement (Figures 6.10a and 6.10c), usually termed as “shear zones”, are smaller than the zones of

volume changes (Figures 6.7a through 6.7f). However, the shear zones are typically close in size to the dilation zones. The contraction zones are typically not captured as a zone of intense particle displacement, possibly because the particle displacements within it are relatively small. Similar results were also reported by (DeJong and Westgate, 2009) who performed experimental interface axial shear tests on dilative soil masses. They also found a complementary zone of contraction outside the zone of intense dilation and particle displacements.

This difference in influenced zones has important implications, especially considering that the shear zones typically undergo dilation while zones found outside the shear zones mainly showed soil contraction, especially during torsional shear. As such, these different induced mechanisms can be utilized to study soil behavior considering that volume-change behavior is critically important to the response of soils under different conditions. Examples of such different soil behaviors include the liquefaction of loose sands that result in contractive volumetric strains and the interface shear behavior of rough concrete piles that involves dilative volume changes.

6.4 Linking the Micro- and Macro-Scale Shear Behaviors

A more detailed study of the shear behavior of axial and torsional shear tests was performed in order to investigate the relationships between global and local shear behaviors. This section presents numerical and experimental results of tests performed against friction sleeves of R_{max} = 1.00 mm under a confining stress of 50 kPa.

6.4.1 Effect of Particle Shape

A series of laboratory drained axisymmetric experiments (R_{max} = 1.00 mm, confining pressure = 50 kPa) were performed with granular materials of different particle shape as described in Chapter 3. Tests with glass beads (D_{50} = 0.5 mm, roundness = 0.97), GRC-3 lunar simulant (D_{50} = 0.17 mm, roundness = 0.54), Ottawa 20-30 sand (D_{50}

= 0.72 mm, roundness = 0.73), Ottawa 50-70 sand (D_{50} = 0.26 mm, roundness = 0.58) and Blasting 20-30 sand (D_{50} = 0.72 mm, roundness = 0.32) were performed. Testing these granular materials allowed for the study of the effect of controlled changes in particle shape. It is noted that these the materials also have different mean particle size and particle surface roughnesses which may have also affected the behavior. Based on visual examination, the Blasting sand and GRC-3 have "high" particle surface roughness, Ottawa sands have "medium" rough surface and the glass beads are smooth. Despite this particle size and roughness differences, it was possible to identify key trends between particle shape and shear behavior. Peak stress ratio results as a function of particle roundness are presented in Figure 6.11a. It is shown that at high and medium particle roundness values (i.e. low and medium angularity) the peak loads from axial and torsional shear are similar. The loads in torsional shear keep increasing with decreasing particle roundness (i.e. increasing angularity) up to a roundness of 0.50, while the axial loads reach a stable value at a roundness of about 0.65.

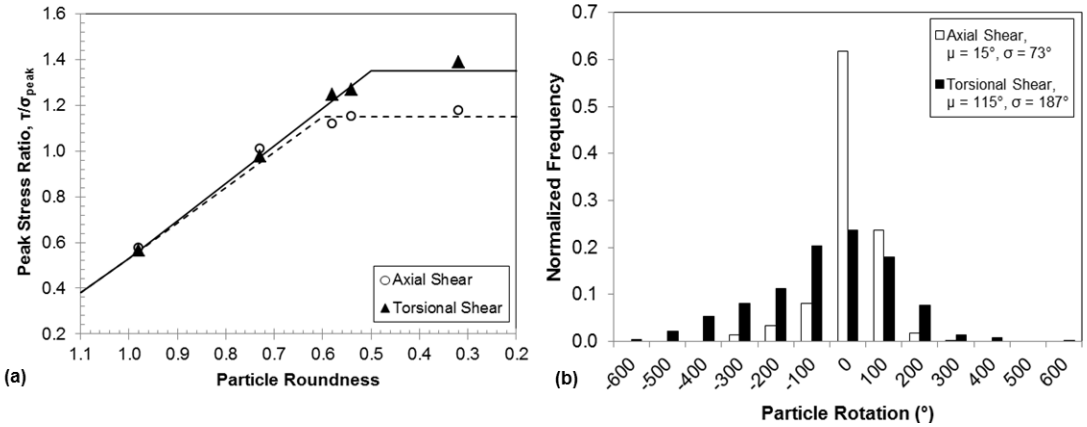

Figure 6.11: (a) Effect of particle roundness on peak stress ratio from laboratory tests. (b) Particle rotation distribution inside shear zone from DEM simulation (R_{max} = 1.00 mm, confining stress = 50 kPa).

This study was expanded by performing DEM simulations (R_{max} = 1.00 mm, confining pressure = 50 kPa) where average particle rotations induced by axial and torsional shear were monitored inside sampling windows 2 (Figures 6.1a and 6.1b). The

results are presented in Figure 6.11b as particle rotation distribution diagrams. These results show that the distribution of particle rotations for torsional shear is much more variable, reaching particle rotation values as large as 600°. The mean standard deviation values from torsional simulations are much larger, with values of 115° and 187° respectively, as compared to those from axial simulations of 15° and 73°. However, it should be noted that the coefficient of variation is larger for axial shear, with a value of 4.87, as compared to torsional shear with a value of 1.63. It should be noted that the DEM particle clumps have a roundness of about 0.75, similar to the Ottawa 20-30 sand.

These results help relate the micro- and macro-scale responses if particle angularity is viewed as a particle rotation resistance mechanism that effectively contributes to shearing resistance by mechanisms such as dilation (Cho, et al. 2006). As such, torsional shear induces larger particle rotations thus mobilizing larger particle rotation resistance that results in larger work done and mobilized loads. Furthermore, this observation could also contribute to the larger dilative behavior observed during torsional shear (Figure 6.2g). This observation can be described in more simple terms if a textured friction sleeve and the soil particles are thought of as engaged gears, as noted in Chapter 5. When there is complete engagement, the full angular displacement of the sleeve gets transferred as particle rotation. While a combination of particle rotation, sliding and translation is a more realistic situation, these results illustrate that particle rotation is the dominant failure mechanism taking place during torsional shearing.

6.4.2 Effect of Particle Friction Coefficient as Proxy for Particle Roughness

The DEM simulations also allowed for the study of the effect of varying interparticle friction coefficient, $\mu_{p\text{-}p}$, as a proxy for particle roughness. While the interparticle friction coefficient does not take into consideration the micro-roughness present in natural particles, it does emulate the effect of particle roughness on mobilized loads and volume change behavior of granular assemblies (Yang, et al. 2012).

The results of axial and torsional simulations (R_{max} = 1.00 mm, confining pressure = 50 kPa) are shown in Figure 6.12a. At low particle friction coefficients, the loads mobilized in axial shear increase at a larger rate that those for torsional shear. The results show that the mobilized stress ratios do not increase with increasing $\mu_{p\text{-}p}$ at values larger than 0.45 because at that point particle rotation becomes a less energy demanding failure mechanism, as shown by Thornton (2000) and Kryut and Rothenburg (2006). These results are complemented by average sliding contact fraction measurements taken from the shear zone captured in sampling window 2 (Figure 6.12b). At a $\mu_{p\text{-}p}$ value of 0.05, the sliding contact fraction is slightly larger for torsional shear. However, it sharply decreases as $\mu_{p\text{-}p}$ is increased to 0.15 and further increases in interparticle friction coefficient result in only modest decreases in the sliding contacts fraction. During axial shear, the sliding contact fraction only slightly decreases with $\mu_{p\text{-}p}$, reaching stable values at larger $\mu_{p\text{-}p}$ values. These results suggest that contact slippage is a more common failure mode during axial shear. Thus, increasing $\mu_{p\text{-}p}$ values result in larger mobilized loads (Figure 6.12a).

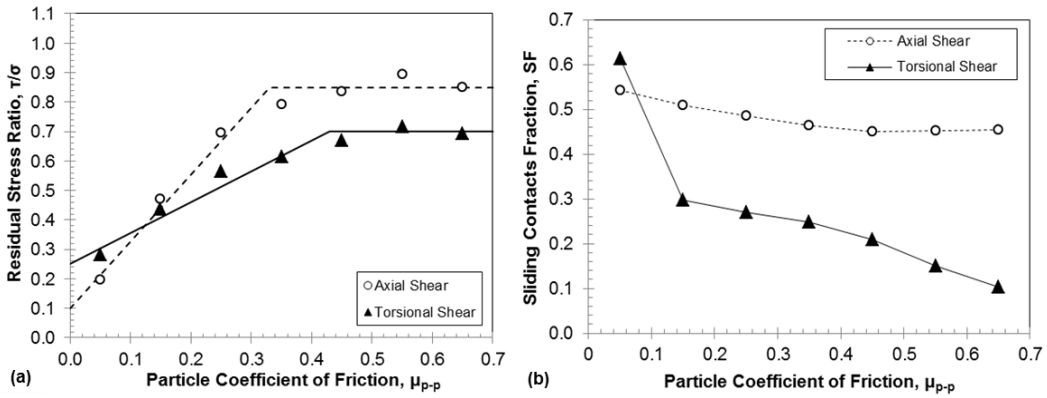

Figure 6.12: (a) Effect of particle-particle coefficient of friction on residual stress ratio and (b) Average sliding contact fractions within the shear zone for axial and torsional shear simulations (R_{max} = 1.00 mm, confining pressure = 50 kPa).

These findings complement those presented in Figures 6.11a and 6.11b. As the moving sleeve transfers forces to the contacting particles, it induces soil deformations. These shear deformations will ultimately take the form of the mechanism that requires

less energy, in this case, particle displacements without rotations that require contacts to slip past each other, or particle rotations which are resisted by particle interlocking. As such, the results indicate that during axial shear, contact slippage is a less energy demanding failure mechanism resulting in a larger sensitivity of axial loads to particle-particle friction coefficient. On the other hand, particle rotations becomes a less energy demanding mechanism during torsional shear, being represented by the larger sensitivity of torsional loads to particle shape, as shown in Figure 6.11a.

6.4.3 Fabric Evolution

Several authors, including Oda, et al. (1985) and Ng (2009), have studied the relationship between the strength responses of granular assemblies with their fabric evolution. For instance, those authors found a close relationship between the material response and the contact normal fabric tensor. Namely, the strength of a granular assembly is linked to its ability to develop fabric anisotropy, as shown by analytical and numerical results presented by Ouadfel and Rothenburg (2001), Maeda (2009) and O'Sullivan and Cui (2009). For the analysis presented in this paper, the second-order fabric tensor is used, along with the major and minor principal fabric magnitudes and their corresponding orientations. These are defined as follows:

$$\phi_{i,j} = \frac{1}{N_C} \sum_{k=1}^{N_C} n_i^k n_j^k$$

$$\phi_{1,3} = \frac{1}{2}(\phi_{xx} + \phi_{yy}) \pm \sqrt{(\phi_{xx} - \phi_{yy})^2 + \phi_{xy}^2}$$

$$\tan\ (2\phi_{1,3}) = \frac{2\phi_{xy}}{\phi_{xx} - \phi_{yy}}$$

where $\Phi_{i,j}$ is the definition of the fabric tensor; Φ_{xx}, Φ_{yy} and Φ_{xy} are the elements of the fabric tensor; Φ_1 and Φ_3 are the principal fabric components; and θ_1 and θ_3 are the orientations of the major and minor fabric components.

Figure 6.13a shows the stress-displacement response for axial and torsional simulations (R_{max} = 1.00 mm, confining pressure = 50 kPa), while Figure 6.13b shows the deviatoric fabric evolution during the same simulations calculated from particle contacts located within sampling window 1. The similarity in the progression of the stress ratio and deviatoric fabric is evident, both showing a larger peak and post-peak strain softening for torsional shear and larger values for axial shear at large sleeve displacements. Figure 6.13c shows the evolution of the orientation of the major and minor principal fabric components with increasing sleeve displacement. The progression of the major principal fabric orientation also resembles the shape of the stress-displacement curves, with larger angles at the peak stage at around 3 mm followed by a larger decrease for torsional shear. This observation agrees with the fact that increasing fabric anisotropy allows granular assemblies to mobilize larger shear resistances.

The coordination number gives an indication of the particle arrangement and stability. Figure 6.13d presents the average coordination numbers for axial and torsional shear computed from sampling windows 2. The 2D coordination numbers are lower than those in a 3D scenario, ranging from 3.0 to 6.0. The results indicate that the coordination number is similar for axial and torsional simulations over the first 6 mm of shearing, corresponding to the pre-peak and peak shear stages. The sharp decrease in coordination number is caused by the intense dilation inside the shear zone. At larger displacements the coordination number for torsional shear reached stable values of about 4.0. However, the values for axial shear kept decreasing until reaching a value of 3.0 at 60 mm of displacement. These stable coordination numbers are in general agreement with those for disk assemblies at critical state provided by Rothenburg and Kruyt (2004). These results reflect the volume-change behavior of the specimens. Torsional shear reaches a critical state fabric at displacements larger than 10 mm (Figure 6.2f), the coordination number in axial simulations keeps decreasing as the sample continues dilating (Figure 6.2e).

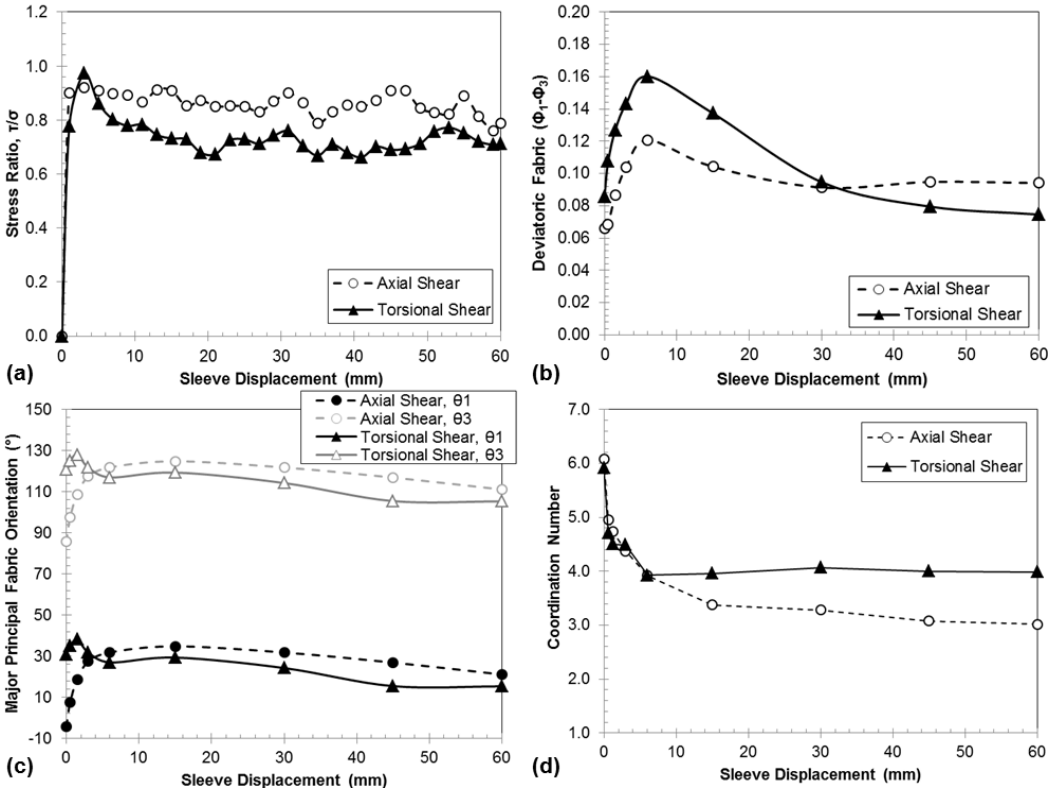

Figure 6.13: (a) Stress ratio-displacement, (b) Deviatoric fabric (c) Major principal fabric orientation and (d) Coordination number for axial and torsional shear simulations against friction sleeves of R_{max} = 1.00 mm under a confining pressure of 50 kPa.

6.4.4 Polar Contact Histograms

Polar histograms of contact normals as well as normal and shear contact forces provide further insights regarding the fabric evolution and the loading conditions within the specimens. Figures 6.14a and 6.14b show normalized polar histograms for axial and torsional shear simulations (R_{max} = 1.00 mm, confining pressure = 50 kPa), respectively, constructed from particle information obtained from sampling windows 1, along with Fourier distributions fitted to the data and fitting parameters (a and θ), as described by Rothenburg and Bathurst (1989).

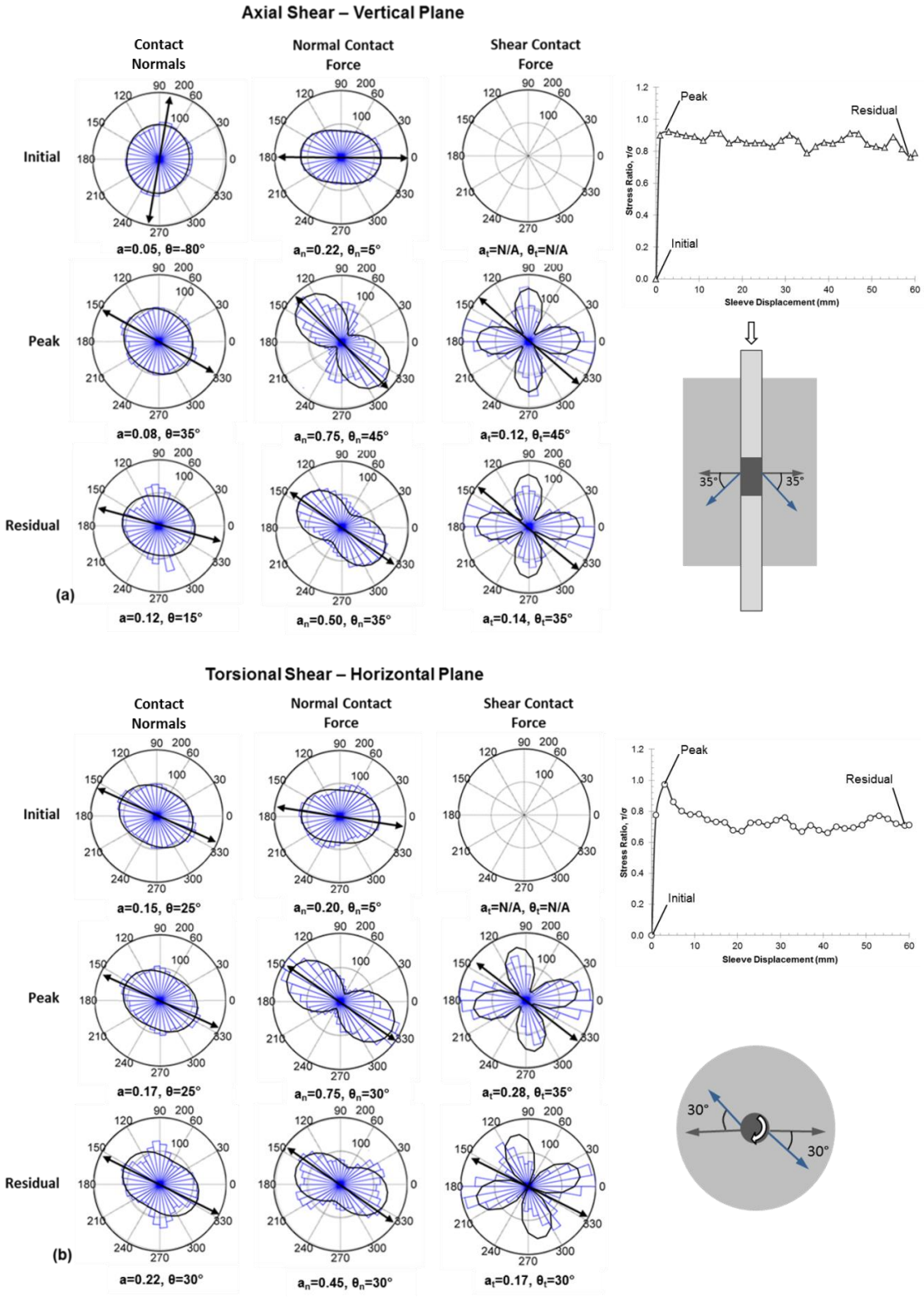

Figure 6.14: Normalized number of contact normals, normal force and shear force for (a) Axial and (b) Torsional simulations (R_{max} = 1.00 mm, confining pressure of 50 kPa).

The results are presented for the initial, peak and residual stages, as defined in the corresponding figures. The length of the histogram bars represents percentages with respect to the mean corresponding quantities, a larger 'a' coefficient represents a more anisotropic distribution and the angles 'θ' are measured from the horizontal axis. The initial conditions in the axial simulation show a nearly uniform contact number distribution, maximum contact normal forces in the horizontal direction induced by the consolidation stage and no shear contact forces. The latter resulted from the interparticle friction coefficient being set to zero during consolidation. At the peak stage, the fabric of the axial simulation starts evolving as shown in the figure. The normal and shear contact forces develop distributions with their maximum magnitudes oriented at 45° and 10° from the horizontal, respectively, and the shear forces are concentrated in two orthogonal directions. At the residual stage, the fabric continues evolving, showing the maximum number of contacts at 15° from the horizontal. The orientation of the maximum magnitudes of normal and shear contact force distributions doesn't evolve significantly. These results show a principal normal contact force rotation (which coincides with the principal stress rotation) from an initial horizontal direction to 35° from the horizontal at the residual stage (Figure 6.14a), which takes place in a vertical plane. Similar results were obtained by Wang and Jiang (2011), who used 2D DEM simulations to investigate interface shear against various surfaces. The authors reported a large rotation of the principal direction of contact forces during the pre-peak and peak stages, but no significant rotation during the residual stage for surfaces composed of periodic profiles similar to the friction sleeves used in this study. Additionally, the authors reported several similarities between the anisotropy evolution of interface and direct shear simulations. As such, similar principal contact force rotations between 35° and 45° were reported by Cui and O'Sullivan (2006) and Wang, et al. (2007b) for direct shear DEM simulations.

The torsional results (Figure 6.14b) show a slightly less uniform contact number distribution at the initial stage. This difference is attributed to the different consolidation

conditions (lateral stress during axial and radial stress during torsional). At the peak stage, the fabric starts evolving and the maximum normal and shear forces concentrate in directions 30° and 5° from the horizontal, respectively. At the residual stage, the fabric evolves in a similar way as axial shear, with the maximum contact number in a direction 30° from the horizontal. The shear forces at the peak and residual stages develop in two main directions that are not orthogonal but inclined 60° from each other. This is attributed to the torsional passive forces that tend to push the particles outwards, as shown in Figures 6.4b and 6.4d. The normal force histograms suggest a principal normal force rotation from a near horizontal direction to one oriented 30° from it, which takes place in a horizontal plane. This is perhaps one of the key differences between axial and torsional shear: axial shear induces stress rotations in a vertical plane while torsional shear induces stress rotations in a horizontal plane.

6.4.5 Comparison of Torsional Interface Shear and Vane Shear Test

The vane shear test (VST) is perhaps the most widely used geotechnical test that induces torsional shear of soil. As such, this section investigates the differences between the VST and the torsional interface shear tests. The torsional shear DEM model described in Chapter 3 and in this chapter was utilized, with the difference that the friction sleeve was replaced with a four bladed vane, as shown in Figure 6.15a.

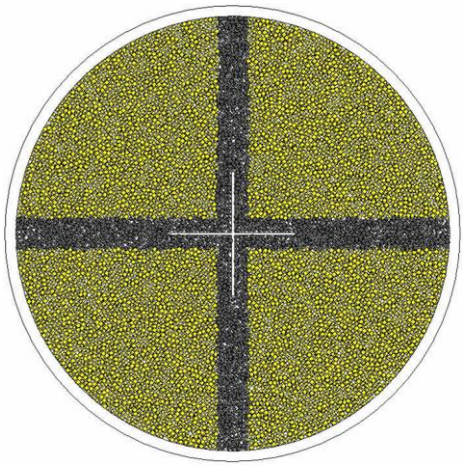

Figure 6.15: DEM model of vane shear test.

Shearing (in the counterclockwise direction) induced a well-defined localized failure in the form of a shear zone for both torsional shear and VST simulations, as shown in Figures 6.16a and 6.16b. The force chain maps shown in Figures 6.16c and 6.16d provide insight into the loading conditions induced during both shear processes. As previously described, during torsional shear the load is transferred from the sleeve to the contacting particles by means of interface friction and passive. This is evident in the force chain map as the contact forces are distributed along the surface of the friction sleeve (representing the interface friction transfer), but force concentrations can be observed at the leading edge of the diamond elements (representing the passive resistance transfer).

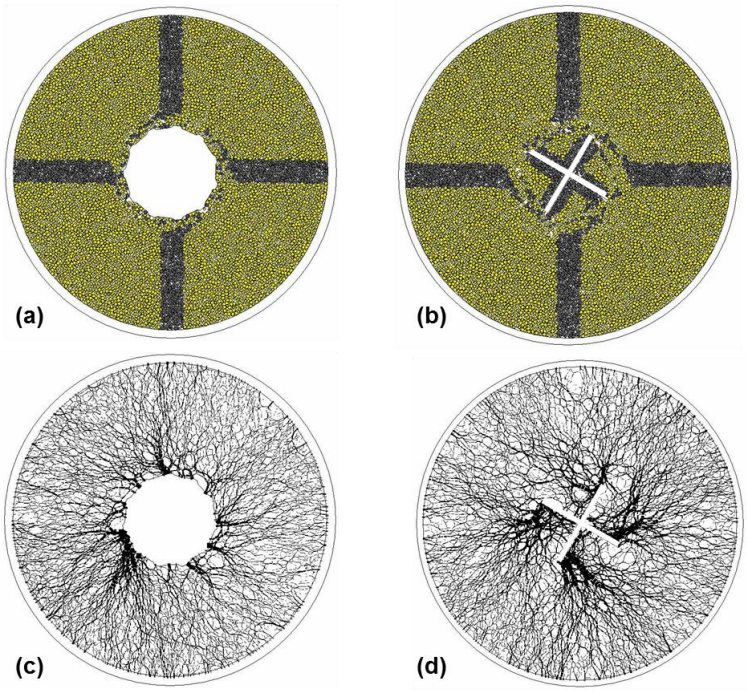

Figure 6.16: Sheared specimens for DEM simulations: (a) Torsional shear and (b) Vane shear tests. Contact force maps for (c) torsional shear and (d) vane shear simulations.

The force chain map for the VST simulation shows an obvious concentration of contact forces at each of the four blades of the vane, which represents a complete transfer of the load by passive resistances. This observation is in general agreement with the geometry of the failure zone reported by Gylland, et al. (2013), Chandler (1988) and

Wilson (1963), which has a rounded quadratic shape as opposed to the cylindrical geometry commonly assumed. In order to illustrate the different loading conditions induced during torsional shear and the VST, Figures 6.17a and 6.17b show mobilized torque and induced volumetric strain during shear. As shown, the vane shear mobilized the largest magnitude of peak and residual torque, followed by those mobilized during the torsional test with a friction sleeve of R_{max} of 1.00 mm and lastly by the torsional test with a smooth sleeve. A similar trend is shown by the volumetric strain results, where the largest magnitudes were induced by the vane shear test. These trends agree with the fact that passive resistances are able to mobilize larger soil strength as they induce compression, as opposed to interface friction which induced soil shear, as further described in Chapter 8 of this thesis.

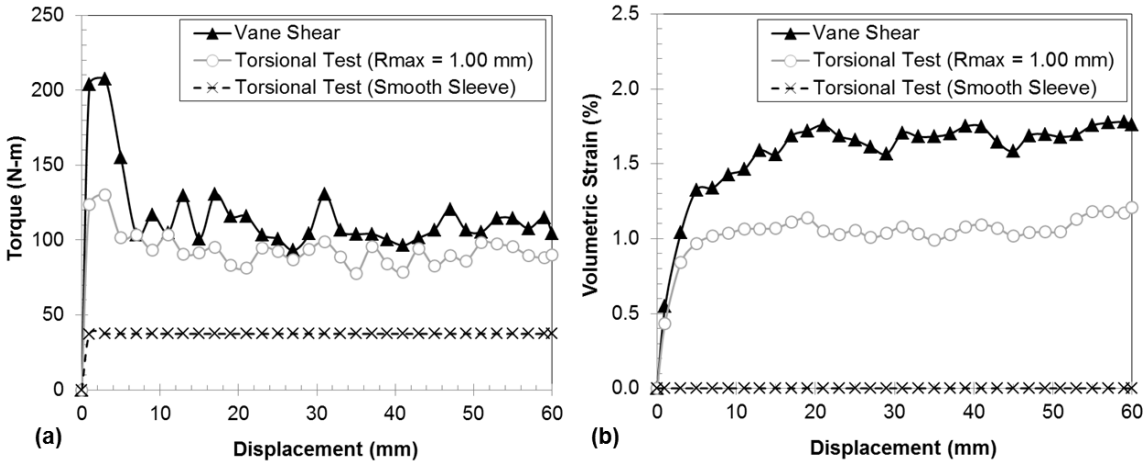

Figure 6.17: (a) Mobilized torque and (b) Induced volumetric strains during vane shear and torsional shear simulations.

6.5 Conclusions

This chapter presented the findings of a numerical simulations study of interface shear behavior under axial and torsional loading conditions complemented with results from experimental studies. DEM has been shown to be a useful tool for identifying links between the observed boundary-measured global behavior and particle-scale processes

such as local volume changes, particle trajectories, particle rotations, contact failure modes and fabric evolution. The following conclusions are made:

- The numerical results showed an increase in interface strength with increasing surface roughness similar to the experimental results for both axial and torsional shear. Also, all the simulations with rough surfaces induced dilation within the contacting assembly.
- A strength non-uniqueness which depended on the imposed loading conditions was shown by different stress paths and failure envelopes for axial and torsional shear simulations.
- Torsional shear showed to be a more dilative behavior as shown by the larger mobilized maximum dilation angles. Specimens subjected to axial shear showed dilation continuing at all shear displacements, as opposed to those subjected to torsional shear which effectively reached a critical state.
- The shear-induced volume changes during torsional shear showed larger dilation magnitudes, as well as larger contraction magnitudes and contraction zones sizes outside the shear zones for the various surface roughness, initial assembly void ratio and confining pressure values studies.
- Numerical simulations based shear zone deformation results confirmed by experimental results indicated that their thickness evolution is similar for axial and torsional shear, reaching stable values at large shear displacements and surface roughnesses. Torsional shearing consistently induced larger shear zones. The shear zone lengths increased linearly with shear displacement but reached stable values for tests against rougher friction sleeves. These results are in agreement with experimental results presented in Chapter 4.
- It was shown that larger and more variable particle rotations are induced during torsional shear. This is linked to the mobilized loads, which showed that particle rotation resistance mechanisms, such as particle angularity, result in larger load

increases for torsional shear. In a similar manner, it was shown that contact slippage is a more dominant contributing factor in axial shear, which explains the larger mobilized loads observed in axial simulations with larger interparticle friction coefficients.

- Coordination numbers within the axial and torsional shear zones suggest that these have similar initial fabrics, and undergo similar evolutions during the pre-peak and peak shear stages. At larger displacements, axial shear further induces coordination number reduction while torsional shear reaches a critical-state fabric. The evolution of the magnitude and orientation of the principal fabric components follows that of the mobilized shear response, agreeing with the fact that increasing fabric anisotropy allows granular assemblies to mobilize larger shear resistances.
- The normalized polar histograms of the number of contact normals as well as normal and shear contact forces showed that both axial and torsional shear induce principal contact force rotations. However, this takes place in a vertical plane during axial shear and in a horizontal plane during torsional shear. This observation has potential uses in the study of granular assemblies under anisotropic states of stresses.
- The different soil-friction sleeve interactions, including the different volume changes induced by axial and torsional shear, have important implications on the study of soils that have different volume-change behaviors. For instance, liquefaction is intimately related to soil contraction while soil dilation is commonly observed in the shear process of soil against rough surfaces.

CHAPTER 7

STUDY OF THE UNDRAINED CYCLIC BEHAVIOR OF TORSIONAL INTERFACE SHEAR TESTS

7.1 Introduction

A series of earthquakes New Zealand in 2011 caused significant damage in the city of Christchurch due to the widespread liquefaction of the sandy soils underlying a large part of the city. At the same token, these earthquakes provided an extremely valuable opportunity for geotechnical engineers to study the behavior of these soils under repeated earthquake loadings. Possibly one of the most significant findings of these studies was the re-liquefaction of a significant amount of soils during the subsequent earthquakes. This contradicts the conventional belief that the compressive volume changes undergone during initial liquefaction results in these soils being able to significantly resist subsequent liquefaction. To this point, the observations gathered during these studies have led to the increased attention on the prediction of properties of post-liquefied soils, such as strength and compressibility. These geotechnical investigations have made significant use of in-situ tests, such as the CPT and DMT, as a result of the well-known difficulties associated with undisturbed sampling for laboratory tests (e.g. Bray, et al. 2013).

The cyclic behavior of geotechnical interface systems has received significant attention during the last decade. These investigations have focused on the cyclic capacity performance of structures such as offshore and wind-energy foundations (Gavin and O'Kelly, 2007; Tsuha, et al. 2012; Rimoy, et al. 2013; Pasten, et al. 2014;). The research presented in this chapter addresses a different problem. Namely, it focuses on the study of the cyclic stress behavior of torsional interfaces with the ultimate goal of developing a

robust methodology for the study of cyclic soil response. This research seeks to advance the development of a new in-situ testing device that measures the soil response under axial and torsional shear loadings, called the Multi-Piezo-Friction-Torsion Attachment (MPFTA). As such, an undrained axisymmetric interface shear testing device was designed and built (see Chapter 3) and utilized to study the influence of initial relative density, confining stress, soil particle angularity, surface roughness and shear direction (torsional versus axial) on the behavior of sand specimens. The results show that torsional shear induces significant excess pore water pressures on saturated sand specimens of low, medium and high relative densities that resulted in soil cyclic mobility conditions. In fact, the results indicate that torsional shear consistently generated pore water pressures at a faster rate than axial shear, making it a more attractive test for the study of soil cyclic behavior. Processes for excess pore water pressure generation are also presented.

The undrained axisymmetric interface shear device (Figure 3.6a and 3.6b) was used for all of the tests presented in this chapter. Specimens of Ottawa 20-30 and Blasting 20-30 sands (see Figures 3.1a through 3.1d, 3.2a and 3.2b and Tables 3.1 and 3.2) of relative densities of 20-70% were subjected to displacement-controlled cyclic shear under 45 and 95 kPa lateral confining stress. A one-way displacement amplitude of 15 mm at the top of the testing rod (equivalent to 40.2° of rotation) was selected because smaller displacements would be difficult to be controlled in field testing conditions. All the tests were performed with diamond textured friction sleeves (Figure 3.3a through 3.3d) of maximum surface roughness, R_{max}, of 1.00 mm (average roughness, R_a, of 0.185 mm) with the exception of the tests performed against sleeves of varying roughness, which covered an R_{max} range of 0.00 to 2.00 mm (R_a from 0.001 to 0.226 mm). Detailed information regarding the specimen preparation procedure and the measurement of global specimen response is included in Chapter 3. The DEM torsional shear simulations were performed using the model shown in Figure 3.20b on assemblies consisting of two-particle clumps (AR = 1.5) that have been previously shown to replicate the behavior of

Ottawa 20-30 sands. Chapter 3 presents detailed information regarding the measurements procedure and the modeling parameters utilized.

7.2 Results

The undrained cyclic interface shear tests performed as part of this study were analyzed in terms of the state parameter, ψ. This was done in order to account for the effect of both the initial void ratio and mean principal stress (p) on the response of the specimens. Vertical stress measurements from an internal load cell indicated an average ratio between applied horizontal stress to vertical stress of 0.96, which was used to calculate p. Figure 7.1a and 7.1b show the initial conditions in e-p space of all the specimens of Ottawa 20-30 and Blasting 20-30 sands, respectively, and Table 7.1 shows a summary of the test configuration and selected results of all the tests performed in this study.

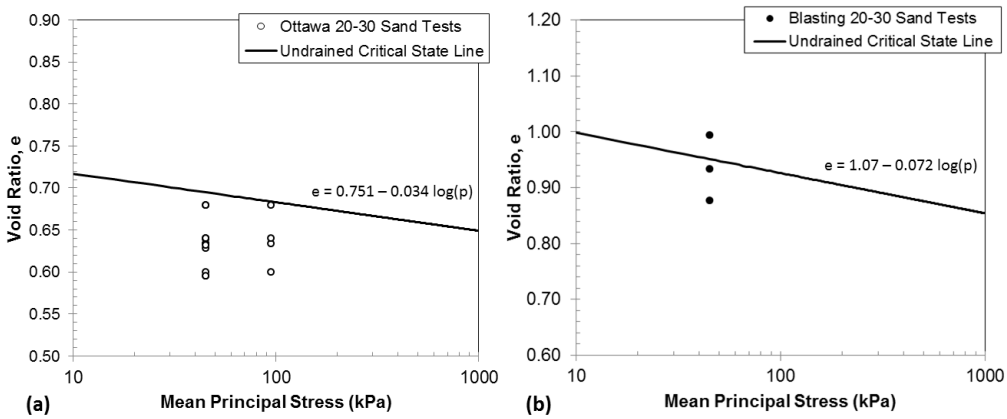

Figure 7.1: Initial state of tests performed on (a) Ottawa 20-30 and (b) Blasting 20-30 sands. Critical state line is from undrained triaxial tests (Santamarina and Cho, 2001).

The state parameter is defined as the difference between the initial specimen void ratio, e_{ini}, and the critical state void ratio, e_{cs}, for a specific mean principal stress (Been and Jefferies, 1985). As such an e_{ini} larger than e_{cs} will yield a positive state parameter which indicates a contractive specimen behavior. On the other hand, a smaller e_{ini} than e_{cs} will yield a negative state parameter that indicates a dilative specimen behavior. All the

Ottawa 20-30 specimens had negative state parameters as a result of the relatively small mean principal stresses applied. Due to the larger angularity of the Blasting 20-30 sand, specimens of positive and negative state parameters were able to be tested.

Table 7.1: Testing configuration and selected results for cyclic interface shear tests.

Shear Direc-tion	Drain-age Condi-tions	Sand Type	Confining Stress, σ'(kPa)	Satura-tion, S (%)	Relative Density, Dr (%)	Initial Void Ratio, e	Initial State Para-meter	Surface Roughness, R_{max} (mm)	Failure Envelope Angle (°)	Cyclic Stress Ratio at 20 Cycles	Normalized Excess Pore Pressure at 20 Cycles	Avg. Excess Pore Pressure Cycle Amp-litude (kPa)	Number of Cycles for Lique-faction	Variable
T	U	OT	45	96.2	48	0.635	-0.060	1.00	31.5	0.12	0.83	5.4	31	Reference
T	D	OT	45	97.2	70	0.595	-0.100	1.00	N/A	N/A	N/A	N/A	N/A	Drainage
T	U	OT	45	99.8	45	0.640	-0.055	0.00	15.1	0.13	0.44	1.9	NL	Surface Roughness
T	U	OT	45	94.2	48	0.634	-0.061	0.25	27.5	0.22	0.56	2.8	NL	
T	U	OT	45	95.9	49	0.628	-0.067	0.50	28.8	0.20	0.61	3.3	53	
T	U	OT	45	96.2	50	0.631	-0.064	2.00	33.4	0.22	0.76	4.8	30	
T	U	BL	45	95.6	32	0.993	0.042	1.00	28.1	0.02	0.95	5.4	14	Sand Type
T	U	BL	45	98.8	46	0.933	-0.018	1.00	31.0	0.12	0.84	3.5	28	
T	U	BL	45	97.6	59	0.877	-0.074	1.00	33.8	0.23	0.65	4.3	57	
T	U	OT	45	94.7	23	0.679	-0.016	1.00	29.2	0.02	0.91	4.0	22	Relative Density
T	U	OT	45	95.2	67	0.595	-0.100	1.00	34.2	0.28	0.60	6.0	NL	
T	U	OT	95	95.5	23	0.679	-0.005	1.00	28.8	0.10	0.79	6.7	29	Relative Density and Confining Stress
T	U	OT	95	96.2	48	0.635	-0.049	1.00	30.8	0.28	0.53	7.2	NL	
T	U	OT	95	95.2	67	0.600	-0.084	1.00	33.0	0.40	0.35	8.4	NL	
A	U	OT	45	95.5	29	0.668	-0.027	1.00	28.5	0.11	0.78	4.3	34	Shearing Direction
A	U	OT	45	99.7	49	0.633	-0.062	1.00	28.1	0.19	0.65	4.5	NL	
A	U	OT	45	95.7	67	0.603	-0.092	1.00	29.2	0.31	0.41	3.5	NL	

T = Torsional, A = Axial, U = Undrained, D = Drained, OT = Ottawa 20-30, BL = Blasting 20-30, NL = No liquefaction showed

7.2.1 Excess Pore Water Pressure Generated during Torsional Shear

During the research presented in this thesis, it has been shown that shearing a rough surface against a soil mass axially or torsionally results in localized soil deformations typically referred to as shear zones (see Figures 4.2b, 4.2d, 4.3b, 4.3c, 4.4a through 4.4d, 4.5c, 4.5d from laboratory tests and Figures 6.8b, 6.8d, 6.8f, 6.8h, 6.9a, 6.9b and 6.10a through 6.10d from DEM simulations). Furthermore, local void ratio measurements have also revealed the formation of a secondary zone where particle displacements are not obvious but volume changes are significant. Chapters 4 and 6 showed that the principal shear zone underwent dilation while the secondary zone underwent contraction (see Figures 4.6c, 4.6d, 4.7a, 4.7b from laboratory tests and 6.7 a through 6.7f from DEM simulations). Figures 4.8a, 4.8b, 4.9a and 4.9b showed proposed micromechanical processes that are considered responsible for these soil deformations, and Figures 6.4c and 6.4d verified those using DEM simulations. The experimentally-measured shear-induced changes in void ratio on a specimen subjected to torsional shear

are shown in Figure 7.2a. Figure 7.2b shows a schematic of these volume changes in the cross-section of an axisymmetric specimen.

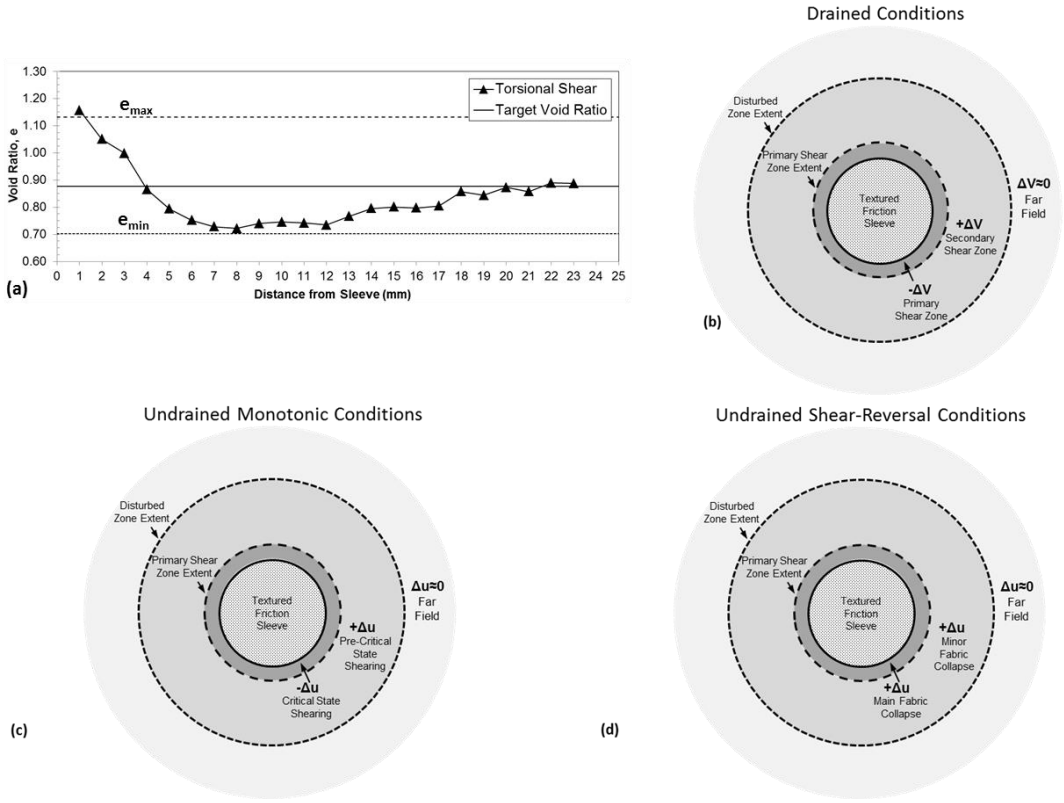

Figure 7.2: (a) Shear-induced changes in local void ratio on a drained axisymmetric torsional interface shear test. Schematic of shear-induced (b) drained volume changes, (c) undrained excess pore pressures during monotonic shear and (d) undrained excess pore pressures during shear reversal shown in the cross-section of a specimen.

All of the studies presented in the previous chapters were performed on specimens subjected to drained loading under a constant confining stress. Considering the understanding of soil mechanics (found in classical texts such as Lambe and Whitman, 1969 and Alarcon-Guzman, et al. 1988), the undrained monotonic and shear-reversal response of specimens subjected to interface torsional shear can be predicted as shown in Figures 7.2c and 7.2d. The dilative volume change tendencies in the primary shear zone result in negative excess pore pressures in monotonic shear; however, this soil volume might reach a critical state at large shear displacements. The soil on the secondary shear

zone shows contractive volume change tendencies thus generating positive pore pressures. This soil volume does not reach a critical state since it undergoes relatively small shear strains. The positive and negative excess pore pressures generated "compete" to show either a contractive or dilative global specimen response. In the shear reversal case (Figure 7.2d), the collapse of the sand fabric results in positive excess pore pressures generated in the primary and secondary shear zones. As shown throughout this chapter, all the specimens showed global positive pore pressure generation upon shear reversal.

7.2.2 Global Undrained Cyclic Torsional Interface Shear Response

Figure 7.3a through 7.3f show the shear stress and excess pore water pressure measurements as a function of testing time for torsional tests on specimens of varying

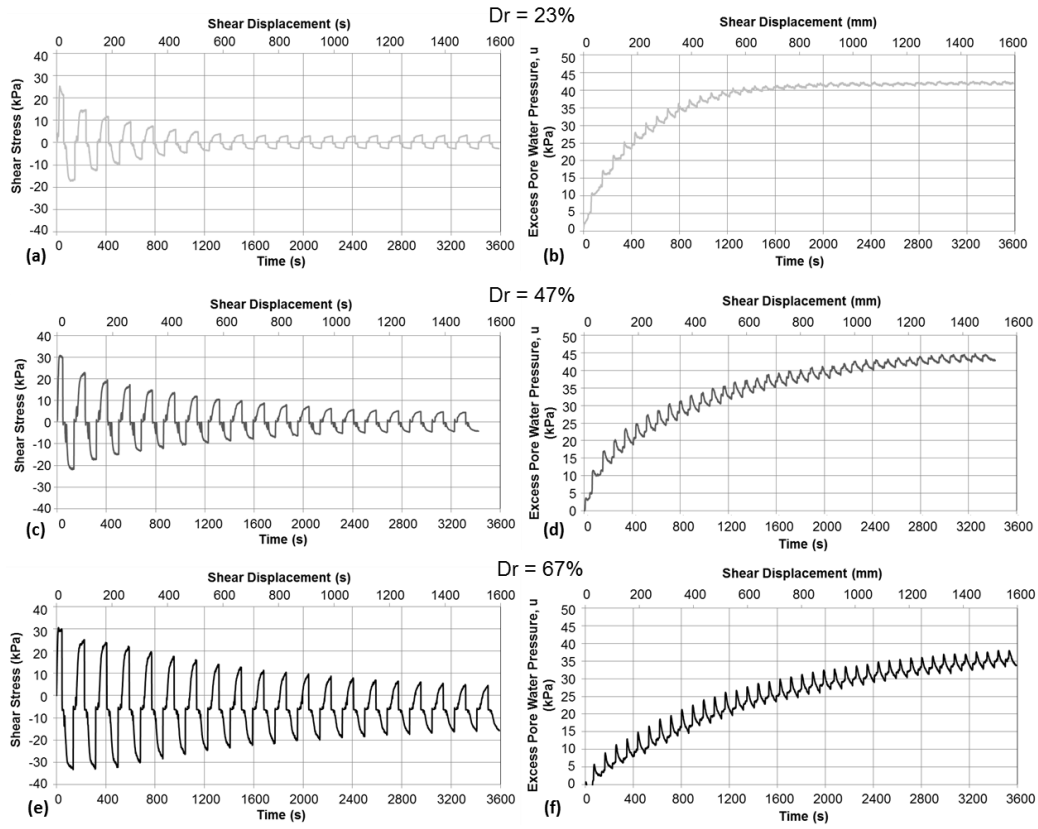

Figure 7.3: Shear stress and excess pore water pressures measured during cyclic torsional tests on specimens of Ottawa 20-30 sand of relative density of (a)–(b) 23%, (c)–(d) 47%, and (e)-(f) 67% under a confining stress of 45 kPa.

relative density (23, 47 and 67%) subjected to cyclic torsional shear under a confining stress of 45 kPa. The mobilized positive and negative shear stresses are a result of the cyclic stress reversals. The excess pore pressure increased with increasing number of cycles, which resulted in smaller shear stresses mobilized as a result of the decreasing effective stress within the specimen. The magnitude of the excess pore pressures was shown to sharply increase at the beginning of each stress reversal as a result of a collapse of the fabric of the soil undergoing large shear strains, as postulated by Alarcon-Guzman, et al. (1988). However, the pore pressures slightly decreased with continuing shearing during each cycle, showing slight dilative tendencies. Both the magnitudes of the excess pore pressure generation and shear stress degradation increased more rapidly on the test with the looser specimen (Dr = 23%), followed by the medium (47%) and high (67%) density specimens.

Figures 7.4a through 7.4i present the same results in terms of hysteresis loops for 40 one-way cycles. The amplitude of the shear stress reversal loops decreased with increasing number of cycles as a result of the increase in positive excess pore pressure that resulted in a decrease of the effective stress (Figures 7.4a, 7.4d and 7.4). The excess pore pressure increased at a larger rate during the first few cycles, as shown in Figures 7.4b, 7.4e and 7.4h. The pore pressure generation responses during all the cycles showed initial sharp increases in pore pressure followed by progressive decreases, showing an initial strong contractive tendency followed by a more subtle dilative tendency at larger shear displacement, which are characteristic of specimens undergoing cyclic mobility (Castro, 1975; Seed, 1979; Alarcon-Guzman, et al. 1988). This trend is more obvious on the response of the specimens of relative densities of 47 and 67%. As previously described, the cumulative excess pore pressures generated are positive and increased with cycle number. The specimens of low and medium relative densities reached cyclic mobility after 21 and 33 one-way cycles, respectively. The shear stress paths are shows to be bounded by straight failure envelopes as shown in Figures 7.4c, 7.4f and 7.4i.

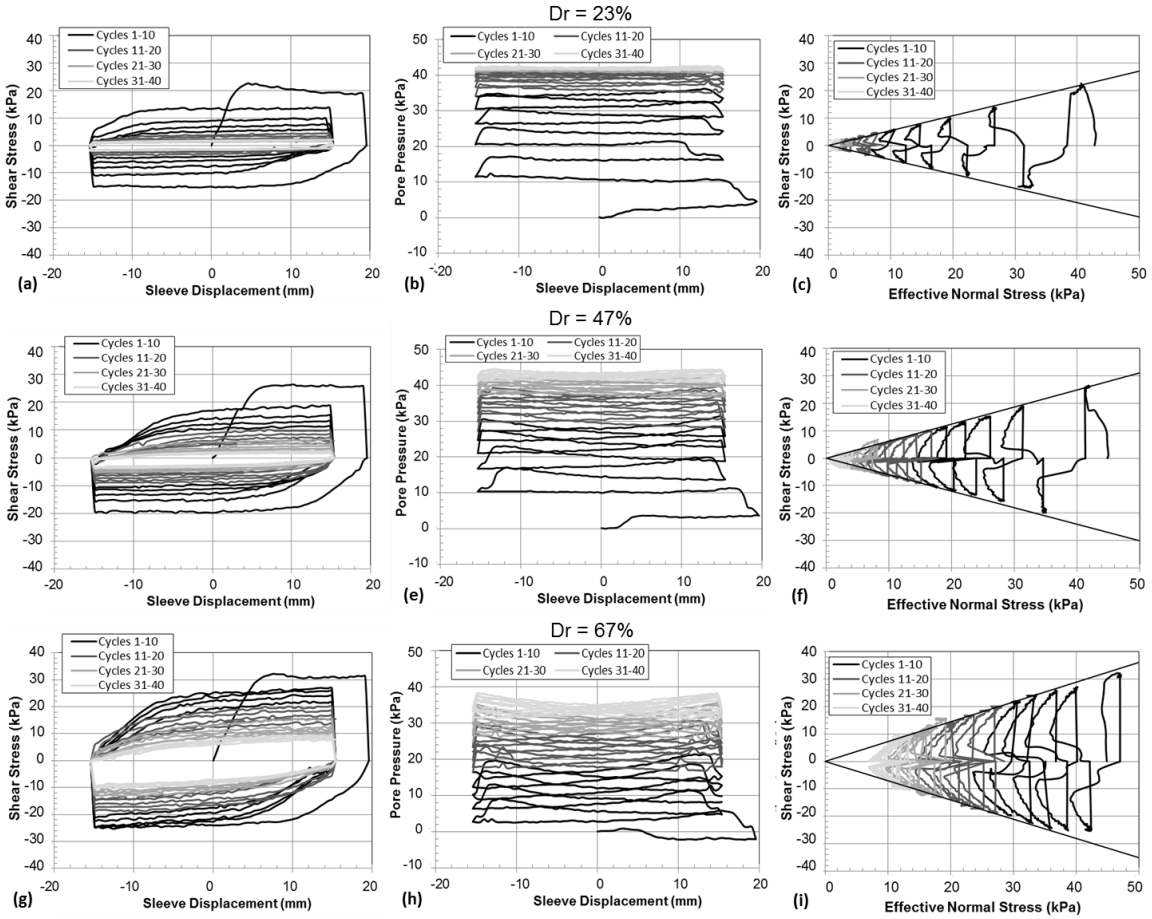

Figure 7.4: Shear stress, excess pore pressure and stress paths observed during cyclic torsional tests on specimens of Ottawa 20-30 sand of relative densities of (a)-(c) 23%, (d)-(f) 47%, and (g)-(i) 67% under a confining stress of 45 kPa.

7.2.3 Effect of Confining Stress and Relative Density

A series of torsional tests on specimens of low, medium and high relative densities (23, 47 and 67%, respectively) was performed under a confining stress of 95 kPa in order to study the combined effect of initial relative density and confining stress. For the purpose of this discussion, the state parameter is utilized because it takes into account the effect of both parameters (σ_c and Dr). The results presented in Figures 7.5a through 7.5i are in terms of mobilized shear stress, measured excess pore pressures and stress paths. In general, these results follow the same trends as the ones presented in

Figures 7.4a through 7.4i. Namely, the amplitude of the shear stress reversal loops decreased with increasing number of cycles as a result of the increase in excess pore water pressures, and the stress paths showed to be bounded by straight failure envelopes. Furthermore, the excess pore pressures indicated faster generation during the first cycles, as previously described. Immediately following the stress reversal, there was a sharp increase in the pore pressures (contractive behavior), followed by a more subtle decrease (dilative behavior). The net result was positive excess pore pressure measurements.

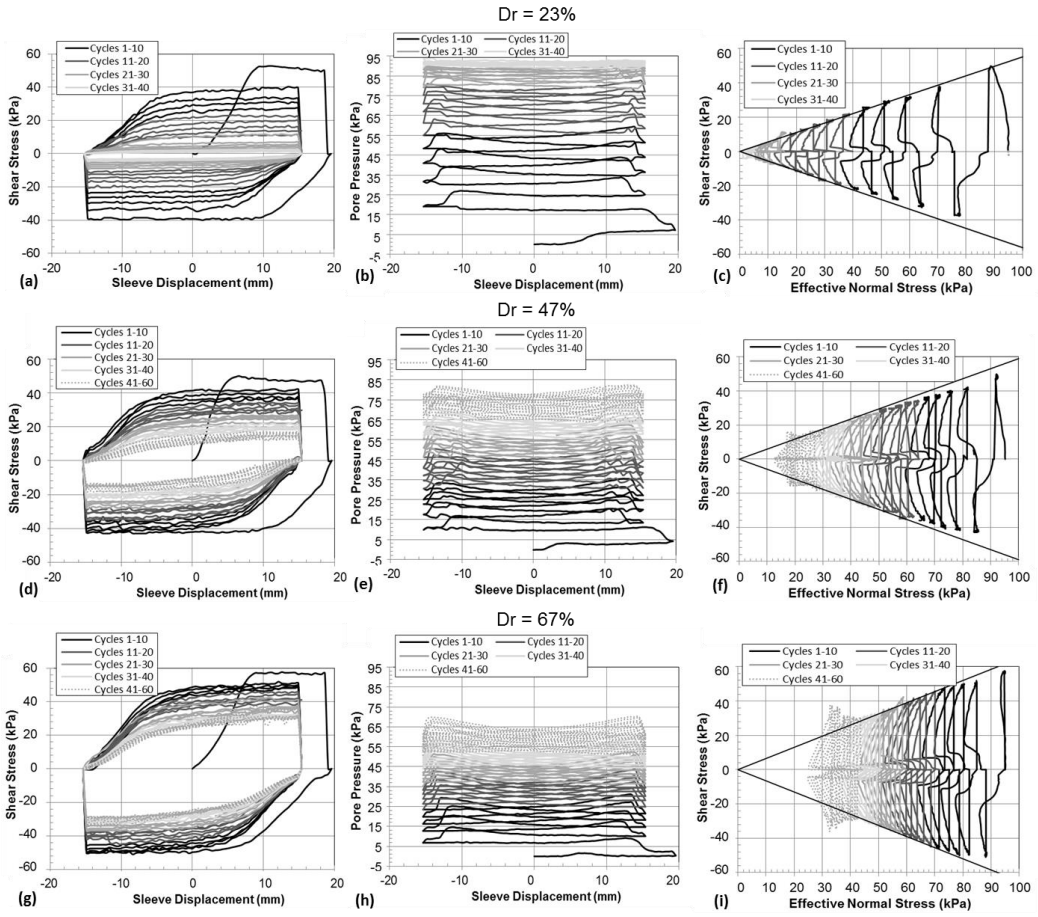

Figure 7.5: Shear stress, excess pore pressure and stress paths observed during cyclic torsional tests on specimens of Ottawa 20-30 sand of relative densities of (a)-(c) 23%, (d)-(f) 47%, and (g)-(i) 67% under a confining stress of 95 kPa.

Figures7.6a and 7.6b show the maximum cycle stress ratio mobilized (τ_{max}/σ_c) and average normalized excess pore pressures generated (u_{avg}/σ_c) as a function of one-way

cycle number for the tests performed under a confining stress, σ_c, of 45 kPa, while Figures 7.6c and 7.6d show the corresponding results for tests performed under a σ_c of 95 kPa (results also shown in Table 7.1). Both test series showed faster shear stress degradation for looser specimens as a result of faster excess pore water pressure generation. These results are reasonable based on the fact that looser assemblies show more contractive tendencies. Additionally, the results show that only the tests performed on specimens of relative densities of 23 and 47% under σ_c of 45 kPa liquefied (cyclic mobility) after 22 and 31 one-way cycles, respectively, and the specimen of relative density of 23% under a σ_c of 95 kPa liquefied (cyclic mobility) after 29 one-way cycles.

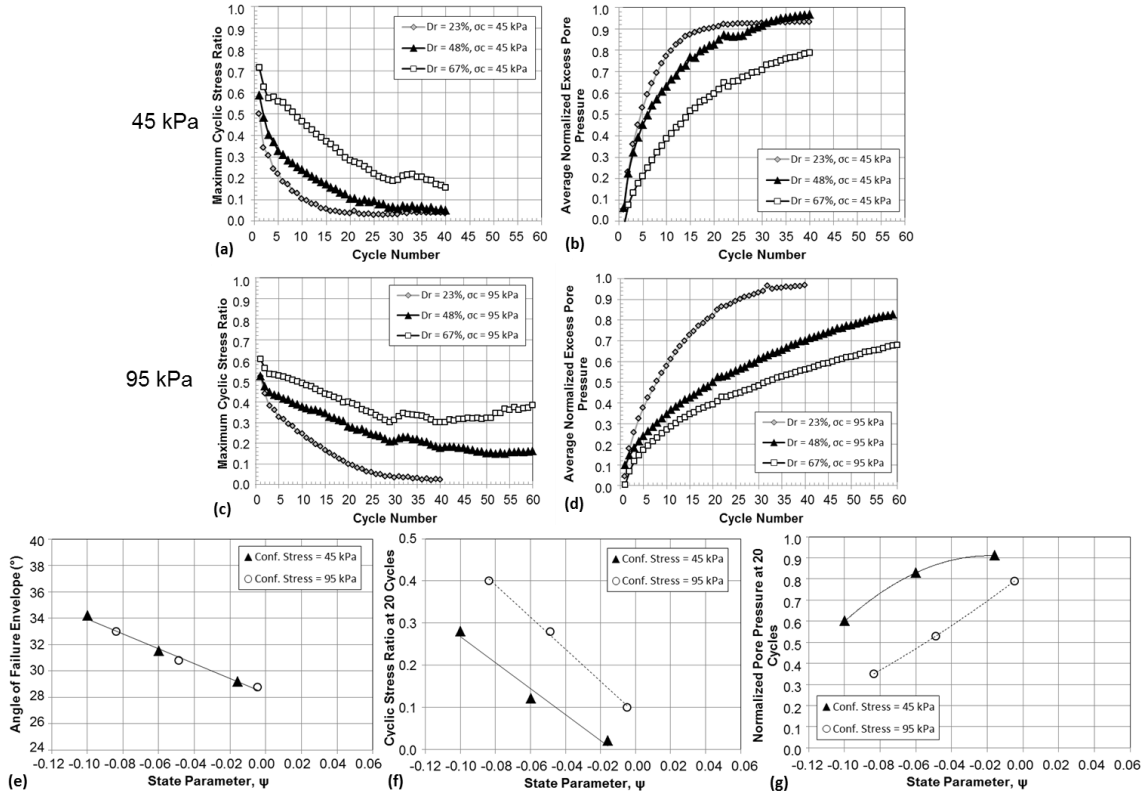

Figure 7.6: Maximum cyclic stress ratio (τ_{max}/σ_c) and average normalized pore pressures (u_{avg}/σ_c) for torsional tests Ottawa 20-30 specimens of varying relative densities under confining stresses of (a) 45 and (b) 95 kPa. (e) Angle of failure envelope and (f) τ_{max}/σ_c and (g) u_{avg}/σ_c at 20 cycles as a function of state parameter.

The results presented in Figures 7.6e through 7.6g present the trends observed as a function of state parameter. The angle of the failure envelopes, which correspond to a residual shear stage, showed to decrease with increasing state parameter, and the results from tests under σ_c of 45 and 95 kPa followed a unique trend (Figure 7.6e). Assuming that 15 mm of sleeve displacement to induce shear strains large enough to take the contacting soil to critical state, these results contradict the classical notion of soil mechanics that the critical state friction angle of a soil is not affected by the initial density or confining stress. On the other hand, the peak friction angle or friction angle at the onset of strain softening that has been shown to decrease with increasing state parameter (Been and Jefferies 1985; Alarcon-Guzman, et al. 1988; Yang 2002; Huang, et al. 2014). However, it should be noted that Been, et al. (1991) published data that suggest that the critical state friction angle does decrease with state parameter for sands of very high initial void ratios. As discussed later in this chapter, this decrease with state parameter is postulated to be an indication of the influence of the combined response of the soil within the shear zone that is in a critical state and the soil within the secondary shear zone which does not reach a critical state and thus its behavior is affected by its initial state.

The results presented in Figures 7.6f and 7.6g correspond to the τ_{max}/σ_c and u_{avg}/σ_c values at 20 one-way cycles, chosen to aid in the results comparison (it should be noted that the trends presented were followed throughout the entire tests). The tests performed under a σ_c of 95 kPa showed a slower rate of shear stress degradation as well as of excess pore pressure generation for all the relative densities. These results contradict the trend typically associated with increasing mean principal stress. Considering specimens of same initial void ratio, increasing the mean principal stress will move the state of the specimen horizontally to the right if plotted in e-p space. This will result in an increase in the magnitude of the state parameter, which should result in a more contractive specimen behavior. However, the results presented in Figure 7.6g indicate a more contractive

behavior for the specimens confined under a lower σ_c of 45 kPa, as shown by their faster rate of excess pore pressure generation.

The study on the effect of confining pressure was complemented with DEM simulations of drained cyclic torsional interface shear tests. Details on the simulation procedure, modeling parameters and calibration procedure can be found in Chapter 3 of this thesis. Table 7.2 and Figures 7.7 show the results of global specimen void ratio and change in global void ratio ($\Delta e_{global} = e_{initial} - e_{measured}$) as a function of one-way cycle number for specimens sheared under confining stresses of 50, 100 and 200 kPa. It should be noted that while the initial void ratio values were smaller for the specimens under larger confining stresses, their state parameters (determined from the initial void ratio and the critical state line presented in Figure 6.3b) were close in magnitude allowing for a direct comparison of the results. It can be observed in Figure 7.7 that after an initial dilative response, all the specimens showed cumulative decreases in global void ratio. The specimen confined under 50 kPa showed the largest amount of contraction, followed by that confined under 100 kPa and then by that under 200 kPa. In undrained conditions the specimen under 50 kPa would have generated excess pore pressures at a larger rate, followed by that under 100 kPa and 200 kPa respectively. This trend agrees with that observed from laboratory tests shown in Figures 7.6f and 7.6g.

Table 7.2: Specimen void ratio as a function of cycle number for torsional simulations.

	50 kPa		100 kPa		200 kPa	
	e_{global}	Δe_{global}	e_{global}	Δe_{global}	e_{global}	Δe_{global}
Initial	0.211	0.000	0.198	0.000	0.177	0.000
1 Cycle	0.213	0.002	0.203	0.006	0.175	-0.002
5 Cycles	0.211	0.000	0.195	-0.002	0.180	0.003
10 Cycles	0.202	-0.009	0.191	-0.007	0.175	-0.002
20 Cycles	0.199	-0.012	0.189	-0.010	0.172	-0.006
40 Cycles	0.195	-0.016	0.188	-0.011	0.169	-0.008
60 Cycles	0.194	-0.017	0.187	-0.013	0.168	-0.010
80 Cycles	0.194	-0.019	0.183	-0.015	0.166	-0.011
100 Cycles	0.193	-0.019	0.184	-0.014	0.164	-0.013

The change in local void results ($\Delta e = e_{initial} - e_{measured}$) as a function of distance from the friction sleeves presented in Figures 7.8a through 7.8c correspond to the same simulation results shown in Table 7.2 and Figure 7.7. The horizontal dashed line shows a

change in void ratio of zero, indicating the "as compacted" void ratio. The results show dilation at distances close to the friction sleeve, of up to 4.5 mm, which agrees closely with the extent of the shear zones observed in experimental and numerical measurements presented in Chapters 4 and 6. However, the magnitude of the dilation was largest at cycle numbers from 1 to 5 for all the simulations. At larger cycle numbers, the magnitude of the dilation did not keep increasing but it decreased slightly. On the other hand, the void ratio change values at locations within the secondary shear zone (see Figure 7.2a) consistently decreased with increasing number of cycles. These results illustrate the contractive tendency of all the specimens.

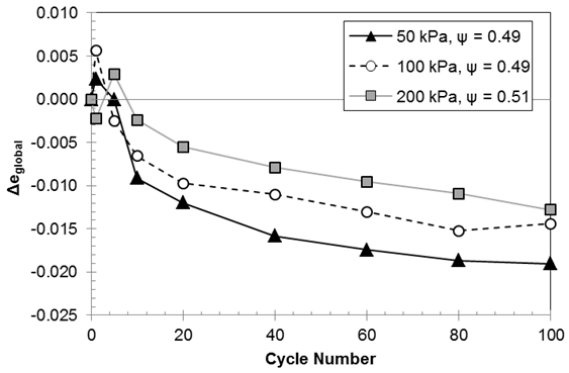

Figure 7.7: Average change in void ratio shown by specimens under different confining stress during cyclic torsional DEM simulations.

These results have important implications that should be considered for the interpretation of the results. As shown in Figures 7.1a and 7.1b, the majority of the tests were performed on specimens with negative state parameters, which in theory should show a dilative behavior. However, all of the specimens showed a contractive behavior with increasing number of cycles. As such, it is proposed that the soil undergoing dilation, located within the shear zone, reaches a critical state (i.e. shearing under constant volume) during monotonic shearing, and subsequent contraction during shear reversals, results in the generation of positive pore pressures in undrained conditions. However, the soil undergoing contraction, located within the secondary shear zone, does not reach a critical state and keeps contracting (or generating positive pore pressures in

undrained conditions) throughout the entire monotonic and shear reversal stages. To this point, it is important to recognize that the torsional interface shear response does not correspond to that of an interface system at critical state, but shows the combined effects of soil that is at critical state and soil that is still undergoing volume change tendencies. Therefore, a specimen with a negative state parameter subjected to torsional shear will not necessarily show a dilative behavior.

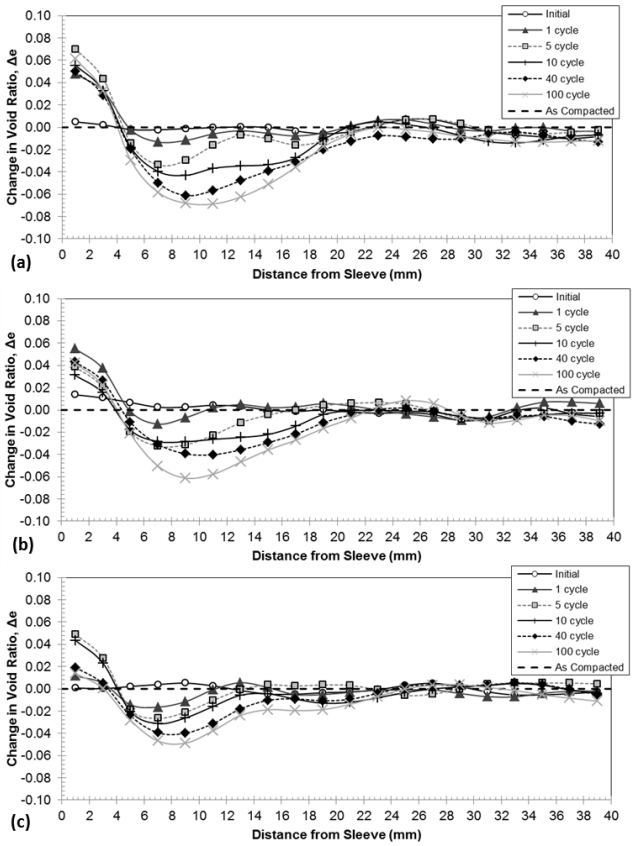

Figure 7.8: Shear-induced changes in void ratio shown by specimens under confining stress of (a) 50, (b) 100 and (c) 200 kPa during cyclic drained torsional DEM simulations.

7.2.4 Effect of Surface Roughness

The effect of friction sleeve surface roughness was studied by means of a series of torsional interface shear tests on specimens of relative densities between 45 and 50% under a confining stress of 45 kPa. The results, in terms of shear stresses, excess pore pressures and stress paths are presented in Figures 7.9a through 7.9o and Table 7.1 for

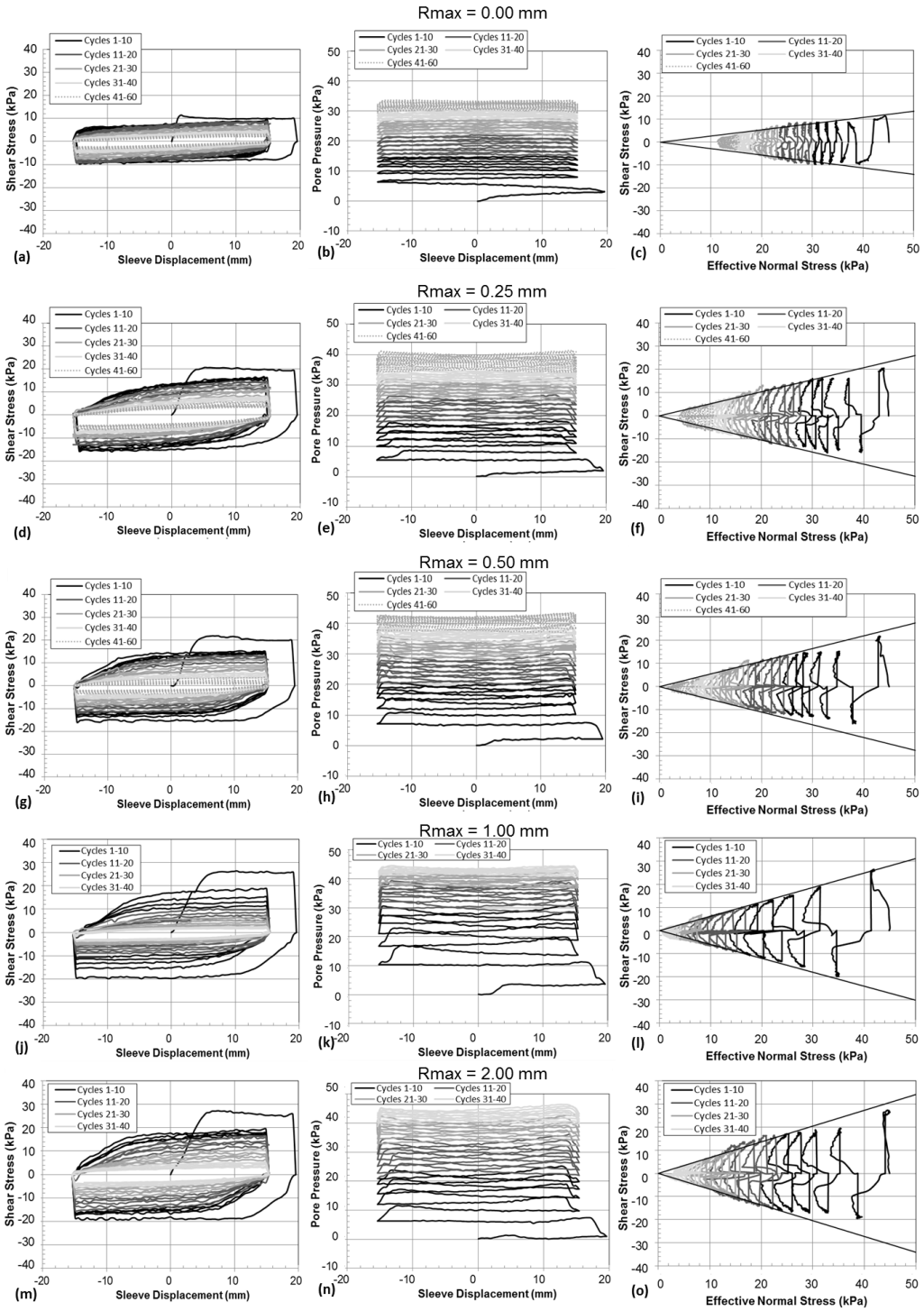

Figure 7.9: Shear stress, excess pore pressure and stress paths measured during cyclic torsional tests on specimens of Ottawa 20-30 sand sheared against friction sleeves of R_{max} of (a)-(c) 0.00 mm, (d)-(f) 0.25 mm, and (g)-(i) 0.50 mm, (j)-(l) 1.00 mm, and (m)-(o) 2.00 mm under a confining stress of 45 kPa.

specimens sheared against friction sleeves of maximum surface roughness, R_{max}, of 0.00, 0.25, 0.50, 1.00 and 2.00 mm. The results show stress reversal loops that decrease in amplitude with increasing number of cycles as a result of increasing excess pore pressures, and stress paths bounded by straight failure envelopes for the tests of this series. Only the specimens sheared against friction sleeves of R_{max} of 2.00, 1.00 and 0.50 mm showed cyclic mobility, at 30, 31 and 53 cycles, respectively. Figures 7.10a and 7.10b show the maximum cyclic stress ratio (τ_{max}/σ_c) and average normalized excess pore pressures (u_{avg}/σ_c) as a function of cycle number, respectively, while Figure 7.10c and 7.10d presents the angle of the failure envelopes and average normalized pore pressures at 20 cycles as a function of surface roughness. The maximum cyclic stress ratio decreases with increasing cycle numbers but do not show a clear trend because they depend on both the interface strength (i.e. angle of failure envelope shown in Figure 7.10c) and the excess pore pressures generated (Figure 7.10b). However, the maximum

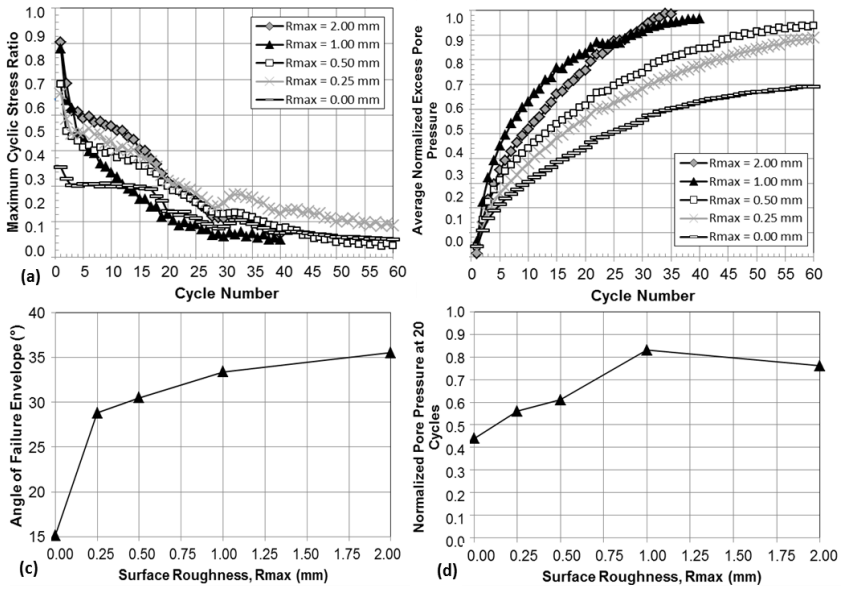

Figure 7.10: (a) Maximum cyclic stress ratio (τ_{max}/σ_c) and (b) average normalized pore pressures (u_{avg}/σ_c) for torsional tests on Ottawa 20-30 specimens of varying relative densities under a σ_c of 45 kPa sheared against sleeves of varying R_{max}. (c) Angle of failure envelope and (d) u_{avg}/σ_c at 20 cycles as a function of R_{max}.

cyclic stress ratio at the first cycle increased with increasing surface roughness, as did the rate of cyclic stress degradation and excess pore pressure generation. The angle of the failure envelope increased sharply with initial increases in surface roughness, and more modestly with subsequent increases (Figure 7.10c). These results show the larger degree of soil shearing induced by sleeves of increasing surface roughness, as previously shown in Chapters 4, 5 and 6 and by other authors (Uesugi and Kishida, 1986; Dove, et al. 1997; Rao, et al. 1998; Frost, et al. 2002; Dietz and Lings 2006). The results also show the ability of the undrained tests to capture this effect.

Figure 7.10d shows the average normalized excess pore pressures at 20 one-way cycles. The results show a near linear increase with surface roughness from R_{max} of 0.00 to 1.00 mm. However, the magnitude of normalized pore pressures decreases with further increases of R_{max}, from 1.00 to 2.00 mm. These result contradicted the expected trend but replicate tests indicated a consistent trend. A plausible explanation for this trend can be provided considering the schematics shown in Figure 7.2c and 7.2d. As the sleeve surface roughness increases, the total magnitude of both negative and positive excess pore pressures increases during monotonic and shear reversals. As such, the decrease in global excess pore pressures generated is originated by a larger increase in negative pore pressures during monotonic shear as compared to the increase in positive ones. This trend can reflect one or both of the following processes: (i) a dilative monotonic response in the shear zone that increased more relative to the contractive response in the secondary shear zone, or (ii) a relative increase of the volume of soil undergoing a dilative response during monotonic shear as compared to that undergoing a contractive response.

Shearing against the sleeves of smooth surfaces (R_{max} = 0.00 mm) induced significant magnitudes of normalized excess pore pressures (u_{avg}/σ_c), reaching values of 0.44 and 0.68 at 20 and 60 cycles, respectively (Figure 7.10d). This is possibly associated to the fact that shearing against smooth surfaces results in non-dilative responses, as

described by Dove and Frost (1999) and Dove, et al. (2006). As such, no negative pore pressures were generated during this test so the measured specimen response reflects only the positive pore pressures generated as a result of small shear strains within the soil mass. This effect can also be observed in the excess pore pressure response shown Figure 7.9b which does not show the progressive decrease in excess pore pressure (dilative behavior) following the stress reversal, as shown in the responses of all other specimens sheared against rougher sleeves (Figures 7.3b, 7.3d. 7.3f, 7.4e, 7.4h, 7.5e, 7.5h, 7.9e, 7.9h, 7.9k, 7.9n). Similar results and conclusions were reported by Mortara, et al. (2007) for cyclic interface shear tests against smooth surfaces (see Figure 2.20b).

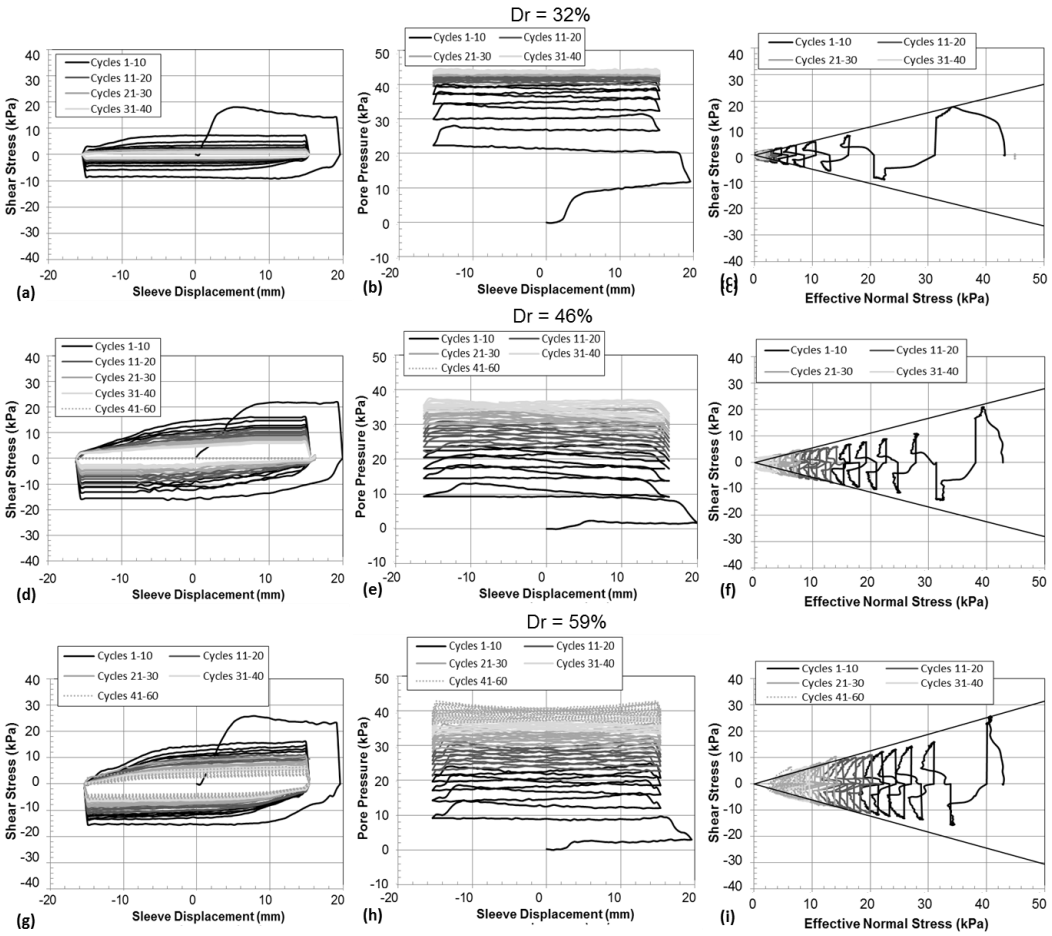

Figure 7.11: Shear stress, excess pore pressure and stress paths observed during cyclic torsional tests on specimens of Blasting 20-30 sand of relative densities of (a)-(c) 23%, (d)-(f) 47%, and (g)-(i) 67% under a confining stress of 45 kPa.

7.2.5 Effect of Grain Angularity

Torsional tests performed on Blasting 20-30 (angular) sand specimens of relative densities of 32, 46 and 59% provided the opportunity to study the effect of the particle angularity. For reference, the peak and residual friction angles for Blasting 20-30 sand measured in direct shear are of 43.5° and 34.6°, respectively, and those for Ottawa 20-30 sand are of 38.5° and 29.2°. The results presented in Figures 7.11a through 7.11i show similar trends as the ones previously described. Namely, the amplitude of the shear reversal loops decreased with increasing cycle number as a result of increasing excess pore pressures, and the stress paths were bounded by linear failure envelopes.

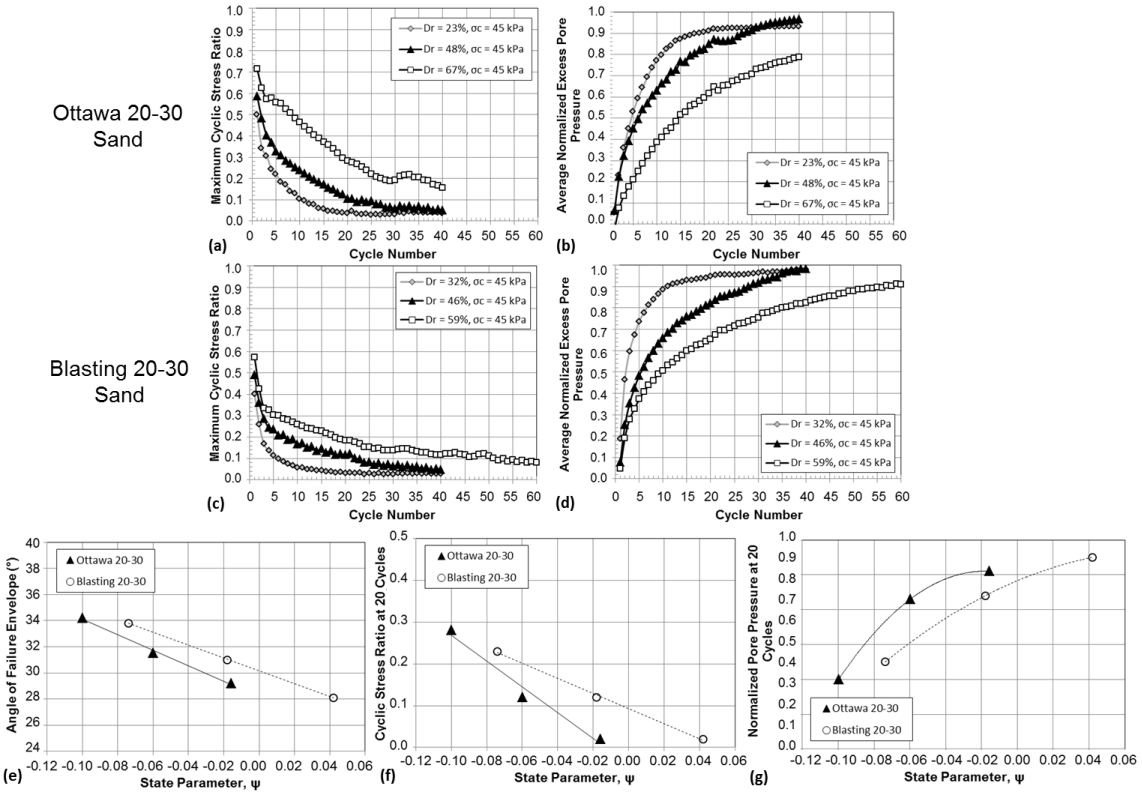

Figure 7.12: Maximum cyclic stress ratio (τ_{max}/σ_c) and normalized pore pressures (u_{avg}/σ_c) for torsional tests on (a) Ottawa 20-30 and (b) Blasting 20-30 specimens of varying relative densities under a σ_c of 45 kPa. (e) Angle of failure envelope, (f) τ_{max}/σ_c and (g) u_{avg}/σ_c at 20 cycles as a function of state parameter.

Figures 7.12a and 7.12b show the maximum cyclic stress ratio and average normalized excess pore pressures as a function of cycle number for tests performed on Ottawa 20-30 sand, while Figures 7.12c and 7.12d present similar results corresponding to tests on Blasting 20-30 sand (results also shown in Table 7.1). When plotted in terms of state parameter, the tests on Blasting 20-30 sand showed larger angles of the failure envelopes as shown in Figure 7.12e. These results are reasonable considering the higher peak and residual friction angle of the Blasting 20-30 sand. The results presented in Figures 7.12f and 7.12g show that the specimens of Blasting 20-30 sand underwent stress degradation and excess pore pressure generation at lower rates than the specimens of Ottawa 20-30 sand, indicating that increasing particle angularity resulted in a greater resistance to cyclic mobility. As described by authors such as Ashmawy, et al. (2003), the larger level of irregularities in terms of angularity and surface roughness of the angular sands provide them with a more dilative fabric and larger resistance to cyclic mobility and/or liquefaction.

7.2.6 Effect of Shear Direction

Cyclic axial interface shear tests performed on Ottawa 20-30 sand specimens of varying relative densities confined under a σ_c of 45 kPa allowed for studying the difference in response as a result of shear direction (torsional versus axial shear). The mobilized shear stress, excess pore pressure generation and stress path results are presented in Figures 7.13a through 7.13i. The results follow similar trends as the torsional tests previously presented, showing excess pore pressure generation with increasing number of cycles and stress paths that are bounded by straight failure envelopes. Only the loosest specimen (Dr = 29%) showed cyclic mobility, after 34 cycles. Axial shear showed a higher resistance to cyclic mobility as compared to the torsional shear, which induced cyclic mobility of the specimens of relative density of 23 and 45% after 22 and 31 cycles, respectively. Figure 7.14a and 7.14b show the maximum cyclic stress ratio (τ_{max}/σ_c) and

average normalized excess pore pressures (u_{avg}/σ_c) as a function of cycle number during torsional tests, while Figures 7.14c and 7.14d show similar results for axial tests (results also shown in Table 7.1). Figure 7.14e shows the angle of the failure envelopes for axial and torsional tests. As previously shown, the angles of the failure envelopes for torsional tests decrease with increasing state parameter. This is an indication of a measured behavior that is a combined response of the soil at critical state within the primary shear zone and the soil that is not in a critical state within the secondary shear zone. In contrast, the angles of the failure envelopes of the axial tests show only a weak decreasing trend with state parameter, more conforming with the theory of critical state soil mechanics.

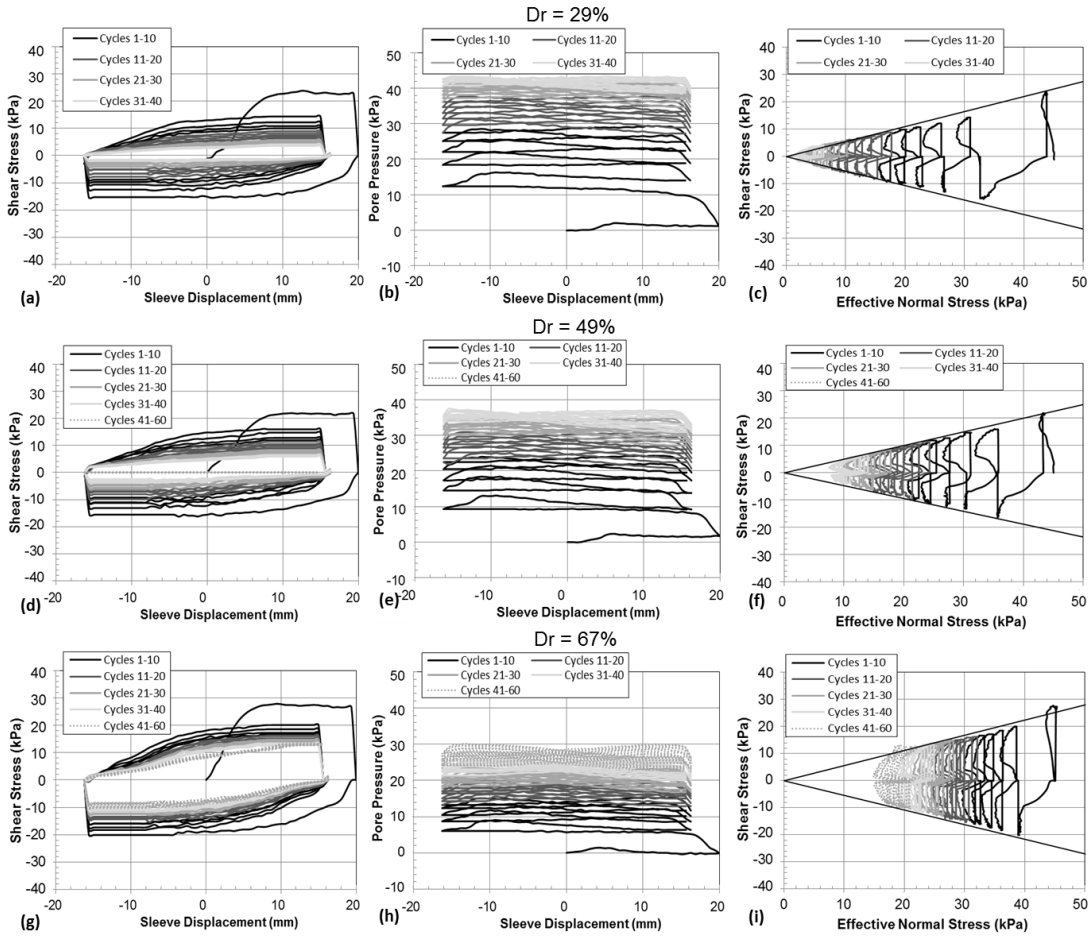

Figure 7.13: Shear stress, excess pore pressure and stress paths observed during cyclic axial tests on specimens of Ottawa 20-30 sand of relative densities of (a)-(c) 29%, (d)-(f) 49%, and (g)-(i) 67% under a confining stress of 45 kPa.

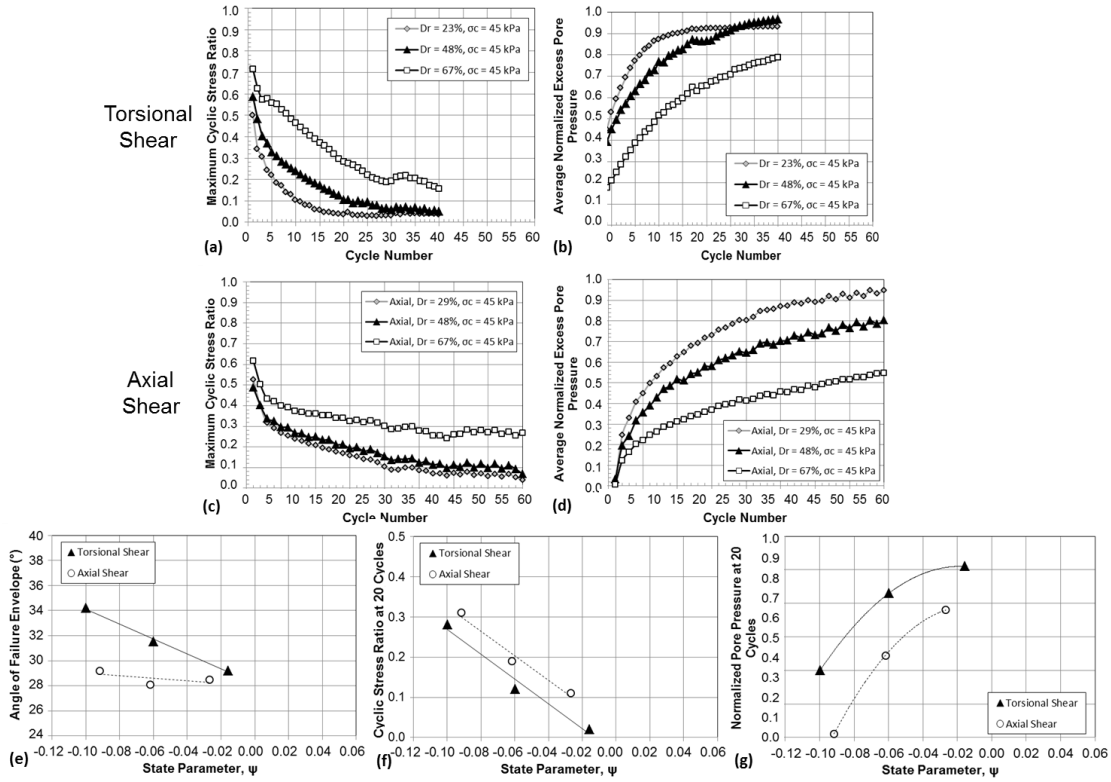

Figure 7.14: Maximum cyclic stress ratio (τ_{max}/σ_c) and average normalized pore pressures (u_{avg}/σ_c) for tests on Ottawa 20-30 specimens of varying relative densities under a σ_c of 45 kPa subjected to (a)-(b) axial and (c)-(d) torsional shear. (e) Angle of failure envelope (f) τ_{max}/σ_c and (g) u_{avg}/σ_c at 20 cycles as a function of state parameter.

The difference in response of specimens subjected to torsional and axial shear can be further analyzed in light of the shear-induced changes in void ratio measured experimentally and presented in Figure 7.15 (and in Chapter 4). Axial shearing engages a volume of soil that consists of the primary shear zone that undergoes dilation and a small volume of soil in the secondary shear zone that undergoes modest contraction. Therefore, it is reasonable to conclude that the soil response to axial shear is strongly influenced by the large shear strain behavior of the soil within the primary shear zone which shows a contractive or dilative response depending on the shearing stage (initiation of shear reversal versus large shear displacement). On the other hand, shearing in the torsional direction engages soil within the primary shear zone and a much larger volume of soil in

the secondary shear zone that only undergoes contraction and has undergone relatively small shear strains, thus being affected by its initial state. These results indicate that the soil response measured in torsional shear is more sensitive to the soil state parameter.

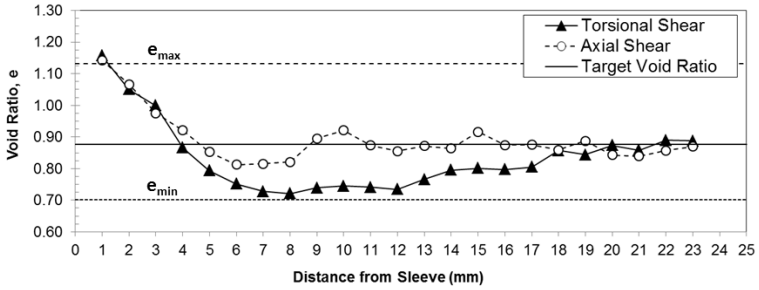

Figure 7.15: Shear-induced local void ratio changes in specimens subjected to drained torsional and axial axisymmetric interface shear.

Figures 7.14f and 7.14g show a comparison of the cyclic shear stress ratio and normalized excess pore pressures at 20 one-way cycles. These results show that torsional shear consistently induced shear stress degradation and excess pore water pressures at a larger rate than axial shear. This trend is shown clearly in the comparison of the excess pore pressures generated as a function of cycle number for specimens of low, medium and high relative densities shown in Figures 7.16a through 7.16c. These results are in agreement with the shear-induced volume changes during torsional shear described above and presented in Chapters 4 and 6 of this thesis. As discussed in the following sections, these results have important implications on the use of cyclic axial and torsional interface shear test as means to study the cyclic behavior and liquefaction potential of soils in-situ.

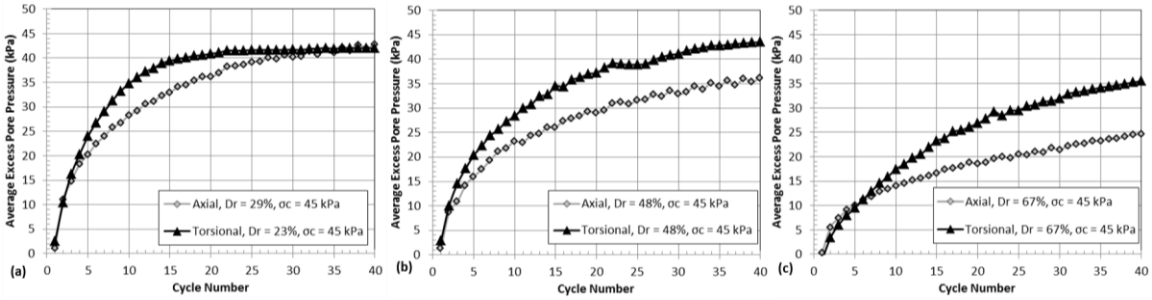

Figure 7.16: Average excess pore pressure generation during torsional and axial tests on specimens of (a) low, (b) medium and (c) high relative densities.

7.3 Implications on Geotechnical Site Characterization for Liquefaction Risk Assessment and Conclusions

Geotechnical site characterization has typically employed invasive penetration tests for the assessment of liquefaction risk potential, such as the Cone Penetration Test (CPT) and the Standard Penetration Test (SPT) (e.g. Boulanger and Idriss, 2014). However, other tests such as the Dilatometer Test (DMT) and the measurement of shear wave velocity (V_s) have also been utilized to study liquefaction in sandy and silty soils (e.g. Monaco, et al. 2005; Andurs and Stokoe, 2000). Apart from the measurement of V_s, these assessment methods rely on device-level disturbed soil response measurements that are controlled by soil density and strength and state of stress. However, up to date, there is no theoretically sound methodology to evaluate or separate the effect of density, strength and state of stresses on these in-situ measurements; therefore, the liquefaction assessment methodologies that rely on these measurements have remained mainly empirical. Authors such as Robertson (2009) and Robertson (2010) have investigated the relationship between the cone tip resistance (q_t) and the state parameter. While these methodologies have the advantage of utilizing theoretically-sound interpretations of critical state soil mechanics to assess liquefaction, the in-situ determination of the state parameter still relies completely on empirical relationships. Jefferies and Been (2006) point out that the relationship between the state parameter and the q_t measurement is complex and depends on soil parameters such as shear strength and stiffness, compressibility, plastic hardening as well as on the soil state of stresses. The authors provide a methodology that uses a combination of CPT data and laboratory tests on reconstituted samples to determine the in-situ state parameter that then can be utilized to assess the liquefaction potential of the soil layer. Nevertheless, none of the mentioned methodologies consider the particle-level response of the soil deposit or specimen, which

represent a drawback as compared to the smaller scale measurement provided by the torsional shear tests presented herein.

The results presented in this chapter have shown that torsional interface shear can induce dilative or contractive soil volume-change tendencies in the vicinity of the friction sleeves and only contractive ones further away from it. In undrained conditions, these tendencies get translated to negative and positive excess pore pressures generated, respectively, in the soil closest to the sleeve and positive ones in the soil further away. These results show that torsional shear involves a more localized measurement that averages the response of a smaller volume of soil as compared to the larger highly stressed bulb captured in measurements such as q_t during CPT (Lunne, et al. 1997; Schmertmann, 1977). Furthermore, contractive tendencies dominate the pore pressure generation response during torsional tests which result in positive excess pore pressures, and loose soils can be taken to cyclic mobility conditions. While the capability of torsional shear to induce significant excess pore pressures in free-draining conditions has not been evaluated, the existence of a more controlled methodology to measure the soil response to cyclic or monotonic loading would certainly be advantageous for liquefaction assessment. In fact, an in-situ torsional shear test could be used to determine both the undrained and drained steady-state responses of the soil. Conceptually, shearing at a fast rate would generate significant pore pressures that would result in undrained loading conditions, while shearing at a sufficiently slow rate would not generate excess pore pressures and would result in drained loading conditions. Furthermore, the results presented herein showed that soil shearing against highly textured surfaces resulted in faster excess pore pressure generation; therefore, these friction sleeves would be utilized during in-situ testing.

Considering the localized soil response captured by torsional interface shear, it is important that this measurement is not governed by external effects, such as insertion disturbance if the friction sleeve is placed behind an invasive penetration device. As such,

the design and fabrication plans of the in-situ device that measures soil response under torsional shear, the Multi-Piezo-Friction-Torsion Attachment (MPFTA) described in Chapter 2, includes the deployment of the friction sleeves behind a self-boring leading unit that would minimize the insertion disturbance effects.

The results presented herein show that torsional shear behavior can be evaluated utilizing classical soil mechanics concepts. Namely, looser specimens generated excess pore pressures at larger rates, higher cyclic mobility resistance was mobilized by more angular assemblies (e.g. soils of larger friction angle) and shearing against rougher surfaces resulted in larger rates of excess pore pressure generation. Thus, a basis for the interpretation of results can be readily developed. However, the results showed that increasing confining stresses resulted in slower pore pressure generation, contradicting the expected trend. It is believed that a reduction in the volume of soil undergoing contractive tendencies or a smaller contribution of the collapsing sand fabric upon stress reversal, is the reason for this,. Finally, torsional interface shear showed to induce excess pore pressures at a larger rate than axial interface shear, and for its measured failure envelope to be more sensitive to the soil state parameter. This makes torsional shear a more attractive mode than axial shear for the study of the strength degradation and excess pore pressure generation responses of soils, and ultimately making torsional shear a more capable test for the assessment of soil liquefaction potential.

The results presented in this chapter showed the effect of confining stress, relative density, sleeve surface roughness, sand angularity and shearing direction. While the results are highly consistent with the understanding of soil mechanics, it is noted that testing under a wider range of conditions should be performed to further understand the effect of soil properties and testing and boundary conditions on the measured response. Future research will expand the database of drained and undrained torsional interface shear results.

CHAPTER 8

OPTIMIZING GEOMATERIAL SURFACE ROUGHNESS FOR INCREASED INTERFACE SYSTEM CAPACITY

8.1 Introduction

This chapter presents a study on the effect of surface roughness form on the capacity and behavior of sand-structure interface systems. Throughout this chapter roughness form is defined as the collection of geometrical characteristics of the roughness profile. The laboratory experiments performed on model-shafts against sands of different grain shapes and sizes showed that surfaces with periodic and non-clogging surface roughness profiles (termed as "structured roughness" surfaces) can mobilize larger interface friction angles than surfaces of non-periodic and clogging-prone roughness profiles (termed as "random roughness" surfaces). The shear strength of surfaces with structured roughness was shown to exceed $\delta = \varphi$ conditions when testing surfaces of large roughness. The surfaces of structured roughness were composed of model-shaft sections with a staggered pattern of protruding diamonds that effectively engaged the soil while preventing interface clogging (see Chapters 3 and 4), while model-shaft sections wrapped in sandpaper sheets were used as the surfaces of random roughness. The reason for the observed difference in behavior is that shearing against structured roughnesses mobilized interface friction as well as passive resistances, as opposed to shearing against surfaces of random roughness that only mobilized structure-sand or sand-sand friction as a result of interface clogging. This observation was validated by means of post-shear sand deformation measurements.

A methodology for quantifying the magnitude of the passive resistances is presented and verified. The magnitude of the passive resistances mobilized during shear

against structured roughnesses was found to be dictated by the sand internal friction. This study was complemented by DEM simulations of interface systems composed of soil particles and random (i.e. sandpaper), structured (i.e. diamond) and ribbed surfaces. These simulations allowed defining in greater detail the differences in behavior by providing information on particle-scale interactions of the surfaces in contact with assemblies of different initial density and particle sizes. The results presented herein have important implications for the attainable capacity of geotechnical structures such as deep foundations and retaining walls, among others, which can be enhanced by engineering the surface roughness characteristics of these structures and how these transfer load to the contacting soil mass.

8.1.1 Experimental and Numerical Methods

The results presented in this chapter correspond to axial tests performed on the axisymmetric device for drained interface shear (Figures 3.5a and 3.5b), as described in Chapter 3 of this thesis. All the tests were performed on specimens of relative densities between 60 and 65% confined under a constant stress of 50 kPa. Ottawa 20-30 (medium-sized, rounded), Ottawa 50-70 (medium-fine, sub-rounded to sub-angular) and Blasting 20-30 (medium sized, angular) sands were used for all tests. Figures 3.1a through 3.1c, 3.2a and 3.2b and Tables 3.1 and 3.2 show photographs, grain size distribution curves, direct shear results, and other particle and packing properties of these sands. The surfaces tested included roughnesses of different form as follows: (i) friction sleeves textured with the diamond pattern used throughout this thesis (Figures 3.3a through 3.3d and 8.1b), (ii) smooth sleeves wrapped with sandpaper sheets (Figure 8.1c) and (iii) a friction sleeve textured with consecutive rings that result in ribs perpendicular to the direction of shear displacement (Figure 8.1d). The former are referred to as surfaces of "structured" roughness throughout this chapter because their periodic texturing pattern consists of elements that protrude outside the base diameter of the sleeve, and they have an

untextured space between any two diamond elements (i.e. passthrough) that prevents particles from clogging the interface (Figure 8.1c). The sandpaper sleeves are referred to as surfaces of "random" roughness because they are composed of non-periodic features that go above and below the surface's baseline (Figures 8.1a and 8.1b). These features cover the entire surface of the sleeves and promote interface clogging. The ribbed sleeve has a profile consisting of closely-spaced square steps of the same height and is also believed to promote interface clogging (Figure 8.1d). Interface clogging was defined in Chapter 2 as the process of surface roughness change during shear as a result of soil particles getting trapped in between the asperities of the surface texture, which can result in systems that behave like soil-soil interfaces (Figures 2.12a through 2.12c).

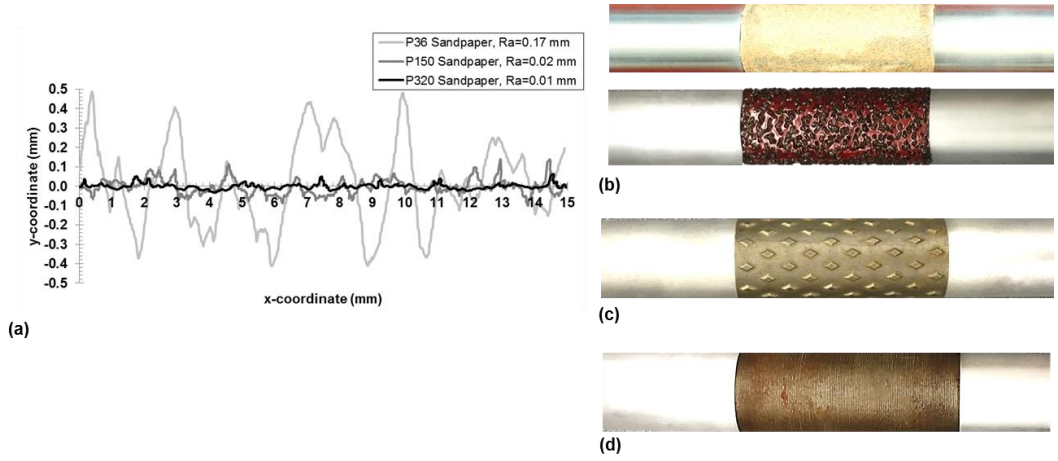

Figure 8.1: (a) Profile of various sandpaper sheets. (b) Sandpaper, (c) textured and (d) ribbed sleeves mounted in between the testing rods.

Table 8.1 shows a summary of all the surfaces tested in this study. It should be noted that only one ribbed sleeve was tested. The surface roughness parameters of the structured and ribbed surfaces were determined from their geometrical configuration, while the roughnesses for the "random" surfaces were measured with a Taylor-Hobson Talysurf profilometer with a stylus diamond conical tip of 2 μm in radius and an angle of 60°. The shear zone deformation tests presented in this chapter were performed following the methodology involving powder phenolic resin described in Chapter 3 for shear zone

characterization tests. Information regarding the repeatability of these tests can also be found in Chapter 3.

Table 8.1: Roughness characteristics of friction sleeves tested.

				20-30 Sands		50-70 Sand	
Surface Type	**Descriptor Name**	**R_a (mm)**	**R_{max} (mm)**	**Rn,a**	**$R_{n,max}$**	**Rn,a**	**$R_{n,max}$**
Structured	H = 0.00 mm	0.001	0.01	0.001	0.01	0.004	0.04
Structured	H = 0.00 mm	0.066	0.25	0.092	0.35	0.254	0.96
Structured	H = 0.00 mm	0.117	0.50	0.163	0.69	0.450	1.92
Structured	H = 0.00 mm	0.185	1.00	0.257	1.39	0.712	3.85
Structured	H = 0.00 mm	0.226	2.00	0.314	2.78	0.869	7.69
Random	Smooth Sleeve	0.001	0.02	0.001	0.03	0.004	0.08
Random	320 Grit	0.010	0.09	0.014	0.13	0.038	0.35
Random	150 Grit	0.020	0.14	0.028	0.19	0.077	0.54
Random	100 Grit	0.034	0.28	0.047	0.39	0.131	1.08
Random	60 Grit	0.076	0.41	0.106	0.57	0.292	1.58
Random	36 Grit	0.171	0.88	0.238	1.22	0.658	3.38
Random	16 Grit	0.290	1.52	0.403	2.11	1.115	5.85
Ribbed	Ribbed	0.067	0.21	0.093	0.29	0.258	0.81

The numerical simulations presented in this chapter were performed with the axial DEM model presented in Figure 8.2. This model was built to simulate as close as possible the configuration of the axisymmetric device for drained interface shear used for the laboratory tests described in Chapter 3. The sample preparation methodology and model parameters used for all the simulations were the same used in the previous chapters of this thesis. A summary of the latter is shown in Table 8.2. The reader can refer to Chapter 3 for details on the parametric study performed in order to calibrate the model and select the parameters. All the specimens consisted of two-particle clumps with an aspect ratio (AR) of 1.5 and the linear-elastic contact model was employed for all simulations.

The friction sleeves consisted of surfaces located at the bottom wall of the model. These surfaces consisted of walls with a 2D profile defined as follows: (i) for the random roughness simulations, the profile was taken from a profilometer measurement of a 36 grit sandpaper, (ii) for the structured and ribbed simulations, the profiles were defined as the geometrical profiles of the actual friction sleeves (H=1.0 mm and ribbed from Table 8.1), as shown in Figure 8.2.

Table 8.2: DEM simulation parameters.

Mean Particle-Clump Size, D_{50} (mm)	Particle Clump Aspect Ratio, AR	Particle Density (kg/m^3)	Interparticle Friction Coefficient, $\mu_{p\text{-}p}$	Particle Normal Stiffness, k_n (N/m)	Particle Shear Stiffness, k_s (N/m)	Sleeve Friction Coefficient, μ_s	Wall Friction Coefficient, μ_w	Wall Normal Stiffness, $k_{n\text{-}w}$ (N/m)	Wall Shear Stiffness, $k_{s\text{-}w}$ (N/m)
0.90	1.50	2650	0.45	$1x10^7$	$1x10^7$	0.25	0.20	$1x10^8$	$1x10^8$

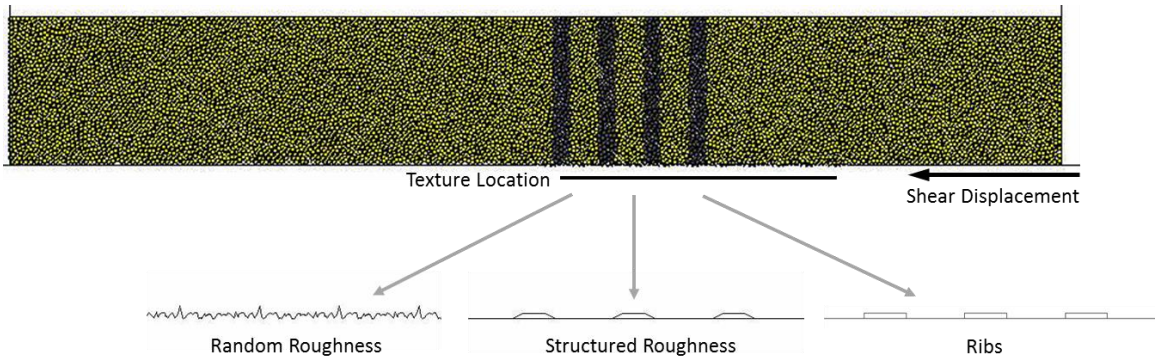

Figure 8.2: DEM model for numerical simulations with different roughness forms.

8.2 Experimental Results

This section presents the results of axisymmetric drained interface shear experimental on surfaces of random, structured and ribbed roughness. These results consist of global stress-displacement responses and soil deformation measurements taken from post-shear specimens impregnated with powder phenolic resin as previously described.

8.2.1 Effect of Soil Internal Friction

According to the classical understanding of interface shear behavior, the soil friction angle has a significant effect on the shear response of interface systems. Figure 8.3a shows that this is not true for interface systems consisting of smooth surfaces such as the smooth friction sleeves tested. These friction sleeves are used for conventional CPT testing, and their surface roughness is prescribed by ASTM D 5778-07 standards to an average roughness, R_a, of 0.001 mm. As such, the stress ratio-displacement curves for the tests on the three different sands show similar mobilized loads. This observation agrees with previous studies by Frost and DeJong (2005) and Martinez and Frost (2014b).

Figures 8.3b, 8.3c and 8.3d show that tests between rough surfaces and Blasting 20-30 sand mobilized larger loads, followed by those with Ottawa 50-70 sand and lastly by tests with Ottawa 20-30 sand for the three types of roughnesses tested (i.e. random, ribbed and structured). This agrees with the measured particle shape of the sands and with the measured direct shear friction angles shown in Tables 3.1 and 3.2 (Blasting 20-30: R = 0.32, φ_{peak} = 43.5°, φ_{res} = 34.6°; Ottawa 50-70: R = 0.50, φ_{peak} = 37.5°, φ_{res} = 31.8°; Ottawa 20-30: R = 0.73, φ_{peak} = 38.5°, φ_{res} = 29.2°).

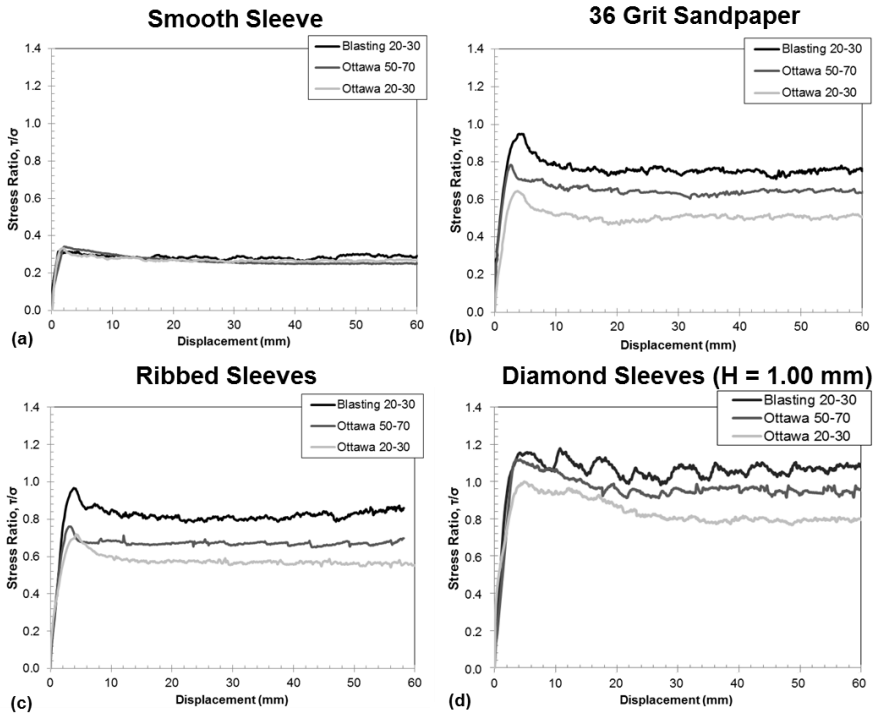

Figure 8.3: Interface shear tests on Blasting 20-30, Ottawa 50-70 and Ottawa 20-30 sands against (a) smooth sleeves, (b) 36 grit sandpaper sleeves, (c) ribbed sleeves and (d) diamond structured roughness sleeves.

8.2.2 Effect of Surface Roughness

Tests with sleeves of random and structured roughness of different magnitudes were performed for the three sands. This allowed defining relationships between the mobilized interface strengths (i.e. interface friction angles or stress ratios) and the magnitude of the surface roughness. Figures 8.4a through 8.4c show selected results of

tests against sleeves of random roughness, while Figures 8.4 d through 8.4f show select results of tests against sleeves of structured roughness. The results show that initial increases in surface roughness result in significant increases in mobilized stress ratio for the tests with both random and structured surfaces. However, the mobilized loads from tests against random surfaces show to reach stable values at larger surface roughnesses, as shown by the curves for tests against sandpaper sleeves of 100 and 16 grits which correspond to average roughnesses of 0.034 and 0.171 mm respectively. On the other hand, the tests against sleeves of structured roughness showed to mobilize larger stress ratios with increasing roughness for all the sleeves tested, which covered an average roughness range of 0.01 to 0.226 mm. This important difference in behavior is shown clearly in Figures 8.5a through 8.5c and Table 8.3 in terms of interface friction angles ($\delta = (\tan^{-1}(\tau/\sigma))$ (note that the direct shear friction angles are also included in the figures).

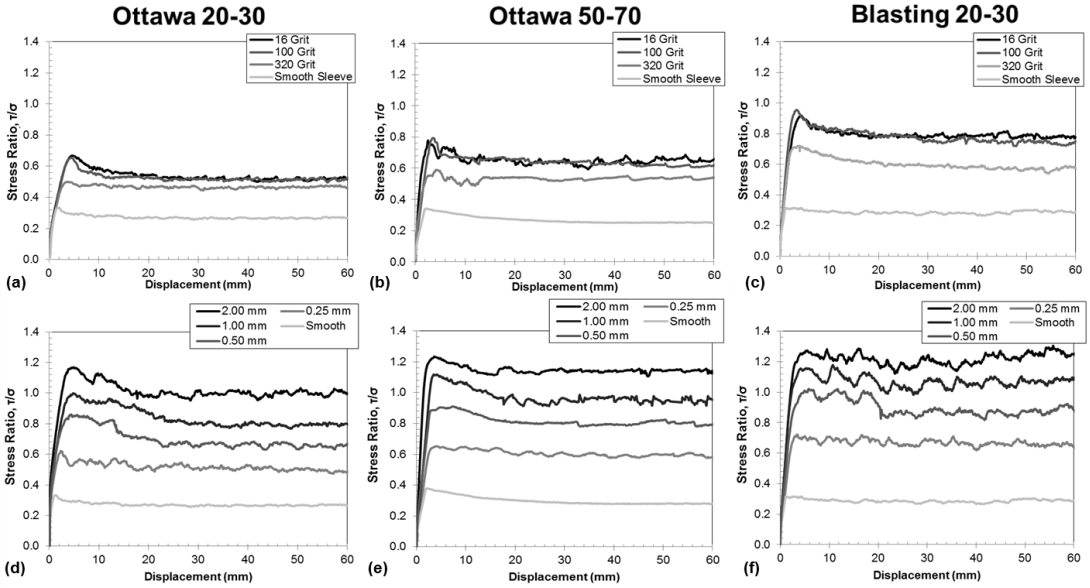

Figure 8.4: Effect of surface roughness on interface shear tests. (a) Ottawa 20-30, (b) Ottawa 50-70 and (c) Blasting 20-30 against sleeves of random roughness. (d) Ottawa 20-30, (e) Ottawa 50-70 and (e) Blasting 20-30 against sleeves of structured roughness.

The peak and residual interface friction angles from tests against sleeves of random roughness (solid symbols) showed to follow the well-known bilinear relationship

described by Uesugi and Kishida (1986) that indicates that at large surface roughnesses, δ = φ conditions are reached. Two important implications can be drawn from this relationship: (i) the surface roughness of a material can be designed so that the interface strength is equal to the internal soil friction; (ii) interface systems that follow this relationship are limited to the shear strength of the contacting soil mass.

The results for the tests performed against sleeves of structured roughness (open symbols in the figures) do not show a bilinear relationship with increasing surface roughness because they reflect the contributions of interface friction as well as passive resistances. The mobilized interface friction angles keep increasing with surface roughness, but at a decreasing rate. This trend is followed by the tests on the three sands tested. The implications of these results are that surfaces of structured roughness can in fact mobilize interface strengths that exceed that of the soil mass. This trend was observed irrespective of the roughness parameter (R_a, R_{max} or R_n) used in the x-axis.

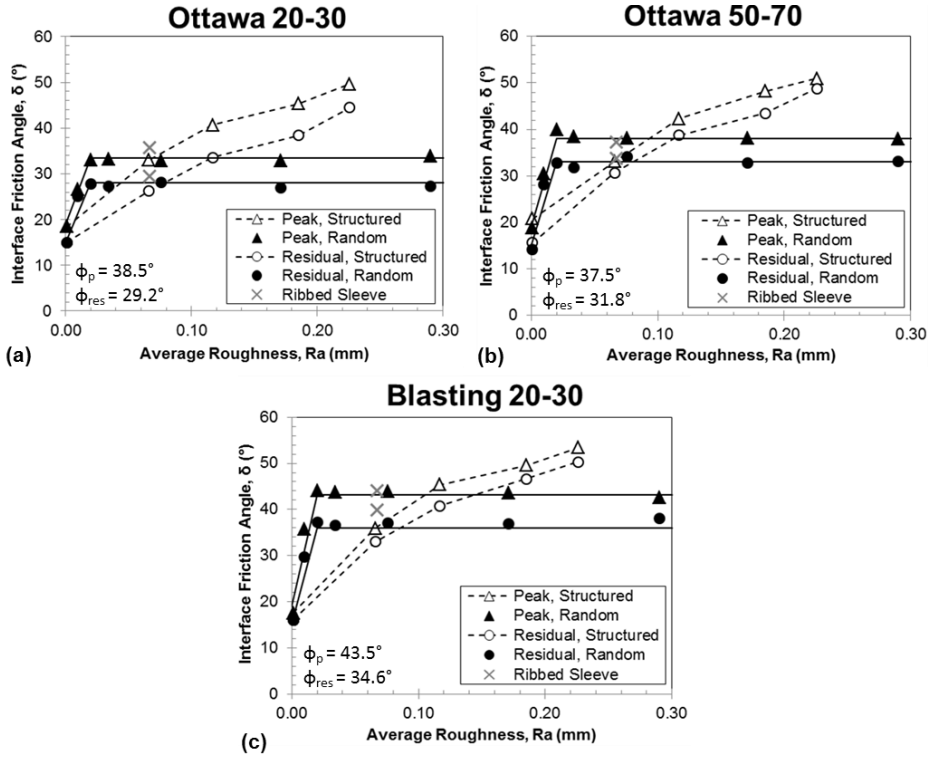

Figure 8.5: Interface peak and residual friction angles mobilized as a function of surface roughness, R_a. Tests on (a) Ottawa 20-30, (b) Ottawa 50-70 and (c) Blasting 20-30 sands.

Table 8.3: Mobilized stress ratios, interface friction angles and annular penetration forces for interface shear tests against surfaces of random, structured and ribbed roughnesses.

Sand Type	Roughness Type	R_a (mm)	$(\tau/\sigma)_{peak}$	$(\tau/\sigma)_{residual}$	Strain Softening (τ/σ)	Measured δ_{peak} (°)	Measured δ_{res} (°)	Annular Penetration Force, AP (τ/σ)	Corrected δ_{peak} (°)	Corrected δ_{res} (°)
Ottawa 20-30	Random	0.001	0.33	0.27	0.07	18.5	15.0	N/A	18.5	15.0
Ottawa 20-30	Random	0.010	0.50	0.47	0.03	26.6	25.0	N/A	26.6	25.0
Ottawa 20-30	Random	0.020	0.65	0.53	0.12	33.0	27.8	N/A	33.0	27.8
Ottawa 20-30	Random	0.034	0.66	0.51	0.14	33.2	27.2	N/A	33.2	27.2
Ottawa 20-30	Random	0.076	0.65	0.53	0.11	32.9	28.1	N/A	32.9	28.1
Ottawa 20-30	Random	0.171	0.65	0.51	0.14	32.8	26.9	N/A	32.8	26.9
Ottawa 20-30	Random	0.290	0.67	0.52	0.15	33.8	27.3	N/A	33.8	27.3
Ottawa 20-30	Ribbed	0.067	0.72	0.56	0.16	35.7	29.4	N/A	35.7	29.4
Ottawa 20-30	Structured	0.001	0.33	0.27	0.06	18.3	15.1	N/A	17.2	14.0
Ottawa 20-30	Structured	0.066	0.65	0.49	0.16	33.0	26.1	0.05	29.4	22.9
Ottawa 20-30	Structured	0.117	0.86	0.67	0.19	40.7	33.8	0.09	35.5	28.1
Ottawa 20-30	Structured	0.185	1.01	0.79	0.22	45.3	38.3	0.17	37.7	29.6
Ottawa 20-30	Structured	0.226	1.18	0.98	0.20	49.7	44.4	0.34	37.1	30.0
Ottawa 50-70	Random	0.001	0.34	0.25	0.09	18.9	14.1	N/A	18.9	14.1
Ottawa 50-70	Random	0.010	0.59	0.54	0.05	30.6	28.2	N/A	30.6	28.2
Ottawa 50-70	Random	0.020	0.84	0.64	0.19	39.9	32.8	N/A	39.9	32.8
Ottawa 50-70	Random	0.034	0.79	0.62	0.18	38.4	31.7	N/A	38.4	31.7
Ottawa 50-70	Random	0.076	0.79	0.68	0.11	38.2	34.1	N/A	38.2	34.1
Ottawa 50-70	Random	0.171	0.78	0.65	0.14	38.1	32.8	N/A	38.1	32.8
Ottawa 50-70	Random	0.290	0.78	0.65	0.13	37.9	33.1	N/A	37.9	33.1
Ottawa 50-70	Ribbed	0.067	0.76	0.67	0.09	37.3	33.8	N/A	37.3	33.8
Ottawa 50-70	Structured	0.001	0.38	0.28	0.10	20.8	15.6	N/A	19.3	14.5
Ottawa 50-70	Structured	0.066	0.65	0.59	0.06	33.1	30.6	0.05	29.1	26.6
Ottawa 50-70	Structured	0.117	0.91	0.80	0.11	42.3	38.7	0.09	36.7	32.9
Ottawa 50-70	Structured	0.185	1.12	0.95	0.17	48.2	43.4	0.18	40.4	33.7
Ottawa 50-70	Structured	0.226	1.23	1.14	0.09	51.0	48.8	0.36	38.8	34.2
Blasting 20-30	Random	0.001	0.32	0.29	0.03	17.6	16.1	N/A	17.6	16.1
Blasting 20-30	Random	0.010	0.72	0.57	0.15	35.8	29.8	N/A	35.8	29.8
Blasting 20-30	Random	0.020	0.97	0.76	0.21	44.1	37.2	N/A	44.1	37.2
Blasting 20-30	Random	0.034	0.96	0.74	0.21	43.7	36.6	N/A	43.7	36.6
Blasting 20-30	Random	0.076	0.96	0.75	0.21	43.9	37.0	N/A	43.9	37.0
Blasting 20-30	Random	0.171	0.95	0.75	0.20	43.5	36.8	N/A	43.5	36.8
Blasting 20-30	Random	0.290	0.92	0.79	0.13	42.5	38.1	N/A	42.5	38.1
Blasting 20-30	Ribbed	0.067	0.97	0.84	0.13	44.0	39.9	N/A	44.0	39.9
Blasting 20-30	Structured	0.001	0.32	0.29	0.03	17.7	16.2	N/A	16.4	15.0
Blasting 20-30	Structured	0.066	0.73	0.65	0.08	36.1	33.0	0.06	32.1	29.1
Blasting 20-30	Structured	0.117	1.01	0.86	0.15	45.3	40.7	0.11	40.3	35.3
Blasting 20-30	Structured	0.185	1.17	1.06	0.11	49.5	46.7	0.21	44.9	38.5
Blasting 20-30	Structured	0.226	1.35	1.20	0.15	53.5	50.2	0.41	46.8	36.7

8.2.3 Load Transfer Mechanisms

It has been shown by several researchers that load transfer between soils and solid surfaces takes place in two distinct mechanisms: either from friction between the soil particles and the surface material or from passive resistances generated as the surface's topography forces particles to displace during shearing (Mitchell and Villet, 1987; Irsyam and Hyrciw, 1991). For smooth surfaces, most of the load is transferred by friction since the surface has no significant asperities that can induce soil deformations. On the other

hand, surfaces with larger values of surface roughness to particle diameter ratio (R_{max}/D_{50} or R_a/D_{50}) effectively mobilize a passive resistance component during shear.

It is proposed that the surfaces of random roughness clog during shear, resulting in systems that effectively behave like sand-sand interfaces and thus mobilize an interface friction angle equal to the soil mass internal friction angle (Figure 8.6a). The surfaces of structured roughness utilized in this study have been shown to avoid interface clogging by Hebeler, et al. (2015), Martinez, et al. (2015) and during Chapter 4 of this thesis. The mobilized loads during tests between sands and structured surfaces consist of friction resistance between the sleeve surface and the soil particles, termed the Interface Friction force (IF), and a passive resistance caused by the difference in diameters between the base of the sleeve and the protruding diamond texturing elements, termed the Annular Penetration force (AP) (Figure 8.6b). The diamond pattern of the structured sleeves has R_{max}/D_{50} values from 0.01 to 8; therefore, the diamond elements effectively mobilize passive resistances within the soil mass. This observation is further studied later in this chapter by means of DEM simulations.

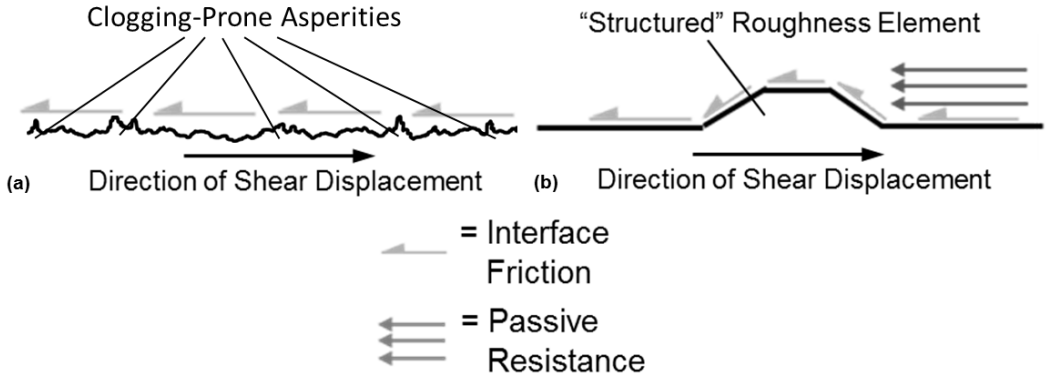

Figure 8.6: Interface load transfer mechanisms during shear for surfaces of (a) structured and (b) random roughnesses.

DeJong (2001), Frost and DeJong (2005) and Hebeler, et al. (2004) provided the following expression to quantify the relative contributions of the IF and AP components from the total force measured during testing with diamond textured sleeves:

$$f_a = f_r * N_r + AP$$

where f_a = average measured force, f_r = average force per ring of texture, N_r = number of rings of texture and AP = Annular Penetration force

The following section of this chapter reviews this methodology. The hypothesis to be tested is that the interface friction force (IF) acting on both sleeve types (i.e. with random and structured roughness) is the same in magnitude. Thus, the difference in response observed in Figures 8.4a through 8.4f and Figures 8.5a through 8.5c are caused by the AP force mobilized during testing with the sleeves of structured roughness.

8.2.4 Quantification of Passive Resistances (Annular Penetration Force)

As previously described in Chapter 5, a methodology for isolating the IF force from the AP force has been proposed by other authors for measurements with diamond textured sleeves (i.e. structured sleeves). This methodology involves a series of tests with partially textured friction sleeves that have the same roughness texture pattern but different degrees of textured versus non-textured areas, as shown in Figure 8.7. In this manner, the magnitude of the AP force can be determined by plotting the measured load on the diamond texture elements versus the number of diamond rings (Figure 8.8 and Table 8.3). The load on the diamond elements is calculated as the difference between the measured sleeve stress and the contribution from the untextured area. The results show a linear trend with the number of diamond rings on the sleeves based on the linear relationship between stress and contact area. Therefore, the magnitude of the AP force is equal to the intercept of the trend line with the y-axis. Consequently, if no AP force is present then the value of the intercept should be zero (measured force – smooth sleeve contribution = IF – IF = 0). The results from a test series performed with friction sleeves of R_a of 0.185 mm (or R_{max} of 1.00 mm), shown in Figure 8.8 and Table 8.3, resulted in AP stress ratios of 0.174 for tests on Ottawa 20-30 sand, of 0.181 for tests on Ottawa 50-70 sand of 0.205 for tests on Blasting 20-30 sand. These results show that the magnitudes

of AP resistances are affected by the soil mass friction angle, showing the largest magnitude for tests on Blasting 20-30 sand, followed by those on Ottawa 50-70 and lastly by tests on the more rounded Ottawa 20-30 sand.

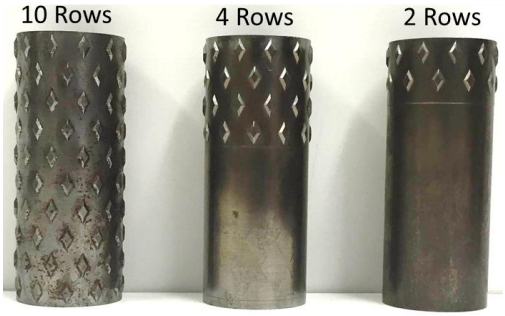

Figure 8.7: Partially textured sleeves used to isolate IF and AP force components.

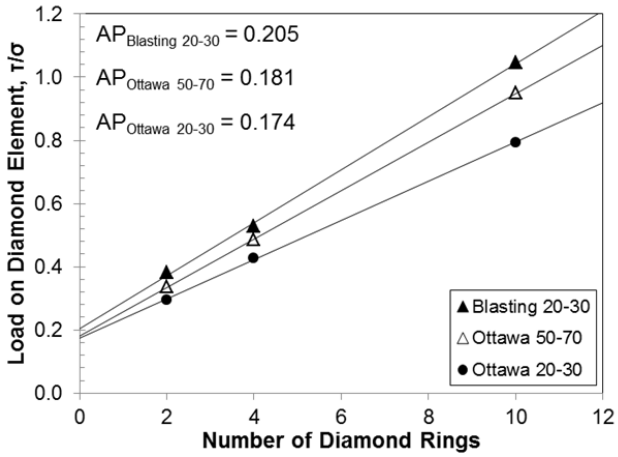

Figure 8.8: Estimation of AP force for tests on Ottawa 20-30, Ottawa 50-70 and Blasting 20-30 sands.

8.2.5 Interface Friction Response

Following the methodology described in the previous section for the estimation of the AP force, the contributions on the sleeves of different roughness (indicated in Table 8.1 under descriptor names of H = 0.25, 0.50 and 2.00 mm) provided the opportunity to compute "isolated" IF forces. This was done by subtracting the corresponding AP contributions from the total measured loads. Then, "isolated" interface friction angles

were calculated from the contribution of the IF forces ($\delta = \tan^{-1}(\tau/\sigma)$). Figures 8.9a through 8.9c show the "isolated" interface friction angles for tests with sleeves of structured roughness, as well as the results for tests on sleeves of random roughness (previously shown in Figures 8.5a through 8.5c).

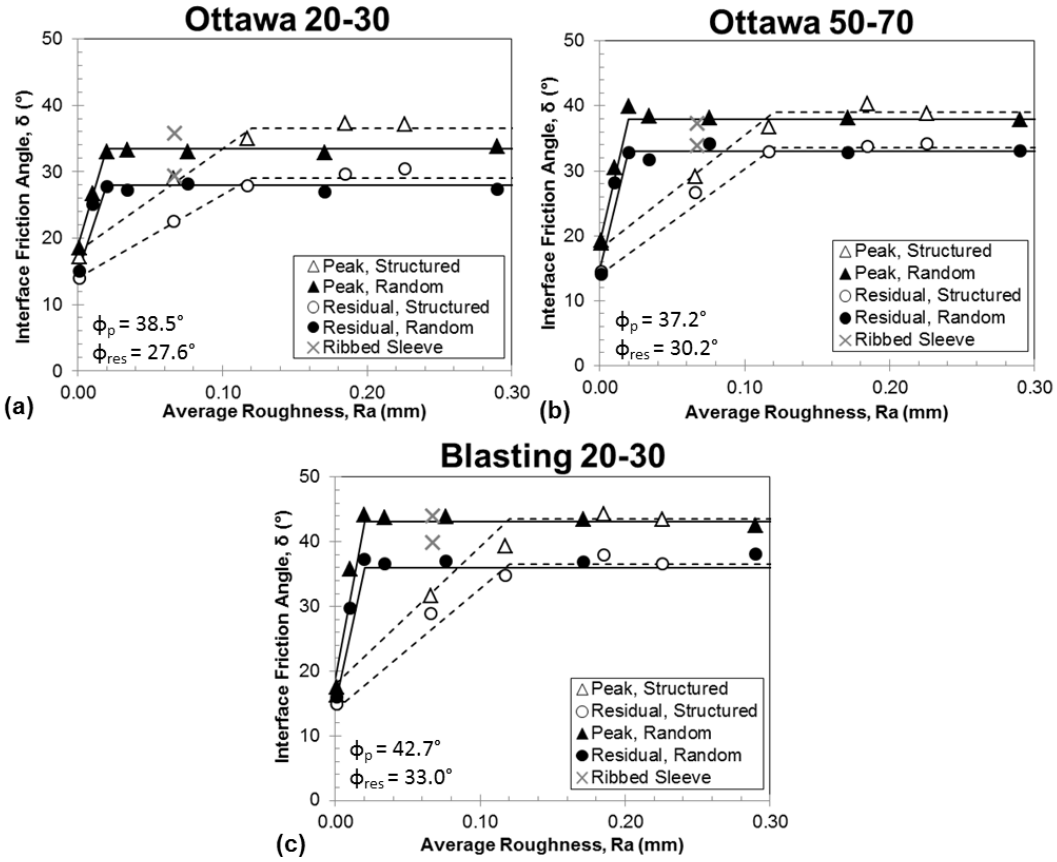

Figure 8.9: "Isolated" interface peak and residual friction angles mobilized during tests on (a) Ottawa 20-30, (b) Ottawa 50-70 and (c) Blasting 20-30 sands.

The results of both test series follow bilinear relationships with surface roughness, with the value of the plateau of these relationships within ±1.5° of the value of the measured direct shear friction angles of the sands. The steeper initial slopes shown by the results from tests on random structured results show that these surfaces can mobilize the full soil strength at smaller average roughness values. The "x" symbols show results from tests with ribbed sleeves which were not affected by the presence of passive resistances. While ribbed sleeves with only one roughness value were tested, the results show to

mobilize interface friction angles of comparable magnitude as those from random surfaces and isolated ones from structured roughnesses. These global-response measurements indicate that the difference in behavior observed in the total measured forces (Figures 8.5a through 8.5c) is originated from the AP forces mobilized during shear against sleeves of structured roughnesses. The results further suggest that the random and ribbed roughness surfaces clogged and thus mobilized an interface strength equal to the soil mass internal strength ($\delta = \varphi$). The following section presents shear zone deformation measurements that complement these observations.

8.2.6 Shear Zone Deformations and Interface Clogging

The shear-induced soil deformations during tests against sleeves with different roughness form were studied in resin-impregnated specimens following the methodology previously summarized in the introduction of this chapter, and described in detail in Chapter 3. Figure 8.10a through 8.10d show dissections of shear zones formed during shear against sleeves of smooth, structured, ribbed and random roughnesses, respectively against Ottawa 20-30 sand (shear displacement = 63.5 mm). Layers of colored sand were used in the specimens in order to allow for the visualization of shear zone deformations. The profiles of the shear zones were obtained with the use of a graph digitizer software (GetData Graph Digitizer). These profiles are shown in Figure 8.11a and show clear differences in soil deformations between the tests. The test against a smooth sleeve showed almost negligible particle displacements in the order of 0.5 mm after 63.5 mm of sleeve displacement. This result agrees with previous results presented in this thesis and by other authors (Frost and DeJong, 2005; Frost, et al. 2012; Martinez and Frost, 2014b; Hebeler, et al. 2015). The results of the structured roughness test show a well-defined shear zone that extends to about 12 mm. These results indicate a normalized shear zone length (shear zone length / sleeve displacement) of about 19% and highlights the ability of the textured diamond sleeves to induce soil shearing while remaining unclogged. The

test results for ribbed and random roughness show much larger shear zones, with lengths of about 40 and 49 mm, respectively, which correspond to normalized shear zone lengths of 63% and 77%. These results indicate that the ribbed and random surface roughnesses are highly prone to clogging since particles were shown to be "dragged" with the surface during most of the shear displacement, indicating the likelihood for particles to get trapped in between the surfaces' asperities. It can be concluded that the ribbed and random roughnesses result in similar clogged interface behaviors. The reason for this is that neither of these surfaces have untextured areas that allow particles to flow through; however, the passthrough zones in the diamond sleeves allow these surfaces to remain unclogged during shearing.

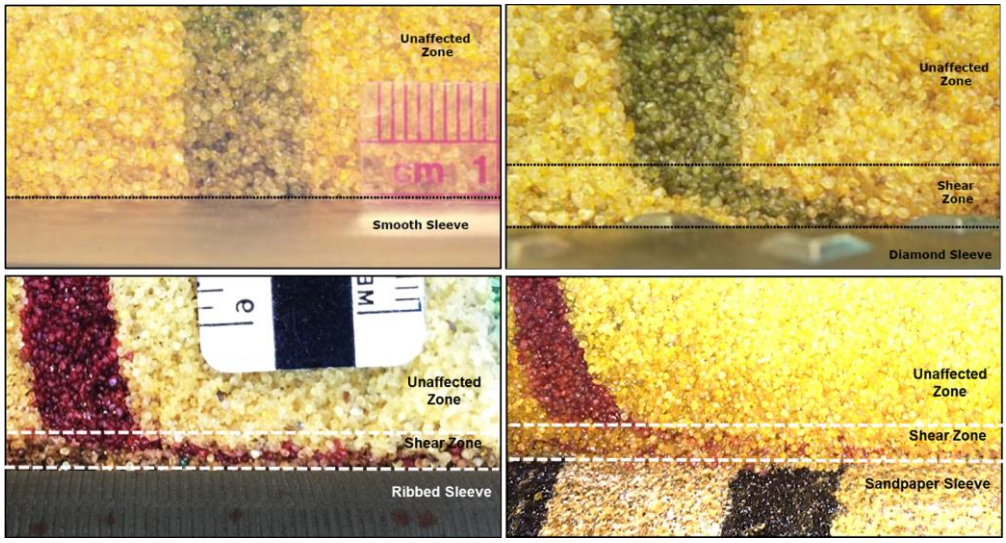

Figure 8.10: Dissections of shear zones formed during shear against sleeves of (a) smooth, (b) structured (from DeJong, 2001), (c) ribbed and (d) random roughnesses.

It should be noted that the profile of the shear zone created when shearing against a sleeve of random roughness shows detectable particle displacement up to distances of 15 mm from the sleeve. This is believed to be caused by a less pronounced gradient in the distribution of the induced shear stresses on the soil mass.

Figure 8.11b and 8.11c show the measured shear zone characteristics as a function of shear displacement taken from tests against surfaces of structured, ribbed and random

roughnesses. All the shear zone measurements for tests against sleeves of specific form were taken on the same specimens. Different degrees of shear displacement were achieved by preparing the specimens with layers of colored sand that underwent different degrees of shearing against the corresponding friction sleeves, as shown in Figure 8.12 and described in detail in Chapter 3. Shearing against the testing rods on either side of the textured section was considered to induce negligible particle displacements because the rod had a prescribed surface roughness equal to the smooth sleeves tested in this study, which showed to induce negligible soil deformations (see Figure 8.10a).

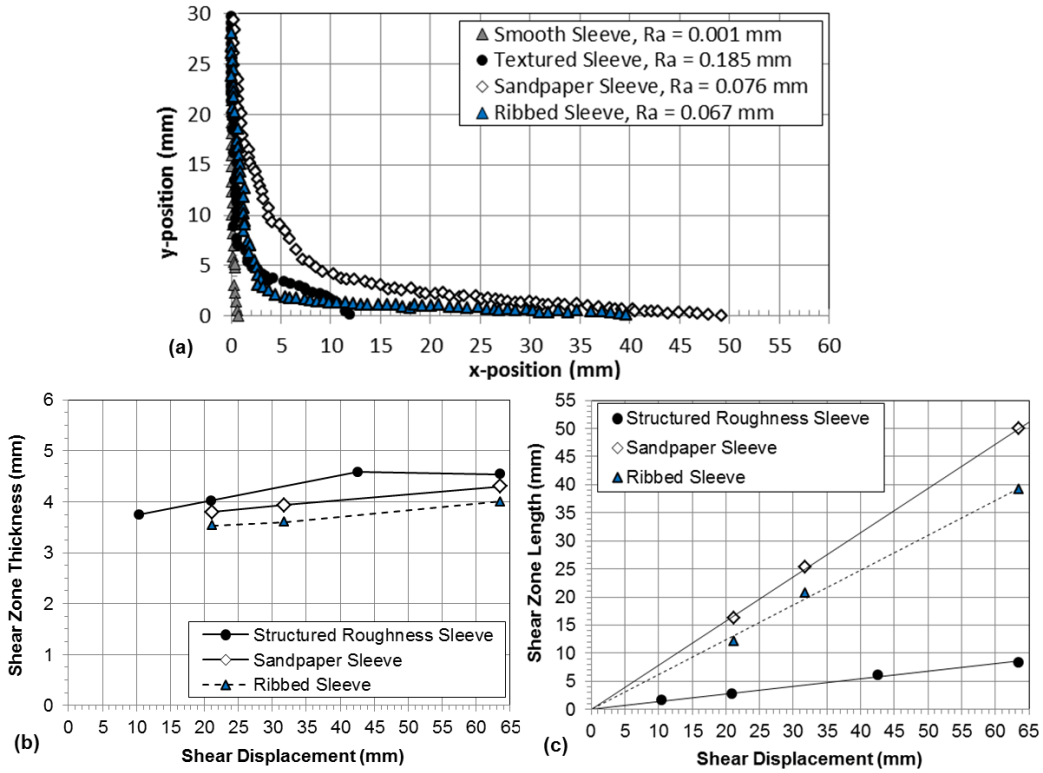

Figure 8.11: (a) Shear zone deformation profiles, (b) shear zone thickness and (c) length as a function of shear displacement.

The shear zone thickness values were estimated by drawing a straight line through the shear zone profile and measuring the length between this straight line and the y-axis at an x-position of zero. The results presented in Figure 8.11a show that the shear zone thicknesses progress in a similar way for the structured, random and ribbed sleeves. The

shear zones are well defined at shear displacements as small as 10 mm, and further increases in displacement result in only small increases in shear zone thickness. In general, the shear zone thickness measurements from tests against sleeves of structured roughness were slightly larger, possibly caused by the influence of the passive resistances mobilized during shear. The shear zone thicknesses from tests against ribbed sleeves were the smallest, and those for tests against sleeves of random roughness showed slightly larger values. The shear zone length results presented in Figure 8.11b show that shearing against the sleeves of random roughness created longer shear zones caused by the larger degree of interface clogging, followed closely by those from tests against ribbed sleeves which also promoted interface clogging. The results from tests against sleeves of structured roughness showed much shorter shear zone lengths. Nonetheless, the shear zone length progression showed a linear relationship with increasing shear displacement for the three surface roughness forms.

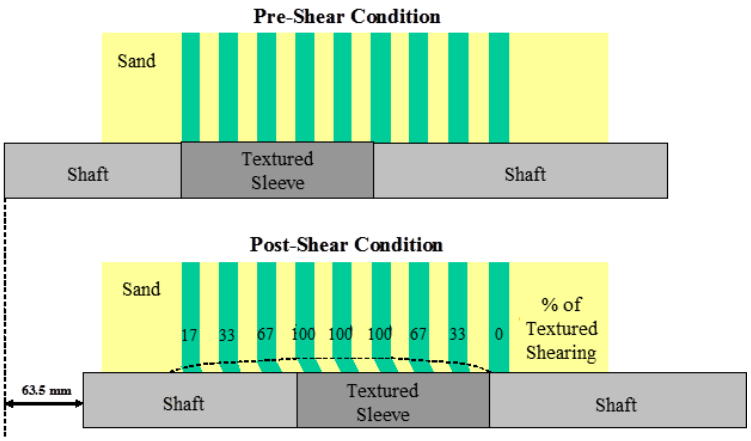

Figure 8.12: Schematic showing the configuration of colored sand layers within each axisymmetric test sample (adapted from Hebeler, 2005).

8.3 Numerical Results

Seven DEM simulations were performed in order to complement the experimental results presented in this chapter, as shown in Table 8.4. These simulations studied the interface response of systems consisting of soil particles against surfaces of structured

(i.e. diamonds), random (i.e. 36 grit sandpaper), and ribbed roughnesses. An important note to add is that these simulations were performed in a 2D geometry. Therefore, the untextured "passthrough" zones in the structured roughnesses were not included, as shown in the diamond profile included in Figure 8.2. This resulted in particles having to climb over the diamond elements during shear. While this geometry does not completely replicate the structured roughness of the sleeve, the simulations showed that the angled leading edge of the diamonds avoided interface clogging and thus the results can be considered as reasonably representative of interface behavior against a structured surface.

Table 8.4: DEM simulations configuration.

Simulation	Texture Type	R_a (mm)	D_{50} (mm)	e_0
A	Random	0.171	0.90	0.14
B	Structured	0.185	0.90	0.14
C	Ribs	0.201	0.90	0.14
D	Random	0.171	0.90	0.23
E	Structured	0.185	0.90	0.23
F	Random	0.171	0.29	0.14
G	Structured	0.185	0.29	0.14

8.3.1 Global Response

The global stress-displacement and volumetric strain-displacement responses of the seven simulations are presented in Figures 8.13a through 8.13f. Figure 8.13a shows that larger loads were mobilized during the simulation against the ribbed surface (simulation C), followed by those mobilized against the structured surface (B) and lastly by those against the random surface (A). This trend possibly results from the fact that the ribbed profile has a slightly larger average surface roughness (0.201 mm), followed by that for the structured profile (0.185 mm) and then by that for the random profile (0.171 mm). Simulation A (random) induced the largest volumetric strains, as shown in Figure 8.13d, followed by simulation C (ribs) and then by simulation B (structured). These results agree with the fact that simulation A underwent the largest amount of strain softening, followed by simulation C and then by simulation B. At larger shear displacements, the dilation rate of all three simulations significantly decreased.

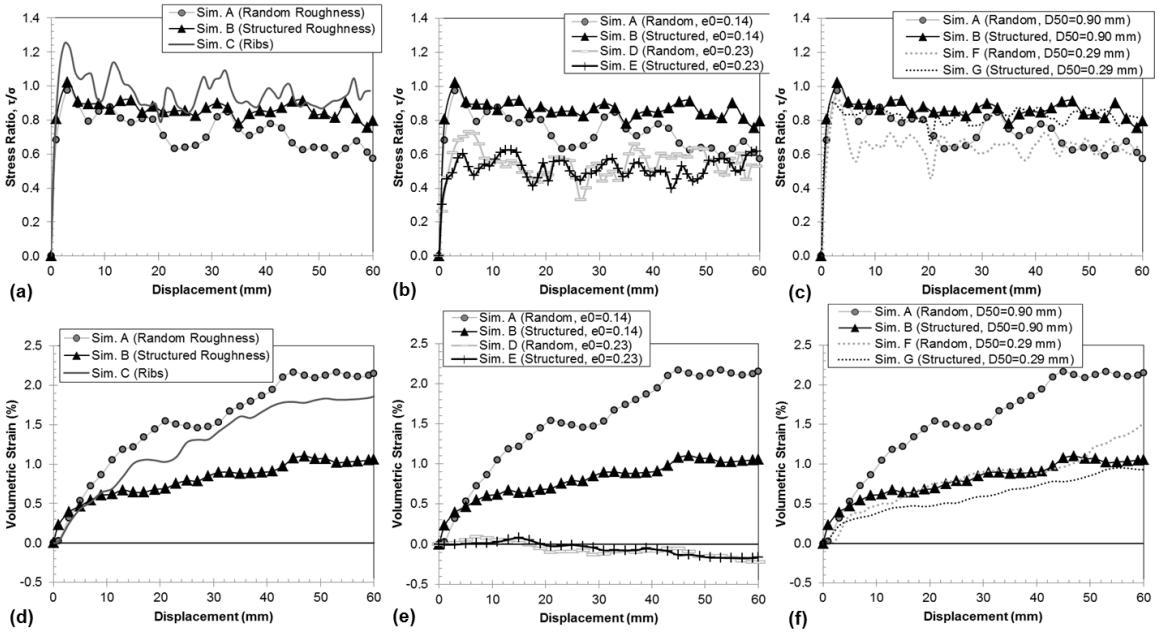

Figure 8.13: Stress ratio-displacement and volumetric strain-displacement response for (a) and (d) simulations A, B and C; for (b) and (e) simulations A, B, D, and E; and for (c) and (f) simulations A, B, F, and G.

Figure 8.13b shows results of simulations A, B, D and E that allow for the effect of initial void ratio to be studied. Simulations A and B, which had an initial void ratio of 0.14 (dense), resulted in larger peak loads than simulations D and E, which had an initial void ratio of 0.23 (medium dense). The residual stress ratios from simulations A and D (random roughness) converged at large shear displacements, following the behavior described by critical state soil mechanics. The residual loads from simulations D and E (structured roughness) did not converge, possibly due to the presence of the AP force which affects a larger volume of soil that is not completely in a critical state and thus is influenced by the assemblies' initial void ratio. Both D and E simulations showed slight contractive volume changes during shear (Figure 8.13e), a fact that is consistent with their initial loose packing.

Figures 8.13c and 8.13f presents the results of simulations A, B, F and G. Both simulations with mean particle diameters, D_{50}, of 0.90 mm (A and B) showed larger peak

loads and larger dilative volumetric changes than the simulations with mean particle diameters of 0.29 mm (D and E). This agrees with the understanding of soil behavior that assemblies composed of larger particles tend to have more dilative tendencies (e.g. Novoa-Martinez, 2003; Cheng and Minh, 2009). The mobilized stress ratios converge at the residual stage for both simulations against random and structured roughnesses. At this stage, the effects of dilation have dissipated to a large extent. Since both large and small particles have the same shape and interparticle friction coefficient (AR = 1.5, $\mu_{p\text{-}p} = 0.45$), it is reasonable to expect that the assemblies mobilize similar residual strengths.

8.3.2 Particle Displacements, Rotations and Local Void Ratio Fields

Tracking the positions of centroids and cumulative rotations of each particle in the specimens, as well as the local void ratios from measurement circles uniformly distributed within the specimens (as shown in Figure 3.21b), allowed defining soil deformation fields. Figures 8.14a through 8.14c present the results for tests against random, structured and ribbed surfaces after 30 mm of shear displacement. The results presented in Figures 8.14a and 8.14b highlight the strain-localization type of deformation within the three specimens, and show that the surfaces of random and ribbed roughnesses induce larger particle displacements and rotations than the simulation performed against structured roughnesses. These results agree with the experimental results presented in Figures 8.11a through 8.11c. The local void ratio fields presented in Figure 8.14c show that the simulations against surfaces of random and ribbed surfaces resulted in larger dilation in the vicinity of the interface. These results agree with the global volumetric strain response of the specimens presented in Figure 8.13d, and agree with the fact that shearing against clogging surfaces (i.e. random and ribbed) results in large shear deformations. Results from simulations D, E, F and G showed similar trends as the results presented in Figures 8.13 a through 8.13c and suggested that the initial assembly void ratio and particle diameter do not affect the clogging behavior of these surfaces.

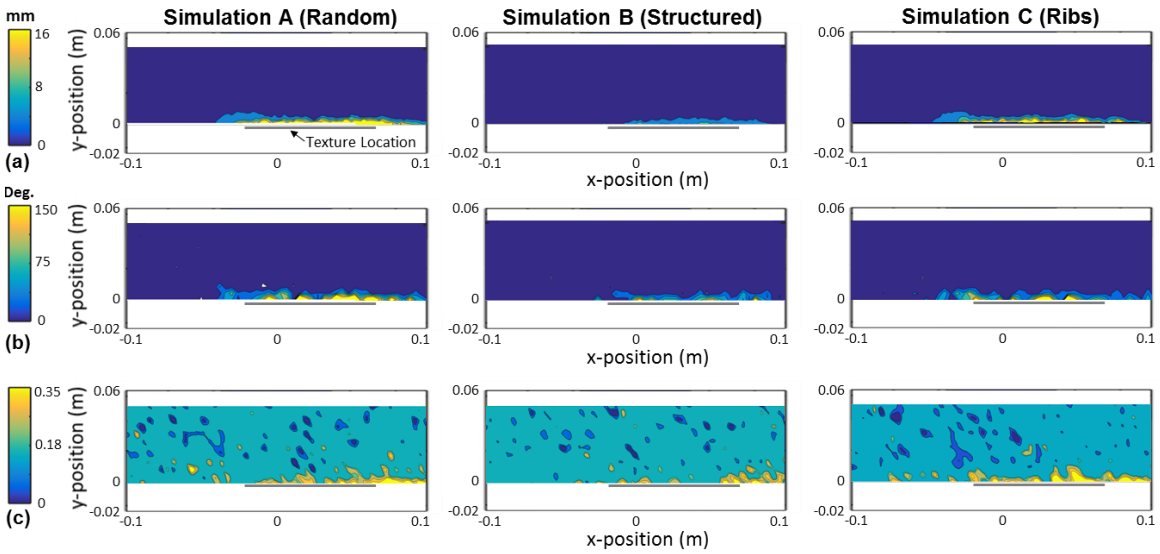

Figure 8.14: (a) Particle displacements, (b) particle rotations and (c) local void ratio fields after 30 mm of shear displacement for simulations A, B and C.

8.3.3 Shear-Induced Soil Deformations

8.3.3.1 Shear Zone Characteristics

Monitoring centroids of columns of particles during the simulations allowed defining the extent and magnitude of induced particle displacements. These results are considered to be directly comparable to those presented in Figures 8.11a through 8.11c for laboratory tests. The results for simulations A, B and C show the same trend observed in previously presented experimental and numerical results. Namely, the simulation against the surface of structured roughness resulted in shorter shear zone lengths, as presented in Figures 8.15a and 8.15c after 63.5 mm of shear displacement, showing a non-clogging behavior. The results from simulations A and C (random and ribs) indicated significant interface clogging. The shear zone thicknesses were fully developed at shear displacements as small as 6 mm and only showed minimal changes with increasing sleeve displacements. The shear zone lengths showed a linear relationship with sleeve displacement. The similarity between these results and those previously presented for laboratory tests (Figures 8.11a through 8.11c) shows that the experimental methodology

used to obtain various shear zone deformation measurements as a function of sleeve displacement in one same specimen is appropriate for the study of soil deformations (Figure 8.12).

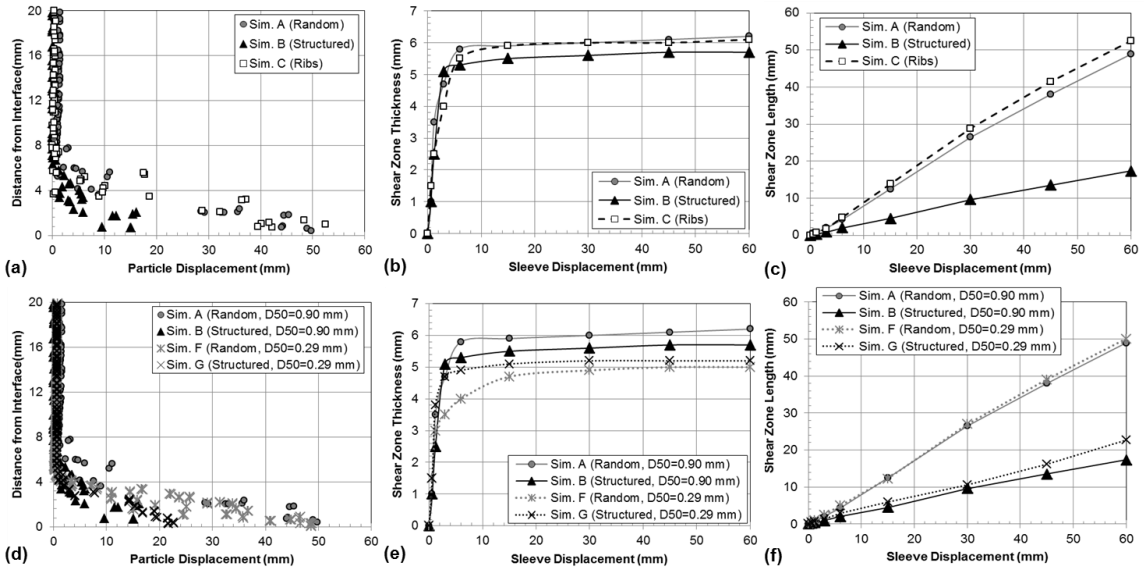

Figure 8.15: Shear zone profiles at 63.5 mm of displacement for simulations (a) A, B and C and (b) A, B, F and G. Shear zone thickness progression with sleeve displacement for simulations (a) A, B and C and (b) A, B, F and G. Shear zone length progression with sleeve displacement for simulations (a) A, B and C and (b) A, B, F and G.

Figure 8.15d through 8.15f presents a comparison of the results from simulations A and B (random and structured roughnesses, D_{50} = 0.90 mm) with simulations F and G (random and structured roughnesses, D_{50} = 0.29 mm). The results show that the simulations with larger particles resulted in larger shear zone thicknesses for both roughness forms. These results are in general agreement with research presented by other authors such as Mühlhaus and Vardoulakis (1987), Oda and Kazama (1998) and Frost, et al. (2004) who showed an increase in shear zone thickness with increasing mean particle diameter. The difference in shear zone thickness with increasing mean particle size for the simulations is of about 1 mm for the random surfaces and of about 0.5 mm for the structured roughnesses. The simulations with smaller particles showed slightly larger

shear zone lengths, especially for the simulations with structured surfaces. The reason is that a given surface roughness has a greater influence when sheared against smaller particles, as defined by researchers such as Uesugi, et al. (1989) and Mortara, et al. (2007). Shear zone characteristics results for simulations D and E (random and structured roughnesses, e_0 = 0.23, not shown for brevity) in comparison with results from simulations A and B showed that the initial assembly void ratio has a negligible effect on the magnitude of the induced shear deformations.

8.3.3.2 Shear-Induced Particle Rotations

DEM codes enable particle rotations to be monitored during shear, a task that is highly challenging to accomplish during laboratory testing. The cumulative particle rotations were monitored for the particles located in a box 6 mm high immediately above the surfaces under study. These results were used to generate histograms of cumulative particle rotations after 63.5 mm of shear displacement (Figures 8.16a and 8.16b).

Shearing against surfaces of random roughness resulted in larger mean and standard deviation of cumulative particle rotations (μ = -73.7°, σ = 115.3°, COV = 1.56), followed by those from simulations against ribbed surfaces (μ = -39.2°, σ = 115.0°, COV = 2.93) and then by those against structured roughnesses (μ = -15.3°, σ = 73.4°, COV = 4.80). Particle rotations are caused by loads transferred to the soil mass from the moving surface. As such, differences in shear-induced particle rotations indicate differences in load transfer mechanisms. The simulations performed with smaller particles (F and G with D_{50} = 0.29 mm) showed larger standard deviations but similar mean values of particle rotations as compared to the corresponding simulations with larger particles (A and B with D_{50} = 0.90 mm), as shown in Figure 8.16b. These results indicate that shearing against smaller particles induced particle rotations of larger magnitudes in both clockwise and counterclockwise directions, resulting in wider distributions. The relative aspect of surface roughness provides an explanation for this observation.

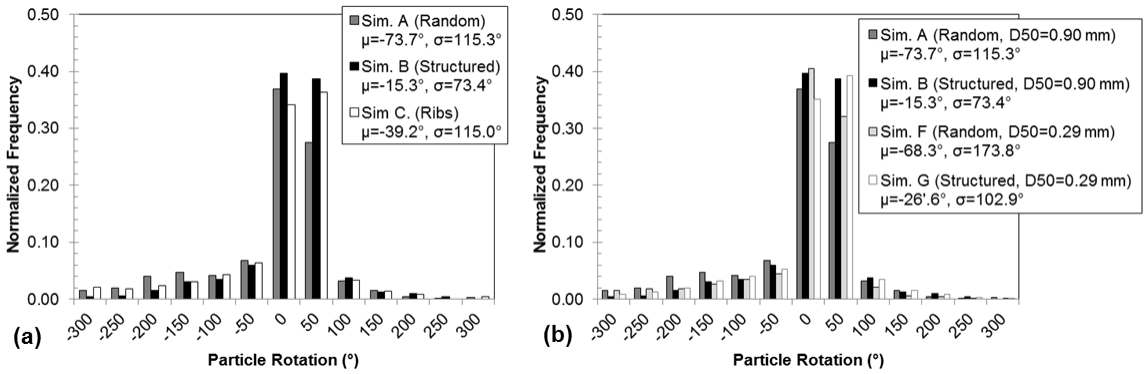

Figure 8.16: Normalized histograms of cumulative particle rotations after 63.5 mm of sleeve displacement for simulations (a) A, B and C, and (b) A, B, F and G.

8.3.3.3 Shear-Induced Changes in Local Void Ratio

The shear-induced soil deformations were further studied by means of local void ratio measurements after 63.5 mm of shearing taken from measurement circles distributed throughout the samples (see Figure 3.21b). These results are presented as a function of distance from the interface in terms of void ratio and in terms of change in void ratio ($\Delta e = e_{initial} - e_{measured}$). Figure 8.17a presents the results for simulations A, B, C (random, structured and ribbed roughnesses, $e_{initial} = 0.14$), D and E (random and structured roughnesses, $e_{initial} = 0.23$). This figure shows the tendency of the soil to reach a critical state void ratio indicated by the values at locations adjacent to the interface which cover a narrow range between 0.26 and 0.30. The void ratio values at greater distances from the sleeve correspond to the initial void ratio of the assemblies. Figure 8.17b shows the same results in terms of Δe. It can be observed that the initial void ratios had a significant effect on the magnitude of the dilation within the shear zones, with looser assemblies undergoing less dilation and simulations against structured roughnesses also showing less dilation. These results agree with the global response previously presented. The looser assemblies (simulations D and E) showed a decrease in void ratio values at locations immediately after the dilation zones. These contraction zones have been previously identified in experimental and numerical studies in Chapters 4 and 6 for axial and

torsional interface shear tests, as well as described by other authors for shear box interface shear tests (DeJong and Westgate, 2009; DeJong and Westgate, 2010). Simulations A, B and C did not show contraction zones. These results show that denser assemblies have more dilative tendencies and resist contractive volume changes. Figures 8.17c and 8.17d show comparisons between the results of simulations A and B (D_{50} = 0.90) and simulations F and G (D_{50} = 0.29). The simulations with smaller particles showed less dilation within the shear zones. These results agree with the global specimen responses previously presented. No contraction zones were observed for these simulations as a result of their dense assembly configuration.

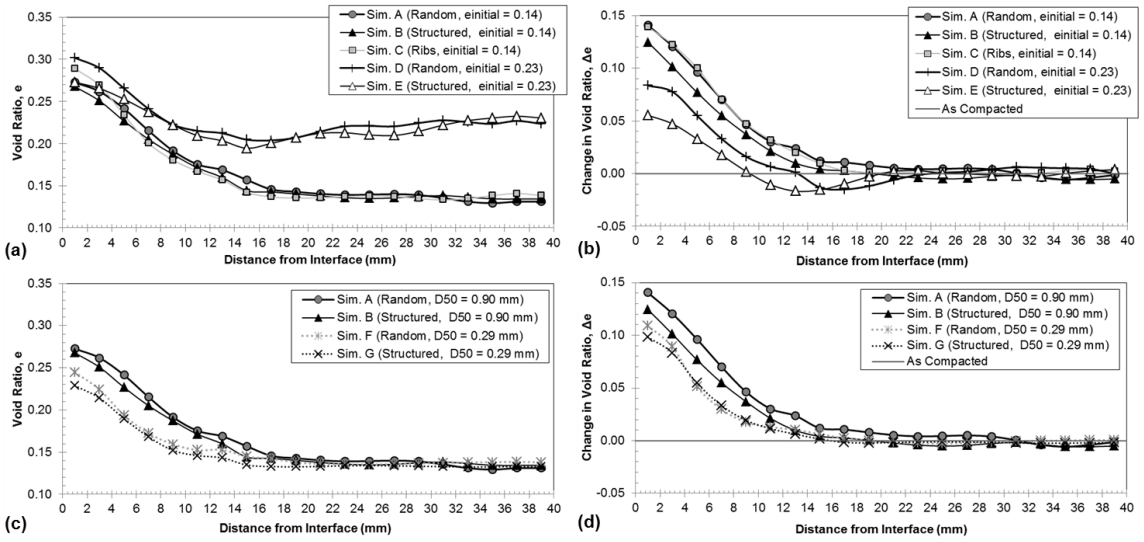

Figure 8.17: Shear-induced volume changes as a function of distance from the interface; (a) and (b) simulations A, B, C, D, and E, and (c) and (d) simulations A, B, F and G.

8.3.4 Fabric Evolution

A study on the evolution of the specimen fabric during shear was performed to complement the shear-induced soil deformation results. This section presents average coordination number and sliding contacts fraction measurements taken from all the particles located in a box 6 mm high immediately above the surfaces under study. The coordination number measurements were between 6 and 2.6, a range that agrees with the

range for disk assemblies reported by Rothenburg and Kruyt (2004). Figure 8.18a shows a comparison for simulations A, B and C (random, structured and ribbed, respectively). The results indicate an initial faster decrease in coordination numbers for simulation A and similar lower decreases for simulations B and C. At large displacements, the specimen of simulation B reached a coordination of 3.0, while the specimens of simulations A and C reached lower coordination numbers of about 2.6. These trends are in agreement with the global volumetric strain results presented in Figure 8.13d which showed larger specimen dilation for simulations on random and ribbed surfaces.

The results presented in Figures 8.18b and 8.18c also agree with the results previously presented. In general, the looser specimens of simulations D and E showed lower initial coordination numbers, and smaller dilation with increasing displacement (Figure 8.18b). The specimens with smaller particles (simulations F and G) showed similar initial coordination numbers that decreased at a slower rate than those for specimens with larger particles. The coordination numbers reached values of about 3.0 (random roughness) and 3.2 (structured roughness) at large displacements (Figure 8.18c).

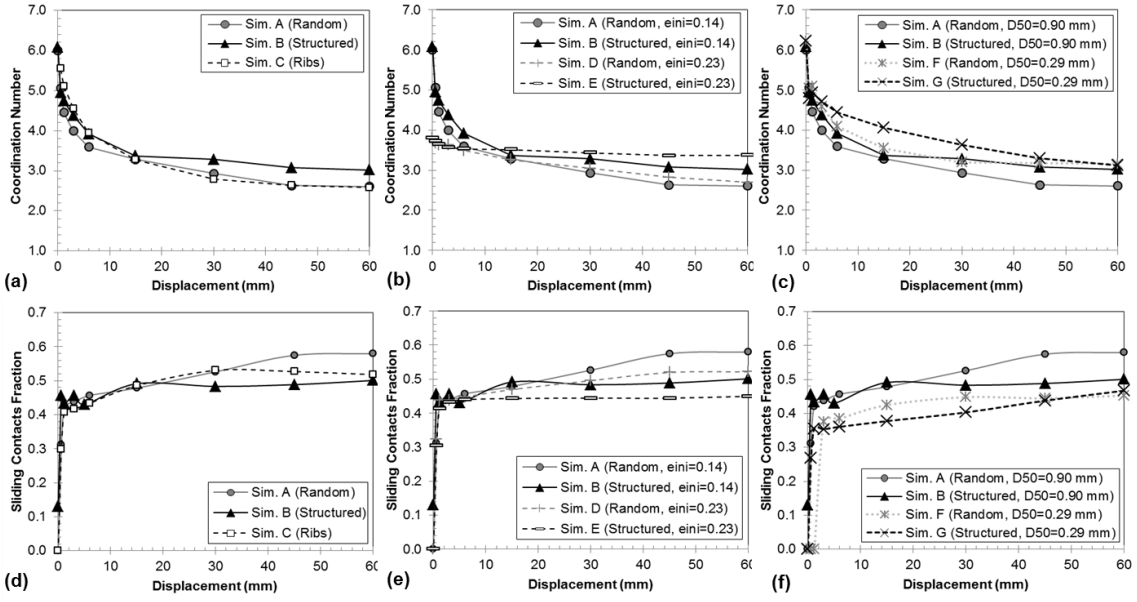

Figure 8.18: (a), (b) and (c) Coordination number and (d), (e) and (f) sliding contacts fraction evolution with displacement for simulations A, B, C, D, E, F and G.

Figure 8.18d presents the average sliding contacts fraction within the shear zones for simulations A, B and C. The results show a very sharp increase at small displacement, with more modest increases at larger displacements. In general, the progression is similar for the three simulations up to a shear displacement of about 15 mm. At large displacements, simulation A (random) reaches a sliding contact fraction of about 0.58, followed by simulation C (ribs) with a value of 0.52, and then by simulation B (structured) with a value of 0.49. These results also are in general agreement with the global and local response of the specimens, showing more intense soil shearing during simulation A, followed by simulations C and B, respectively. Figures 8.18e and 8.18f show the effect of initial void ratio and mean particle diameter, respectively. Increasing initial void ratio and decreasing particle size resulted in smaller sliding contacts fraction, especially at large displacements, caused by the lesser dilation undergone by these specimens.

8.3.5 Shear-Induced Loading Conditions

8.3.5.1 Normal and Shear Stress Fields and Contact Force Maps

The normal and shear stress fields at different stages throughout the simulations were defined by measurements taken from measurement circles uniformly distributed throughout the specimens (see Figure 3.21b). Figures 8.19a and 8.19b show these results after 15 mm of shear displacement. The normal stress field for simulation A shows a significant increase in stress at locations adjacent to the surface of random roughness that extended vertically to distances up to 50 mm from the interface. The results also show an increase in stress on the left side of the specimen where the textured surface has not reached yet (note the location of the texture). The results from simulation B (structured) also show significant increases in normal stress at locations adjacent to the sleeve. However, these increases only reach locations 35 mm vertically away from the interface. Also, the left side of the specimen underwent an increase in normal stress that is smaller

than that for simulation A. The results from simulation C (ribs) show significant increases in normal stress that reach the top of the specimen, located 60 mm away from the interface. This simulation shows an increase of stress on the left side of the specimen with magnitudes that fall between those for simulations A and B. Figure 8.19b shows that the increases in shear stress propagated diagonally. These results show similar trends as those shown by the normal stress fields, with shear stresses that propagate farther vertically and horizontally for simulations A and C.

The differences in induced loading conditions can also be analyzed in terms of the contact force maps presented in Figures 8.19c and 8.19d, where each line represents force transferred through a contact, and the thickness of the lines indicates the magnitude of such force. It should be noted that the scale for the thickness for the contact force lines is not the same for the results of the three simulations. Therefore, these results can be used to analyze trends in the results but not to estimate contact force differences between the simulations.

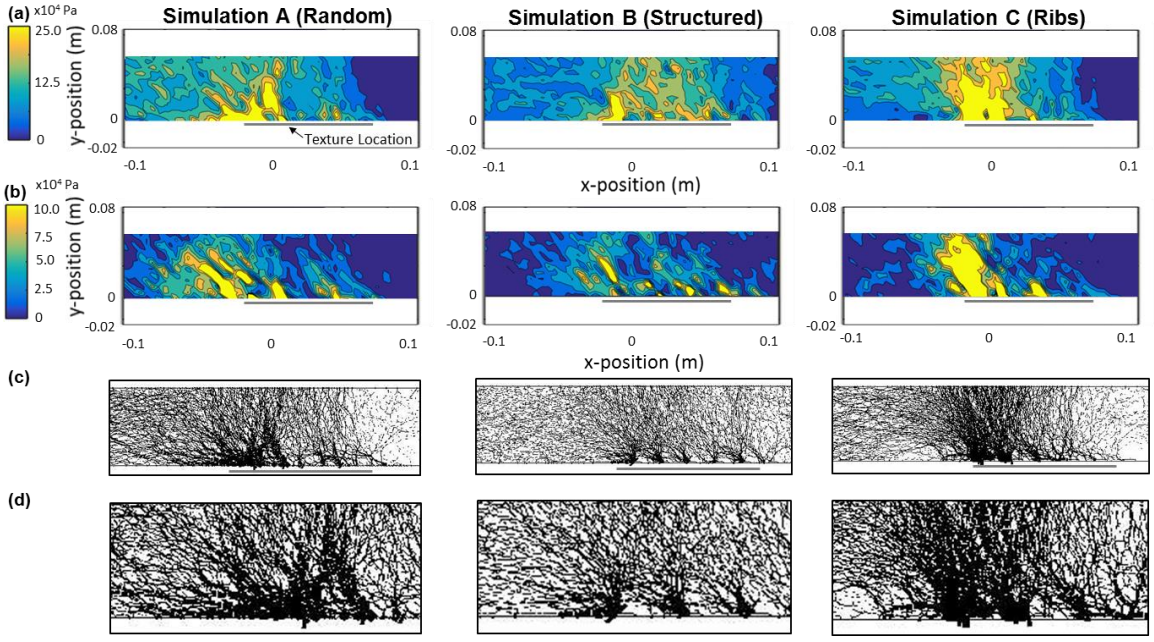

Figure 8.19: Loading conditions induced during simulations A, B and C. (a) Normal and (b) shear stress fields, (c) contact force maps and (d) detail of contact force maps.

The results for simulation A (random) show large contact forces at the leading edge of the textured surface that extend vertically and horizontally from it. In contrast, the results from simulation B (structured) show periodic increases in contact forces at the leading edge of each individual diamond element. These results indicate that passive resistances (i.e. AP forces) were mobilized by each diamond element, as described earlier in this chapter and shown schematically in Figure 8.6b. This difference in contact force increase can be observed at a greater detail in the magnified views shown in Figure 8.19d, and can also be observed in the stress fields if analyzed closely. As previously mentioned, the mobilization of these passive resistances is the reason for the difference in global shear behavior and loading conditions observed between interfaces composed of random and structured surfaces. The contact force map for simulation C (ribs) shows an increase in contact forces at the leading edge of the surface that spreads mainly in a vertical direction. There is a slight periodic increase in contact forces at the leading edges of the ribs; however, this trend is less clear than that observed in simulation B.

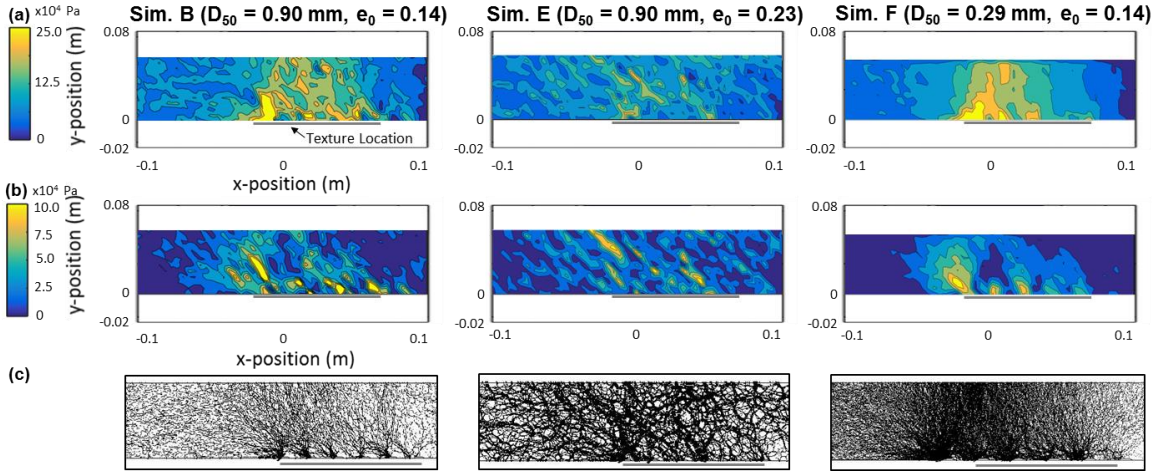

Figure 8.20: (a) Normal and (b) shear stress fields and (c) contact force maps for shearing against structured roughnesses for simulations B, E and F.

Further analyses of simulations E and F showed similar trends as those described in this section for the surface of structured roughness and indicated that increasing initial

void ratio and decreasing particle size did not significantly affect the loading conditions induced, as shown in Figure 8.20a through 8.20c. The increase in shear stress at the leading edge of each diamond element is especially clear for simulation F. The smoothness for the stress fields of simulation F is due to the larger ratio of measurement circle diameter to particle diameter.

8.3.5.2 Polar Histograms

Polar histograms of contact normal orientations and normal and shear contact forces provide further insights regarding the fabric evolution and the loading conditions within the specimens. Figures 8.21 through 8.23 show normalized polar histograms for simulations A, B and C (random, structured and ribbed), respectively, constructed from particle information obtained from all the particles located in a box 6 mm high immediately above the surfaces under study, along with Fourier distributions fitted to the data and fitting parameters (a and θ), as described by Rothenburg and Bathurst (1989). The results are presented for the initial, peak and residual stages, as defined in the corresponding figures. The length of the histogram bars represents percentages with respect to the mean corresponding quantities, a larger 'a' coefficient represents a more anisotropic Fourier distribution and the angles 'θ' are measured from the horizontal axis.

Figure 8.21 shows the normalized polar histograms for simulation A (random). The contact normals for this simulation showed an isotropic initial distribution and a maximum magnitude of normal contact forces oriented in a vertical direction as a result of the constant vertical stress applied to the specimen. No shear forces are shown because at this stage the interparticle friction coefficient was set to zero in order to create dense specimens. At the peak stage, the fabric started evolving showing an increase in contacts at an angle of 35°. The normal contact forces histogram shows a rotation of the direction with the maximum magnitudes (θ_n) to an orientation of 43° from the horizontal. This direction indicates the orientation of the major principal stress in the shear zone and it

roughly coincides with the previously mentioned direction where most contacts are oriented. The shear contact forces at the peak stage developed in two orthogonal directions. The orientation of the plane where no shear forces were located (θ_t) is roughly 45°, which coincides with the θ_n angle. At the residual stage, the fabric kept evolving in a similar manner, the θ_n angle for the normal contact forces distribution did not change significantly (from 43° to 45°), but its anisotropy decreased. The shear contact forces rotated, resulting in a θ_t angle of 70°, and their distribution anisotropy decreased. The decrease in anisotropy of the normal and shear contact force distributions is an indication of the strain softening shown in the stress ratio-displacement curve.

Figure 8.22 presents the normalized polar histograms for simulation B (structured). At the initial stage, the contact normal vectors showed an isotropic distribution and the θ_n angle for the normal contact forces is of 90°. At the peak stage, more contacts were oriented at an angle of 60° from the horizontal, and the major

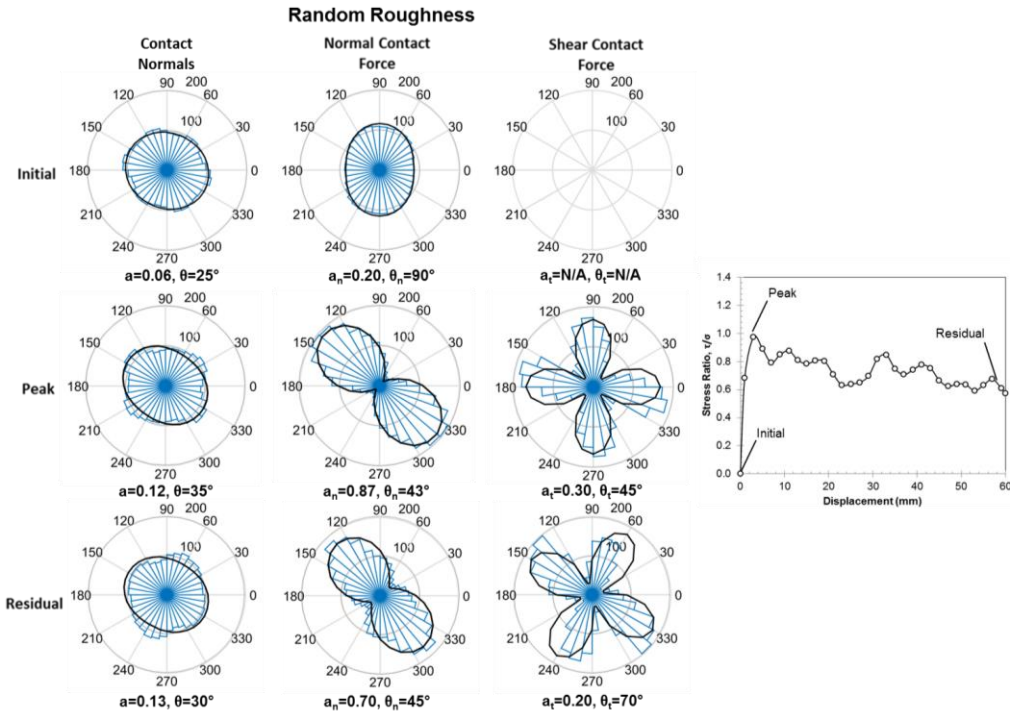

Figure 8.21: Normalized histogram of contact normal orientations, normal and shear contact forces at initial, peak and residual stages of simulation A (random roughness).

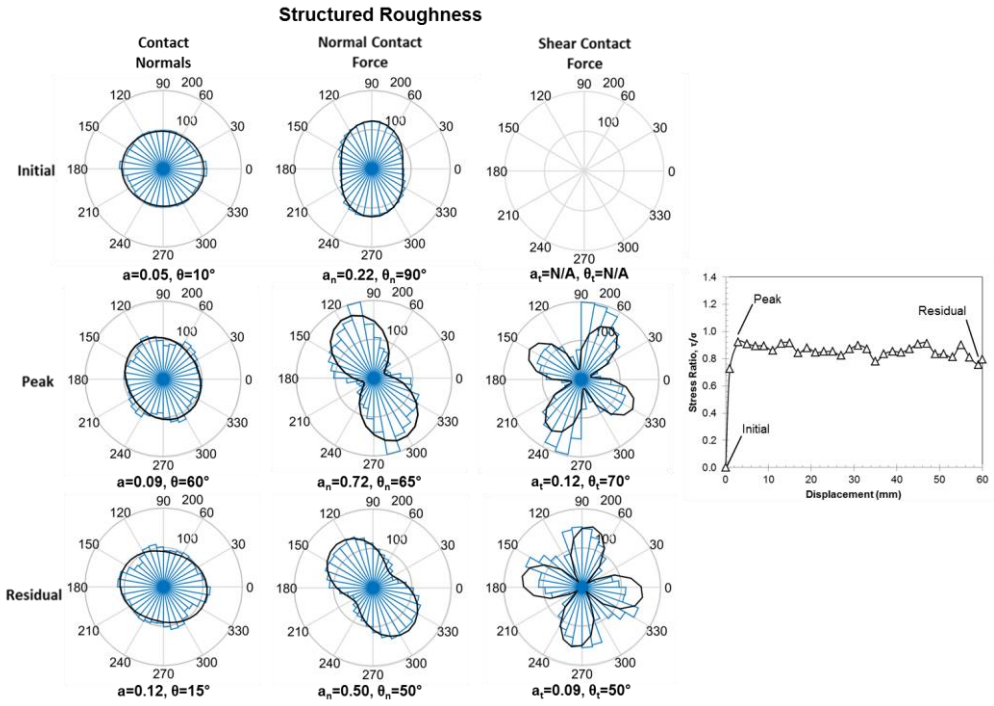

Figure 8.22: Normalized histogram of contact normal orientations, normal and shear contact forces at initial, peak and residual stages of simulation B (structured roughness).

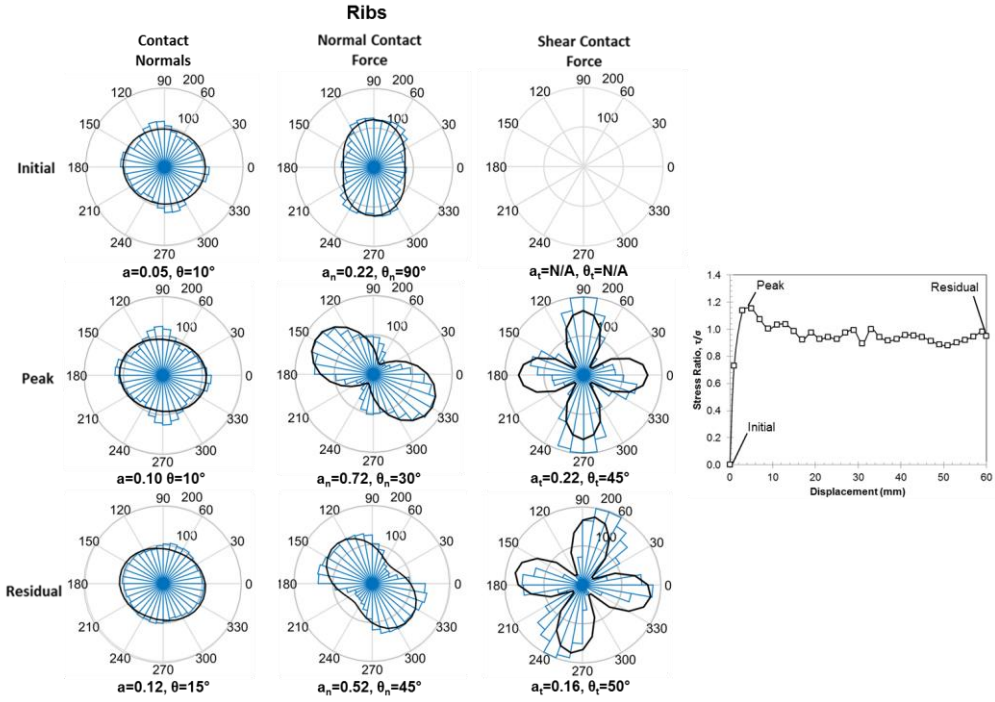

Figure 8.23: Normalized histogram of contact normal orientations, normal and shear contact forces at initial, peak and residual stages of simulation C (ribbed roughness).

principal normal stress was oriented in a similar angle of 65° (θ_n). It should be noted that the orientation of the principal stress at the peak stage for simulation B (structured) is closer to the vertical direction than that observed during simulation A (random), oriented at 43° from the horizontal. This difference is believed to be caused by the presence of the passive resistances (AP force) in simulation B that results in induced loads closer to the vertical direction. At the peak stage, the shear contact forces were concentrated in two orientations that are close to orthogonal to each other, and the θ_t angle is equal to 70°. At the residual stage, the contact normal distribution kept evolving and showed its principal direction at 15°, the distribution of contact normal forces rotates, resulting in a θ_n angle of 50°, and its anisotropy decreases. The shear contact forces also rotate slightly, showing a θ_t angle of 50°, and its distribution anisotropy decreased. The normalized polar histograms for simulation C (ribs) (Figure 8.23) show a trend similar to the results from simulation A. At the peak stage the normal contact force distribution rotated 30°, and the shear contact forces shows a θ_t angle of 45°. At the residual stage, the anisotropy of both distributions decreased, and the corresponding θ_n and θ_t angles were of 45 and 50°.

8.4 Implications on Geotechnical Systems

8.4.1 Interface System Capacity

The research presented in this chapter has important implications on the behavior and performance of interface systems. In particular, the experimental results presented in Figure 8.5a through 8.5c show that surfaces of structured roughness can mobilize interface friction angles that are 20-60% larger than those mobilized by clogging-prone surfaces of random roughness. This is important because most construction materials that have rough surfaces have a random form, as shown in the profiles for randomly textured HDPE geomembranes and rough finished concrete presented in Figures 8.24c and 8.24d. Therefore, the capacity of interface systems consisting of typical construction materials

will be limited to that corresponding to the friction angle of the contacting soil mass. However, it should be noted that certain types of textured HDPE geomembranes do employ a structured roughness surface The results presented herein indicate that larger interface capacities could be achieved if the surfaces were designed with a structured form. A quantitative assessment of the specific roughness geometric characteristics that allow interfaces to mobilize passive resistances is highly desirable but has not been performed as part of this study. This aspect will be addressed in future research studies.

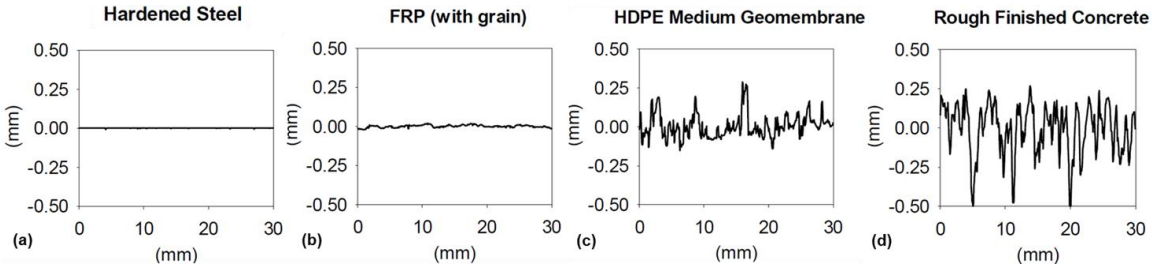

Figure 8.24: Profiles of typical construction materials (from Frost, et al. 2002).

8.4.1 Engineered Interface Loading Conditions

Several of the results presented throughout this chapter indicate that surfaces that clog, such as the random and ribbed surfaces, have a greater ability to induce soil engagement than the structured roughnesses. For instance, the results presented in Figures 8.11a through 8.11c, as well as those in Figures 8.14a, 8.15a, 8.15c, 8.15d and 8.15f show that shearing against random and ribbed surfaces result in much larger shear-induced particle displacement. Furthermore, Figures 8.14b, 8.16a and 8.16b showed that random and ribbed surfaces also induce larger particle rotations during shear. In addition, shearing against these surfaces resulted in more dilative specimen responses, as shown in Figures 8.13d through 8.13f, 8.14c and 8.17a through 8.17d. Considering these observations, the larger interface friction angles mobilized by surfaces of structured roughness (Figure 8.5a through 8.5c) might seem counterintuitive.

The reason for the higher strength of interfaces with structured roughnesses can be explained considering the following mental experiment. A specimen subjected to

direct shear loading conditions, as shown in Figure 8.25a, will develop strain localization in a nearly horizontal plane that coincides with the plane where the shear box is split (see Jewell, 1989 and Cui and O'Sullivan, 2006 for a detailed assessment of the loading conditions induced by direct shear). As such, testing a sand specimen in a direct shear apparatus will give a measure of the sand's shear strength under the applied normal stress. In comparison, if the same sand specimen is tested in an oedometer (Figure 8.25b), loaded vertically under increasing normal stress, it will undergo volumetric compression and no obvious plane of strain localization will be formed, as shown by Cha (2012). Undoubtedly, the sand specimens will behave differently under direct shear and oedometer loading conditions. In displacement controlled direct shear, the specimen's ability to resist force increases at small displacements, but its ability might decrease or remain constant at larger displacements (i.e. strain softening or hardening). In comparison, in load controlled oedometer testing the specimen's ability to resist force keeps increasing asymptotically. Apart from the volume of soil undergoing shear deformations (i.e. strain localization), the main difference in the loading conditions is the orientation of the principal stresses. In direct shear, the load is applied on a horizontal plane that results in soil shearing, while on oedometer testing it is applied on a vertical plane which results in soil compression. In short, a volume of soil can have significantly different ability to resist force depending on the loading conditions applied to it.

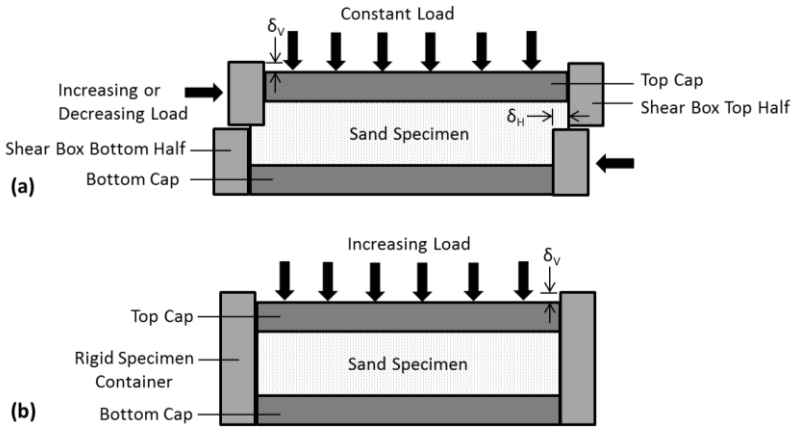

Figure 8.25: Schematic of (a) direct shear and (b) oedometer tests.

These concepts can be used to analyze the different loading conditions observed during the laboratory tests and DEM simulations presented in this chapter. Interface shear has been shown to induce similar loading conditions as direct shear by Wang and Jiang (2011) for DEM simulations performed on surfaces of random roughness and closely spaced saw tooth profiles. As presented by Wang, et al. (2007a) and Wang, et al. (2007b), these surfaces clogged during shear and thus resulted in systems that behaved as sand-sand interfaces and showed loading conditions similar to those from direct shear tests. The experimental results from tests against random surfaces (i.e. sandpaper sleeves) support these findings since they were able to reach $\delta = \varphi$ conditions. Furthermore, the shear-induced loading conditions from simulation A (Figure 8.21) are similar to those presented by Wang and Jiang (2011). On the other hand, the results from laboratory tests against structured surfaces (i.e. diamond sleeves) were able to mobilize larger interface friction angles than the measured direct shear friction angles. Furthermore, the loading conditions observed in simulation B indicated a principal stress direction closer to the vertical (Figure 8.22), oriented 65° from the horizontal at the peak shear stage, as compared to a corresponding orientation of 43° during simulation A. In this case, a principal stress orientation of 90° from the horizontal corresponds to oedometric compression, while a direction closer to the horizontal corresponds to direct shear. Therefore, shearing of soil against a structured surface results in combined loading conditions of shear (i.e. Interface Friction force, IF) and soil compression, or passive resistances (i.e. Annular Penetration force, AP). Interface shear between a random surface and soil will result in direct shear loading conditions and thus the interface capacity will be limited by that of the weakest link, either the soil-structure plane of contact ($\delta < \varphi$) or the soil mass ($\delta = \varphi$).

This discussion can be concluded by analyzing the different load transfer mechanisms present in a deep foundation embedded in a homogenous soil layer loaded axially. The load from the pile will be transferred to the underlying soil in bearing

capacity and to the soil contacting the pile's sides in shear. Considering the schematic shown in Figure 8.26a, the soil located in volume A will be subjected to compression transferred from the pile tip, while the soil in volume B will be subject to shear transferred from the pile sides. Figure 8.26b shows the results of a load test presented by Reese (1978). From these results it can be observed that the pile tip is transferring a load of about 140 tons to the soil beneath it (volume A in Figure 8.26a), while the lowest segment of the pile side is transferring a load of about 25 tons to the contacting soil (volume B). This simple example shows that a soil's ability to carry load greatly depends on the nature of the loading conditions applied to it. In sands, the soil's resistance to compression is likely to be significantly larger than its resistance to shear. Therefore, systems that transfer load to the soil in compression should be more attractive for design; thus, it would seem that an evaluation of the existing systems would be beneficial to determine whether their capacity and efficiency can be improved by engineering the way they transfer load to the contacting soil mass.

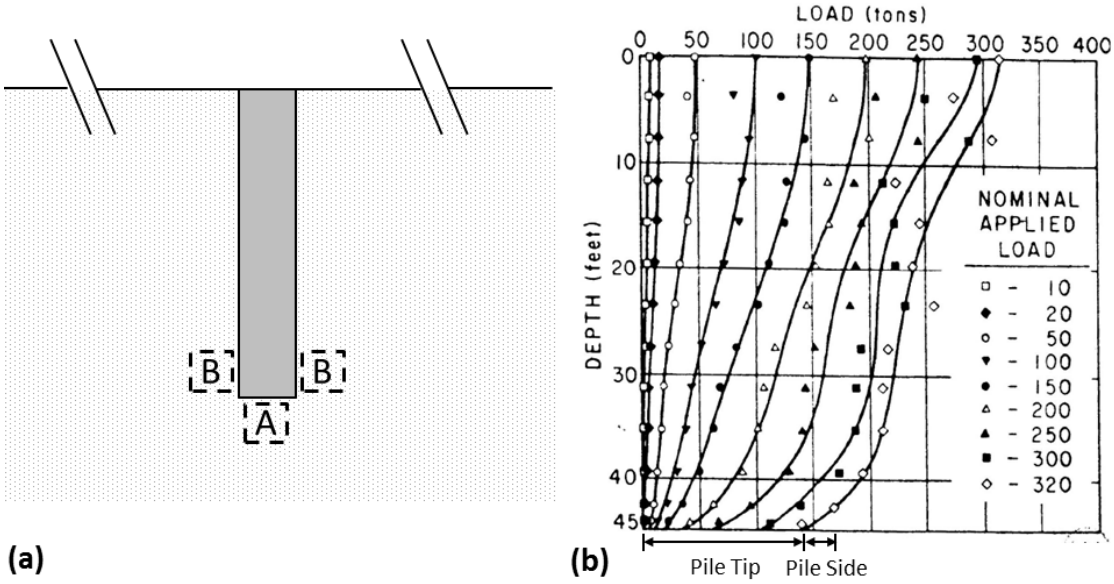

Figure 8.26: (a) Pile embedded in homogenous soil layer. (b) Load transfer results from pile axial load test. "Pile Tip" and "Pile Side" notes refer to the corresponding magnitudes of load transferred to the soil mass (adapted from Reese, 1978).

8.5 Conclusions

This chapter has presented the findings from an experimental and numerical study on the effect of surface form in the load-carrying capacity and behavior of interface systems. In particular, surfaces with random, structured and ribbed roughnesses were studied. Important observations regarding the shear-induced soil deformations and loading conditions, as well as on the implications on geotechnical engineering systems were provided. The following conclusions were drawn from this study:

- The results from laboratory tests showed that shearing against surfaces of random, structured and ribbed roughnesses effectively mobilized the internal friction of the contacting soils. As such, larger loads were mobilized during tests on angular (Blasting 20-30) sands, followed by those during tests with sub-angular to sub-rounded (Ottawa 50-70) sands, and then by those during tests with rounded (Ottawa 20-30) sands. On the other hand, the loads mobilized during shear against smooth surfaces did not show an influence of the soil's internal friction angle.
- Increasing surface roughness resulted in larger interface friction angles mobilized for both random and structured roughnesses. However, the results from tests against random surfaces showed to reach $\delta = \varphi$ conditions, thus mobilizing, at most, an interface strength equal to the soil strength. On the other hand, the interfaces with structured surfaces showed to mobilize interface friction angles up to 60% larger than the sand friction angles. These results represent an important implication for the design of interface systems and opens the door for engineered surface characteristics for optimized interface performance.
- It was identified that the load transfer mechanisms during shearing against random roughnesses consisted only of friction transfer. However, shearing against structured roughnesses mobilized an additional passive resistance which resulted in larger interface capacity. A methodology for isolating the interface friction force (IF) from the passive resistance force (AP) was presented and the results

verified the hypothesis. Once the magnitude of the AP component was subtracted from the total measured force during tests against structured surfaces, the "isolated" interface friction angles also showed to reach $\delta = \varphi$ conditions, in a similar way as the results from tests against random surfaces.

- Shear zone deformation measurements from laboratory experiments showed that shearing against random and ribbed surfaces resulted in interface clogging. These results support the observation that interfaces consisting of clogging-prone interfaces with random and closely-spaced ribbed profiles behave as sand-sand interfaces.
- DEM simulations of interfaces against structured, random and ribbed surfaces verified the results described in the previous bullet. Shearing against random and ribbed surfaces resulted in larger particle displacements and rotations and also induced larger specimen dilation. Measurements of the specimens' fabric, in terms of coordination number and sliding contacts fractions, supported the results indicating larger dilation shown by clogged interface systems. The simulations against random and ribbed surfaces showed larger decreases in coordination number and larger increases in fractions of sliding contacts with shear displacement.
- The normal and shear stress fields from numerical simulations indicated that shearing against random and ribbed surfaces induced larger stress increases within the soil above and ahead of the surface. On the other hand, the contact force maps showed that passive resistances are mobilized at the leading edge of every diamond element during shear against structured surfaces.
- The orientations of contact normal vectors and magnitudes of normal and shear contact forces from the simulations provided further insight into the evolution of the fabric and loading conditions. Shearing against the three surfaces showed a rotation of the principal stresses. However, the major principal stress direction for

the simulation against the structured surface resulted in a smaller rotation which remained closer to the vertical. In this case, a vertical major principal stress direction corresponds to oedometric compression, while a direction closer to the horizontal represents direct shear conditions. As such, the former loading conditions result in a much greater ability of the soil to resist load than for direct shear. These findings open the door to consider new geotechnical systems that transfer load to the contacting soil mass in more efficient ways. In addition, the results of this study could help evaluate the existing geotechnical systems and determine whether viable modifications can be implemented on them to improve their performance and efficiency.

- The results presented in this chapter can contribute to the development of more resilient infrastructure. It has been shown that modifications to the surface roughness characteristics can result in significantly larger interface strengths, which can in turn contribute subsurface structures that are more safe and/or economical. Furthermore, the capacity of interfaces that only transfer load in friction is linearly dependent on the magnitude of effective normal stress applied to them (i.e. $\tau = \sigma \tan(\delta)$); thus their performance (i.e. shear strength) is significantly affected by increases in pore water pressure that result in decreases in normal effective stress. The capacity of interfaces that transfer the load by means of combined loading conditions (i.e. interface friction and passive resistance) are also dependent on the magnitude of the normal effective stress; however, they passive resistance component is controlled by the soil compressibility, which depends on soil state and other soil properties such as fabric, mineralogy and particle shape and roughness. As such, the latter kind of interfaces can represent more resilient alternatives to nature- or man-induced hazards that are likely to increase the magnitude of pore water pressures, such as rainfall, floods and earthquakes.

CHAPTER 9

CONCLUSIONS AND FUTURE WORK RECOMMENDATIONS

9.1 Conclusions on the Behavior of Axial and Torsional Interface Systems

The research presented in this thesis consists of combined experimental and numerical studies on the shear behavior of particulate-continuum interfaces. The methodologies utilized throughout these studies were shown to provide accurate and useful information regarding the behavior of interface systems. Namely, the use of external sensors to measure the global specimen response and of resins and image analysis to study the post-shear local response of the sand specimens during the laboratory experiments showed to provide an accurate representation of the processes taking place during shear. Similarly, the use of Discrete Element Modeling (DEM) simulations to further investigate specimen response in terms of the global behavior, individual particle-particle and particle-surface interactions and induced loading conditions provided useful information that complemented the experimental results.

Figure 9.1 presents a schematic of the different interface systems encountered in geotechnical systems. Continuum-continuum interfaces can be composed of natural materials, such as rock joints, or of manmade materials, such as geomembrane-geonet systems in landfill liners. Particulate-particulate interfaces are observed in internal soil shear bands, which have been thoroughly studied during the last four decades. Lastly, the behavior of continuum-particulate interfaces depends on the material properties of both components; thus potentially making them more complex systems. Figure 9.2 presents a framework for the analysis of continuum-particulate interface shear behavior that considers the influence of previously understood factors, such as that of the surface hardness of the continuum material as well as other properties of the continuum and

particulate materials. However, this framework is expanded by introducing the effect of the surface roughness form of the continuum material, as well by expanding the understanding of the effect of particle shape, particle roughness and state of the particulate material. However, the effect of other properties such as cementation and soil gradation should be further studied. This thesis has shown that the shear behavior of interfaces is affected in different manners by the properties of the continuum and particulate materials depending on the loading conditions imposed, such as axial and torsional shear. Therefore, the loading conditions should be readily considered in the prediction of interface behavior and capacity. The following bullets summarize the main findings presented throughout this thesis.

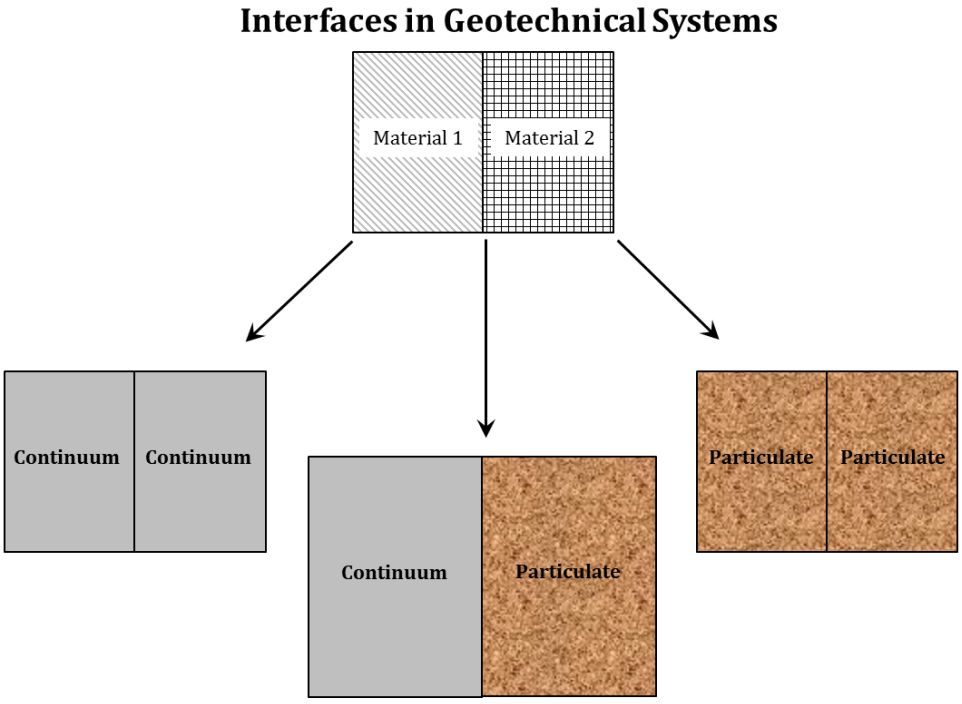

Figure 9.1: Interfaces in geotechnical systems

- The global response of torsional and axial interface shear tests was shown to agree with the conventional understanding of soil and interface shear behavior. Specifically, increasing surface roughness of the continuum and increasing particle angularity (i.e. soil friction angle) resulted in larger mobilized loads.

- Experimental assessment of the soil deformations induced by torsional and axial shear revealed that both shear modes induced uniform shear zones within the contacting sand when shearing against diamond-textured friction sleeves. Torsional shear was shown to induce more intense shear as observed in larger shear zones, which are an indication of larger particle displacements.

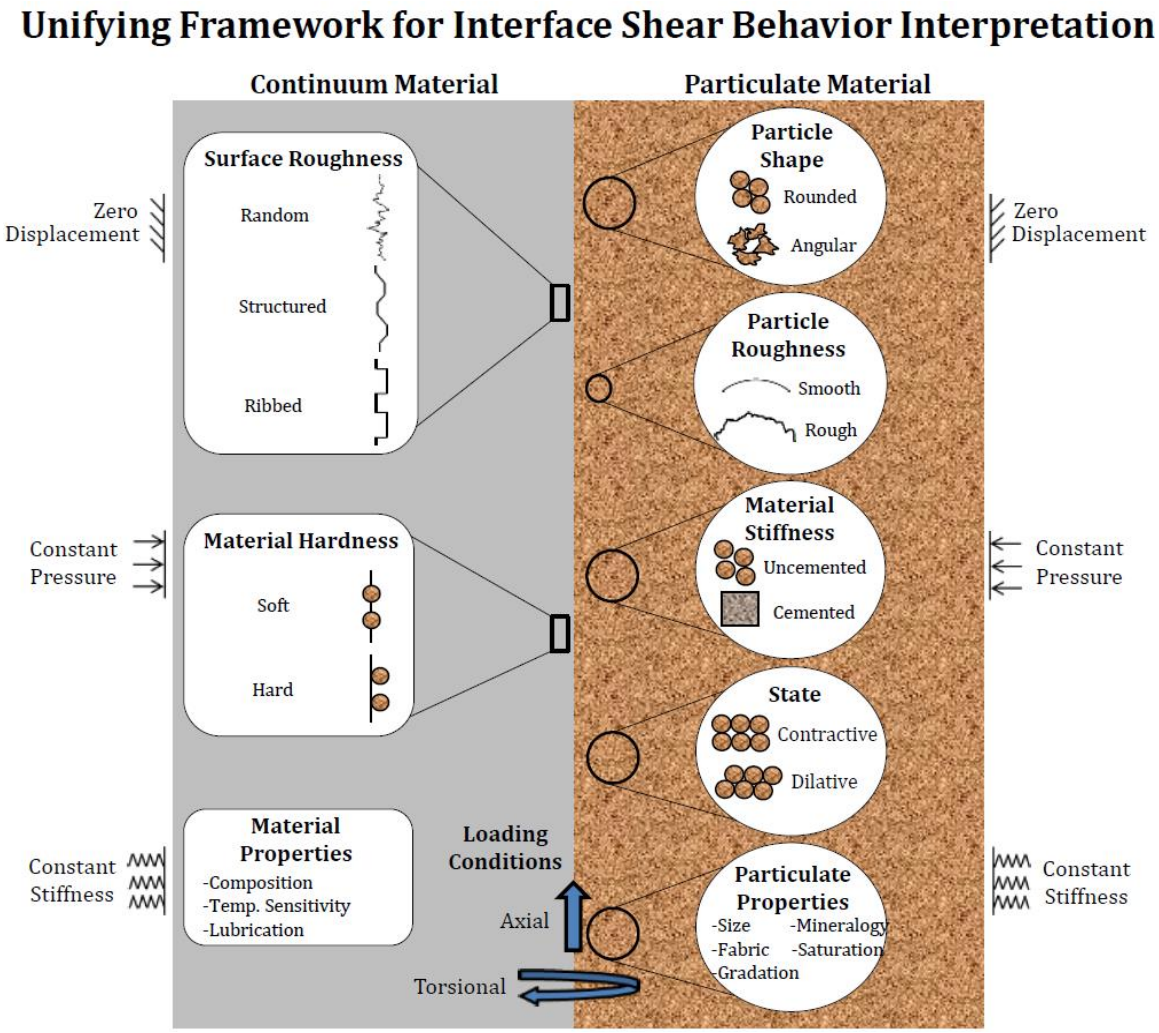

Figure 9.2: Framework for the analysis of continuum-particulate interface shear behavior.

Furthermore, post-shear local void ratio measurements on specimens subjected to torsional shear revealed the formation of a principal shear zone characterized by dilative volume changes and a secondary shear zone where particle displacements were not identified but significant contractive volume changes were induced. On

the other hand, specimens subjected to axial shear showed a well-defined primary shear zone with soil dilation and a small secondary shear zone with more modest reductions in void ratio. Proposed micro-mechanical processes for torsional shear are related to the induced loading conditions and involve particles migrating from the primary shear zone to the secondary shear zone as a result of a Tangential Component (TC) force. In contrast, particle migration does not take place during axial shear because the Annular Penetration (AP) force results in particle displacements parallel to the friction sleeve displacement. These findings are presented in detail in Chapter 4.

- Significant differences were observed in the measured global behavior of torsional and axial interface shear tests. Namely, the loads measured during torsional shear were shown to be more sensitive to changes in particle shape, while the loads measured during axial shear were shown to be more sensitive to particle surface roughness. Also, torsional shear was shown to mobilize larger maximum dilation angles. A series of numerical simulations under varying levels of confining stress showed different peak and residual failure envelopes for axial and torsional shear, highlighting the non-uniqueness of interface strength response. A methodology for the quantification of the passive resistance components of the measured sleeve stresses from axial and torsional shear tests was presented and evaluated. The results showed that both measurements are composed of an interface friction force and a passive resistance force. The interface friction force was shown to be equal in magnitude for both torsional and axial tests, while the passive resistance forces (TC for torsional and AP for axial) were shown to have different magnitudes. Consequentially, the difference in shear-response was identified to be caused by the difference in passive resistance components mobilized during torsional and axial shear. These findings are presented in detail in Chapter 5.

- The DEM simulations were shown to successfully replicate the observed global behavior of both torsional and axial laboratory tests. The DEM results further validated experimental observations of shear-induced soil deformations. Namely, the simulations also indicated that larger shear zones are formed during torsional shear. Furthermore, this shear mode created a primary shear zone of large particle displacements and dilative volume changes and a secondary shear zone with small particle displacement and contractive volume changes. Additional differences in the behavior of axial and torsional interface systems observed during DEM simulations include larger particle rotations induced by torsional shear and differences in the fabric evolution (presented in terms of deviatoric fabric and polar histograms of contact normal vectors distributions) of specimens subjected to axial and torsional shear. The shear-induced loading conditions also showed significant differences, with the most significant one being that axial shear induces a principal stress rotation on a vertical plane, while torsional shear induces that on a horizontal plane. These findings are presented in detail in Chapter 6.
- Undrained cyclic torsional tests performed experimentally on a newly developed axisymmetric testing device provided insight into the effect of various soil properties and testing conditions on the global-response of the specimens. While monotonic shearing resulted in dilative responses, the cyclic shear behavior of all the specimens of varying relative density (20-70%) showed contractive tendencies. The trends followed by the results agree with the conventional understanding of soil mechanics, such as: (i) specimens of lower relative density generated excess pore pressures at a larger rate than specimens of large relative density, and the former specimens were taken to cyclic mobility conditions after several dozens of cycles, (ii) specimens composed of angular sands showed larger cyclic mobility resistance than those composed of rounded sands, (iii) the rates of

excess pore pressure generation and strength degradation increased with increasing surface roughness. The results also indicated that increasing confining stress resulted in lower rates of excess pore pressure generation, which contradicts the notion of critical state soil mechanics. Proposed positive and negative excess pore pressure generation mechanisms provide a plausible explanation for the observed behavior. Finally, comparison of cyclic torsional and axial tests showed that torsional shear induced excess pore pressures at a faster rate and is more sensitive to the specimens' state parameter, thus showing advantages over axial shear for soil liquefaction assessment applications. These findings are presented in detail in Chapter 7, and implications on geotechnical applications are discussed in latter sections of this chapter.

- An experimental study on the behavior of axial interfaces revealed that roughness form can have a significant effect on their capacity. Specifically, model piles with structured surface roughnesses (consisting of periodic protruding elements that prevent interface clogging) mobilized interface friction angles that were 20 to 60% larger than those mobilized by model piles of random roughness (consisting of random profiles that promote interface clogging). This investigation showed that shearing with structured surfaces of large surface roughness resulted in $\delta > \varphi$ conditions, while shearing with random surfaces reached a limiting condition of $\delta = \varphi$. The reason for this difference in behavior is that surfaces of random roughness clog, resulting in an interface that effectively behaves as a sand-sand interface, as shown by shear zone deformation measurements taken experimentally. Isolation of the Interface Friction force (IF) from the passive resistances mobilized during shear with structured roughnesses showed that both surface types mobilize the same IF force. Therefore, the increased interface capacity of the structured roughnesses is originated by the additional passive resistances mobilized. Numerical simulations provided further insight into the

particle-scale behavior of interfaces with structured and random roughness. For instance, random surfaces induced larger soil dilation, cumulative particle rotations and resulted in larger fractions of sliding contacts within the shear zone. Normal and shear stress fields, as well as polar histograms of normal and shear contact forces, showed that shearing against structured surfaces induced principal stresses increases in a direction closer to that corresponding to oedometric compression. On the other hand, the direction of the increase in principal stresses during simulations with random surfaces showed loading conditions similar to those in direct shear tests. These results show that engineering the way in which the continuum material of the geotechnical structure transfers the load to the contacting soil mass can result in significant increases in system capacity. These findings are presented in detail in Chapter 8

9.2 Conclusions on Implications for the Development of the Multi-Piezo-Friction-Torsion Attachment (MPFTA) for Site Characterization

The results presented throughout this thesis have shown that axial and torsional shear induce different loading conditions within the contacting soil mass that highlight the non-uniqueness of interface strength. As such, the development of an in-situ testing device that can capture the soil response under different loading conditions has the potential for providing a more complete site characterization than devices that rely only on the measurement of the soil response to one loading condition. This is particularly obvious if one considers the combined loading conditions induced by most geotechnical systems. Furthermore, the undrained cyclic tests showed that torsional shear induces loading conditions that more efficiently result in the generation of excess pore pressures which is advantageous for the study of soil liquefaction potential. As such, the Multi-Piezo-Friction-Torsion Attachment (MPFTA), described in more detail in Chapter 2, is under development at Georgia Tech. This device is equipped with various friction sleeve

sensors that can measure the soil response to axial and torsional shear by means of independent load and torque cells. Furthermore, this device is equipped with pore pressure sensors before and after each sleeve location, as well as with several lateral stress loads that allow for the state of stress in the vicinity of the friction sleeves to be considered for in interpretation of the results. Finally, the plans for the development of the MPFTA include multi-sensor attachments deployed behind CPT and self-boring leading units that will allow assessing the effects of the insertion disturbance caused by the CPT device on the measured axial and torsional soil response.

9.3 Conclusions on Implications for the Improved Performance of Geotechnical Engineering Systems

Two findings from the research presented in this thesis have important implications on the capacity of geotechnical structures that rely on interface friction: (i) torsional shear can mobilize larger interface strength when the contacting soil mass is composed of angular particles, and (ii) surfaces with a structured roughness are capable of mobilizing interface strengths that are 20 to 60% larger than those mobilized by surfaces with random roughness. Consequently, these findings open the door for the consideration of geotechnical structures of enhanced capacity that have the potential to result in more sustainable, resilient and economical designs. Two obvious examples are driven piles that have a prescribed structured surface roughness that will result in larger skin friction capacity, and drilled shafts embedded in a deposit of angular sand with a mechanism on the shaft head that transfers linear displacement to angular displacement that will also mobilize larger skin friction. Both of these configurations would result in shorter or fewer foundation elements needed.

9.4 Recommendations for Future Work

This concluding section presents recommendations for future work that were considered beyond the scope of this thesis but that would be beneficial for the advancement of this research. The following bullets present these recommendations:

- Expand the experimental studies on the global response of the axial and torsional shear considering a wider range of states of stresses. In particular, the development of a laboratory testing device with a chamber that allows for the vertical and horizontal stresses to be simultaneously controlled would greatly aid for the development of an interpretation framework for in-situ axial and torsional tests. The author believes that there is potential for the axial and torsional tests to provide insight into the state of stresses of the soil (i.e. K_0), and such testing device would allow for this to be evaluated.
- In complement to the recommendation in the previous bullet, a 3D DEM model would further assist in the development of an interpretation framework for axial and torsional interface shear test. This model would allow studying a wider range of stress states while implementing measurements of induced loading conditions, particle-particle and particle- sleeves interactions and fabric evolution.
- A study on the time-dependent behavior of the microstructure induced during axial and torsional shear would be of interest for deep foundation applications. Specifically, the time-dependent evolution of the microstructure of the dilatation and contraction zones observed during torsional and axial shear could provide valuable information regarding the phenomenon known as "pile setup."
- The development of an interpretation framework in terms of the concept of "dispersivity" for the analysis of shear zones characteristics. This framework could provide useful information on the relationship between the shear zone thickness and length and surface roughness, as well as on the different shear zone

characteristics induced by the axial and torsional shear. The development of the 3D DEM model is required for this task.

- To further understand the undrained cyclic behavior of the torsional and axial interface shear test, laboratory tests on specimens with a wider range of relative densities confined under different stresses should be tested. Furthermore, this study can be expanded by testing specimens of finer sandy or silty soils since the research presented herein only considered medium-sized sands. Finally, cyclic torsional tests should be performed in free-draining conditions to assess their ability to induce excess pore water pressures in more realistic conditions.
- Load tests on larger-scale models in the laboratory or in the field are required to further study the effect of surface roughness form on the interface friction capacity. The tests performed as part of the research presented in this thesis utilized model piles with textured lengths of 110 mm. It is necessary to assess whether the increased interface capacity shown by surfaces of structured roughness scales up to full-sized geotechnical structures.
- The development for a methodology to assess whether a given surface roughness profile will mobilize passive resistances when sheared against a soil. This methodology should consider the particle size of the granular assembly in order to take into account the relative aspect of surface roughness.
- A mechanism capable of turning linear displacement into angular displacement that can be placed at the head of deep foundations should be developed. This way, the loading conditions can be changed from axial shear to torsional shear with the objective of corroborating the findings from laboratory tests that indicate that torsional shear mobilizes larger interface strength when the contacting soil is composed of angular particles. This should also be tested on larger model- and full-sized deep foundation systems.

APPENDIX A

RESULTS OF DIRECT SHEAR TESTS FOR SAND CHARACTERIZATION

A.1 Tests on Ottawa 20-30 Sand

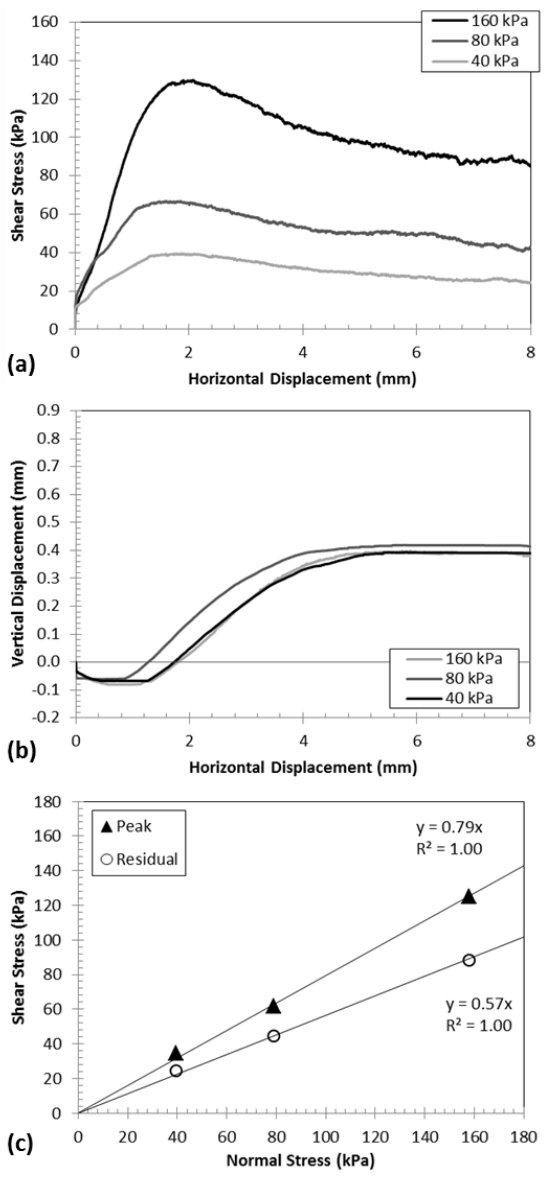

Figure A.1: Direct shear results for tests on Ottawa 20-30 sand. (a) Mobilized shear stress, (b) specimen volume changes, and (c) peak and residual failure envelopes.

Table A.1: Direct shear results for tests on Ottawa 20-30 sand.

Normal Stress (kPa)	Relative Density (%)	Shear Stress (kPa)		Strain Softening (kPa)	Friction Angle (°)		Measured Dilation Angle (°)
		Peak	Residual		Peak	Residual	
39.4	72.3	34.5	24.6	9.8	38.5	29.2	10.2
78.9	69.3	61.8	44.6	17.2			10.2
157.7	75.3	124.9	88.5	36.3			10.6

A.2 Tests on Ottawa 50-70 Sand

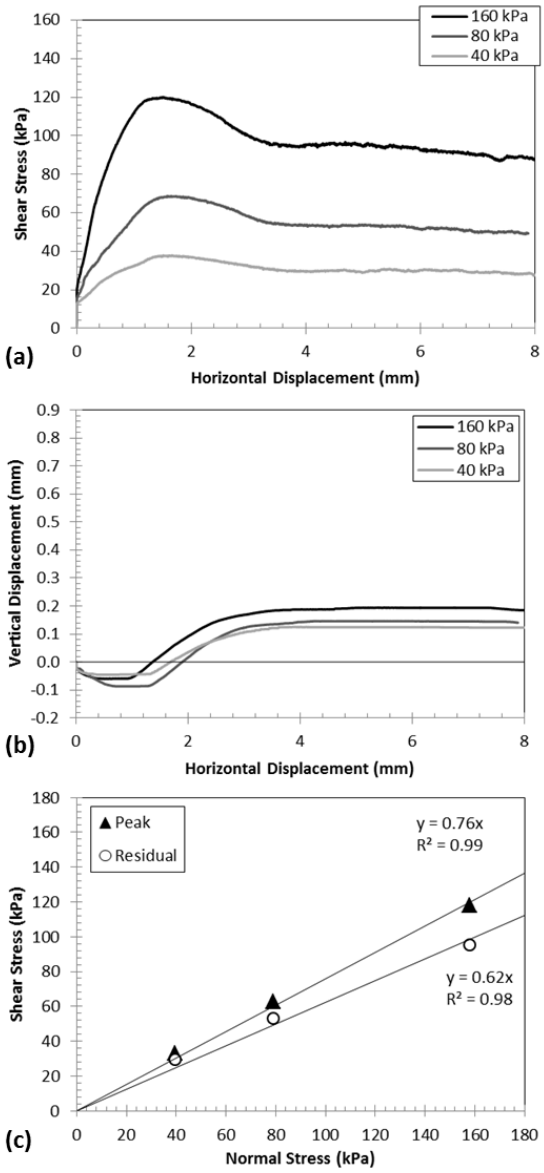

Figure A.2: Direct shear results for tests on Ottawa 50-70 sand. (a) Mobilized shear stress, (b) specimen volume changes, and (c) peak and residual failure envelopes.

Table A.2: Direct shear results for tests on Ottawa 50-70 sand.

Normal Stress (kPa)	Relative Density (%)	Shear Stress (kPa)		Strain Softening (kPa)	Friction Angle (°)		Measured Dilation Angle (°)
		Peak	Residual		Peak	Residual	
39.4	62.2	32.9	29.5	3.3	37.5	31.8	5.6
78.9	68.5	62.7	53.1	9.6			7.9
157.7	67.5	117.7	95.3	22.4			7.0

A.3 Tests on Blasting 20-30 Sand

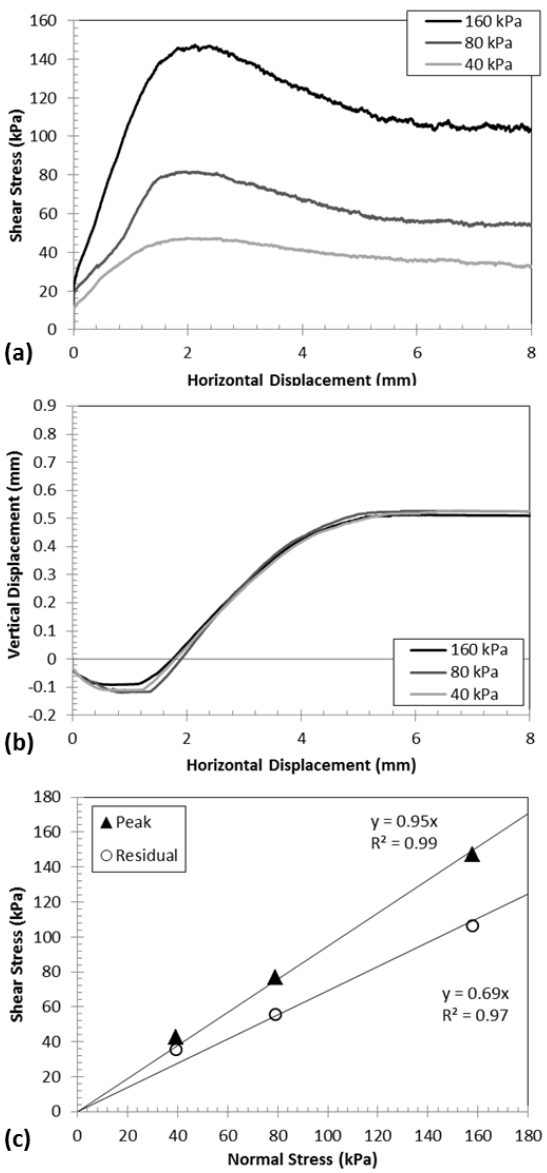

Figure A.3: Direct shear results for tests on Blasting 20-30 sand. (a) Mobilized shear stress, (b) specimen volume changes, and (c) peak and residual failure envelopes.

Table A.3: Direct shear results for tests on Blasting 20-30 sand.

Normal Stress	Relative Density (%)	Shear Stress (kPa)		Strain Softenin	Friction Angle (°)		Measured Dilation Angle (°)
		Peak	Residual		Peak	Residual	
39.5	72.1	42.5	35.4	7.1	44.1	34.6	12.1
78.9	68.3	76.8	55.8	21.0			13.9
157.8	69.9	147.4	106.5	40.9			12.2

APPENDIX B

CALIBRATION FACTORS FOR SENSORS USED WITH THE DRAINED AND UNDRAINED AXISYMMETRIC INTERFACE SHEAR DEVICES

Table B.1: Calibration factors for sensors used with the Drained Axisymmetric Interface Shear Device

Sensor	Calibration Factor for 10 V of Excitation	Calibration Factor for 15 V of Excitation
LVDT	-7.3158 mm/V	-4.8772 mm/V
RVDT	0.056 °/V	0.037 °/V
Pressure	10795.5 kPa/V	7197 kPa/V
Load Cell	-99981 lb/V	-66654 lb/V
Torque Cell	5111.13 N-m/V	3407.42 N-m/V

Table B.2: Calibration factors for sensors used with the Undrained Axisymmetric Interface Shear Device

Sensor	Calibration Factor for 10 V of Excitation	Calibration Factor for 15 V of Excitation
LVDT	-7.3158 mm/V	-4.8772 mm/V
RVDT	0.056 °/V	0.037 °/V
Pressure	10795.5 kPa/V	7197 kPa/V
Load Cell	-100000 lb/V	-66667 lb/V
Torque Cell	5111.13 N-m/V	3407.42 N-m/V

REFERENCES

Airey, D.W. and Kelly, R.B. (2010). "Interface behaviours from large diameter ring shear tests." *Proceedings of the Research Symposium on Characterization and Behavior of Interfaces*, Atlanta, GA, IOS Press, Fairfax, VA, pp. 1-6.

Alarcon-Guzman, A., Leonards, G.A., and Chameau, J.L. (1988). "Undrained monotonic and cyclic strength of sands." *Journal of Geotechnical Engineering*, 114, No. 10, pp. 1089-1109.

Alshibli, K.A. and Alramahi, B.A., (2006). "Microscopic evaluation of strain distribution in granular materials during shear," *Journal of Geotechnical and Geoenvironmental Engineering,* 132, No. 1, pp. 80-91.

Andrus, R.D. and Stokoe, K.H. II (2000). "Liquefaction resistance of soils from shear-wave velocity." *Journal of Geotechnical and Geoenvironmental Engineering*, 126, No. 11, pp. 1015-1025.

Ashmawy, A.K., Sukumaran, B., and Hoang, V.V. (2003). "Evaluating the influence of particle shape on liquefaction behavior using discrete element modeling." *Proceedings of the Thirteenth International Offshore and Polar Engineering Conference (USOPE 2003),* Honolulu, HI. pp. 542-549.

ASTM D 3080-11. "Standard test method for direct shear test of soils under consolidated drained conditions." *Annual Book of ASTM Standards*, West Conshohocken, PA.

ASTM D 4253-14. "Standard test methods for maximum index density and unit weight of soils using a vibratory table." *Annual Book of ASTM Standards,* West Conshohocken, PA.

ASTM D 4254-14. "Standard test methods for minimum index density and unit weight of soils and calculation of relative density." *Annual Book of ASTM Standards,* West Conshohocken, PA.

ASTM D 5321–14. "Standard test method for determining the shear strength of soil-geosynthetic and geosynthetic-geosynthetic interfaces by direct shear." *Annual Book of ASTM Standards*, West Conshohocken, PA.

ASTM D 5778-07. "Standard test method for electronic friction cone and piezocone penetration testing of soils," *Annual Book of ASTM Standards*, West Conshohocken, PA.

Azadi, M.R.E., Nordal, S. and Sadein, M. (2008). "Nonlinear behavior of pile-soil subjected to torsion due to environmental loads on jacket type platforms." *World Scientific and Engineering Academy and Society (WSEAS) Transactions on Fluid Mechanics*, 4, No. 4, pp. 390-400.

Barden, L., Ismail, H., and Tong, P., (1969). "Plane strain deformation of granular material at low and high pressures." *Géotechnique*, 19, No. 4, pp. 441-542.

Bardet, J.P., (1994). "Observations on the effect of particle rotations on the failure of idealized granular materials," *Journal of Mechanics of Materials*, 18, No. 2, pp. 159-182.

Barmpopoulos, I.H., Ho, T.Y.K., Jardine, R.J., and Anh-Minh, N. (2010). "The large displacement shear characteristics of granular media against concrete and steel interfaces". *Proceedings of Characterization and Behavior of Interfaces*, Atlanta, GA, IOS Press, Fairfax, VA pp. 16-23.

Basack, S. and Sen. S. (2014). "Numerical solutions of single pile subjected to simultaneous torsional and axial loads." *International Journal of Geomechanics*, 14, No. 4, pp. 1-14.

Been, K. and Jefferies, M.G. (1985). "A state parameter for sands." *Géotechnique*. 35, No. 2, pp. 99-112.

Been, K., Jefferies, M.G., and Hachey, J. (1991). "The critical state of sands." *Géotechnique*, 41, No. 3, pp. 365-381.

Bolton, M.D. (1986). "The strength and dilatancy of sands." *Géotechnique*, 36, No. 1, pp. 65-78.

Bond, T. (2011). "Rotary jacking of tubular piles." M.S. Thesis, *University of Cambridge*, Cambridge.

Boulanger, R.W. and Idriss, I.M. (2014). "CPT and SPT based liquefaction triggering procedures." *Center for Geotechnical Modeling,* University of California, Davis. Report No. UCD/CGM-14/01, 138 pp.

Boulon, M. and Foray, P. (1986). "Physical and numerical simulation of lateral shaft friction along offshore piles in sand." *Proceedings of 3rd International Conference on Numerical Methods for Offshore Piling*, Nantes, France, Editions Technip, France, pp. 127-147.

Bray, J.D., O'Rourke T.D., Cubrinovski, M., Zupan, J.D., Jeon, S.S., Taylor, M., Toprak, Sl., Hughes, M., van Ballegooy, S. and Bouziou, D. (2013). "Liquefaction impact on critical infrastructure in Christchurch." *Final Technical Report, USGS.*

Cargill, P.E. (1999) "The influence of friction sleeve roughness on cone penetration measurements," M.S. Thesis, *Georgia Institute of Technology,* Atlanta, 140 pp.

Castro, G. (1975). "Liquefaction and cyclic mobility of saturated sands." *Journal of Geotechnical Engineering Division*, 101, No. 6, pp. 551-569.

Cha, M. (2012). "Mineral dissolution in sediments." PhD Dissertation, *Georgia Institute of Technology,* Atlanta, 152 pp.

Chandler, R. (1988). "In-situ measurement of the undrained shear strength of clays using the field vane." *Proceedings of Vane shear testing in soils: Field and laboratory studies*. ASTM, Philadelphia, PA. pp. 13 - 44.

Cheng, Y.P. and Minh, N.H. (2009). "DEM investigation of particle size distribution effects on direct shear behavior of granular agglomerates." *Powders and Grains, Proceedings of the 6th International Conference on Micromechanics of Granular Media*, Golden, CO, American Institute of Physics (AIP), Melville, NY, pp. 401-404.

Cho, G.C., Dodds, J. and Santamarina, J.C. (2006). "Particle shape effects on packing density, stiffness and strength: Natural and Crushable Sands." *Journal of Geotechnical and Geoenvironmental Engineering*, 132, No. 5, pp. 591-602.

Chow, F. C. (1997). "Investigations into the behaviour of displacement piles for offshore foundations." PhD thesis, *Imperial College*, University of London.

Chow, Y. K. (1985). "Torsional response of piles in nonhomogeneous soil." *Journal of Geotechnical Engineering*, 111, No. 7, pp. 942–947.

Cui, L. and O'Sullivan, C. (2006). "Exploring the macro- and micro-scale response of an idealized granular material in the direct shear apparatus." *Géotechnique*, 56, No.7, pp. 455-468.

Cundall, P.A. and Strack, O.D.L. (1979). "A discrete numerical model for granular assemblies", *Géotechnique*, 29, No.1, pp. 47-65.

DéCourt, L. and Filho, A.R.Q. (1994). "Practical application of the standard penetration test complemented by torque measurements, SPT-T, present stage and future trends." *Proceedings of the 13th International Conference on Soil Mechanics and Foundation Engineering*, New Delhi, India, CRC Press, Boca Raton, FL, pp. 143-146.

Deeks, A.D. and White, D. (2008). "Centrifuge modelling of rotary-jacked tubular piles: gyropiling." Proceedings of the 2nd BGA International Conference on Foundations (ICOF). UK, pp. 532-544.

DeJong, J.T., (2001). "Investigation of particulate-continuum interface mechanics and their assessment through a multi-friction sleeve penetrometer attachment," PhD Dissertation, *Georgia Institute of Technology*, Atlanta, 360 pp.

DeJong, J.T., Frost, J.D., and Sacs, M. (2000) "Relating quantitative measures of surface roughness and hardness to geomaterial interface strength," *Proceedings Geo-Eng 2000*, Sydney, AUS.

DeJong, J.T., Frost, J.D., and Cargill, P.E., (2001). "Effect of surface texturing on CPT friction sleeve measurements," *Journal of Geotechnical and Geoenvironmental Engineering*, 127, No. 2, pp. 158-168.

DeJong, J.T. and Frost, J.D., (2002). "A multi-friction sleeve attachment for the cone penetrometer," *ASTM Geotechnical Testing Journal*, 25, No. 2, pp. 111-127.

DeJong, J.T., Randolph, M.F. and White, D.J. (2003). "Interface load transfer degradation during cyclic load: a microscale investigation." *Soils and Foundations*, 43, No. 4, pp. 81-93.

DeJong, J.T., White, D.J. and Randolph, M.F. (2006). "Microscale observation and modeling of soil-structure interface behavior using particle image velocimetry." *Soils and Foundations*, 46, No. 1, pp. 15-28.

DeJong, J.T., and Westgate, Z.J., (2009). "Role of initial state, material properties, and confinement condition on local and global soil-structure interface behavior," *Journal of Geotechnical and Geoenvironmental Engineering*, 135, No. 11, pp. 1646-1660.

DeJong, J.T. and Westgate, Z. J. (2010). "Linking global interface response to microscale particle-interface behavior." *Proceedings of the Research Symposium on Characterization and Behavior of Interfaces*, Atlanta, GA, IOS Press, Fairfax, VA, pp. 24-34.

Dietz, M. and Lings, M. (2006). "Postpeak strength of interfaces in a stress-dilatancy framework." *Journal of Geotechnical and Geoenvironmental Engineering*, 132, No. 11, pp. 1474-1484.

Dietz, M. and Lings, M. (2010). "Changes in surface roughness in multi-reverse sand-steel interface tests." *Proceedings of the Research Symposium on Characterization and Behavior of Interfaces*, Atlanta, GA, IOS Press, Fairfax, VA, pp. 7-15.

Dove, J.E., Frost, J.D., Han J., and Bachus, R.C. (1997) "The Influence of geomembrane Surface roughness on interface strength," *Proceedings, Geosynthetics '97*, 2, Indus Fabr, pp. 863-876.

Dove, J.E., and Frost, J.D., (1999). “Peak friction behavior of smooth geomembrane-particle interfaces,” *Journal of Geotechnical and Geoenvironmental Engineering,* 125, No. 7, pp. 544-555.

Dove, J. and Jarrett, J. (2002). ”Behavior of dilative sand interfaces in a geotribology framework.” *Journal of Geotechnical and Geoenvironmental Engineering.*, 128, No.1 , pp. 25–37.

Dove, J.E., Bents, D.D., Wang, J. and Gao, B. (2006). “Particle-scale surface interactions of non-dilative interface systems.” *Geotextiles and Geomembranes*, 24, No. 3, pp. 156-168.

Dutt, R.N. and O’Neill, M.W. (1983). “Torsional behavior of model piles in sand.” *Proceedings of Geotechnical practices in offshore engineering, ASCE, Reston, VA*, Austin, pp. 315-334.

Edil, T.E., Bosscher, P.J., and Sundberg, A.J. (2006). “Soil-structure interface shear transfer behavior”. *Proceedings Geomechanics II*, Japan, ASCE, Reston, VA, pp. 528-543.

Finno, R.J., Harris, W.W., Mooney, M.A. and Viggiani, G., (1996). “Strain localization and undrained steady state of sand,” *Journal of Geotechnical and Geoenvironmental Engineering*, 122, No. 6, pp. 462-473.

Frost, J.D. and Han, J. (1999) "Behavior of interfaces between fiber-reinforced polymers and sands," *Journal of Geotechnical and Geoenvironmental Engineering*, 125, No. 8, pp. 633-640.

Frost, J.D., DeJong, J.T., and Recalde, M. (2002). “Shear failure behavior of granular-continuum interfaces.” *Engineering Fracture Mechanics*, 69, No. 17, pp. 2029-2048.

Frost, J.D., Hebeler, G.L, Evans, T.M., and DeJong, J.T. (2004) "Interface behavior of granular soils," *Proceedings ASCE Earth and Space 2004 Conference*, Houston, TX, ASCE, Reston, VA, pp. 65-72.

Frost, J.D., and DeJong, J.T., (2005). "In situ assessment of the role of surface roughness on interface response," *Journal of Geotechnical and Geoenvironmental Engineering*, 131, No. 4, pp. 498-511.

Frost, J.D., and Martinez, A., (2012). "Axial-torsional multi-sleeve friction penetration system for lunar subsurface studies," *Proceedings ASCE Earth and Space 2012 Conference*, Pasadena, CA, ASCE, VA, pp. 335-343.

Frost, J.D., Hebeler, G.L., and Martinez, A., (2012). "Cyclic multi-piezo-friction sleeve penetrometer testing for liquefaction assessment," *Proceedings of 4th International Conference on Geotechnical and Geophysical Site Characterization (ISC'4)*, Pernambuco, Brazil, 1, CRC Press, Boca Raton, FL, pp. 629-636.

Frost, J.D., and Martinez, A., (2013). "Multi-sleeve axial-torsional-piezo friction penetration system for subsurface characterization," *Proceedings of the 18th ISSMGE International Conference on Soil Mechanics and Geotechnical Engineering*, Paris, France., pp. 527-530.

Frost, J.D., and Martinez, A., (2014). "Advances in development of axial-torsional multi-sleeve penetrometer for extra-terrestrial studies," *Proceedings ASCE Earth and Space 2014 Conference*, St. Louis, ASCE, Reston, VA, pp. 1-9.

Gavin, K.G. and O'Kelly, B.C. (2007). "Effect of friction fatigue on pile capacity in dense sand." *Journal of Geotechnical and Geoenvironmental Engineering*, 133, No. 1, pp. 63-71.

Georgiadis, M., and Saflekou, S. (1990). "Piles under axial and torsional loads." *Computers and Geotechnics*, 9, No. 4, pp. 291–305.

Ghionna, V., and Jamiolkowski, M., (1991). "A critical appraisal of calibration chamber testing of sands," *Proceedings of the 1st International Symposium on Calibration Chamber Testing (ISOCCT1)*. Elsevier, Potsdam, NY, pp 13-39.

Guo, W. D., and Randolph M. F. (1996). "Torsional piles in nonhomogeneous media." *Computers and Geotechnics*, 19, No. 4, pp. 265–287.

Gylland, A.S., Jostad, H.P., Nordal, S. and Emdal, A. (2013). "Micro-level investigation of the in situ shear vane failure geometry in sensitive clay." *Géotechnique*, 63, No. 14, pp. 1264-1270.

Hazla, E. (2012). "Rotary press-in piling in hard ground." Undergraduate Project, *University of Cambridge*, Cambridge. 50 pp.

He, C., Zeng, X., and Wilkinson, A. (2013). "Geotechnical properties of GRC-3 lunar simulant." *ASCE Journal of Aerospace* Engineering, 26, No. 3, pp. 528-534.

Hebeler, G.L., (2005). "Multi scale investigations of interface behavior," PhD Dissertation. *Georgia Institute of Technology*, Atlanta, 772 pp.

Hebeler, G.L., Frost, J.D. and Shinn, J.D., (2004). "Using textured friction sleeves at sites traditionally problematic to *CPT," Proceedings of the 2nd International Conference on Site Characterization*, Portugal, IOS Press, Amsterdam, Neatherlands, pp. 693-699.

Hebeler, G.L., and Frost, J.D., (2006), "A multi piezo-friction attachment for penetration testing", *Proceedings of ASCE Geo-Institute Congress: Geotechnical Engineering in the Information Technology Age*, Atlanta, GA, ASCE, Reston, VA, pp. 1-6.

Hebeler, G.L., Martinez, A. and Frost, J.D., (2015). "Shear zone evolution of granular soils in contact with conventional and textured CPT friction sleeves," published online in the *KSCE Journal of Civil Engineering.*

Ho, T.Y.K, Jardine, R.J., and Anh-Minh, N., (2011). "Large-displacement interface shear between steel and granular media." *Géotechnique*, 61, No. 3, pp. 221-234.

Hu, M., O'Sullivan, C., Jardine, R.R. and Jiang, M. (2010). "Stress-induced anisotropy in sand under cyclic loading potential particles: a method for modelling non-circular particles in DEM." *Proceedings of the International Symposium on Geomechanics and Geotechnics: From Micro to Macro*. Shanghai, CRC Press, London, UK, pp. 469-476.

Huang, X., Hanley, K.J., O'Sullivan, C., and Kwok, C.Y. (2014). "Exploring the influence of interparticle friction on critical state behavior using DEM." *International Journal of Numerical and Analytical Methods in Geomechanics*, 38, No. 12, pp. 1276-1297.

Huang, X., O'Sullivan, C., Hanley, K.J. and Kwok, C.Y. (2014) "Discrete-element method analysis of the state parameter." *Géotechnique*, 64, No. 12, pp. 954-965.

Hryciw, R.D. and Irsyam, M. (1993). "Behavior of sand particles around rigid ribbed inclusions during shear". *Soils and Foundations*, 33, No. 3, pp. 1-13.

Irsyam, M. and Hryciw, R.D. (1991). "Friction and passive resistance in soil reinforced by plane ribbed inclusions". *Géotechnique*, 41, No. 4, pp. 485-498.

Iscimen, M. (2004). "Shearing behavior of curved interfaces." PhD Dissertation, *Georgia Institute of Technology*, Atlanta, 130 pp.

Iwashita, K., and Oda, M., (1998). "Rolling resistance at contacts in simulation of shear band development by DEM," *Journal of Engineering Mechanics*, 124, No. 3, pp. 285-292.

Iwashita, K., and Oda, M., (2000). "Micro-deformation mechanisms of shear banding processes based on modified distinct element method," *Powder Technology*, 109, No. 3, pp. 192-205.

Jang, J.D., Frost, J.D. and Park, J.Y. (1999). "Preparation of epoxy impregnated sand coupons for image analysis." *ASTM Geotechnical Testing Journal*, 124, No. 2, pp. 147-158.

Jardine, R. J. and Chow, F. C. (1996). "New design methods for offshore piles," MTD96/103. *London: Marine Technology Directorate*.

Jefferies, M.G. and Been, K. (2006). "*Soil liquefaction – a critical state approach*." Taylor & Francis, 478 pp.

Jewell, R.A. (1989). "Direct shear tests on sand." *Géotechnique*, 39, No. 2, pp. 309-322.

Juang, C.H. and Holtz, R.D., (1986). "Preparation of specimens of noncohesive material for mercury intrusion porosimetry," *Geotechnical Testing Journal*, 9, No. 3, pp. 154-155.

Kelley, S.P. and Lutenegger, A.J. (2004). "Unit skin friction from standard penetration test supplemented with the measurement of torque." *Journal of Geotechnical and Geoenvironmental Engineering*, 130, No, 5, pp. 540-543.

Kong, L.G. and Zhang, L.M. (2008). "Experimental study of interaction and coupling effects in pile groups subjected to torsion." *Canadian Geotechnical Journal*. 45, No. 7, pp. 1006-1017.

Kryut, N.P. and Rothenburg, L. (2006). "Shear strength, dilatancy, energy and dissipation in quasi-static deformation of granular materials." *Journal of Statistical Mechanics: Theory and Experiment*., 7, pp. 1-13.

Kulhawy, F.H. and Mayne, P.W. (1990). "Manual for estimating soil properties for foundation design," *Electric Power Research Institute*, EL-6800 Research Project 1493-6.

Lambe, W.T., and Whitman, R.V. (1969). "*Soil mechanics*," John Wiley & Sons, New York, US.

Latzel, M., Luding, S. and Herrmann H. (2000). "Macroscopic material properties from quasi-static, microscopic simulations of a two-dimensional shear cell." *Granular Matter*, 2, No. 3, pp. 123-135.

Lehane, B. M. (1992). "Experimental investigations of pile behavior using instrumented field piles." PhD Dissertation, *Imperial College*, University of London.

Lee, S.W. (1998) "Influence of surface topography on interface strength and counterface soil structure," PhD Dissertation, *Georgia Institute of Technology*, Atlanta, 336 pp.

Lu, Y. (2010). "Reconstruction, characterization, modeling and visualization of inherent and induced digital sand microstructures." PhD Dissertation. *Georgia Institute of Technology*, Atlanta, 215 pp.

Lutenegger, A.J. and Kelley, S.P. (1998). "Standard penetration tests with torque measurements." *Proceedings of Geotechnical Site Characterization ISC'98*, 2, Atlanta, GA, Balkema, Brookfield, VT, pp. 939-945.

Lunne, T., Robertson, P.K. and Powell, J.J.M. (1997). "*Cone penetrating testing in geotechnical practice*." New York: Blackie Academic, EF Spon/Routledge Publishers, 312 pp.

Maeda, K. (2009). "Critical state-based geo-mechanics on granular flow." *Powders and Grains 2009: Proceedings of the 6th International Conference on Micromechanics of Granular Media,;* Golden CO, American Institute of Physics (AIP), Melville, NY pp. 17-24.

Martinez, A. and Frost, J.D., (2014a). "Axisymmetric shearing of sand-steel interfaces under axial and torsional loading," *Proceedings of GeoCongress 2014*. Atlanta, Georgia, ASCE, Reston, VA, pp. 644-653.

Martinez, A., and Frost, J.D., (2014b). "Axial and torsional axisymmetric laboratory interface shear tests for CPT attachment studies*," Proceedings of the 3rd International Symposium on Cone Penetration Testing*, Las Vegas, Nevada, pp. 179-187.

Martinez, A., Frost, J.D., and Hebeler, G.L. (2015). "Experimental study of shear zones formed at sand/steel interfaces in axial and torsional axisymmetric tests." *ASTM Geotechnical Journal,* 38, No. 4, pp. 409-426.

Masson, S. and Martinez, J. (2001). "Micromechanical analysis of the shear behavior of a granular material." *ASCE Journal of Mechanical Engineering* 2001, 127, No. 10, pp. 1007-1016.

Mitchell, J.K and Villet, W.C.B. (1987). "Reinforcement of earth slopes and embankments*." National Cooperative Highway Research Program Report 290*. Washington, D.C.L Transportation Research Board of the National Research Council.

Mitchell, J.K. and Soga, K (2005). "*Fundamentals of soil behavior*." Third Edition. John Wiley & Sons, Hoboken, N.J.

Misra, A., Saggu, R., Basu, D and Chakraborty, T. (2014). "Analysis of pile subjected to torsion in multi-layered soil." *International Journal for Numerical and Analytical Methods in Geomechanics*, 38, No. 5, pp. 475-492.

Mohamed, A., and Gutierrez, M., (2010). "Comprehensive study of the effect of rolling resistance on the stress-strain localization behavior of granular materials," *Granular Matter*, 12, No. 5, pp. 527-541.

Monaco, P., Marchetti, S., Totani, G. and Calabrese, M. (2005). "Sand liquefiability assessment by Flat Dilatometer Test (DMT)." *Proceedings XVI International Conference of Soil Mechanics and Geotechnical Engineering*, Japan, Millpress, The Netherlands, pp. 2693-2697.

Mortara, G., Mangiola, A. and Ghionna, V.N. (2007). "Cyclic shear stress degradation and post-cyclic behavior from sand-steel interface direct shear tests." *Canadian Geotechnical Journal*, 44, No. 7, pp. 739-752.

Mühlhaus, H.B. and Vardoulakis, I., (1987). "The thickness of shear bands in granular materials." *Géotechnique*, 37, No. 3, pp. 271-283.

Novoa-Martinez, B. (2003). "Strength properties of granular materials," Master's thesis. *Louisiana State University*, Baton Rouge, 92 pp.

Ng, T.T. (2009). "Discrete element simulations of the critical state of granular media." *International Journal of Geomechanics*, 9, No. 5, pp. 209-216.

Oda, M., Konishi, J., and Nemat-Nasser, S., (1982). "Experimental micromechanical evaluation of strength of granular materials: Effect of Particle Rolling," *Mechanics of Materials*, 1, No. 4, pp. 269-283.

Oda, M., Nemat-Nasser, S., and Konishi, J. (1985). "Stress-induced anisotropy in granular masses." *Soils and Foundations*, 25, No. 3, pp. 85-97.

Oda, M and Kazama, H (1998). "Microstructure of shear bands and its relation to the mechanisms of dilatancy and failure of dense granular soil." *Géotechnique*, 48, No. 4, pp. 465-481.

Oda, M., and Iwashita, K., (2000). "Study of coupled stress and shear band development in granular media based on numerical simulation analysis," *International Journal of Engineering Science*, 38, pp. 1713-1740.

O'Sullivan, C. and Cui, L. (2009). "Micromechanics of granular material response during load reversals: combined DEM and experimental study." *Powered technology*, 193, No. 3, pp. 289-302.

O'Sullivan, C. (2011). "*Particulate discrete element modelling: a geomechanics perspective.*" Routledge, New York, N.Y.

Ouadfel, H. and Rothenburg, L. (2001). "'Stress-force-fabric' relationship for assemblies of ellipsoids." *Mechanics of Materials*, 33, No. 4 , pp. 201-221.

Pasten, C., Shin, H. and Santamarina, J.C. (2014). "Long-term foundation response to repetitive loading." *Journal of Geotechnical and Geoenvironmental Engineering*, 140, No. 4, pp. 1-11.

Piexoto, A.S.P. and Carvalho, D. (1999). "Standard penetration test with torque measurements (SPT-T) and some factors that affect the T/N ratio*." Proceedings of the XI Panamerican Conference on Soil Mechanics and Geotechnical Engineering*, Brazil, pp. 1605-1612.

Poulos, H.G. (1975). "Torsional response of piles." *Journal of the Geotechnical Engineering Division*, 101, No. 10, pp. 1019-1035.

Randolph, M.F. (1981). "Piles subjected to torsion." Journal of the Geotechnical Engineering Division, 107, No. GT8, pp. 1095 – 1111.

Randolph, M. F., Dolwin, J. & Beck, R. (1994). "Design of driven piles in sand." *Géotechnique*, 44, No. 3, pp. 427–448.

Rao, K.S.S., Allam, M.M. and Robinson, R.G. (1998). "Interfacial friction between sands and solid surfaces." *Proceedings Of the Institution of Civil Engineers – Geotechnical Engineering,* 131, No. 2, pp. 75-82.

Reese, L.C. (1978). The 12th Terzaghi Lecture, "Design and construction of drilled shafts." *ASCE Journal of the Geotechnical Engineering Division*, 104, No. GT1, pp. 91-116.

Rimoy, S., Jardine, R., and Standing, J.R. (2013). "Displacement response to axial cycling of piles driven in sand." *Proceedings of the Institution of Civil Engineerin, Geotechnical Engineering*, 166, No. 2, pp. 131-146.

Robertson, P.K. (1990) "Soil classification using the cone penetration test," *Canadian Geotechnical Journal*, 27, No. 1, 151-158.

Robertson, P.K. (2009). "CPT interpretation – a unified approach." *Canadian Geotechnical Journal*, 46, No. 11, pp. 1337-1355.

Robertson, P.K. (2010). "Estimating in-situ state parameter and friction angle in sandy soils from CPT." *Proceedings of the 2nd International Symposium on Cone Penetration Testing*, Huntington Beach, CA.

Rothenburg, L. and Bathurst, R.J. (1989). "Analytical study of induced anisotropy in idealized granular materials." *Géotechnique*, 39, No. 4, pp. 601-614.

Rothenburg, L. and Kruyt, N.P. (2004). "Critical state and evolution of coordination number in simulated granular materials." *International Journal of Solids and Structures*, 41, No. 21, pp. 5763-5774.

Rowe, P.W. (1962). "The stress-dilatancy relation for static equilibrium of an assembly of particles in contact," *Proceedings of the Royal Society*. 269A, 500-527.

Santamarina, J.C. and Cho, G. C. (2001). "Determination of critical state parameters in sandy soils – simple procedure." *ASTM Geotechnical Testing Journal*, 24, No. 2, pp. 185-192.

Santamarina, J.C. and Cho, G.C., (2003). "The omnipresence of localizations in particulate materials," *Proceedings of the International Symposium on Deformation Characteristics of Geomaterials*, Lyon, France, Swets & Zeitlinger B.V., The Netherlands, pp. 465-473.

Scarpelli, G., and Wood, D.N., (1982). "Experimental observations of shear band patterns in direct shear tests," *IUTAM Conference on Deformation and Failure of Granular Materials*, The Netherlands, pp. 473-484.

Schmertmann, J (1977). "Guidelines for Cone Penetration Test: Performance and Design." *Dept. of Transportation Federal Highway Administration, Offices of Research and Development*, Washington.

Seed, H.B. (1979). "Soil liquefaction and cyclic mobility evaluation for level ground during earthquakes." *Journal of Geotechnical Engineering Division*, 105, No. 2, pp. 551-569.

Simpson, D.C., (2014). "Behavioral thresholds in mixtures of sand and clay." Master's dissertation, *Oregon State University*, Corvallis, 135 pp.

Stoll, U.W. (1972). "Torque shear test of cylindrical friction piles. *Civil Engineering*, 42, No. 4, pp. 63-64.

Tabucanon, J. T. (1997). "Shaft resistance of piles in sand." PhD dissertation, *University of Sydney*, Australia.

Thomson, E., (1930). "Quantitative microscopy analysis," *Journal of Geology*, 38, No. 3, pp. 193-222.

Tsuha, C.H.C., Foray, P.Y., Jardine, R.J., Yang, Z.X., Silva, M. and Rimoy, S. (2012). "Behavior of displacement piles in sand under cyclic axial loading." *Soils and Foundations*, 52, No. 3, pp. 393-410.

Uesugi, M. and Kishida, H., (1986). "Frictional resistance at yield between dry sand and mild steel," *Soils and Foundations*, 26, No. 4, pp. 139-149.

Uesugi, M, Kishida, H. and Tsubakihara, Y. (1989). "Friction between sand and steel under repeated loading." *Soils and Foundations*, 29, No. 3, pp. 127-137.

Vardoulakis, I., (1980). "Shear band inclination and shear modulus of sand in biaxial tests," *International Journal of Numerical and Analytical Methods in Geomechanics*, 4, No. 2, pp. 103-119.

Thornton, C. (2000). "Numerical simulations of deviatoric shear deformation of granular media." *Géotechnique*, 50, No.1, pp. 43-53.

Wang, J., Gutierrez, M.S., and Dove, J.E., (2007a). "Numerical studies of shear banding in interface shear tests using a new strain calculation method," *International Journal for Numerical and Analytical Methods in Geomechanics*, 31, No. 12, pp. 1349-1366.

Wang, J., Dove, J.E. and Gutierrez, M.S. (2007b). "Discrete-continuum analysis of shear banding in the direct shear test." *Géotechnique*, 57, No.6, pp. 513-526.

Wang, J. and Jiang, M. (2011). "Unified soil behavior of interface shear test and direct shear test under the influence of lower moving boundaries." *Granular Matter*, 13, No. 5, pp. 631-641.

White, D.J. and Lehane, B.M. (2004). "Friction fatigue on displacement piles in sand." *Géotechnique*, 54, No. 10, pp. 645-658.

Williams, J. (2004). *Engineering tribology*. Cambridge University Press, Oxford, UK.

Wilson, N. (1963). "Laboratory vane shear tests and the influence of pore-water stresses." *Proceedings of Vane shear testing in soils: Field and laboratory studies*. ASTM, Philadelphia, PA. pp. 377-385.

Yang, J. (2002). "Non-uniqueness of flow liquefaction line for loose sand." *Géotechnique*, 52, No. 10, pp. 757-760.

Yang, Z.X., Yang, J. and Wang, L.Z. (2012). "On the influence of inter-particle friction and dilatancy in granular materials: a numerical analysis." *Granular Matter*. 14, No. 3, pp. 433-447.

Zelasko, J.S., Krizek, R.J. and Edil, T.B. (1975). "Shear behavior of sand as a function of grain characteristics." *Istanbul Conference on Soil Mechanics and Foundation Engineering*, Turkey, pp. 55-64.

Zhang, L. (2010). "Nonlinear analysis of torsionally loaded piles in a two-layer soil profile." *International Journal of Geomechanics*, 10, No. 2, pp. 65–73.

Zhang, L.M. and Kong, L.H. (2006). “Centrifuge modeling of torsional response of piles in sand.” *Canadian Geotechnical Journal*. 43, No. 5, pp. 500-515.

VITA

ALEJANDRO MARTINEZ

Alejandro Martinez was born in Torreón, México, in January 24th, 1988 to Arturo Martínez and Hilda Vela de Martínez. Alejandro was the youngest of three children, after Liliana and the late Arturo. He lived in Torreón until the age of 12, where he finished elementary school and started playing tennis. He then moved to Monterrey, México, where he completed middle school and after one year of high school enrolled in the International Baccalaureate program of the Universidad de Monterrey, where he obtained an IBO diploma. Meanwhile, he practiced tennis for three hours a day and competed in national tournaments, reaching top 10 national ranking for the 14 and 16 years categories. In 2006, he started his undergraduate studies at Jackson State University in civil engineering with an athletic scholarship for being part of the tennis varsity team. After two years, he transferred to the University of Texas at Austin where he got involved with different student organizations (OLA and Chi Epsilon) and started assisting Dr. Jorge Zornberg and Jeff Kuhn as an undergraduate researcher. In 2010, he obtained his bachelor's degree in civil engineering.

Three weeks after his bachelor's graduation commencement, he moved to Atlanta to start his master's studies at Georgia Tech working with Dr. David Frost. While he was not initially sure he wanted to pursue a Ph.D. degree, the graduate-level classes and interactions with Dr. Frost quickly convinced him that a Ph.D. was the path to follow. In 2012, he obtained his master's degree, started his Ph.D. studies and started dating Chelsea Hopkins. Throughout his Ph.D. studies, Alejandro has performed multi-scale studies of particulate-continuum interface systems under axial and torsional loading conditions. He has also had the chance to get involved in teaching activities that include serving as the instructor of record and teaching assistant of classes at Georgia Tech. Alejandro enjoys classic and modern rock, reading Latin American literature and science fiction and the company of his family and friends. He expects to obtain his Ph.D. degree in December in 2015.